THESIS

THE EFFECTS OF BEND RADIUS ON FLOW AROUND A CONFIGURATION OF BENDWAY WEIRS: INSIGHT FROM A NUMERICAL MODEL

Submitted by

Taylor Hogan

Department of Civil and Environmental Engineering

In partial fulfillment of the requirements

For the Degree of Master of Science

Colorado State University

Fort Collins, Colorado

Summer 2019

Master's Committee:

Advisor: Christopher Thornton
Co-Advisor: Robert Ettema

John Williams

ABSTRACT

THE EFFECTS OF BEND RADIUS ON FLOW AROUND A CONFIGURATION OF BENDWAY WEIRS: INSIGHT FROM A NUMERICAL MODEL

Bendway weirs have been used and refined for decades by hydraulic engineers to control thalweg location within alluvial rivers and to decrease flow velocity along the outer bank of channel bends. Although these structures have been used in a variety of applications, there are still a wide range of acceptable design parameters that vary in accordance with the specific design methodology being used. Since the early 2000s, Colorado State University's Hydraulics Lab has assisted The U.S Bureau of Reclamation (USBR) in refining the design of bendway weirs and similar in-stream rock structures. During this period of time, Colorado State University and The USBR have utilized hydraulic and numerical models to develop systematic design guidelines for bendway weirs and other in-stream rock structures. Hydraulic modeling has also provided a large database of velocity and water surface measurements that have been used to calibrate and validate subsequent numerical models.

The partnership between Colorado State University and the USBR has led to design recommendations and equations in which the effect of many variables and their sensitivity in overall bendway weir design has been identified. This study investigates the parameter radius of curvature over channel top width, R_c/T_w, and its effect on the flow field around bendway weirs, as its significance in bendway weir design is not well known. To investigate the effects of R_c/T_w on the bendway weir flow field, the 2D numerical model SRH-2D was used in conjunction with AutoCAD Civil3D software. The SRH-2D model was created using the bathymetry of the hydraulic model and then also calibrated and validated using data collected in the hydraulic model. AutoCAD Civil3D was used to create four different bend radii while holding T_w constant, representing R_c/T_w values between 3.0 and 8.0 which are typical of the Middle Rio Grande that the hydraulic model represented. Two additional trapezoidal channel models were also created to isolate the possible effects from specific channel geometry on the bendway weir flow field comparisons.

2D numerical modeling results revealed that the bend radius of curvature had negligible effect on the bendway weir flow field. Velocity patterns in the trapezoidal and native bathymetry channels changed negligibly in location and magnitude across varying bend radii. Cross-sectional velocity distributions were also evaluated and showed that the inner and middle third lateral sections of the channel showed the same (within fractions of a percent) velocity increase after the installation of bendway weirs. The outer fifth of the channel resulted in 6% velocity decrease only varying approximately 0.1% between bend radii. Overall numerical modeling results showed that the bendway weir flow field was negligibly affected by the bend radius of curvature, R_c.

ACKNOWLEDGEMENTS

I would first like to thank my advisor, Dr. Chris Thornton for not only giving me the opportunities to work in the CSU hydraulics lab but also the countless hours he has spent teaching me about hydraulics in both the theoretical and applied fields. I would not be in the academic and professional position that I am in today without him.

Thanks are also due in high order to Dr. Rob Ettema who has helped guide me through the majority of this study. Dr. Ettema has spent many hours reviewing my work, problem solving, and discussing results. I greatly appreciate his time and energy that he has put into this project. I also thank my third committee member Dr. John Williams for his time and input.

I also thank my colleagues at the Engineering Research Center for their collaboration on this project, specifically Seth Siefken and Dr. Shin. Their support and knowledge helped me tremendously during the course of this study.

Finally, I would like to thank my family for their never-ending support during my time in school. They have offered invaluable encouragement that has helped me push through my graduate studies. I specifically thank my Dad, Scott Hogan for helping me grow my love for hydraulic engineering and always encouraging me to strive for my goals.

TABLE OF CONTENTS

LIST OF TABLES

LIST OF FIGURES

LIST OF SYMBOLS

A^* = percentage of baseline cross-sectional flow area blocked by structure

D_b = average thalweg depth in bend before the installation of structures

D = hydraulic depth

Δz = elevation difference between the baseline water surface and structure crest at the tip

L_c = length of the structure crest, measured as the distance along the structure crest from the waterline at the design flowrate to the tip of the crest

L_{proj} = projected length of the structure, defined as the shortest distance from the tip of the structure crest to the waterline along the outer bank

L_{arc} = arc length along the bank between the centerline of adjacent structures

m = slope of the structure toe, given as mH:1V (1 for bendway weirs)

$\tan\phi$ = slope of the structure crest; $\tan\phi = 0$ for bendway weirs

R_c = radius of curvature of channel bend centerline

T_w = average top-width of channel in the bend at the design flowrate before the installation of structures

θ = structure planform angle measured from the bank on the upstream side of the structure to the structure crest

W = width of structure crest

CHAPTER 1. INTRODUCTION

Since the early 2000s, Colorado State University (CSU) has been working with the United States Bureau of Reclamation (USBR) to research and improve the design of rock structures used as in-stream structures for control of alluvial channels. During this time, hydraulic and numerical models have been used to investigate the effectiveness of designs and to generate sets of data for rock structures such as rock vanes and bendway weirs. This study refers to a hydraulic model (also known as a physical model) as using hydraulic similitude in a physical environment to model open channel flow. CSU's hydraulic model was created using field data from a reach of the Middle Rio Grande River and included two, connected bends of the river. Hydraulic modeling enabled collection of flow velocity, water-surface elevation, and general visual inspection of the flow field leading to insight into the design parameters of these rock structures. Resulting work with the hydraulic model provided nearly 3,000 data points for use in calibrating a series of numerical computational fluid dynamic (CFD) models using the commercially available codes FLOW-3D and SRH-2D.

Objectives

The objective of the study was to determine the effect of bend radius of curvature on the flow field around a varying bend radii when bendway weirs are installed. The study used the depth-averaged, two-dimensional hydraulic model SRH-2D as the study's main method for addressing this objective. Additionally, the following secondary objectives were identified in support of this objective:

1. Construct, calibrate, and validate the SRH-2D model with selected baseline and bendway weir configurations to hydraulic model data.

2. Use the software AutoCAD Civil3D to adjust the original hydraulic model downstream bend bathymetry into three additional bends of differing radii. The top width of the bend was retained. The range of values of bend radius to channel top width encompassed the values occurring along the Middle Rio Grande.

CHAPTER 2. BACKGROUND

Bendway Weir Geometry

Bendway weirs are in-stream, rock structures that extend from the channel bank toward the channel center. They have a flat crest and are angled slightly upstream to re-direct flow towards the channel center. Their shape closely mimics a rock pile with a flat top and curved front as seen in Figure 1. This specific weir was installed in one CSU's outdoor test facilities to evaluate scour around the bendway weir. Bendway weirs were initially developed for use on the Mississippi River to reduce the magnitude of secondary flows and to enhance navigation, alleviate bend migration, and reduce bank erosion (Julien and Duncan 2003).

Figure 1: A bendway weir in CSU's outdoor flume

To stabilize bend migration and mitigate bank erosion, a series of bendway weirs redirects high-energy flow away from the susceptible banks and creates a zone of lower velocity between bendway weirs (Heintz 2002). An example of bendway weirs installed in series in a field application can be seen in Figure 2.

Figure 2: Bendway weirs installed in the field (Heintz 2002)

Bendway weirs are typically designed with the following geometric parameters (adopted from Siefken 2019). Plan and profile schematics of a bendway weir configuration are also provided in Figure 3.

A^* = percentage of baseline cross-sectional flow area blocked by structure

T_w = average top-width of channel in the bend at the design flowrate before the installation of structures

R_c = radius of curvature of channel bend centerline

L_c = length of the structure crest, measured as the distance along the structure crest from the waterline at the design flowrate to the tip of the crest

L_{proj} = projected length of the structure, defined as the shortest distance from the tip of the structure crest to the waterline along the outer bank

L_{arc} = arc length along the bank between the centerline of adjacent structures

Δz = elevation difference between the baseline water surface and structure crest at the tip

D_b = average thalweg depth in bend before the installation of structures

θ = structure planform angle measured from the bank on the upstream side of the structure to the structure crest

$\tan\phi$ = slope of the structure crest; $\tan\phi = 0$ for bendway weirs

m = slope of the structure toe, given as mH:1V

W = width of structure crest

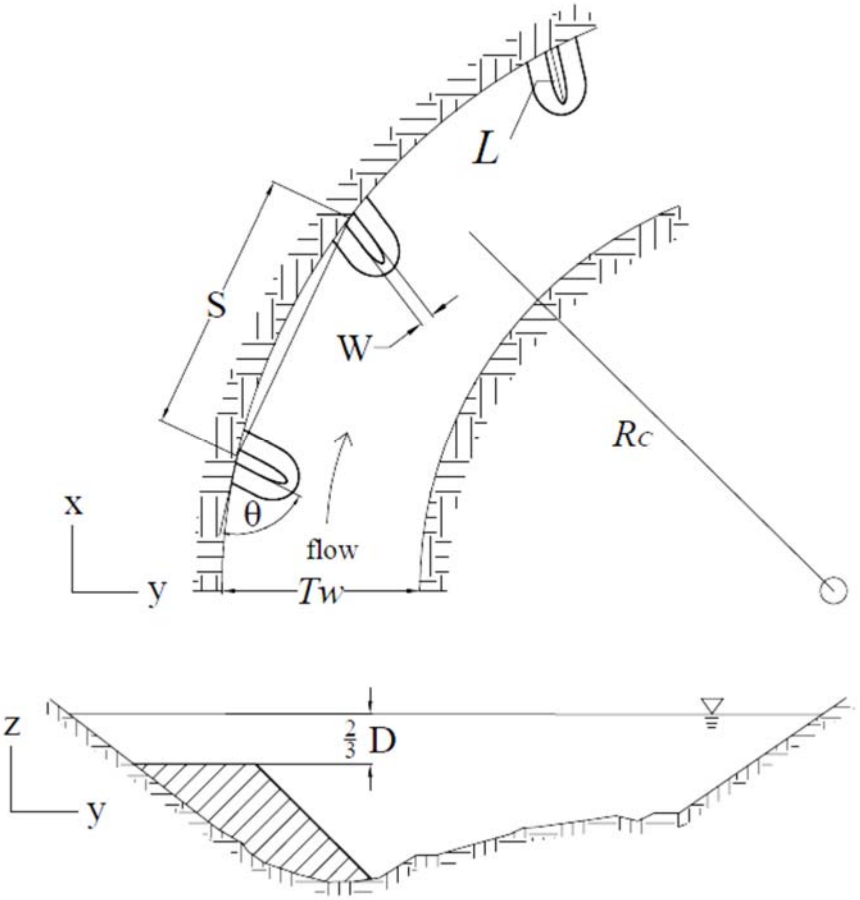

Figure 3: Geometric variables associated with bendway weirs (Scurlock et al. 2014)

The projected length, L_{proj}, of a bendway weir is calculated as:

$$L_{proj} = L_c sin\theta \tag{1}$$

The submergence of the bendway weir, Δz is defined as:

$$\Delta z = \frac{2}{3}D \tag{2}$$

The flow blocked by the bendway weir, A^* was defined as:

$$A^* = \frac{A_{structure}}{A_{flow}} \tag{3}$$

In Equation 3, A_{flow} is the cross sectional area of flow at the baseline condition located at the root of the structure. The term $A_{structure}$ was determined by projecting the structure onto the cross-section perpendicular to the flow direction. Figure 4 illustates these parameters for a bendway weir installed in a channel bend.

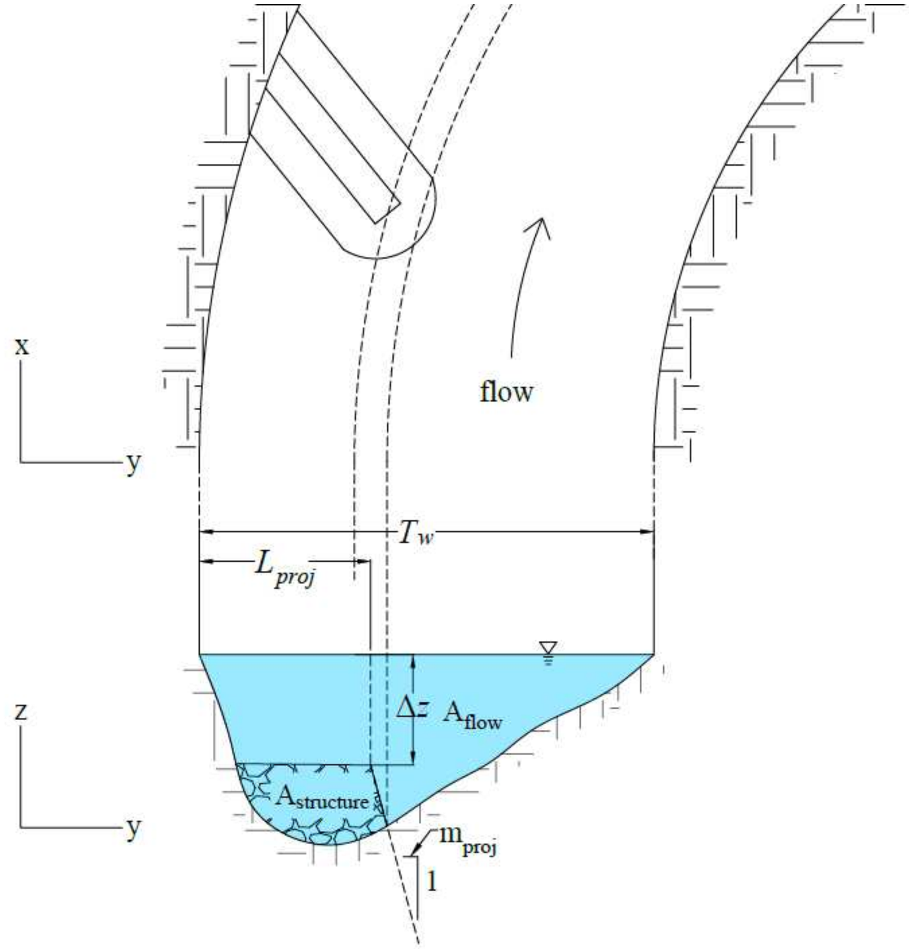

Figure 4: The projection of bendway weir onto a perpendicular cross-section (Adapted from Siefken 2019)

Existing Bendway Weir Design Guidelines

Existing guidelines for bendway weir configurations vary significantly depending on the source. Researchers and designers have struggled to converge on an optimal design of bendway weirs due to the complex flow regime that is associated with bendway weirs. Table 1 summarizes several design parameters from recent design guides and studies.

Table 1: Existing design guidelines for bendway weirs (after Scurlock 2014ab). The height is given in terms of hydraulic depth (D) or bank full depth (BF)

	Length		Length Type	Spacing		θ		Height	
Source	min	max		min	max	min	max	min	max
NCHRP 544 (2005)	$T_w/3$	$T_w/2$	crest	$1.5L_c$		70°	80°	$D/2$	D
HEC 23 (2009)	$T_w/10$*	$T_w/3$	crest	$4L_c$	$5L_c$	60°	80°	0.3B	0.5B
Julien and Duncan (2003)	case-by-case		N/A	$2L$	$3L$	60°		Max permitting navigation	

*HEC 23 further recommends that the crest be long enough to cross the thalweg

Project Background

The Middle Rio Grande is a 29-mile long reach of the Rio Grande in central New Mexico, extending from the downstream side of Cochiti Dam to Bernalillo, New Mexico. A map of the Middle Rio Grande reach is presented in Figure 5. In recent years, the Middle Rio Grande has been a test location for a variety of channel restoration techniques, including the use of native material and rock structures in attempts to control rates of bank erosion and channel migration, and mitigate habitat degradation (e.g., Darrow 2004).

The Middle Rio Grande is typically classified as a being perennial braided stream. In 1973, Cochiti Dam was built for flood control and sediment detention for the Albuquerque area, resulting in the dam trapping nearly all sediment supplied by a 14,600 square mile watershed (Richard 2001). Due to the sediment deficit downstream of the dam, the planform of the Middle Rio Grande changed. Richard (2001) stated that the channel has generally been transformed from a braided channel to a meandering stream containing a pool-riffle sequence. Schmidt (2005) also notes that Galesteo Creek and the Jemez River, two large tributaries to the Middle Rio Grande, were dammed previously to 1970 which contributed to the sediment deficiency.

Figure 5: Middle Rio Grande project reach (highlighted in red)

Due to this sediment deficiency and consequent lateral migration of the channel, the USBR has recognized the need for channel stabilization. While the stabilization efforts could take the form of riprap and concrete revetment, these efforts are not aesthetically pleasing and do not improve the aquatic habitat or riparian vegetation of the channel (Heintz 2002). Rock vanes and bendway weirs began to be used in the Middle Rio Grande as a suitable option for bank stabilization but lacked technical design guidance. Due to the lack of technical design guidelines for these structures, the USBR began a series of test programs with CSU to determine suitable design parameters.

Hydraulic Modeling

With the intent of developing design guidelines for in stream structures the USBR contracted with CSU to build a hydraulic model to evaluate the influences of selected design parameters. Since the area of interest was 29 miles long, the entire length would not fit in the modeling facility, so the reach was determined using GIS software to have 3 types of bends (Heintz 2002). Due to space limitations and use of a 1:12 length scale to maintain suitably high resolution, Type 1 and Type 3 bends were selected for use in the hydraulic model. Type 1 and 3 bends encompassed ranges of geometric channel characteristics that existed within the Middle Rio Grande River. Table 2 summarizes the prototype geometry used for the Type 1 and Type 3 bends, and Table 3 summarizes scaled characteristics used for the hydraulic model.

Table 2: Prototype characteristics of Types 1 and 3 bends

Type	Top Width ft (m)	Radius of Curvature ft (m)	Bend Angle degrees	Relative Curvature R_c/T_w	Channel Length ft (m)
1	230.4 (70.2)	465 (141.73)	125	2.02	1014 (309)
3	180 (54.86)	789.96 (240.77)	73	4.39	1002 (305)

Table 3: Characteristics of Types 1 and 3 bends (model scale)

Type	Top Width ft (m)	Radius of Curvature ft (m)	Bend Angle degrees	Relative Curvature R_c/T_w	Channel Length ft (m)
1	19.2 (5.9)	38.75 (11.81)	125	2.02	84.5 (25.8)
3	15 (4.6	65.83 (20.06)	73	4.39	83.5 (25.5)

The original hydraulic model utilized trapezoidal cross-sections to form both channel bends for the sake of simplicity and consistency as seen in Figure 6. Many rock structures and other in-stream structure configurations were tested in this prismatic channel resulting in design guidelines for spur dikes and in stream structures in a prismatic channel as well as many other design guidelines (Heintz 2002, Darrow 2004, Cox 2005, Kasper 2005, Kinzli 2005, Schmidt 2005, Walker 2009).

Figure 6: Trapezoidal channel used in the physical hydraulic model (Scurlock 2014)

After testing was completed with the prismatic channel and initial design guidelines were developed, the hydraulic model was retrofitted in 2006 to include a native bathymetry. To reduce construction costs and utilize the existing trapezoidal model foundation, native bathymetry cross-sections were built to fit within the existing trapezoidal channel (Walker 2009). These cross-sections were modeled after the Cochiti and San Felipe Bends that Figure 7 illustrates. Figure 8 shows the plan view layout of the channel after addition of native bathymetry and Figure 9 shows native bathymetry installed within the trapezoidal cross-sections. Native bathymetry was used to continue design parameter investigations of bendway weirs (Scurlock 2014) and rock vanes (Thornton 2016). Results of the tests provided nearly 2,500 velocity data points of the velocity field around the bendway weirs and rock vanes per configuration. Water surface measurements were also made, and in conjunction with velocity data can be used to calibrate future numerical models.

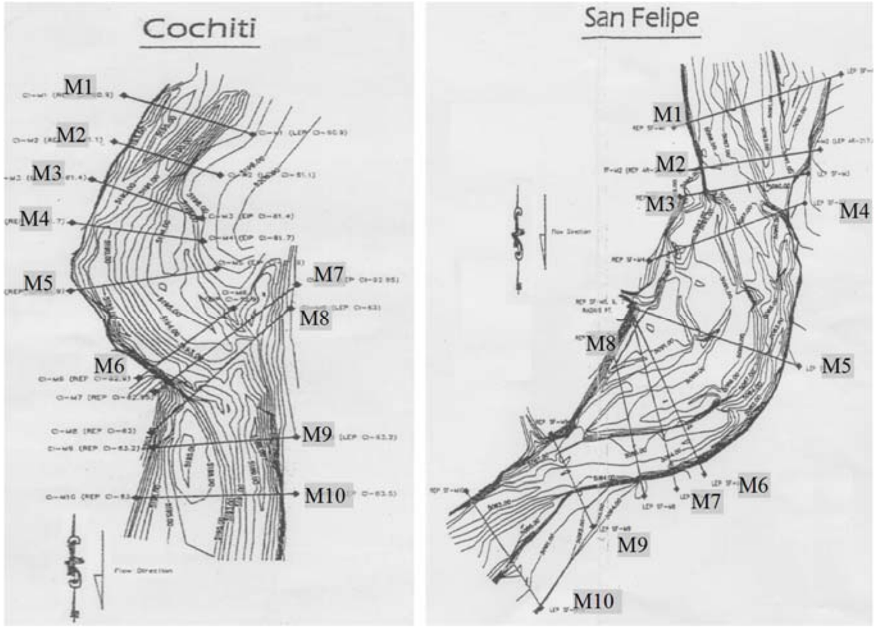

Figure 7: Plan view of cross-sections provided by the USBR for the Cochiti and San Felipe Bends (Walker 2009)

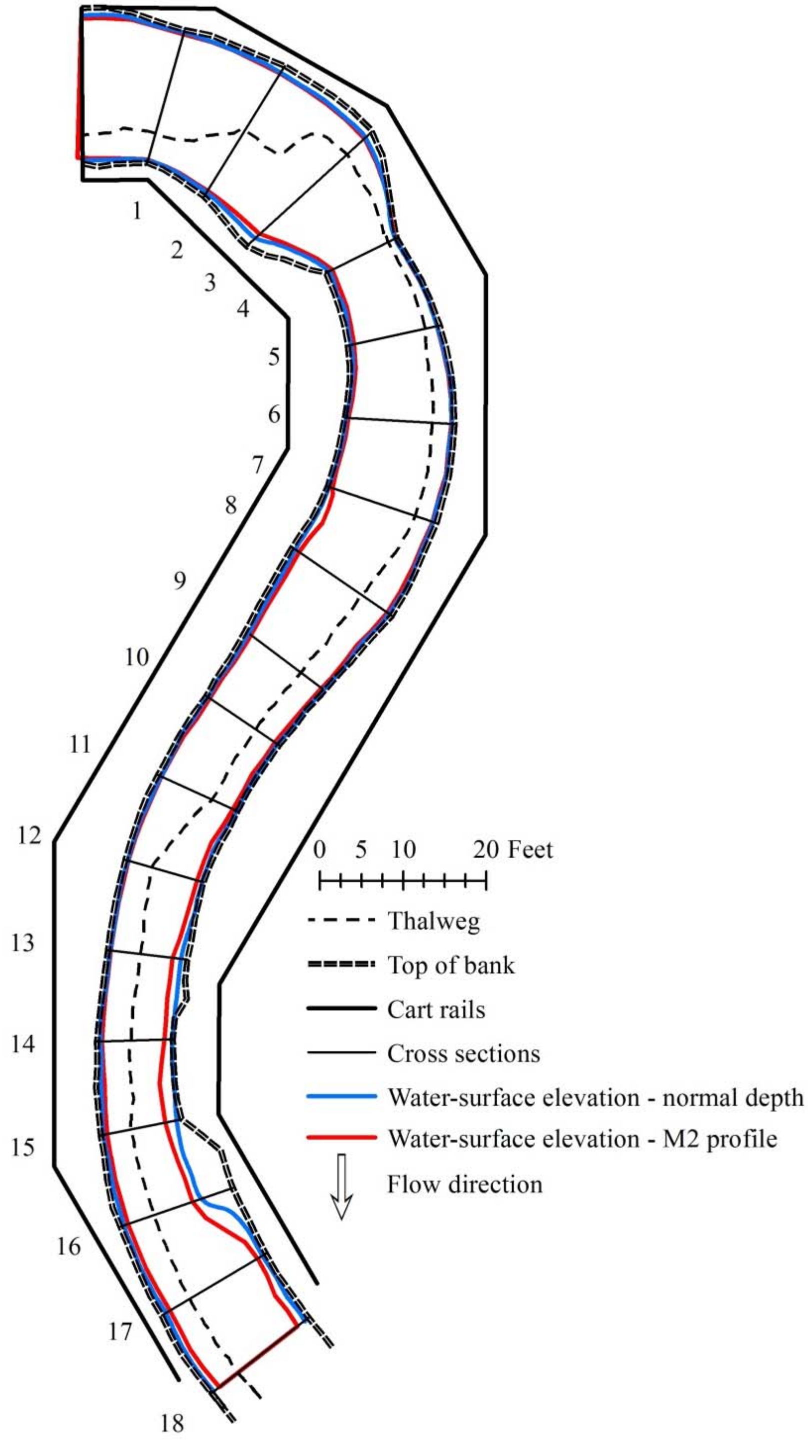

Figure 8: Plan view layout of the S-Curve hydraulic model after the addition of the native bathymetry (Thornton et al. 2016)

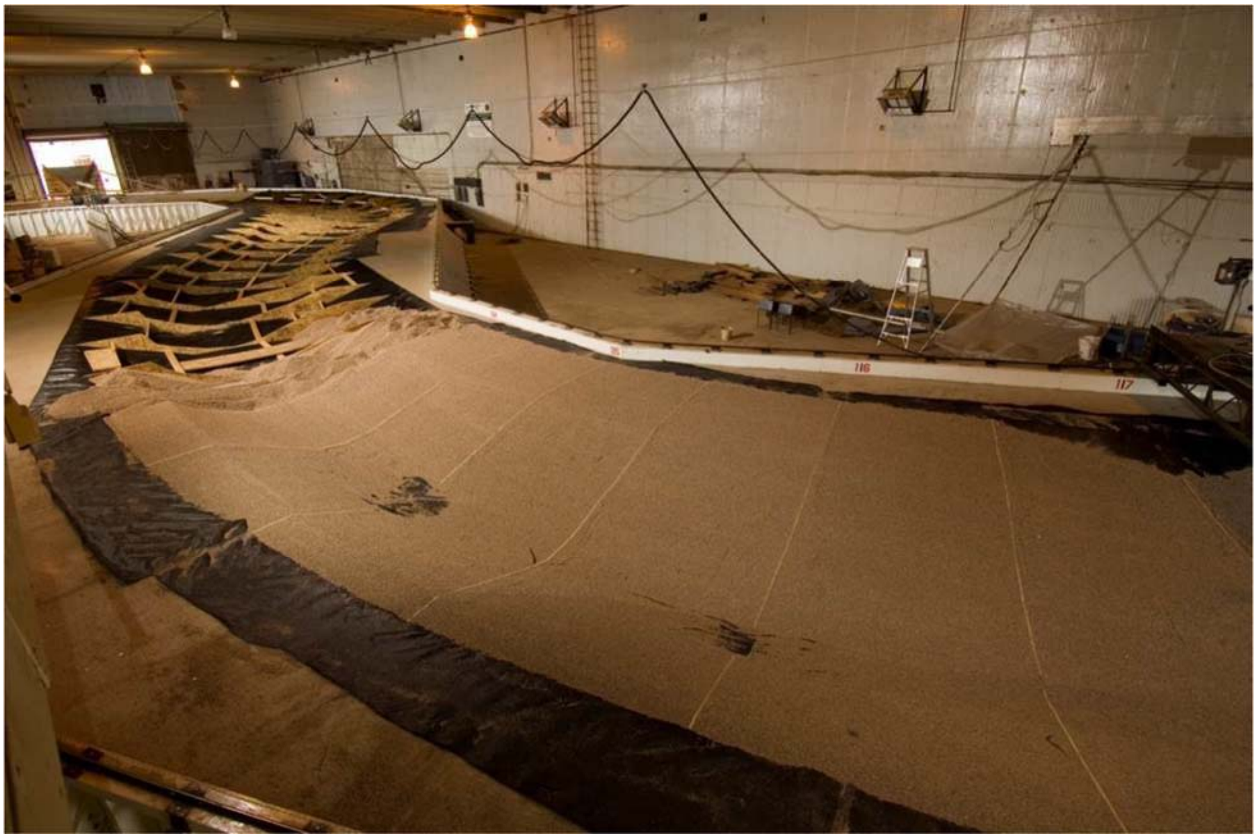

Figure 9: Construction of the simulated native bathymetry used in the hydraulic model (Scurlock 2014)

Data from hydraulic model configurations were used to calibrate the SRH-2D model used in this study. In specific, the baseline and BW01 configurations were used for calibration. The baseline configuration consisted of native bathymetry without bendway weirs or other rock structures installed in the channel. 'Baseline' will continue to be used as a phrase throughout the present study to refer to a channel without bendway weirs. BW01 consisted of a series of bendway weirs installed in the downstream bend. Table 4 summarizes the design characteristics of the BW01 series of weirs. Figure 10 also illustrates the layout of the BW01 in the downstream bend.

Table 4: BW01 Design characteristics

BW01 Characteristics

Length (ft)	Height (ft)	Crest Width (ft)	Spacing (ft)	θ (degrees)
Tw/3	D/3	$2D_{100}$	3.43L	2.02
3.09	0.247	1	10.6	4.39

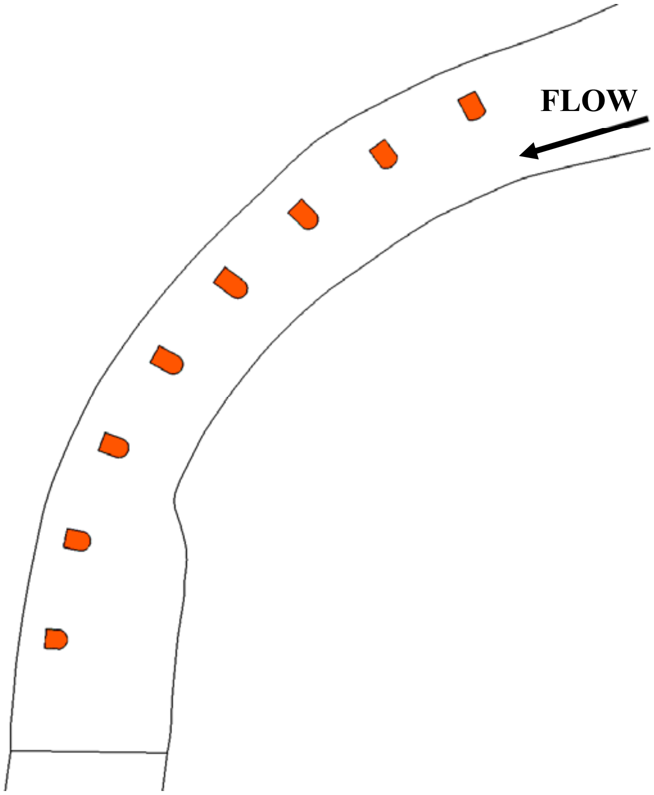

Figure 10: Bendway weir configuration used for the BW01 calibration

CSU Numerical Model Studies

Throughout CSU's study of transverse rock structures, several numerical models have been developed to gather additional insights on design parameters of these structures. CSU's numerical modeling program to this point has primarily used numerical models such as HEC-RAS (1-

dimensional (1D) representation of the flow around the bends) and FLOW-3D (3-dimensional (3D) representation of the flow around the bends) to simulate flow around bends fitted with bendway weirs.

Kasper (2005) created a 1D HEC-RAS model with the trapezoidal channel geometry of the hydraulic model. She found that his simulation matched the cross-sectional average flow depth very well. Differences in hydraulic and 1D models differed by about 3% for both bends. Sclafani (2010) then developed a 1D HEC-RAS model with bendway weirs and found that the flow depths he obtained matched flow depths in the hydraulic model to within about 3%. Section-average velocities for the two models differed between 4-32%. The larger magnitude of difference was not surprising as flow around the bendway weirs was noted to be highly three dimensional by Scurlock (2014a) and Siefken (2019) using FLOW3D. Accordingly, large errors readily arise when using 1D or 2D models to simulate bendway weir flow fields.

Scurlock (2014a) created a 3D numerical model using the commercially available code, FLOW-3D, and LiDAR scans of the native bathymetry replicated in the hydraulic model. Development of the FLOW-3D model enabled additional configurations of rock structures to be tested at a faster pace than the hydraulic model. In addition to the bathymetry replicated in the hydraulic model, Scurlock's model added a straight upstream extension to the upstream bend in order to develop stable flow conditions into the model. Figure 11 depicts Scurlock's FLOW-3D model geometry.

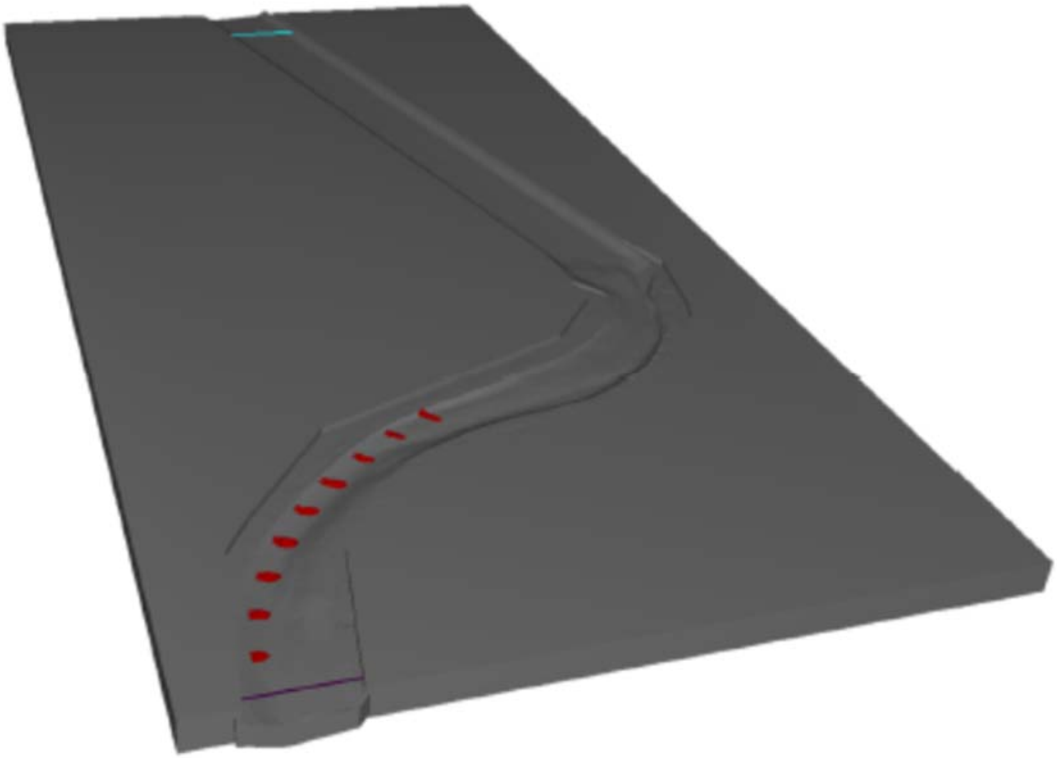

Figure 11: Channel geometry (gray) and installed structures (red) (Scurlock 2014a).

Scurlock (2014a) calibrated the model to match the flow field observed in the hydraulic model. His model was first calibrated for baseline conditions with no rock structures installed. Calibration yielded an optimal roughness height of 0.07 feet for the channel and a flow rate of 11.5 cfs to best match the flow observed in the hydraulic model. 12.0 cfs was used for the hydraulic model at baseline conditions, but due to flow leakage, Scurlock (2014a) used a reduced flow rate in his FLOW3D model. Calibration of Scurlock's FLOW3D model compared to the hydraulic model had a Mean Absolute Percent Difference (MAPD) of 3.78% for flow depth and 11.67% for velocity at 60% flow depth. Roughness height of the rock structures was varied but found not to affect the flow field. Form roughness of the rock structure evidently had a greater effect on flow field than did the surface roughness of the structure itself.

Scurlock (2014a) also calibrated his numerical model with bendway weirs and confirmed that the roughness height of the rock structures did not affect the flow field substantially, resulting in bendway weir roughness height set to 0.07 feet. MAPD for the calibration with bendway weirs was 4.61% for flow depth and 14.3% for velocity at 60% depth. It is important to note that the MAPD was higher for the calibration with bendway weirs as the flow field is complicated with the introduction of the bendway weirs.

Shin (2018) used the same FLOW3D model as developed by Scurlock (2014a) but modified the downstream boundary to include a straight extended channel that would allow the instream structures to create their own tail water conditions as depicted in Figure 12. He further calibrated the model and concluded that a further-reduced flow rate of 10.5 cfs produced the closest result to the hydraulics model results. He also found that the same roughness height for the channel and bendway weirs, of 0.07 ft, as had Scurlock (2014a).

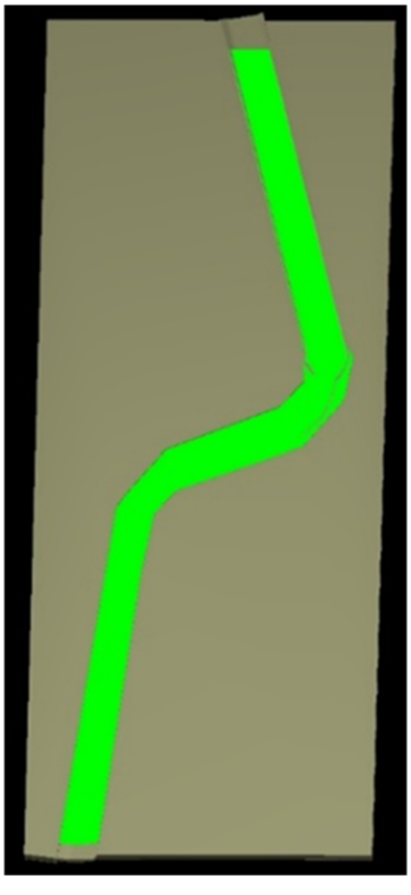

Figure 12: Scurlock (2014a) channel with Shin (2018) straight downstream extension (flow top to bottom)

Modification of the Hydraulic Model Channel Contraction

Original hydraulic model bathymetry included a contracted section at the upstream end of the model that created an undesirable expansion and eddy effects on the flow field. Holste (2016) mentioned that the contraction caused the flow to accelerate and be directed away from the outer bank. Since the contraction negatively affected Shin's (2018) numerical simulations, Shin used Civil 3D to modify the bathymetry and create a bend without a contraction; he called this bend the "modified baseline bathymetry". The present study used the contracted bathymetry used in Scurlock (2014a) for calibration purposes as it was the same as the hydraulic model. All bend configurations in this present study except for the two calibration simulations study used the modified baseline bathymetry (non-contracted channel) of Shin (2018). To ensure removal of the channel contraction didn't affect flow in the downstream bend, Shin conducted a HEC-RAS model that confirmed the water-surface elevation in the downstream bend did not change with removal of the channel contraction. Figure 13 shows the modified baseline channel bathymetry and Figure 14 shows the original contracted hydraulic model geometry.

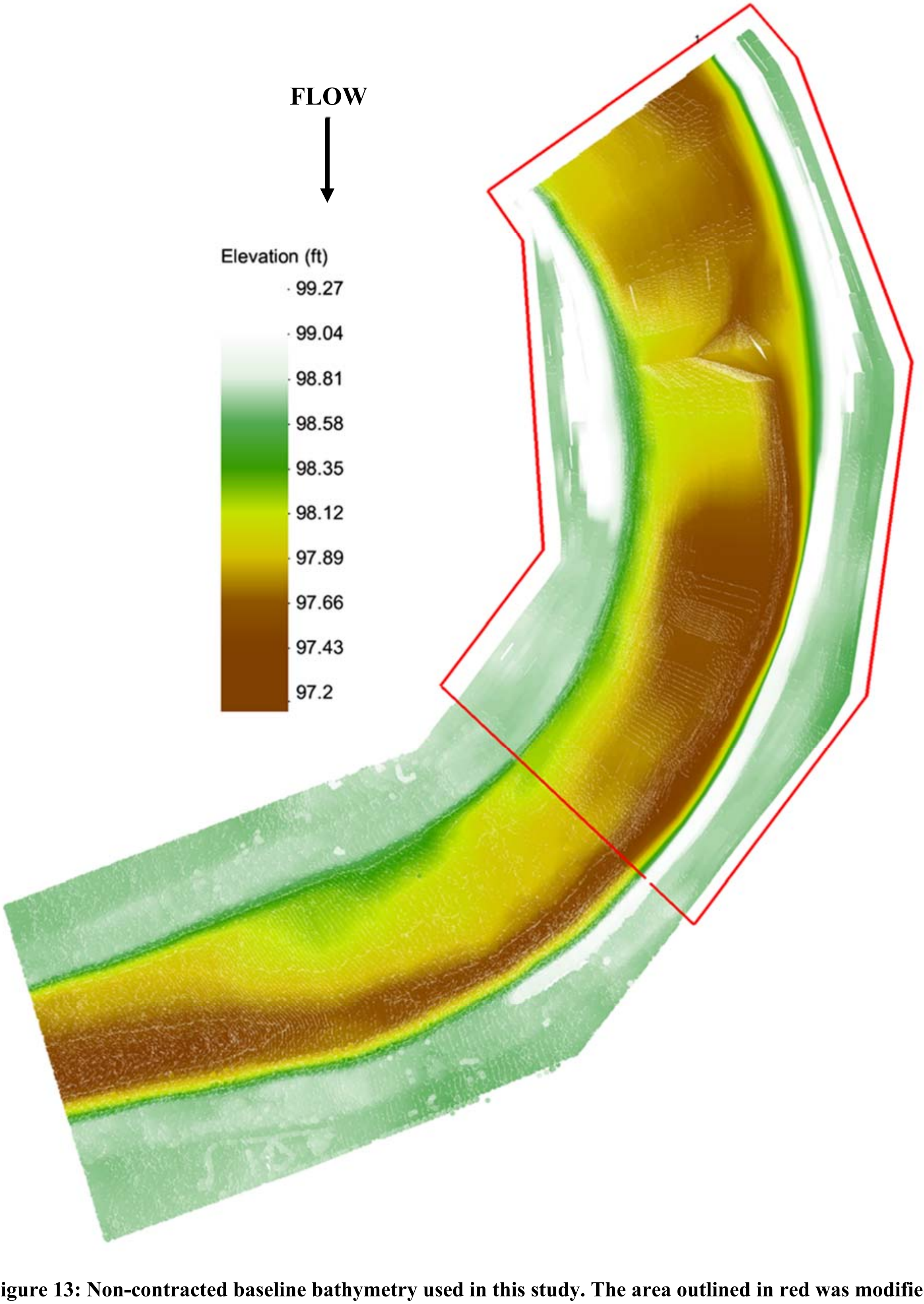

Figure 13: Non-contracted baseline bathymetry used in this study. The area outlined in red was modified from the contracted section in Figure 14.

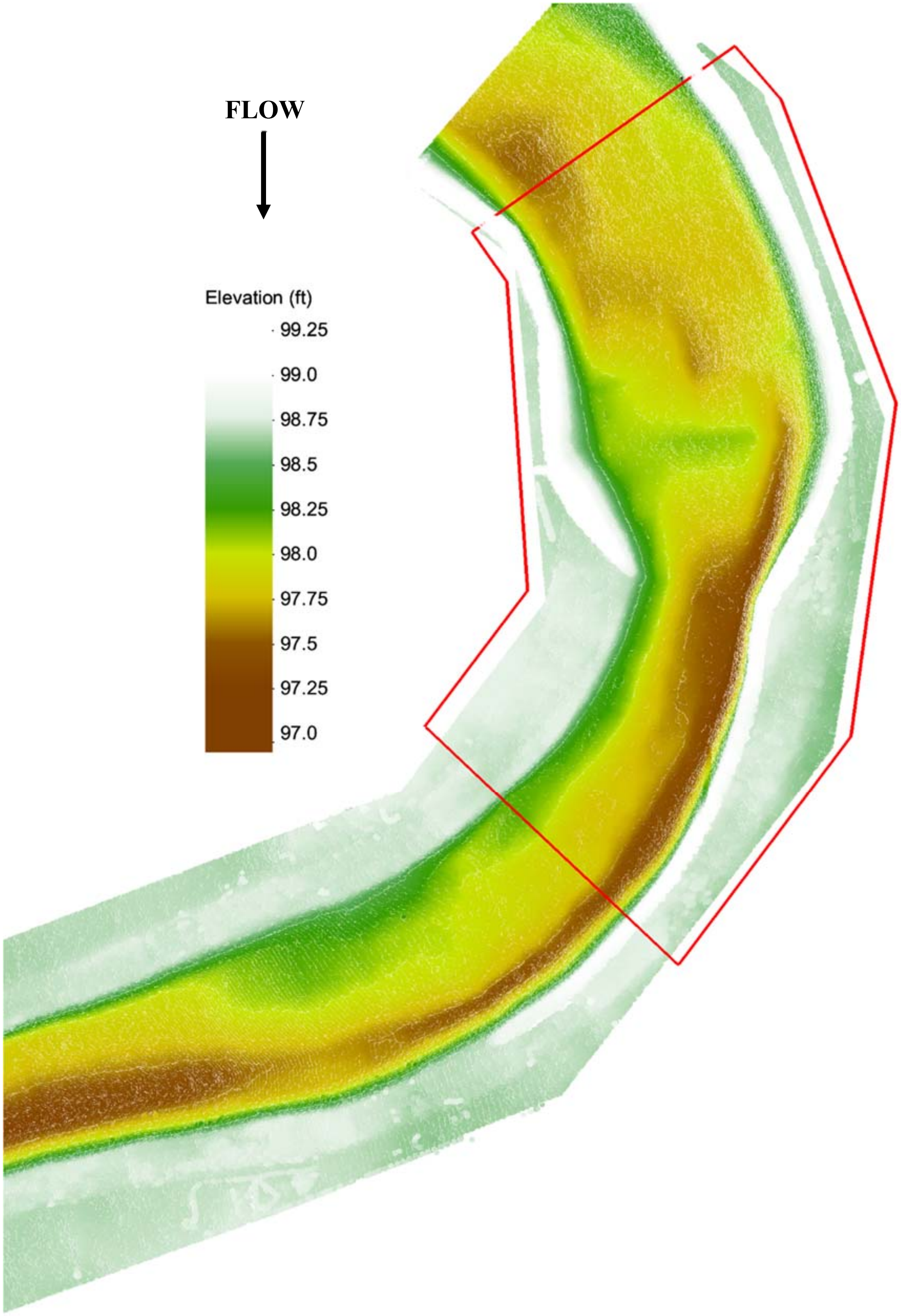

Figure 14: The original hydraulic model contracted bathymetry

Coordinate System Change From Previous Studies

Models developed by Scurlock (2014) and Shin (2018) transformed and rotated collected data from the hydraulic model coordinate system as FLOW3D required the downstream exit cross-section to be parallel with its horizontal x-axis. FLOW3D models of Scurlock and Shin used stereo-lithography (.stl) files to create their computational mesh. An inherent quality of .stl files is that they do not maintain the original coordinate system as their source. Instead, the new (0,0) coordinate is set to the bottom left corner of the object (when viewing a top/plan view). Creation of the .stl files caused inconsistencies between the coordinate systems of Scurlock and Shin. This present study created a consistent coordinate system transformation and rotation from the hydraulic model coordinate system that could be used by FLOW3D, Civil3D, and SRH-2D interchangeably.

The transformation matrix in Equation 4 was used for the present study to transform and rotate collected data from the hydraulic model to the numerical model coordinate system (similar to Scurlock (2014a) and Shin (2018)):

$$\begin{bmatrix} x_{num} \\ y_{num} \end{bmatrix} = \begin{bmatrix} \cos\psi & -\sin\psi \\ \sin\psi & \cos\psi \end{bmatrix} \begin{bmatrix} (x - T_X) \\ (y - T_Y) \end{bmatrix} \tag{4}$$

Where:

x = easting location in physical model [L];

y = northing location in physical model [L];

x_{num} = easting location in numerical model [L];

y_{num} = northing location in numerical model [L];

ψ = rotational angle between physical and numerical model = -38.543°;

T_X = linear translation in x-direction = 32.102 ft.; and

T_Y = linear translation in y-direction = 12.442 ft.

After applying the transformation and rotation in Equation 4, the data was also translated by +36.2956 feet in the x-direction and +152.6005 feet in the y-direction.

CHAPTER 3. MODEL CREATION

The USBR's Sedimentation and River Hydraulics model – Two Dimensional model (SRH-2D) was chosen to be used for this study. The model was created by Dr. Yong Lai of the USBR to assess channelized flow hydraulics and geomorphic change (Lai 2008). SRH-2D solves the 2D dynamic wave equations (depth-averaged St. Venant equations) using a flexible mesh design that can contain both quadrilateral and triangular elements to maximize accuracy and computational efficiency. SRH-2D has been proven to be robust and offer reliable results with very few tuning parameters, therefore becoming widely used (Lai 2008). For example, the Federal Highway Administration (FHWA) is currently developing additional tools, training, and support for SRH-2D and its user interface as part of a campaign called Every Day Counts (EDC).

In conjunction with SRH-2D a graphical user interface (GUI), SMS (Surface-water Modeling System) was used to create the model geometry and analyze results from the model. SMS, developed by Aquaveo, LLC was not crucial to run SRH-2D, but improved modeling utility. SMS was used in tandem with Autodesk Civil 3D to manipulate and create geometry for various bend radii.

Previous FLOW3D meshes in Scurlock (2014a), Shin (2018), and Siefken (2019) were created using Civil3D with LiDAR elevation data filtered until about 40% of the original elevation points remained. Filtering was necessary as Civil3D had limitations on the number of points that could define a surface. SMS did not have the same point limitation, so the original unfiltered LiDAR scan was used to allow the mesh to more accurately represent the hydraulic model bathymetry.

The mesh for the calibration simulations of this study included a straight-channel extension at the model's upstream and downstream boundaries from Shin (2018). Lengths of the upstream and downstream extensions were 170 feet and 150 feet respectively. Both extensions were created by extruding the furthest upstream or downstream cross section linearly at a 0.000863 feet/feet slope. Figure 15 depicts the mesh geometry used for the calibration simulations.

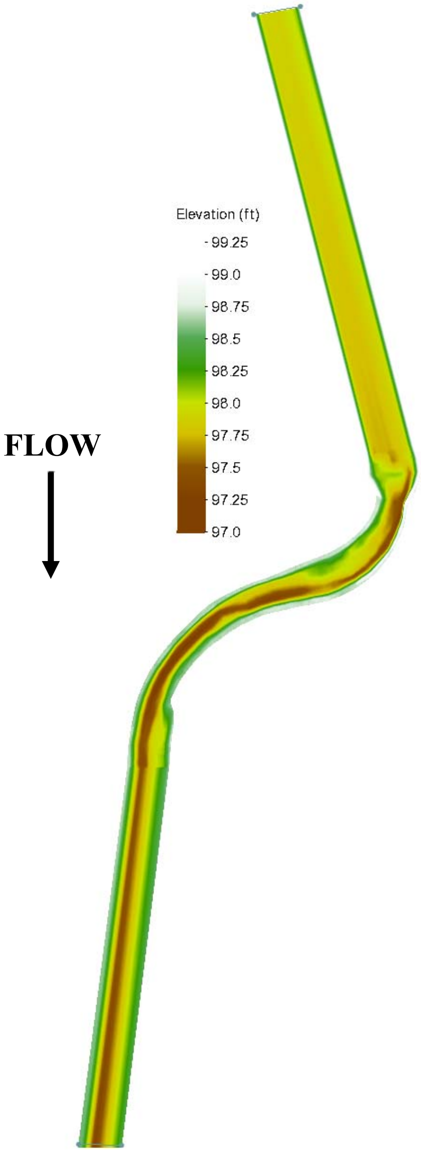

Figure 15: Mesh geometry used for the baseline and bendway weir calibration models

Figure 16 illustrates the mesh used in the present study for subsequent simulation runs after calibration. Two channel bends of equal radii to the upstream hydraulic model bend (40.41 feet) were added to replace the straight-channel extension at the model's upstream end that was used for calibration, as detailed in Siefken (2019). Further downstream bathymetry remained unchanged from calibration bathymetry for subsequent simulations.

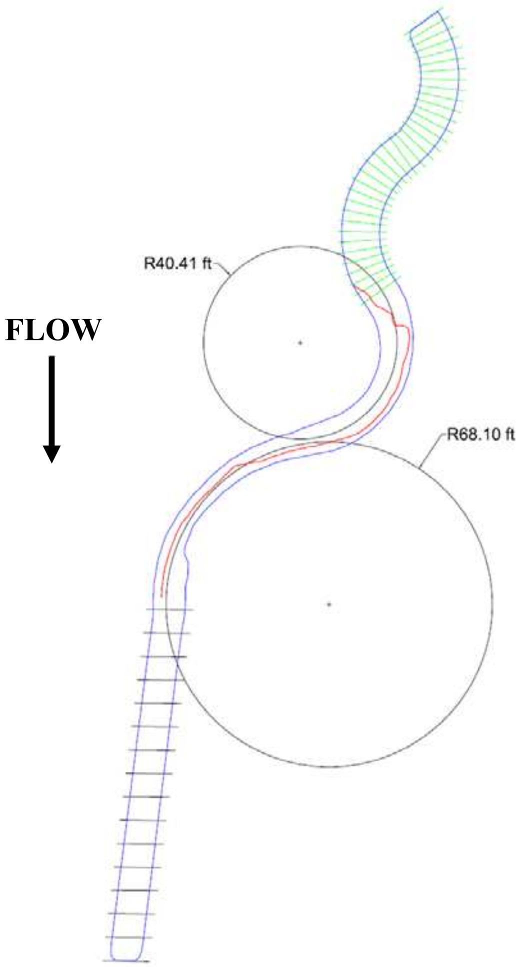

Figure 16: Hydraulic model geometry with straight downstream extension and double bend upstream extension with average radii values of upstream and downstream bends

CHAPTER 4. MODEL CALIBRATION

The previous numerical model studies conducted by Scurlock (2014a), Shin (2018) and Siefken (2019) used FLOW-3D and hydraulic model data to calibrate parameters of their models. The present study used the 2D numerical model, SRH-2D, which was calibrated to the same hydraulic-model data used in previous studies. Calibration of the SRH-2D model focused on calibrating flow rate, the Manning's roughness value of the channel and bendway weirs, and a parabolic turbulence parameter. Although Scurlock (2014a), Shin (2018), and Siefken (2019) verified that roughness of bendway weir did not change with respect to the channel, the calibration check was still performed to verify this finding for the 2D numerical model.

Data from hydraulic-model test BW01 and the baseline configuration as introduced in Chapter 2 of the two bends were used to calibrate the SRH-2D model. The two calibration configurations helped calibrating the flow rate, parabolic turbulence coefficient and Manning n roughness of the channel and bendway weirs. The baseline configuration (without weirs) was used to calibrate the channel roughness and flow rate since turbulence effects were minimal without the bendway weirs installed. Velocity and water depth measurements from the baseline hydraulic model were used in the calibration. The BW01 calibration configuration focused on calibrating Manning n roughness of the bendway weirs as well as the parabolic turbulence coefficient used in SRH-2D to account for energy loss due to turbulence.

The baseline model simulation led to calibration of the channel roughness and flow rate of the model. Previous studies gave insight on the general range of bed roughness and flow rate to use. The native bathymetry hydraulic model was designed to have a model roughness of n = 0.018, which agrees with the findings by Scurlock (2014a) and Shin (2018); their calibrated model roughness height values were found to be equivalent to a Manning n of 0.018. Though the roughness values agreed with previous studies, there were discrepancies regarding the calibrated flow rate. Scurlock (2014a) used a flow rate of 11.5 cfs whereas Shin (2018) used 10.5 cfs. Siefken (2019) explained that Scurlock's use of a higher flow rate reduced the depth MAPE (Mean Average Percent Error) to 3.78%, but at the expense of a velocity error of 20.4%. In comparison, Shin used a lower flow rate and ended his calibration with a depth MAPE of 5.6% and a velocity MAPE of 13.8%, which balanced the total error between both the depth and velocity. The present study sought to calibrate the roughness and flow rate to ensure the same values are determined for the SRH-2D model applied to all bends considered.

The SRH-2D baseline model was run with four values of Manning roughness, n (n = 0.017, 0.019, 0.021 and 0.023) and with four values of flow rate, Q (Q = 10.5, 11, 11.25, and 12 cfs). As Siefken (2019) used 11.25 cfs for his models, this value was used as the flow rate to calibrate the channel roughness for present study. The calibrated bed roughness was then used to calibrate and confirm the flow rate of the model. The error of the model compared to the hydraulic model data was computed using the MAPE approach detailed in Equation 5. MAPE values were calculated for both the depth and velocity of the baseline condition when calibrating roughness and flow rate.

$$Mean\ Absolute\ Percent\ Error = \left|\frac{Hydraulic\ model\ value - Numerical\ Value}{Hydraulic\ model\ value}\right| * 100 \qquad (5)$$

Calibration of the baseline model revealed the ideal bed roughness to be 0.019. The plot of baseline model roughness versus MAPE values in Figure 17 shows that, as the bed roughness increased, the velocity error also increased, but the depth error has a parabolic shape with the minimum error at a bed roughness of 0.019. As the depth error was parabolic in shape and the velocity error increased with bed roughness, the ideal bed roughness was chosen to be 0.019 which balanced both the velocity and depth errors. The calibrated depth error using a bed roughness of 0.019 was 3.10% and the velocity error was 26.78%.

After the bed roughness was determined, the model flow rate was calibrated using the baseline condition. Previous studies used a flow rate between 10.5 and 11.5 cfs. The present calibration used four flow rates of: 10.5, 11, 11.25, and 12 cfs. Previously calibrated bed roughness of 0.019 was used when calibrating the model flow rate. Calibration revealed that as flow rate increased, velocity error increased, and depth error decreased, as shown in Figure 18. Similar to the bed roughness calibration, depth and velocity errors were balanced to determine the optimal flow rate to be 11.25 cfs, which agreed with Siefken (2019). The calibration flow rate of 11.25 cfs and bed roughness of 0.019 produced an MAPE of 3.10% for depth and 26.78% for velocity. Final spatial calibration results are depicted in Figure 19 for both depth and velocity. This was the final calibration case for the baseline condition. Calibrated bed roughness and flow rate were then used to calibrate weir roughness and the SRH-2D turbulence parameter in the BW01 configuration.

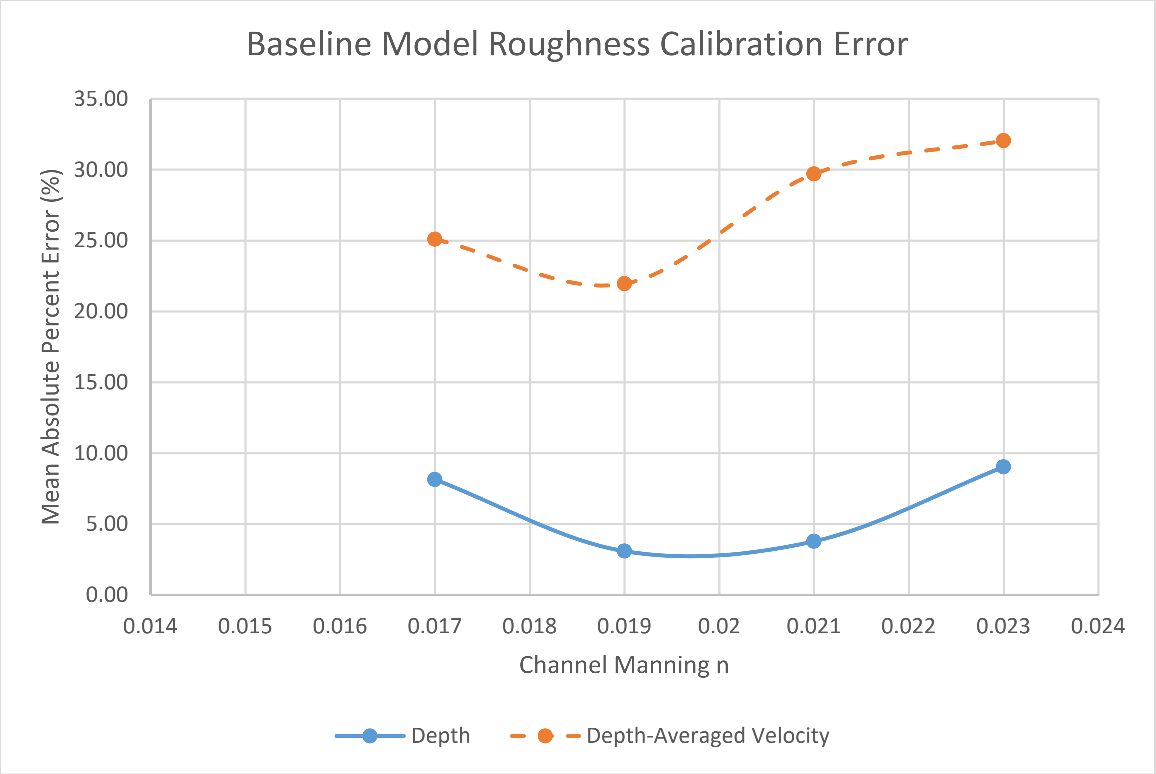

Figure 17: Baseline model roughness calibration error

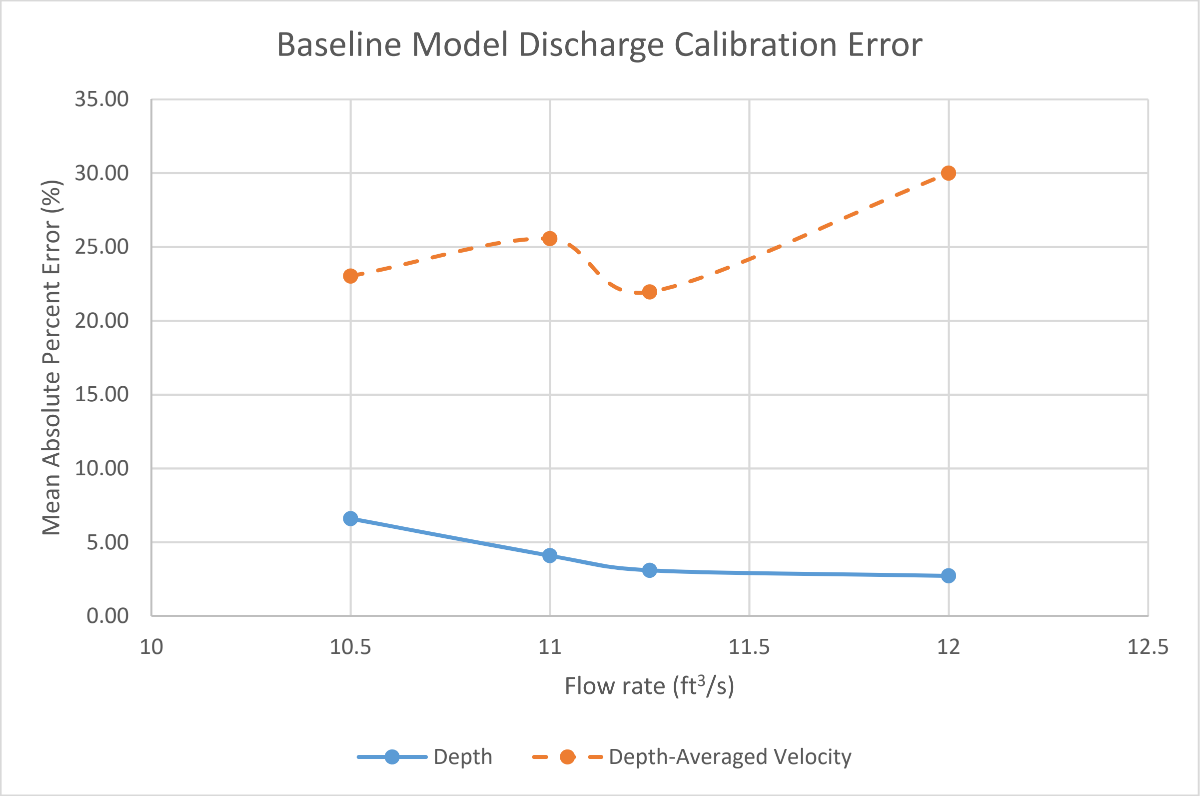

Figure 18: Baseline model flow rate calibration error

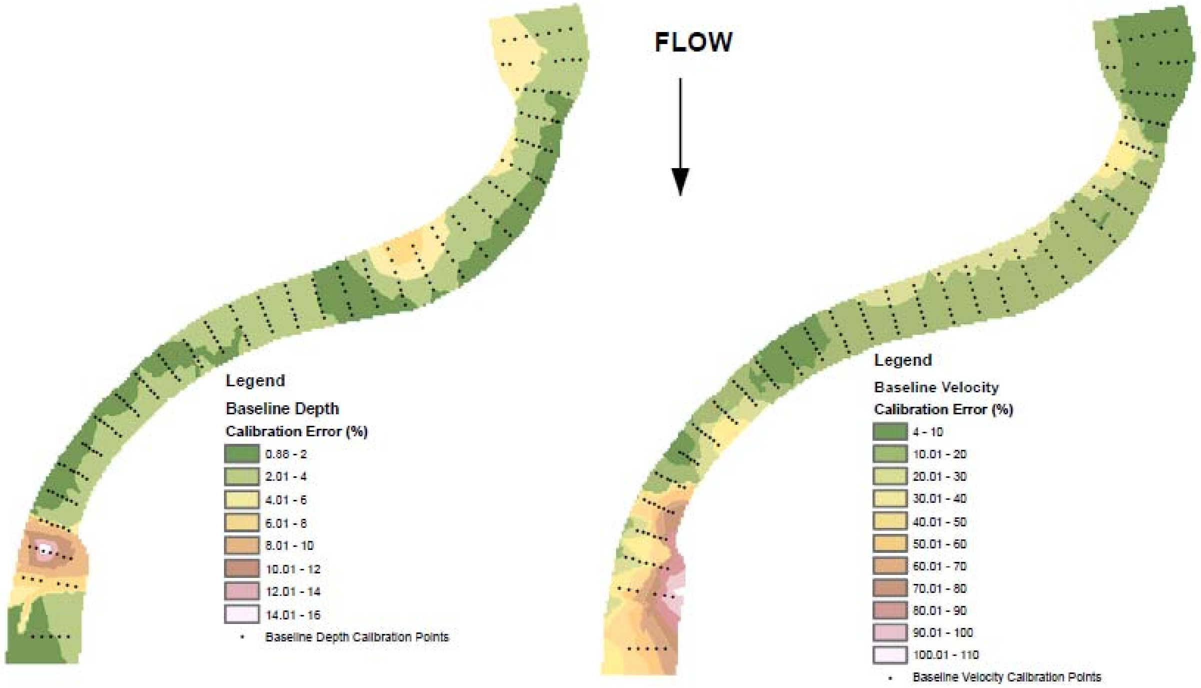

Figure 19: Error contour map for calibration to the baseline condition. (a) baseline depth calibration error (b) baseline velocity calibration error

The hydraulic model configuration for BW01 was used to calibrate bendway weir roughness and the SRH-2D parabolic turbulence parameter. The Manning n value of the bendway weirs was tested at four values of: 0.017, 0.019, 0.021 and 0.023. The results revealed that varying bendway weir roughness did not affect flow along the model and thereby the calibration error. Figure 20 shows that depth and velocity error only changed by a fraction of a percent when varying the weir roughness. Calibration also showed the same was true of the parabolic turbulence parameter. Calibration evaluated the parabolic turbulence parameter values of 0.3, 0.4, 0.5, 0.6, and 0.7 as the allowable range was 0.3-1.0. The default value in SRH-2D is 0.7 for field applications (Lai 2008). Velocity error of the calibration increased as the turbulence parameter value increased to 0.7, but the depth error remained nearly the same for all parameter values. Figure 21 shows MAPE for all five values. Since the turbulence value of 0.3 caused a slightly lower velocity error, 0.3 was to be used in the present study. Final results of calibration showed MAPE error for depth to be 6% and 21% for velocity comparing the BW01 configuration of the hydraulic model to the SRH-2D model.

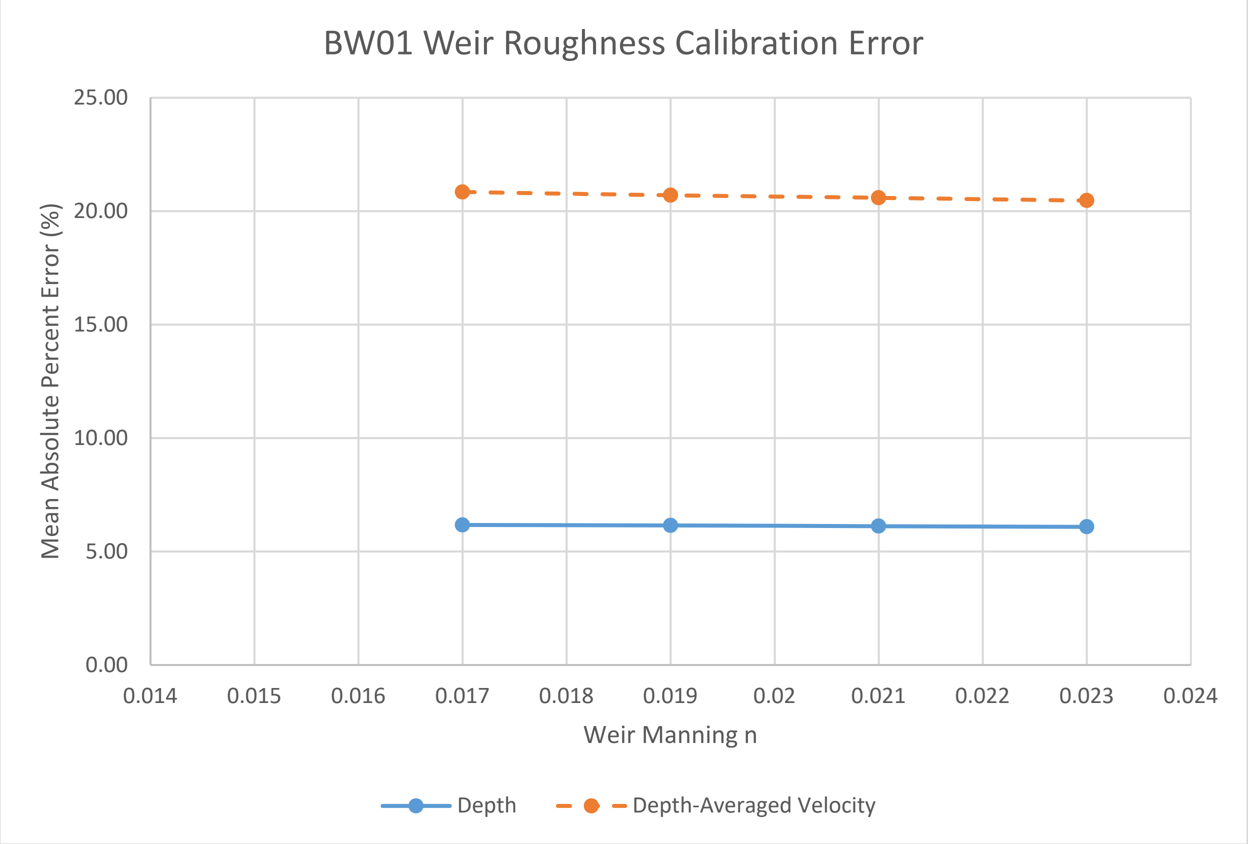

Figure 20: Calibration error for bendway weir roughness, BW01

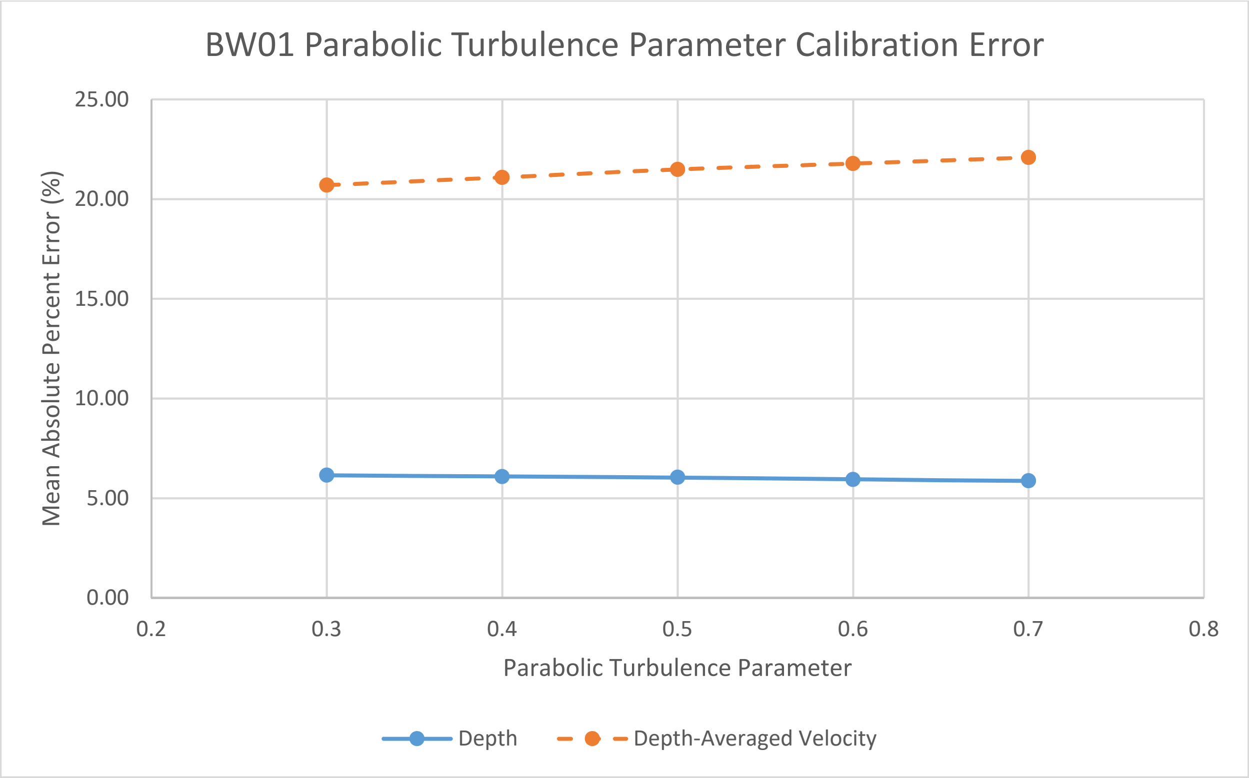

Figure 21: Calibration error for the parabolic turbulence parameter, BW01

CHAPTER 5. TEST CONFIGURATIONS

To investigate the effect of bed radius of curvature over top width, R_c/T_w, on the bendway weir flow field, the original hydraulic model native bathymetry was bent into three additional values of R_c, such that $R_c/T_w = 3.0$, 5.0, 7.35 (the radius of the original hydraulic model bend), and 8.0. The hydraulic model included two bends that represented the maximum and minimum R_c/T_w values found along the Middle Rio Grande. The upstream bend of the hydraulic model had an R_c/T_w value of 2.02 whereas the downstream bend had a value of 7.35. To keep the channel bathymetry constant between models, only the downstream bend radius was adjusted to form the new bend R_c values. $R_c/T_w = 3.0$ formed the tightest bend possible for the downstream bend without the bend's channel wrapping back on itself. Table 5 summarizes the bend characteristics for the 12 test configurations that were used in this study. The SRH-2D models will be detailed further in this chapter.

Table 5: Bend characteristics for configuration # 1-12

Bend Characteristics						
Configuration #	R_c (ft)	T_w (ft)	R_C/T_w	Bend Angle (degrees)	Channel Bathymetry	Bendway Weirs?
1	27.81	9.27	3.00	163	Native	Yes
2	27.81	9.27	3.00	163	Native	No
3	46.35	9.27	5.00	98	Native	Yes
4	46.35	9.27	5.00	98	Native	No
5	68.10	9.27	7.35	66	Native	Yes
6	68.10	9.27	7.35	66	Native	No
7	74.16	9.27	8.00	61	Native	Yes
8	74.16	9.27	8.00	61	Native	No
9	27.81	12.1	2.30	163	Trapezoidal	Yes
10	27.81	12.1	2.30	163	Trapezoidal	No
11	74.16	12.1	6.13	61	Trapezoidal	Yes
12	74.16	12.1	6.13	61	Trapezoidal	No

General Geometry Creation Procedure

Testing the effect of R_c/T_w on bendway weir flow field required the geometry of the channel to remain constant. Otherwise, additional geometric variables could negatively affect results.

Bathymetry of the downstream bend was extracted in the form of cross sections from the hydraulic model native bathymetry, as shown in Figure 22. This series of cross-sections began at the end of the transition between the upstream and downstream bend geometry, from the start of bend curvature, and extended to a point just before the beginning of the straight downstream extension. The cross-sections were extracted perpendicular to the main flow direction and parallel to the radii lines of the bend. SMS was used to extract the bathymetry from the hydraulic model native bathymetry. Points were extracted from the hydraulic model native bathymetry every 0.25 feet along the cross-section lines in Figure 22. After the bathymetry was extracted, it was imported into Civil 3D to determine the average bend radius. Bend radius was approximated by averaging the distance to the center of each cross section from the bend's center of curvature. Cross-section center was defined as the center point between the inner and outer bank high water line of the hydraulic model baseline configuration. Average bend radius was found to be 68.10 feet for the original hydraulic model condition. Subsequent models calculated the necessary bend radius to provide the specified values of R_c/T_w and then measured from the center of the furthest upstream cross-section to find the new center of curvature.

After the center of curvature was found, cross-sections were moved to their new locations where they formed a bend of new radius. To keep variations to a minimum between models, bend length, and therefore distance between cross sections was kept constant for all configurations.

Therefore, the smaller radius bends had a much larger angle between cross sections than did the larger radius bend. All cross-sections were kept parallel to the bend radii lines. The process of moving the cross-sections began by determining their intersection point with the average radius curve of 68.10 feet. Their point of intersection with this curve became the point in which they would intersect the next average bend radius arc. After cross-sections were moved to the right location, they were then rotated so that they were parallel with the radii lines of the new bend curvature. Figure 23 illustrates the cross-sections with the radii lines and the average bend radius. This method enabled cross-sections to be aligned in the same way for all configurations.

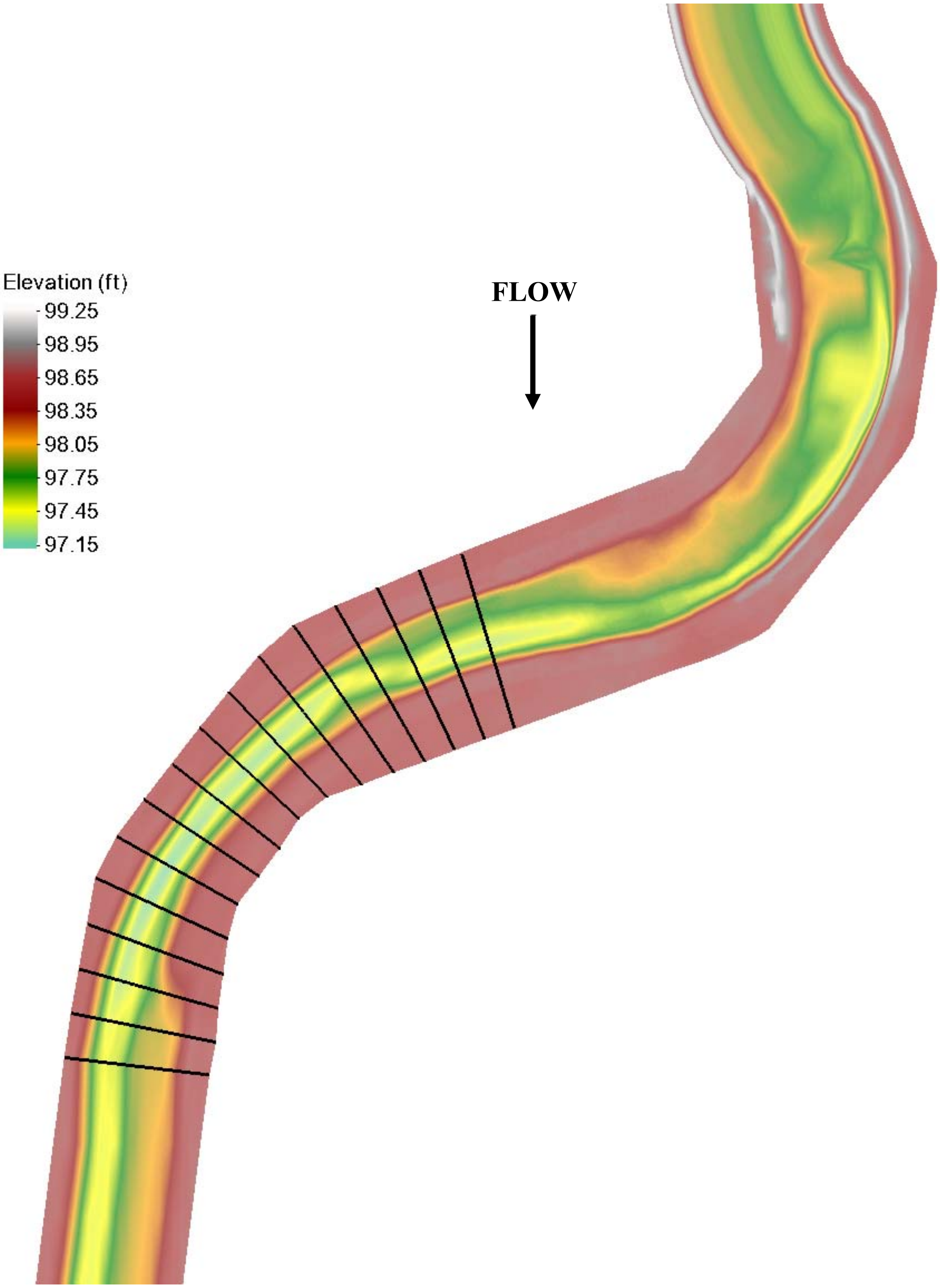

Figure 22: Hydraulic model cross-section bathymetry extraction locations (indicated by the black lines)

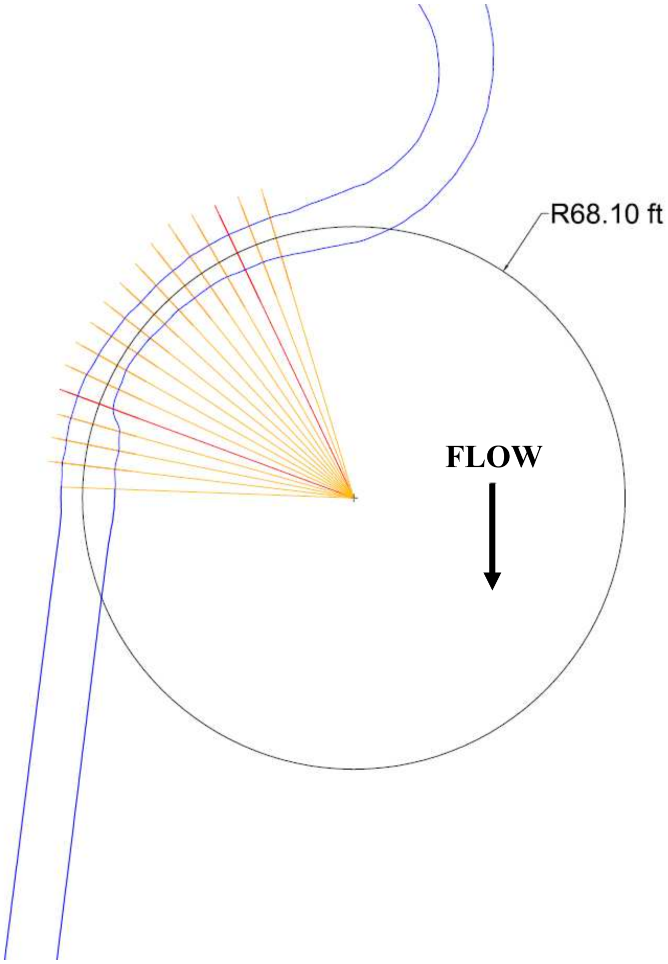

Figure 23: Hydraulic model average radius with the lengthened downstream reach

After extracting the cross-sectional bathymetry from the hydraulic model native bathymetry, the baseline models were designed and built in SMS and then results generated from SRH-2D. Resulting water surface elevations of the outer bank were used to design the bendway weirs for the bend of given radius. The water surface elevations allowed for the bendway weir planform angle, θ to be set in relation to the water line as well as the bendway weir height to be determined. Design of the bendway weirs were completed using a design spreadsheet developed and refined by Scurlock (2014a), Shin (2018) and Siefken (2019). Bendway weirs were designed with their root at the intersection of the water surface and the cross-section as shown in left side of Figure 24. It is important to note that, as the bendway weir begins at this point, much of the bendway weir's area may not protrude above the ground level (depending on the cross-section shape of the channel). An example of a weir minimally protruding above the ground level of the cross-section is shown in Figure 25. Plots of the remaining bendway weir designs similar to Figure 25 are included in Appendix A. Bendway weirs were designed using the parameters in Table 6. These parameters were determined based on the configuration of bendway weirs that decreased outer bank velocity the most, as determined by Siefken (2019), and accounted for recommended design values in Table 1. Definitions of these design parameters are shown in Figure 3 and Figure 4.

After the bendway weir designs were completed, they were imported into Civil 3D to be drawn in 3D, which facilitated easy import into SMS. Next, 3D design drawings of the bendway weirs were merged with the baseline mesh for each bend configuration in SMS. Following sections of this chapter detail the final mesh properties for configuration #1-12.

Table 6: Bendway weir design parameters for configuration #1-12

Bendway Weir Design Parameters						
Configuration #	L (ft)	θ (degrees)	Δz (ft)	L_{W-PROJ} (ft)	Larc (ft)	Channel Bathymetry
1	2.80	65	2D/3	2.32	6.95	Native
2	N/A	N/A	N/A	N/A	N/A	Native
3	2.80	65	2D/3	2.32	6.9525	Native
4	N/A	N/A	N/A	N/A	N/A	Native
5	2.80	65	2D/3	2.32	6.95	Native
6	N/A	N/A	N/A	N/A	N/A	Native
7	2.80	65	2D/3	2.32	6.95	Native
8	N/A	N/A	N/A	N/A	N/A	Native
9	3.66	65	2D/3	3.03	9.08	Trapezoidal
10	N/A	N/A	N/A	N/A	N/A	Trapezoidal
11	3.66	65	2D/3	3.03	9.08	Trapezoidal
12	N/A	N/A	N/A	N/A	N/A	Trapezoidal

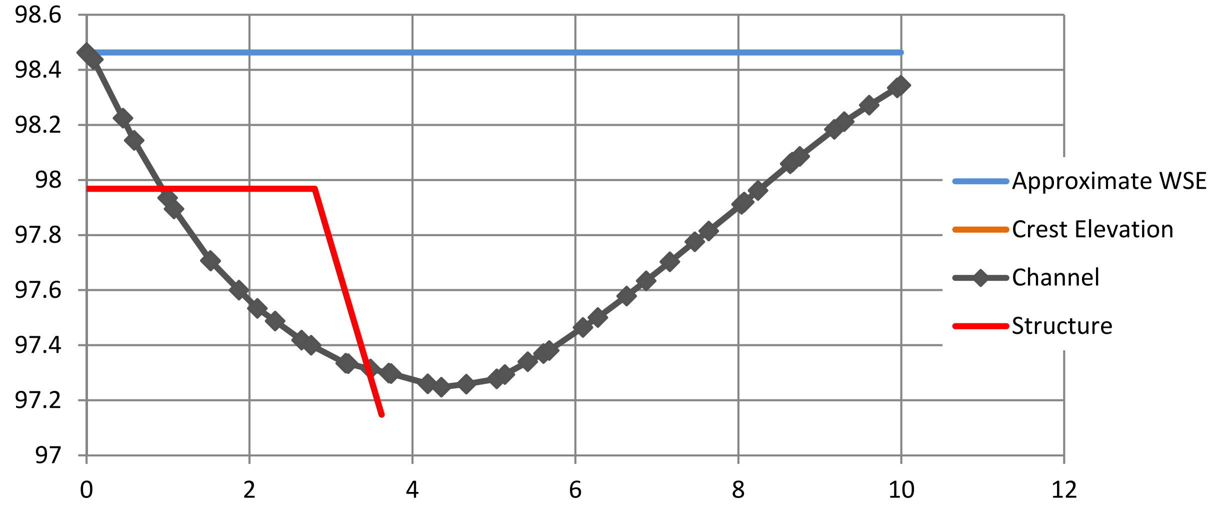

Figure 24: Example of bendway weir profile in cross section

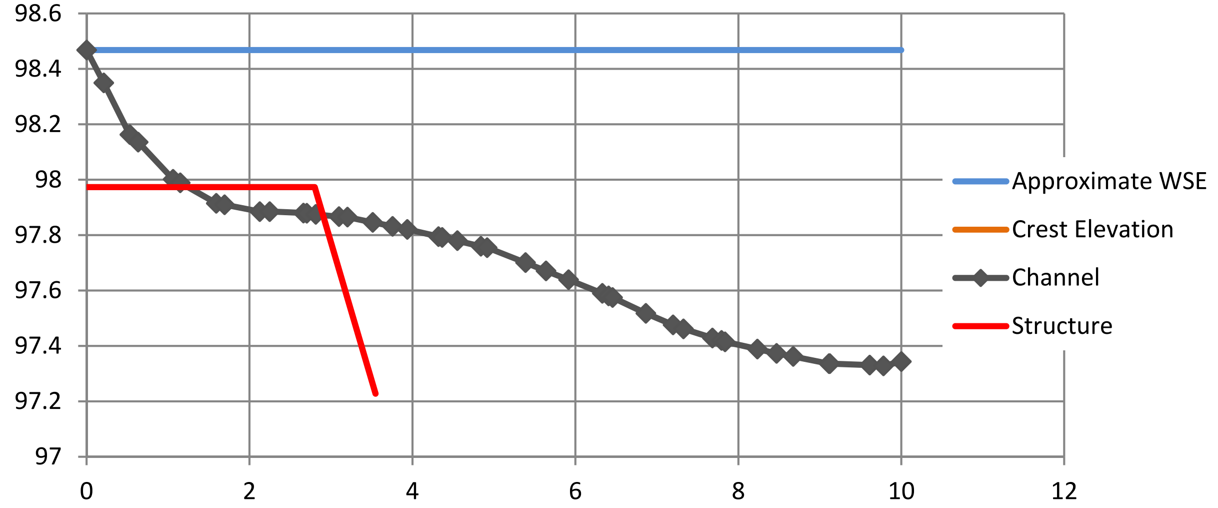

Figure 25: Example of low protrusion of bendway weir in cross section

$R_c/T_w = 3.0$

The model with $R_c/T_w = 3.0$ was the tightest configuration of the downstream channel bend and was also the lowest integer value of R_c/T_w that was able to be tested without the bend wrapping back on itself. Table 7 summarizes the geometric bend parameters for configurations 1 and 2.

The baseline mesh for configuration 2 (Table 5) was constructed with a combination of quadrilateral and triangular mesh elements. Quadrilateral elements were used for the upstream double bend entrance since the channel was relatively trapezoidal in shape and followed a very uniform curve. The spacing of the elements for the upstream double bend was approximately 1.5 feet in the stream-wise direction and 0.7 feet in the cross-stream direction. After the double bend entrance to the main reach of the model, the mesh transitioned to triangular elements to more accurately represent the non-uniform nature of the native bathymetry. Elements in the main upstream and downstream bend were approximately 0.5 feet in the stream-wise direction. Triangular elements in the two main bends also allowed for better consistency when adding the bendway weirs to the baseline mesh as a triangular mesh was required to accurately form the bendway weir geometry. Quadrilateral elements were also used for the straight downstream channel extension since the channel was straight. Mesh stream-wise spacing for this section was also set to 1.5 feet and 0.7 feet in the cross-stream direction. There were a total of 29,340 mesh elements in the configuration 2 mesh. Figure 26 shows the mesh for configuration 2 along with the cross section locations in the downstream bend.

Table 7: Model parameters when R_c/T_w = 3.0

Bend			
R_c (ft)	T_w (ft)	R_C/T_w	Bend Angle (degrees)
27.81	9.27	3.0	163

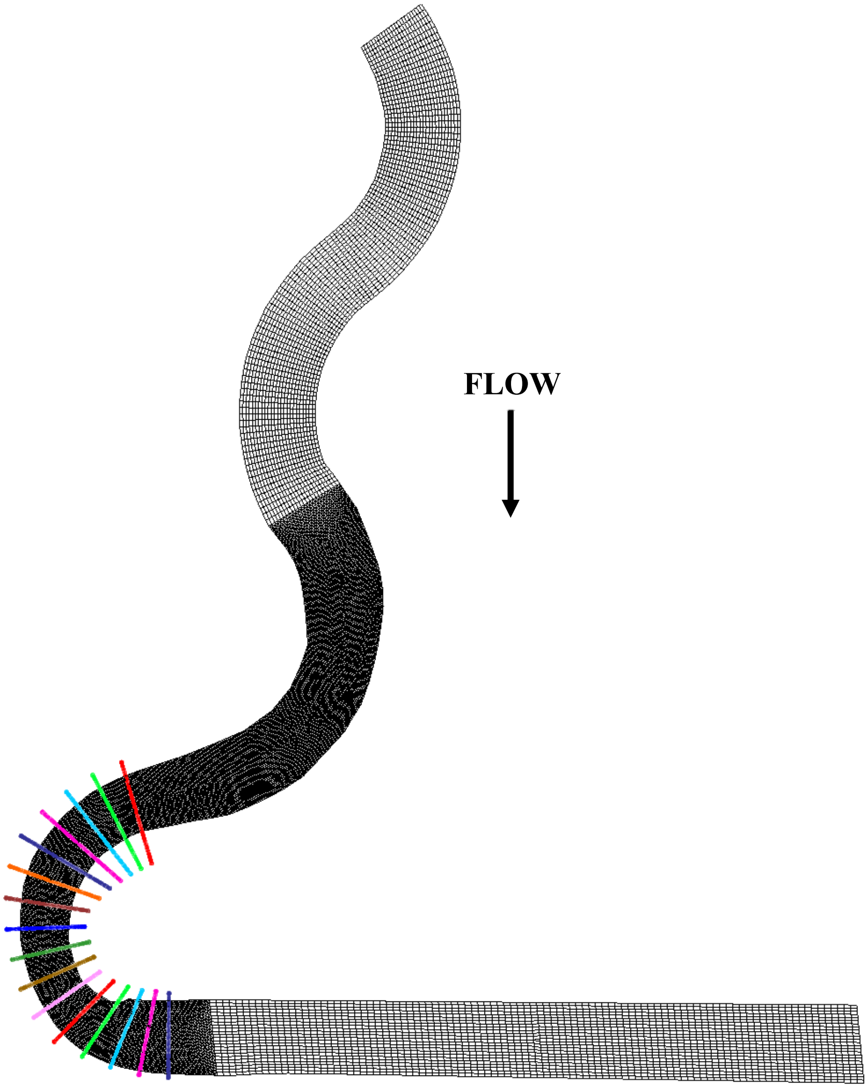

Figure 26: Configuration 2 mesh (cross sections indicated) when $R_c/T_w = 3.0$

The bendway weir mesh for configuration 1 was then built from the baseline mesh. Changes only occurred in the downstream bend of the mesh as this is where the bendway weirs were installed. In order to force bendway weir geometry to be formed in the mesh, a 0.25 foot mesh spacing was used around the weirs themselves and then transitioned back to 0.5 feet in the rest of the channel. Since the weir crests were flat, quadrilateral mesh elements were used and triangular elements were used on the side slopes of the weirs to form the curved geometry and also to tie into the channel mesh. The mesh for configuration 1 contained 36,420 elements. Figure 27 shows the downstream bend mesh of configuration 1 and 2. Figure 28 shows a 3D view of the furthest upstream bendway weirs in configuration 1.

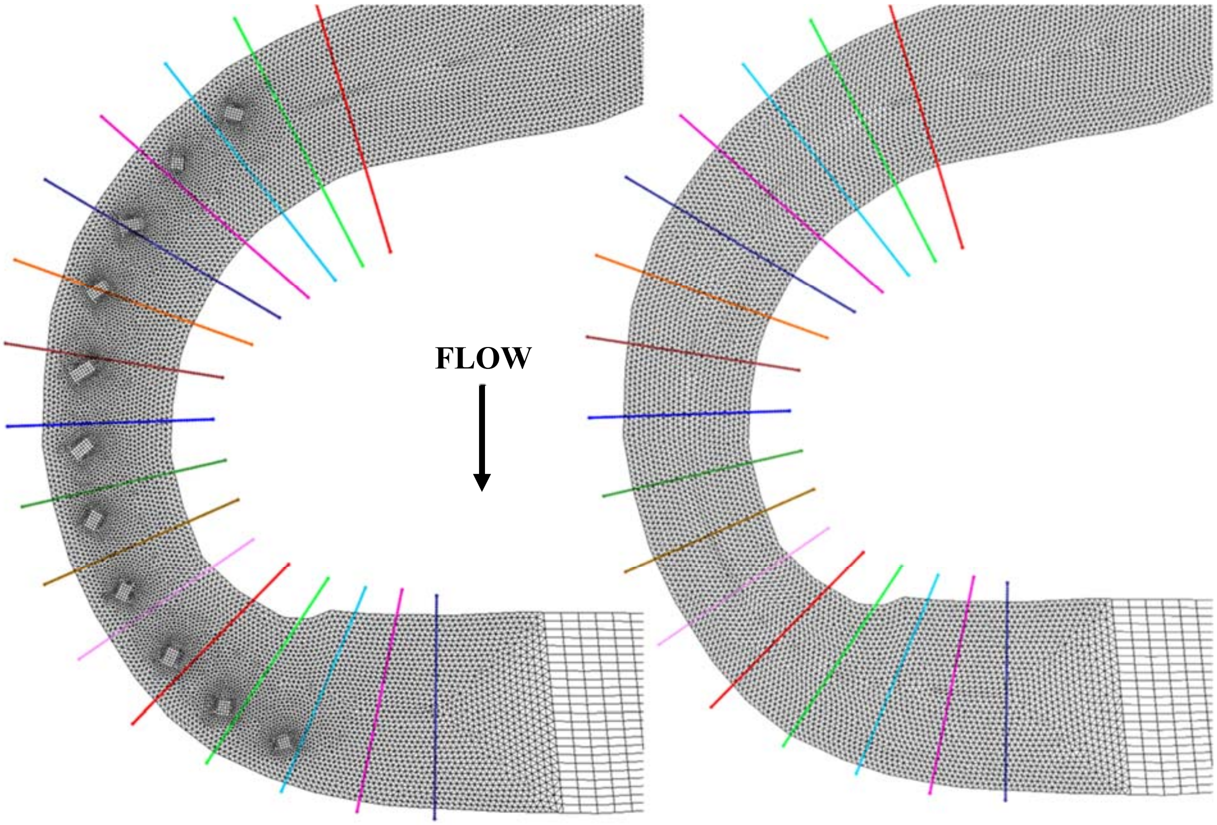

Figure 27: The downstream bend mesh when $R_c/T_w = 3.0$. (a) bendway weir configuration (b) baseline configuration

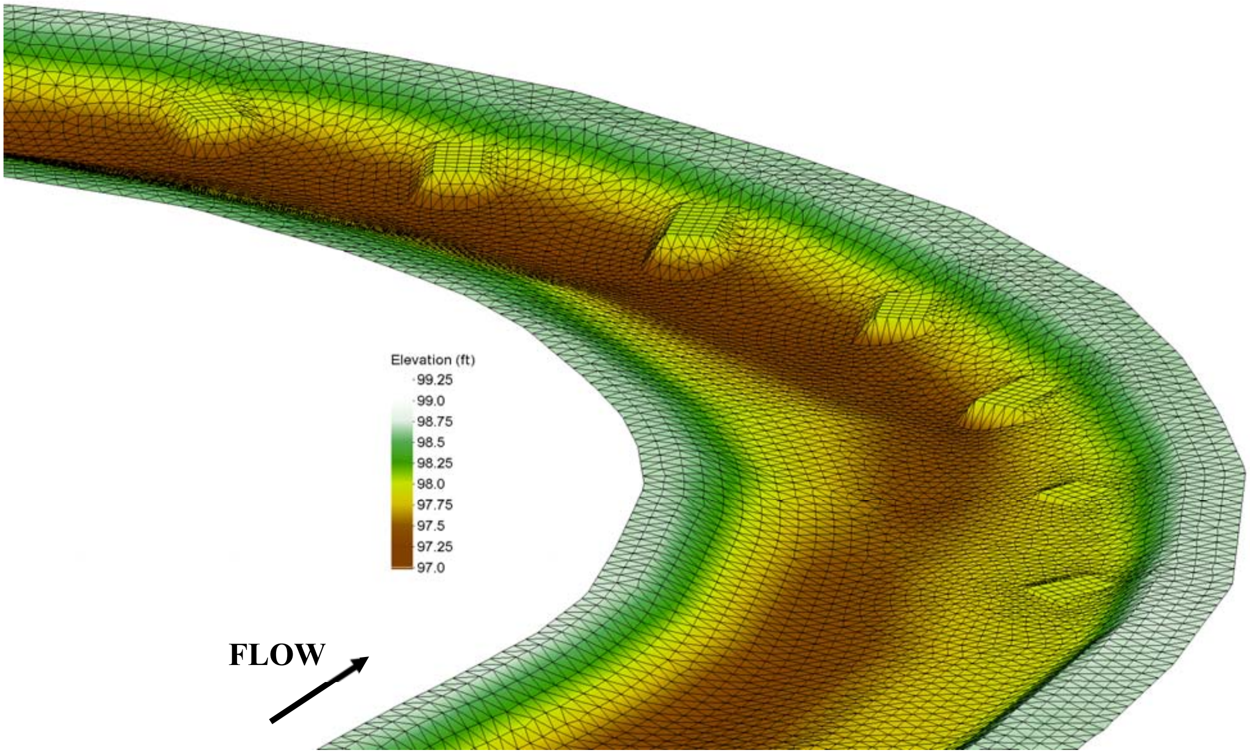

Figure 28: View of bendway weir mesh when $R_c/T_w = 3.0$

$R_c/T_w = 5.0$

$R_c/T_w = 5.0$ was chosen as an intermediate configuration of a bend that had a slightly tighter radius than the original hydraulic model native bathymetry but slightly larger than the smallest radius. Table 8 details the geometric bend parameters of configurations 3 and 4. The mesh for configuration 3 and 4 were constructed in a similar manner as configuration 1 and 2. Quadrilateral elements were spaced 1.5 feet in the stream-wise direction and 0.7 feet in the cross-stream direction in the upstream double bend entrance. Triangular mesh elements spaced 0.5 feet in the stream-wise direction as well were used in the main two bends downstream of the double bend entrance. Quadrilateral mesh elements spaced 1.5 feet in the stream-wise direction and 0.7 feet in the cross-stream direction were used for the straight downstream channel extension. Configuration 4 contained a total of 29,128 elements in its mesh. Figure 29 shows the baseline model mesh with the cross-sections used to build the geometry in the downstream bend.

Table 8: Model parameters when $R_c/T_w = 5.0$

Bend			
R_c (ft)	T_w (ft)	R_C/T_w	Bend Angle (degrees)
46.35	9.27	5.0	98

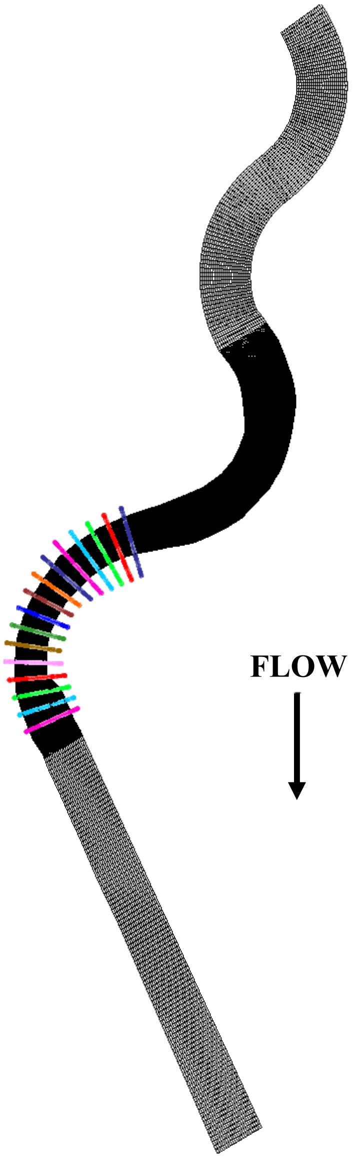

Figure 29: Configuration 4 mesh for $R_c/T_w = 5.0$ (cross sections indicated in the downstream bend)

The configuration 3 mesh was created from configuration 4. The upstream double bend entrance remained the same as well as the downstream straight extension. Channel mesh elements remained triangular and their length in the stream-wise direction remained 0.5 feet. Bendway weir crests were meshed using quadrilateral elements and triangular elements on their side slopes. The bendway weir mesh spacing remained at 0.25 feet. In total, there were 36,298 elements in the configuration 3 mesh. Figure 30 shows the bendway weir mesh in the downstream bend side-by-side with the baseline mesh.

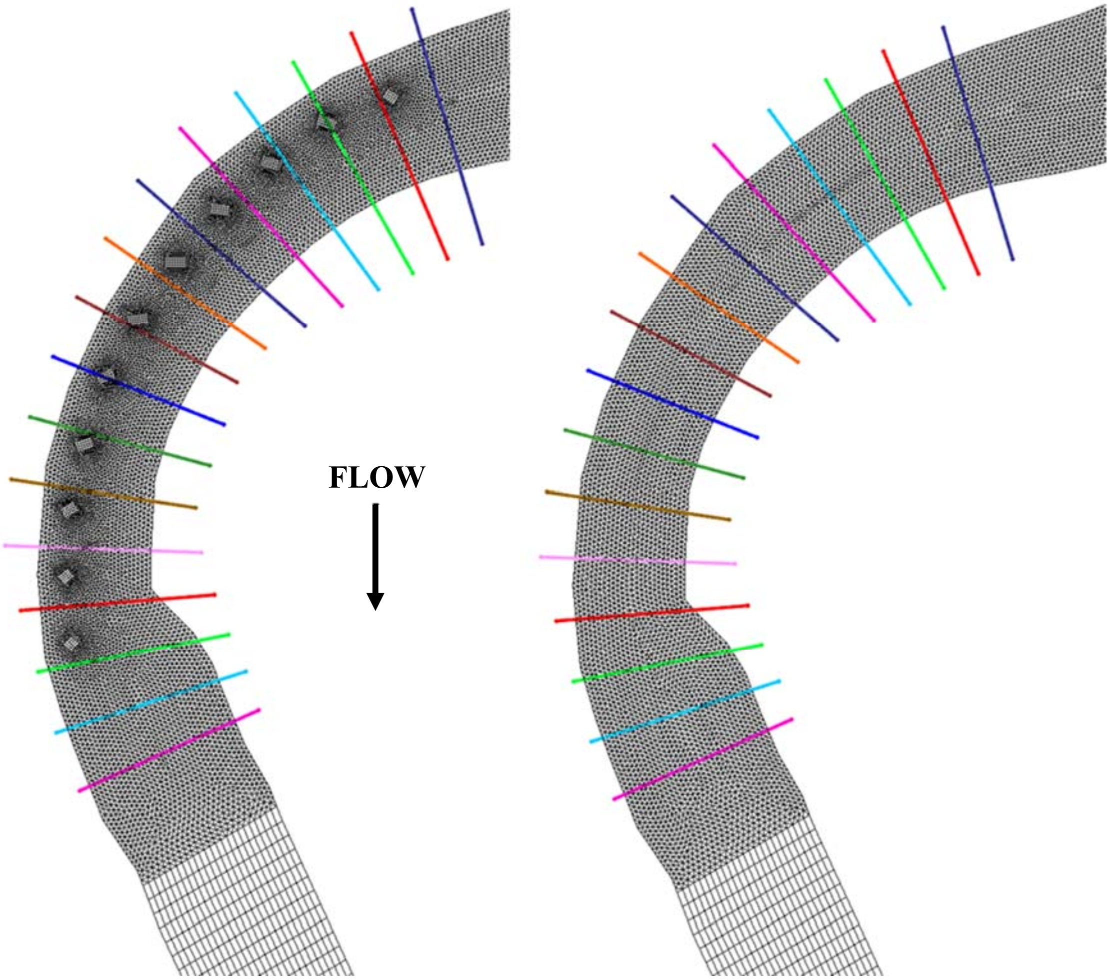

Figure 30: The downstream bend mesh when $R_c/T_w = 5.0$. (a) bendway weir configuration (b) baseline configuration

R_c/T_w = 7.35

R_c/T_w = 7.35 was the original configuration of the hydraulic model. Table 9 details the geometric bend parameters of configurations 5 and 6, which were built in a similar manner as configuration 1-4. Quadrilateral elements spaced 1.5 feet in the stream-wise direction and 0.7 feet in the cross-stream direction were used in the upstream double bend entrance. Triangular elements spaced 0.5 feet in the stream-wise direction were used in the two main bends and the straight downstream extension used quadrilateral elements spaced 1.5 feet in the stream-wise direction and 0.7 feet in the cross-stream direction. Configuration 6 contained a total of 29,334 mesh elements within its domain. Figure 31 shows the mesh for configuration 6 with the cross sections used to build the geometry in the downstream bend.

Table 9: Model parameters for R_c/T_w = 7.35

Bend			
R_c (ft)	T_w (ft)	R_c/T_w	Bend Angle (degrees)
68.1	9.27	7.35	66

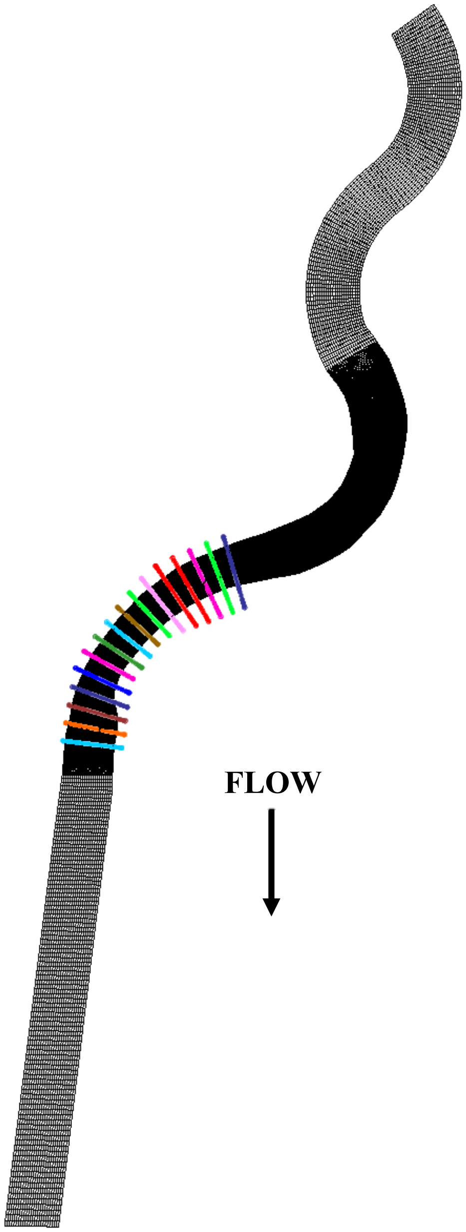

Figure 31: Configuration 6 mesh with cross sections for R_c/T_w = 7.35

Mesh from configuration 6 was used to build the mesh of configuration 5. Geometry and mesh of the upstream double-bend entrance and the straight downstream extension remained the same. Channel mesh spacing remained 0.5 feet in the stream-wise direction with triangular elements and the bendway weir crests were still formed with quadrilateral elements spaced at 0.25 feet. Sides of the bendway weirs were meshed with triangular elements spaced 0.25 feet. In total, the configuration 5 contained 36,718 mesh elements within its domain. Figure 32 shows the bendway weir mesh in the downstream bend side-by-side with the baseline mesh.

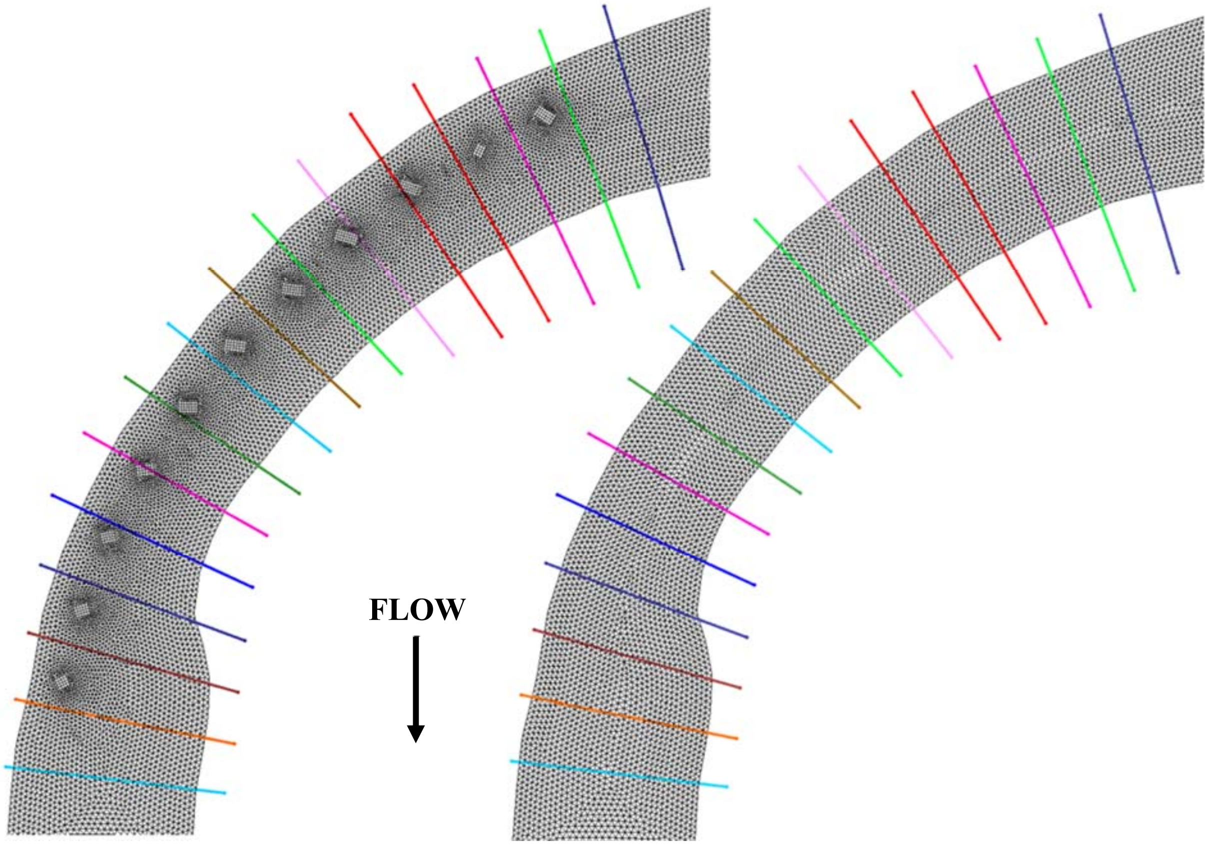

Figure 32: The downstream bend mesh when $R_c/T_w = 7.35$. (a) bendway weir configuration (b) baseline configuration

$R_c/T_w = 8.0$

$R_c/T_w = 8.0$ was the largest bend radius tested, which was approximated as the largest value observed in the Middle Rio Grande in previous studies. Table 10 details the geometric bend parameters of configurations 7 and 8. This model continued the same mesh practices as the previous three models. Quadrilateral elements spaced 1.5 feet in the stream-wise direction and 0.7 feet in the cross-stream direction were used for the upstream double bend entrance and the straight downstream extension remained quadrilateral elements, spaced 1.5 feet in the stream-wise direction. The two main channel bends used triangular mesh elements spaced at 0.5 feet in the stream-wise direction. Configuration 8 contained 29,322 mesh elements in its model domain. Figure 33 shows the configuration 8 mesh along with the cross sections used to create the downstream bend geometry.

Table 10: Model parameters for $R_c/T_w = 8.0$

Bend			
R_c (ft)	T_w (ft)	R_C/T_w	Bend Angle (degrees)
74.16	9.27	8.0	61

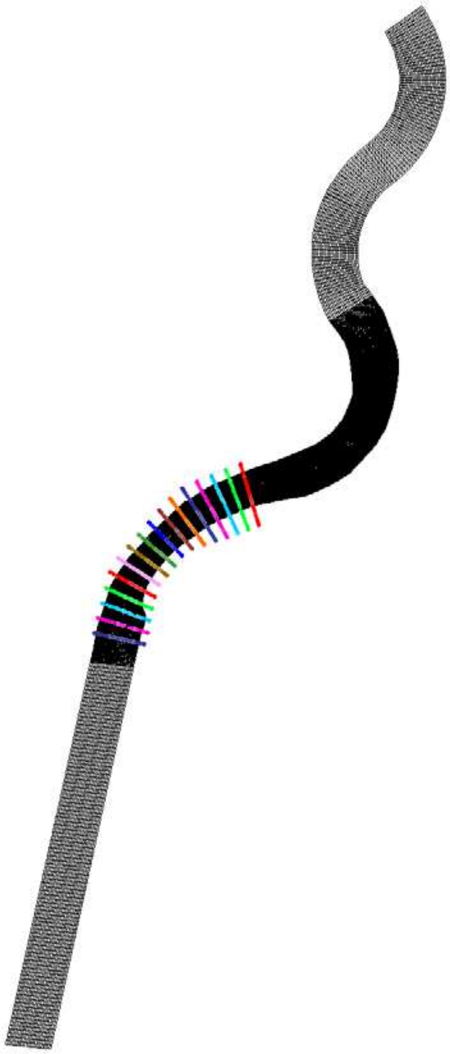

Figure 33: Configuration 8 mesh with cross sections for $R_c/T_w = 8.0$

Configuration 7 was then created from configuration 8. The upstream double-bend entrance and the straight, downstream extension remained the same. Channel mesh spacing remained triangular elements spaced at 0.5 feet in the stream-wise direction. Bendway weir crests remained quadrilateral elements spaced at 0.25 feet and their sides remained triangular elements spaced at 0.25 feet. Configuration 7 contained 39,160 mesh elements in its domain. Figure 34 shows the bendway weir mesh in the downstream bend side-by-side with the baseline mesh.

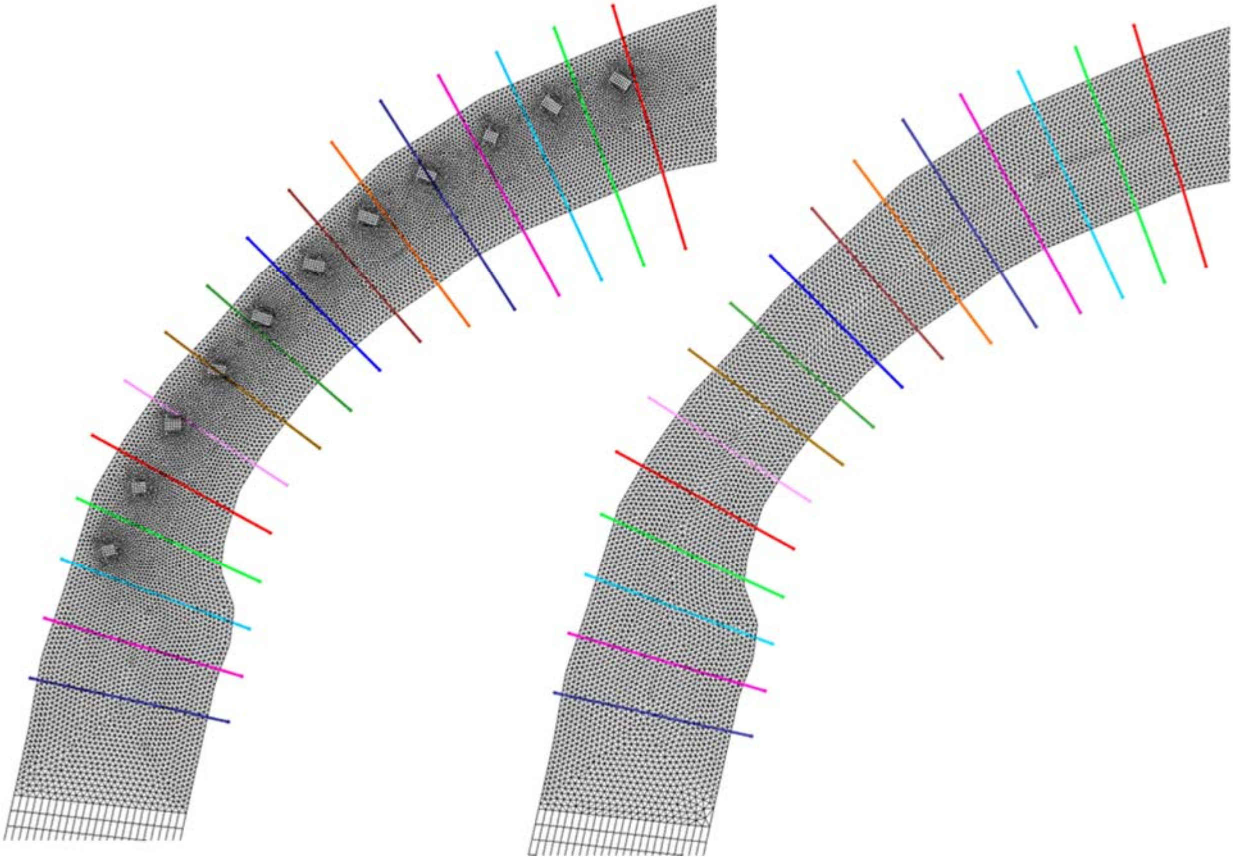

Figure 34: The downstream bend mesh when $R_c/T_w = 8.0$. (a) bendway weir configuration (b) baseline configuration

Trapezoidal Models

In addition to the native bathymetry, trapezoidal geometry was also used to ensure results weren't dictated by native bathymetry. The trapezoidal channels were created using the same radii as the R_c/T_w = 3.0 and 8.0 bends. Changing the bathymetry of the sections and therefore channel top width also slightly affected the Rc/T_w values in the trapezoidal channels. The new R_c/T_w values were 2.3 and 6.13.

The trapezoidal geometry was formed in a very similar manner to the native bathymetry channels. The same channel centerlines as the native channels at R_c/T_w values of 3.0 and 8.0 were used as the centerline for the trapezoidal channels. This channel centerline included points spaced at approximately every 5 feet and were assigned elevations based on the channel slope of 0.000863 feet/feet. The same double bend entrance and straight channel exit conditions as the native bathymetry were used. All cross-sections throughout the channel used a trapezoidal section with an 8 foot bottom width and a 3H:1V side slope. The channel centerline was used as the extrusion path with the cross-sections remaining perpendicular to the channel centerline. The baseline and bendway weir configurations were also tested as part of the trapezoidal model. Bendway weirs were designed using the same specifications as the native bathymetry bendway weir configurations. Figure 35-Figure 38 show the mesh for the R_c/T_w values of 2.3 and 6.13 for the baseline and bendway weir configurations. Configurations 10 and 12 without bendway weirs used quadrilateral elements spaced at 0.5 feet in the longitudinal and lateral directions. Configurations 9 and 11 used 0.5 feet triangular elements in the downstream bend with 0.25 feet spacing around the bendway weirs. Quadrilateral elements were used in the remaining areas of the model.

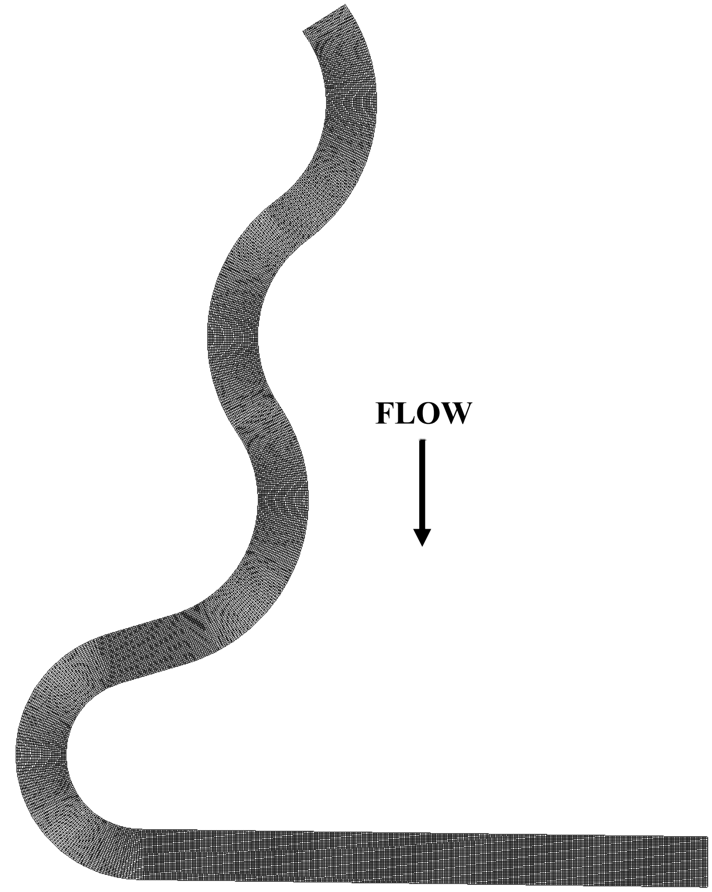

Figure 35: The trapezoidal baseline channel mesh when R_c/T_w = 2.3 (configuration 10)

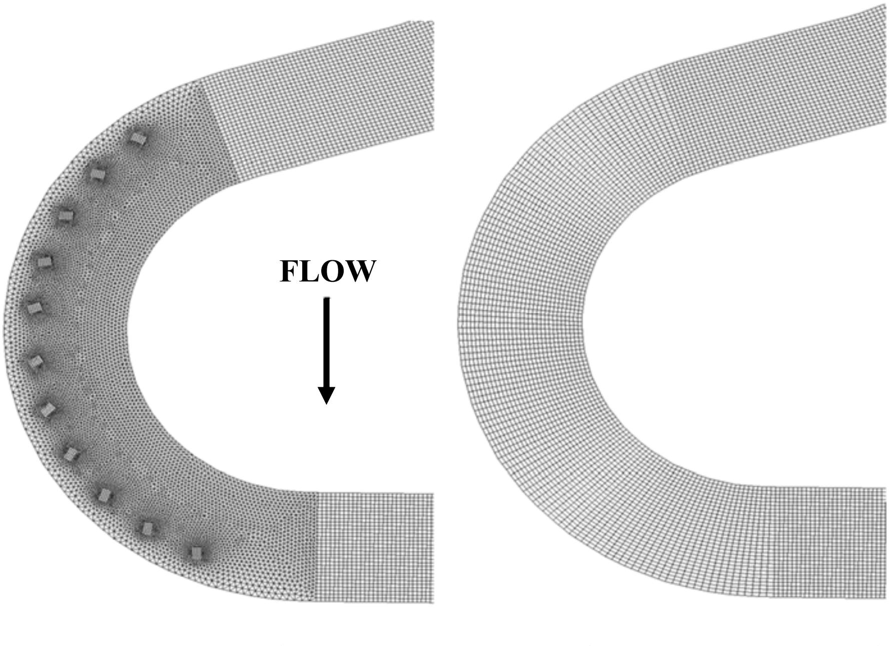

Figure 36: The downstream bend trapezoidal channel mesh when R_c/T_w = 2.3. (a) bendway weir configuration

(b) baseline configuration

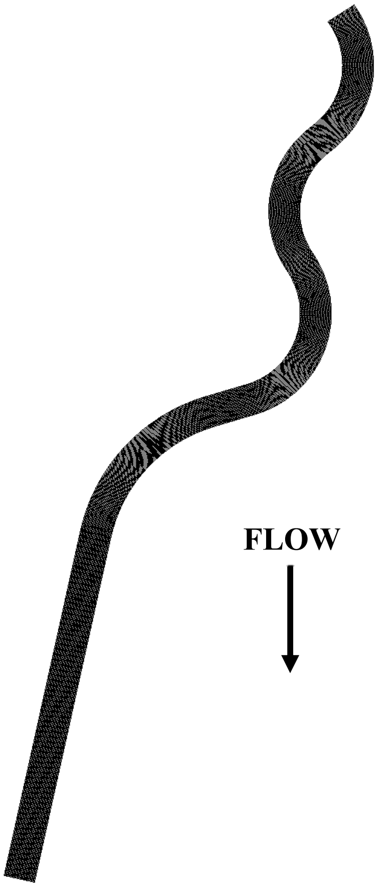

Figure 37: Trapezoidal baseline channel mesh when $R_c/T_w = 6.13$ (configuration 12)

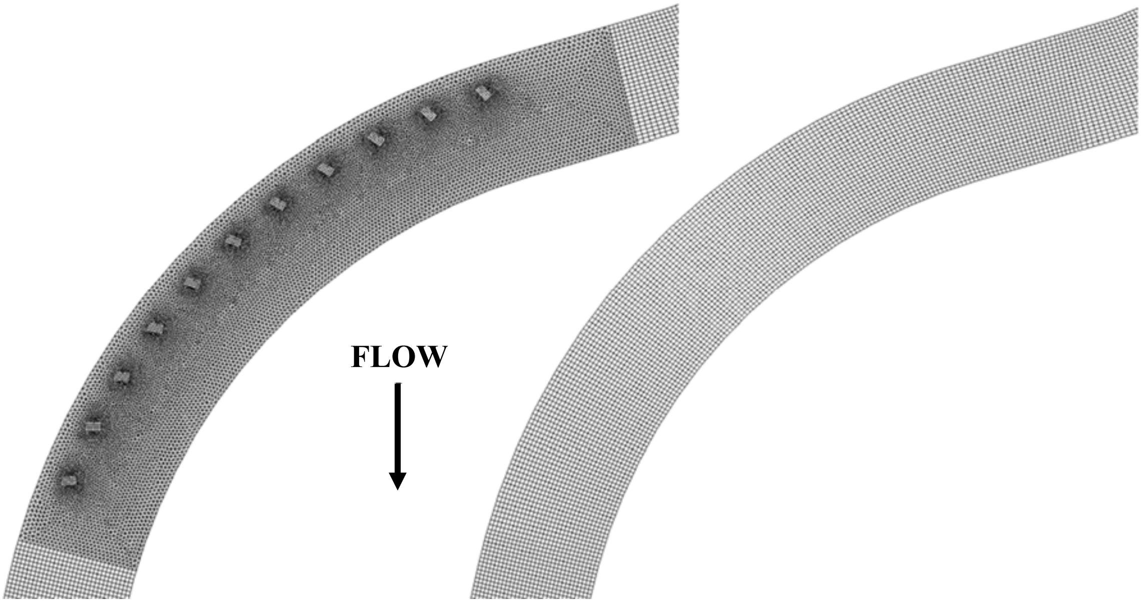

Figure 38: The downstream bend trapezoidal channel mesh when $R_c/T_w = 6.13$. (a) bendway weir configuration (b) baseline configuration

CHAPTER 6. RESULTS AND ANALYSES

Following completion of the twelve model runs (Table 5) of the baseline and bendway weir configurations in the native and trapezoidal channels, data in the form of color contour plots and cross-sectional velocity and water surface were extracted to evaluate how the bend radius of curvature affected the flow field with and without the presence of bendway weirs.

The following results were compiled for flow around the native and trapezoidal channels. To evaluate how the flow field around the bends was affected with and without the presence of bendway weirs, the maximum velocity at cross-sections in the downstream bend were compared to the upstream approach velocity at the entrance of the bend. Additionally, the average and maximum velocity in three lateral sections of each cross-section were computed to evaluate how the bendway weirs and the radius of curvature affected the flow field at the inner, middle, and outer portions of the bend. Velocity and shear stress contour plots were used to evaluate the overall flow field effects throughout the bend for each radius of curvature modeled. In conjunction with contour plots, cross-sectional plots of velocity and water surface elevation (WSE) were evaluated to show the distributions of velocity across each cross section as well as the super-elevation of the water surface throughout the bend.

Velocity and Shear Stress Contour Plots

Native Bathymetry

Contour plots enabled spatial patterns of high velocity and shear stress to be compared between values of R_c/T_w. Resulting color contour plots of depth-average velocity for flow in native bathymetry channels are shown in Figure 39 through Figure 46 (configuration 1 through 8). Contour plots show that there were very minimal differences in the velocity field between the various bend radii. Baseline conditions for the four bend radii show that there were zones of higher velocity between cross-sections 3 and 4 and cross-sections 10 and 11. Magnitude of these zones are detailed with cross-section evaluation in the sections below. Zones of higher velocity seemed to be caused by the bathymetry of the channel. Figure 47 through Figure 50 show that there was a natural contraction at cross-sections 4, 5, 10, 11 which was likely causing the higher velocities in these zones. Overall, the velocity distribution in the baseline channel was very balanced throughout the bend due to the thalweg of the channel following very close to the channel centerline.

Resulting color contour plots of depth average velocity showed that the main effect of the bendway weirs was an increase of depth average velocity toward the center and inner bank of the bends. This result was attributable to the blockage effect exerted by the bendway weirs. A further effect of the bendway weir presence was that flow velocity decreased along the channel's outer bank. Bend radius affected the flow field essentially to the same extent as radius influence on the baseline flow fields. The zone of continuous high velocity started at about cross-section 7 and continued to about cross-section 13 in all bend radii. Magnitude of velocities in these zones is elaborated in the sections below.

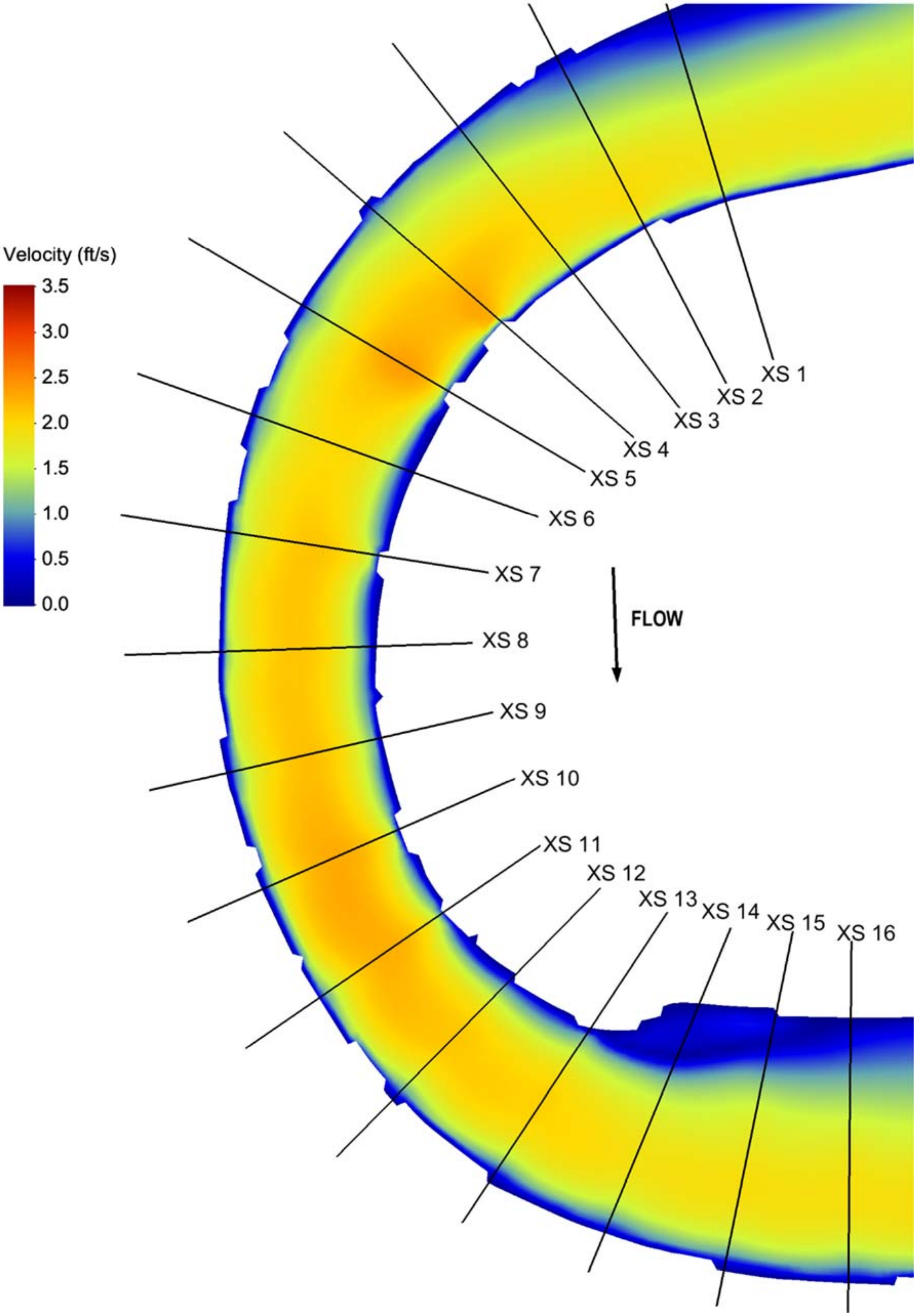

Figure 39: Baseline velocity contour plot when $R_c/T_w = 3.0$ (configuration 2)

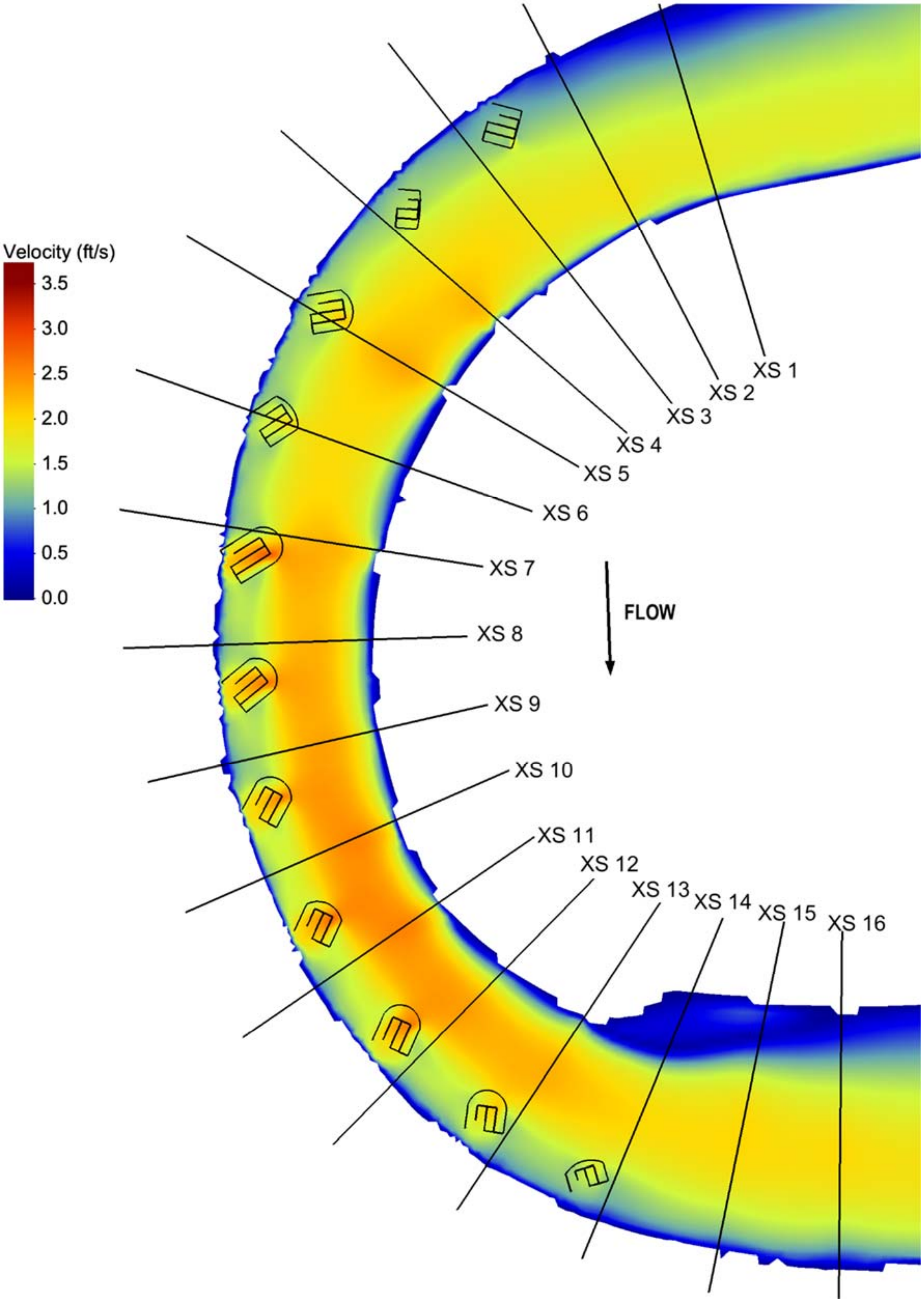

Figure 40: Bendway weir velocity contour plot when $R_c/T_w = 3.0$ (configuration 1)

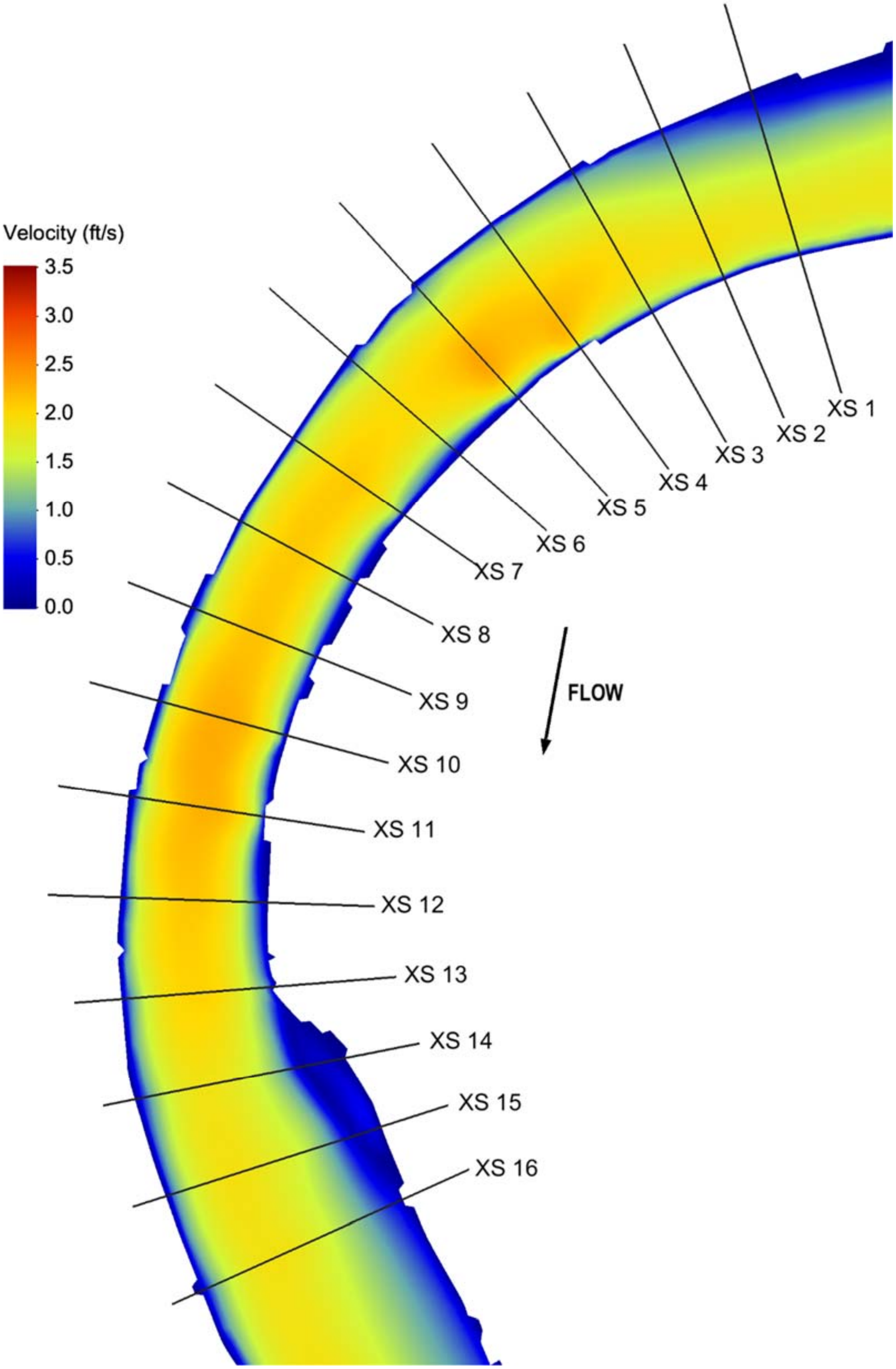

Figure 41: Baseline velocity contour plot when $R_c/T_w = 5.0$ (configuration 4)

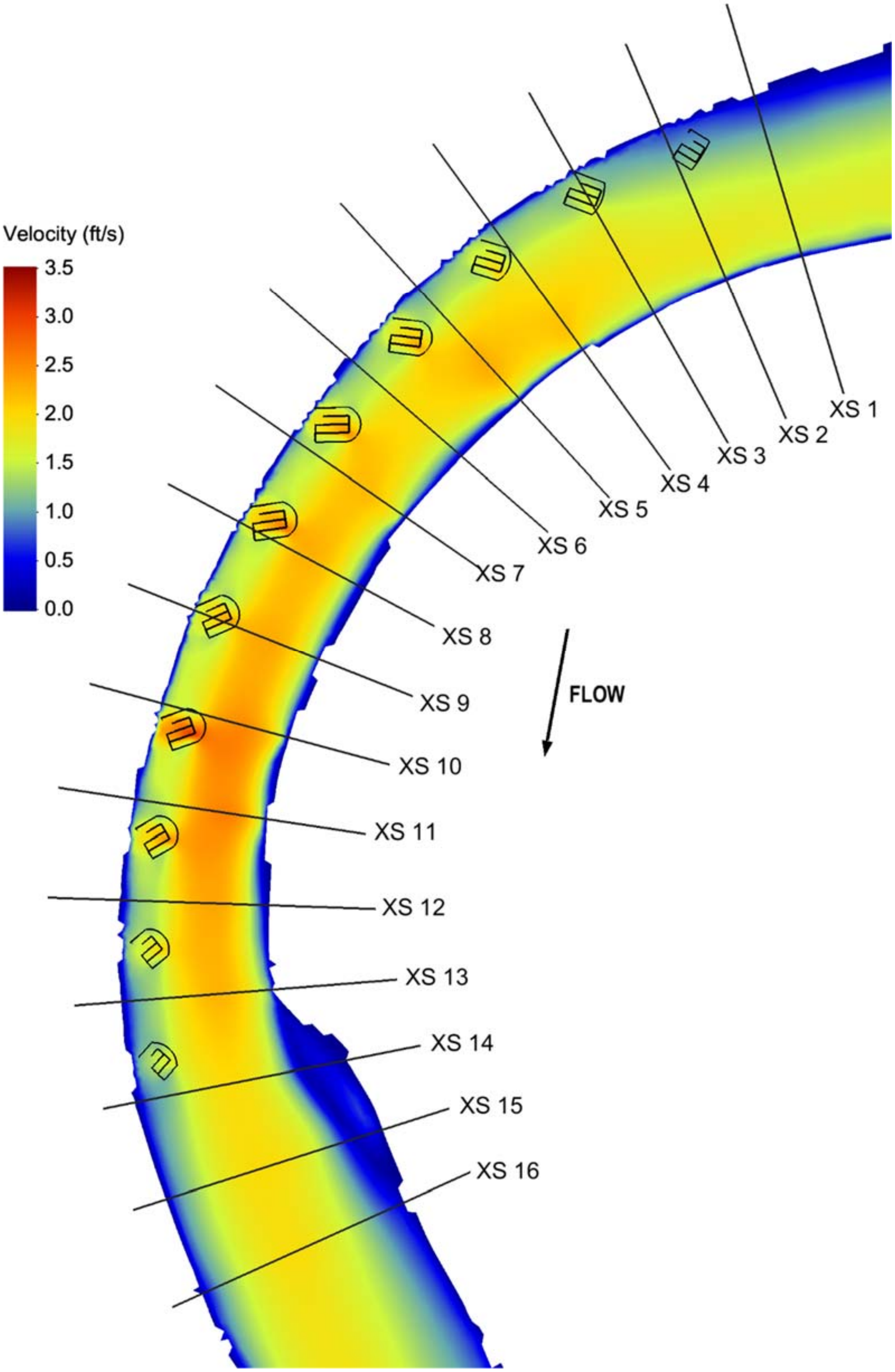

Figure 42: Bendway weir velocity contour plot when $R_c/T_w = 5.0$ (configuration 3)

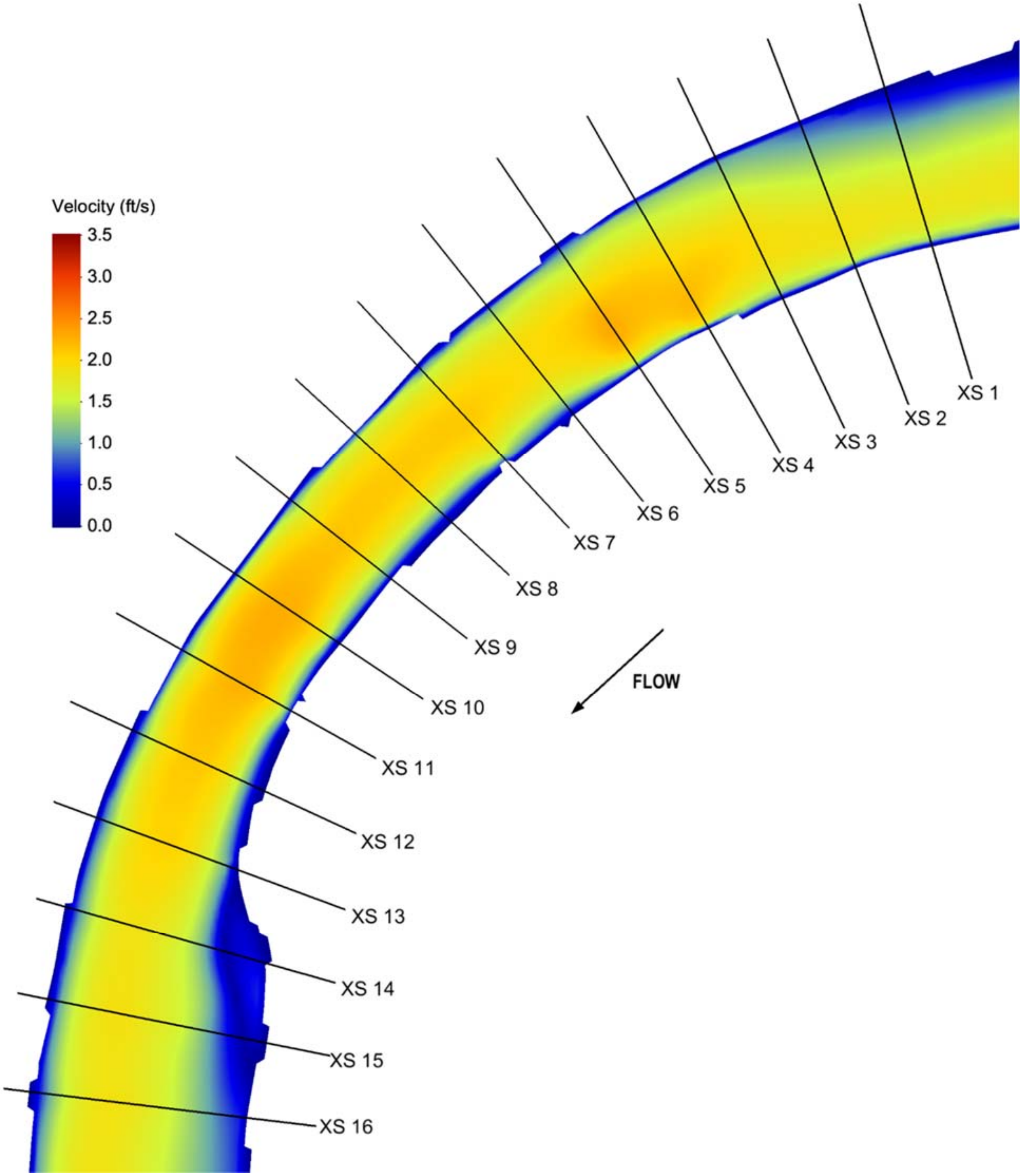

Figure 43: Baseline velocity contour plot when $R_c/T_w = 7.35$ (configuration 6)

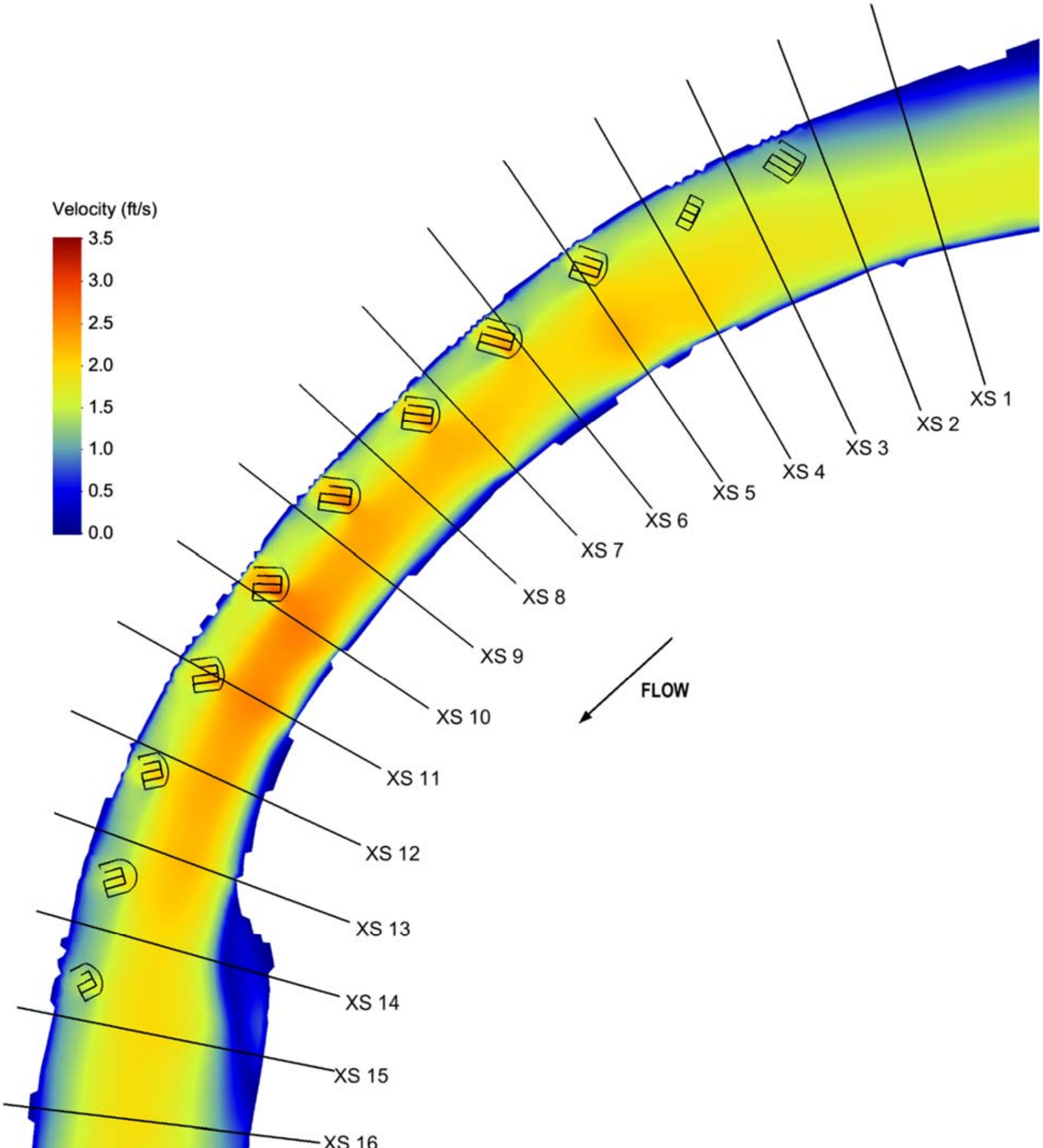

Figure 44: Bendway weir velocity contour plot when $R_c/T_w = 7.35$ (configuration 5)

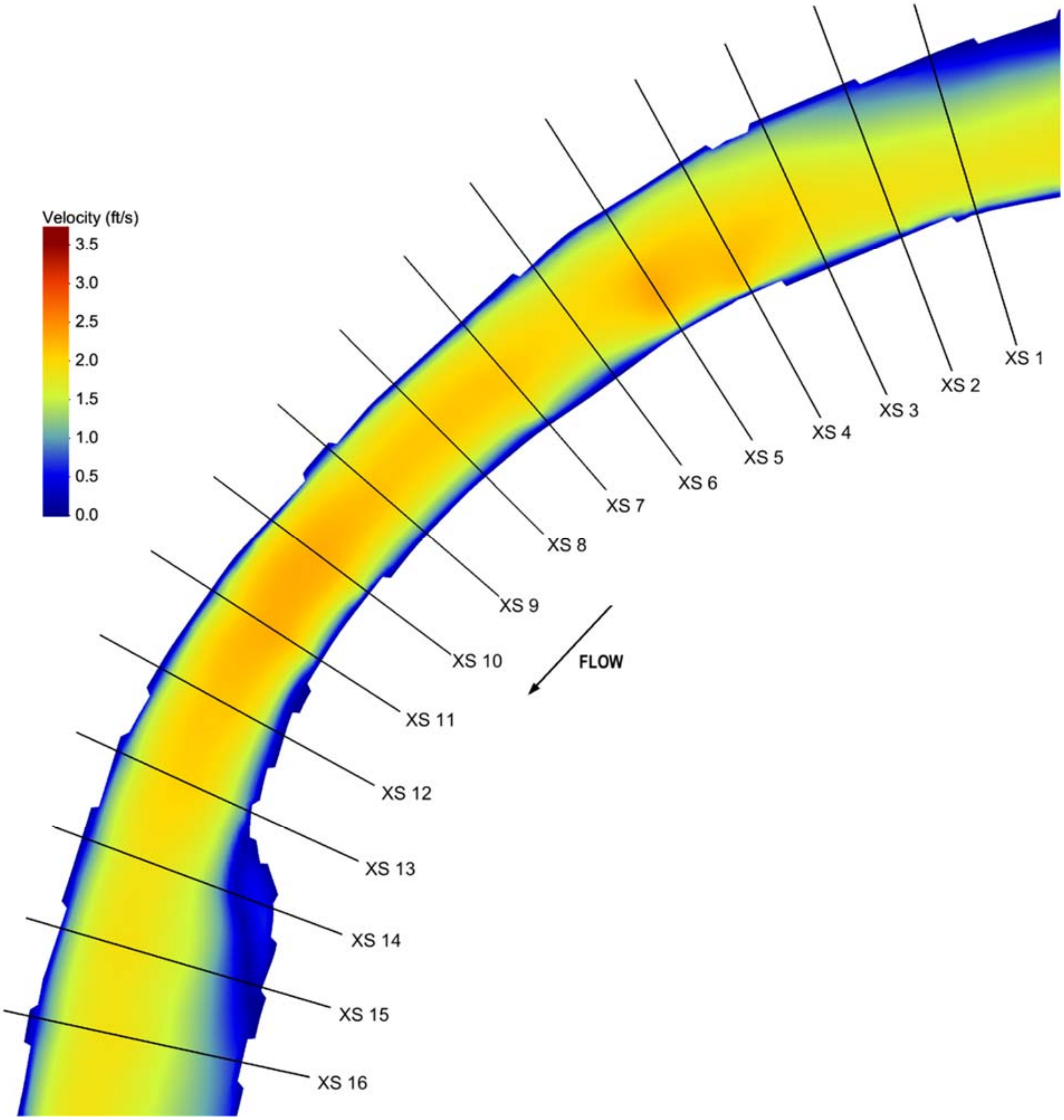

Figure 45: Baseline velocity contour plot when $R_c/T_w = 8.0$ (configuration 8)

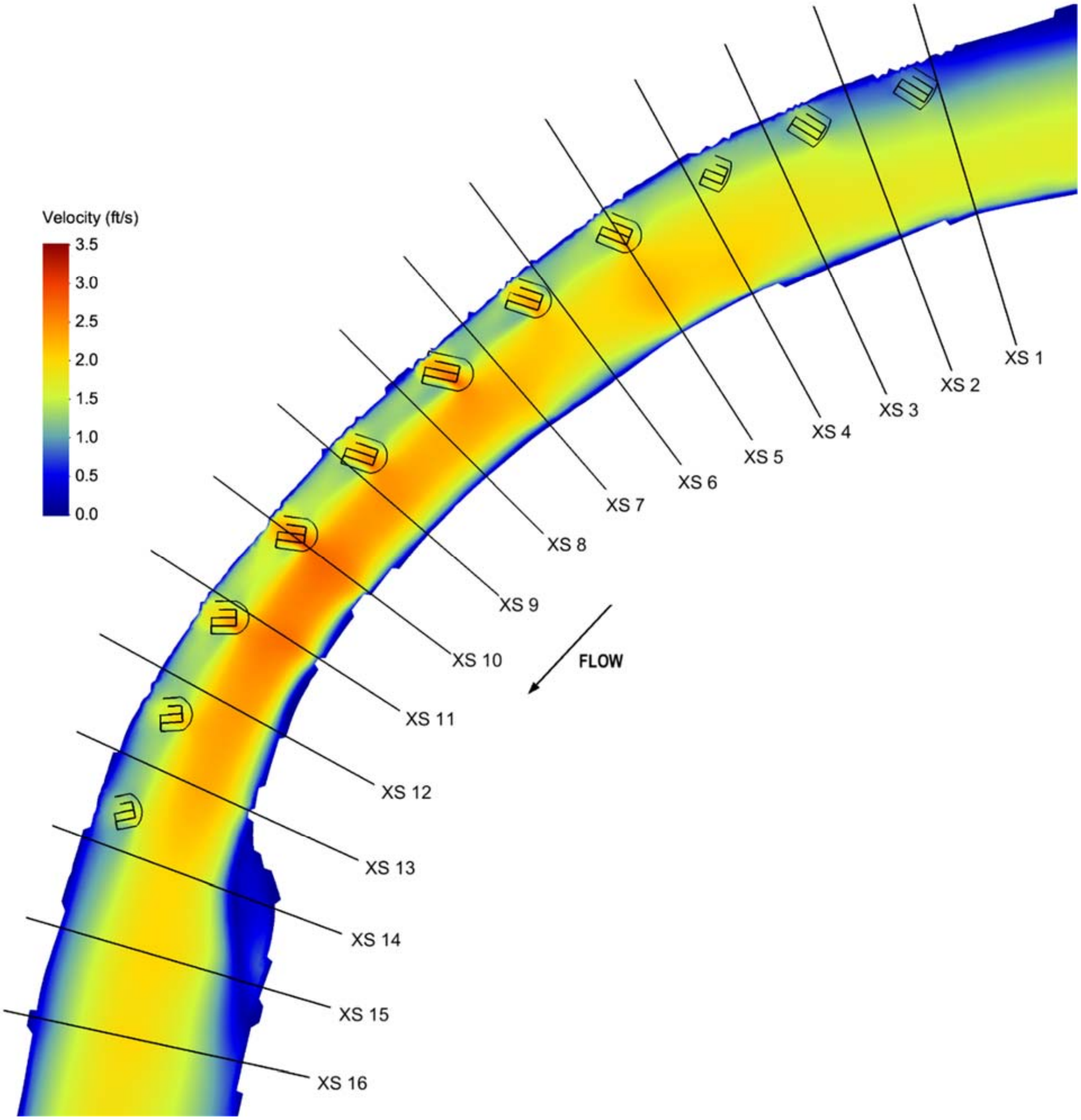

Figure 46: Bendway weir velocity contour plot when R_c/T_w = 8.0 (configuration 7)

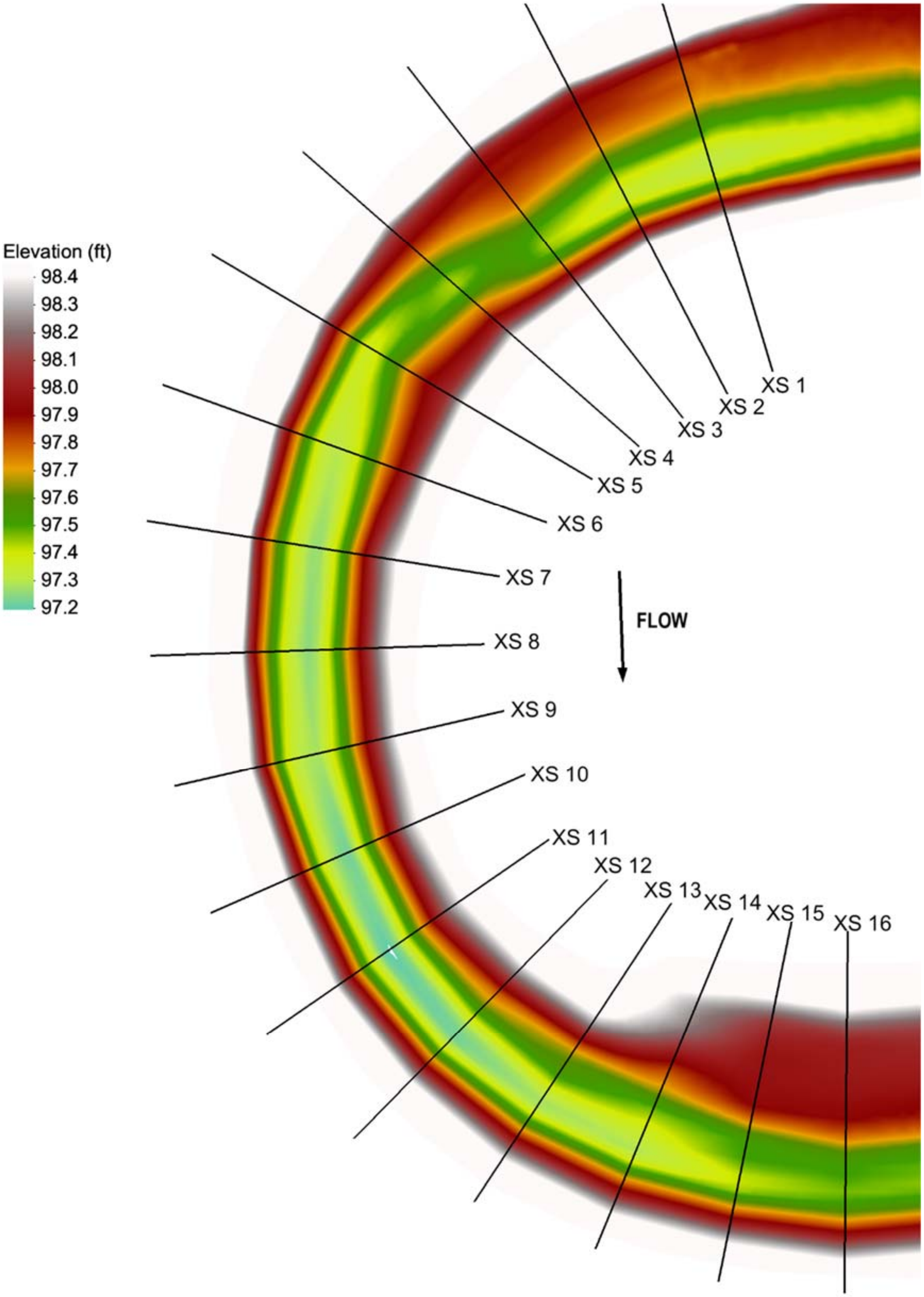

Figure 47: Bed elevation when $R_c/T_w = 3.0$ (configuration 2)

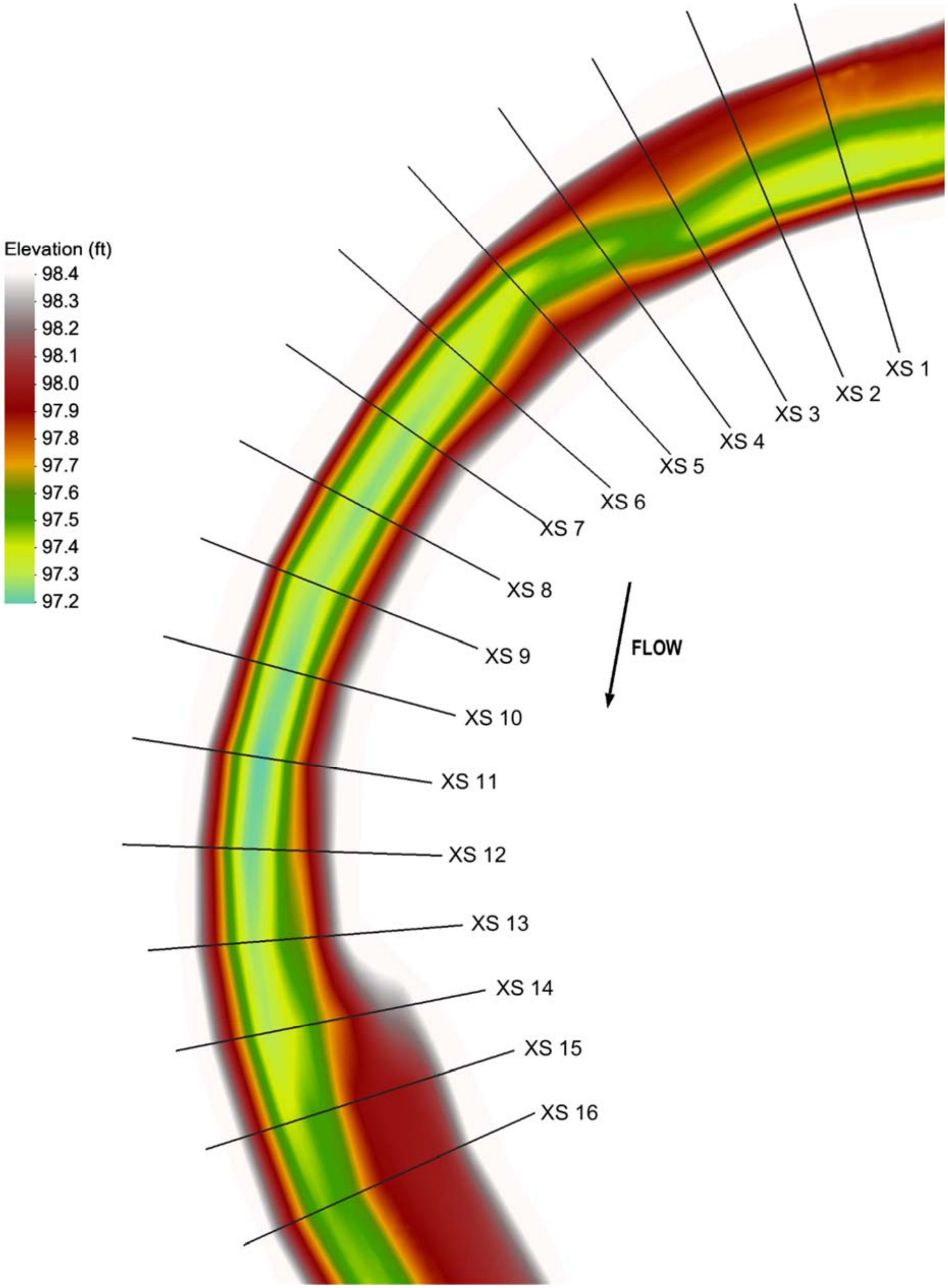

Figure 48: Bed elevation when $R_c/T_w = 5.0$ (configuration 4)

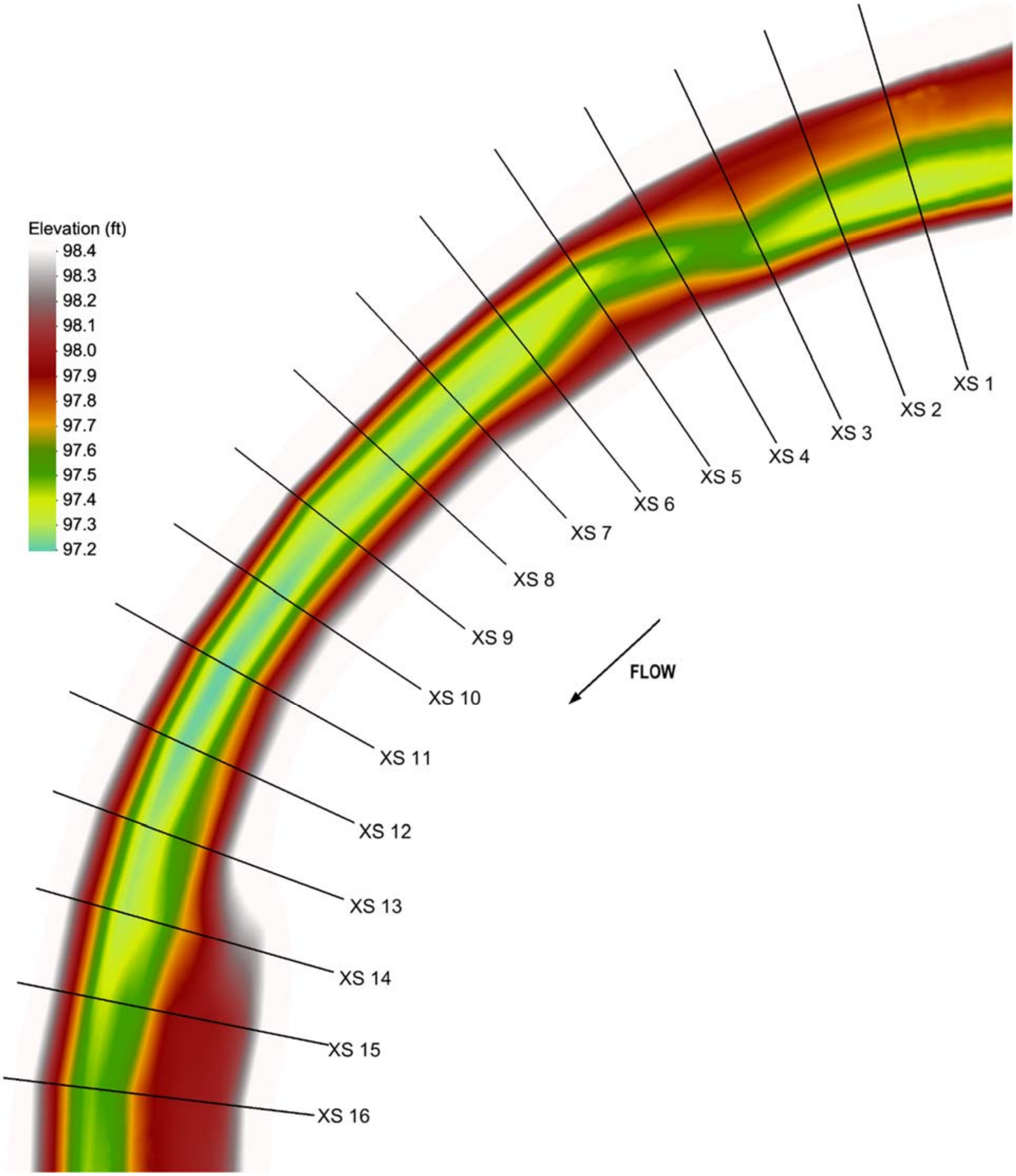

Figure 49: Bed elevation when $R_c/T_w = 7.35$ (configuration 6)

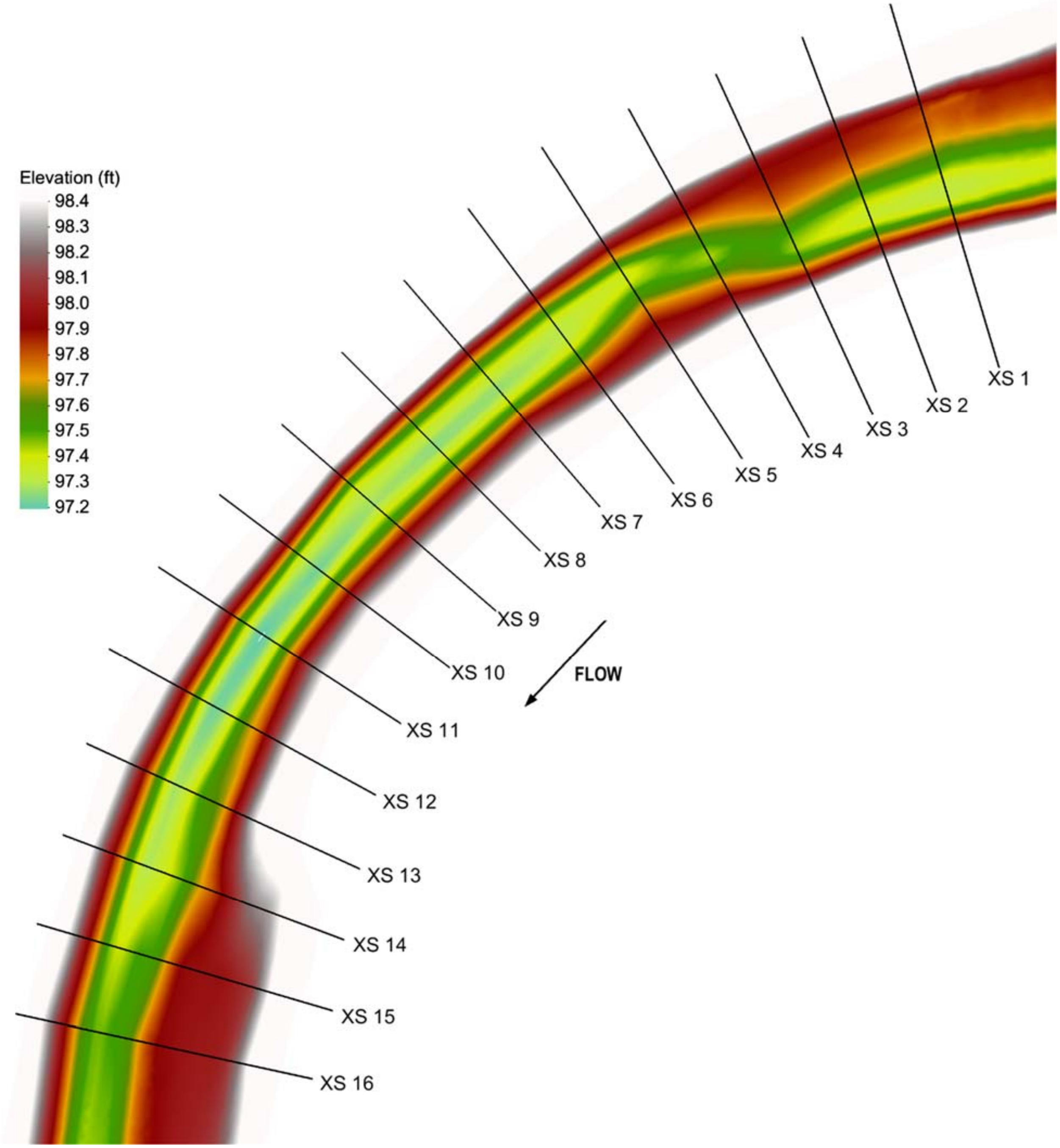

Figure 50: Bed elevation when $R_c/T_w = 8.0$ (configuration 8)

In addition to velocity contour plots, the channel shear stress was plotted using contours so that patterns of high shear stress could be seen spatially throughout the bend. These shear stress plots provide useful insight for bendway weir designers as to where zones of high shear stress zones would be located. Figure 51 through Figure 58 show the shear stress contour plots for each bend radii. The contour plots of depth average velocity compared with the plots of shear stress contours, show that zones of high velocity coincide with zones of high shear stress; this outcome is to be expected, given the known flow depths in these zones. The baseline (configurations 2, 4, 6, 8) contour plots show zones of high shear stress were located between cross-sections 4 and 5 and cross-section 10 and11 for all bend radii. This same result was found for the contour plots of depth average velocity. The bendway weir configurations also showed that the highest shear stress zone began at cross-section 7 and continued to cross-section 13, which was the same extent as the high velocity zone. The shear stress contour plots also showed that the bend radius of curvature had little effect on the shear stress distribution within the bend when a configuration of bendway weirs was installed.

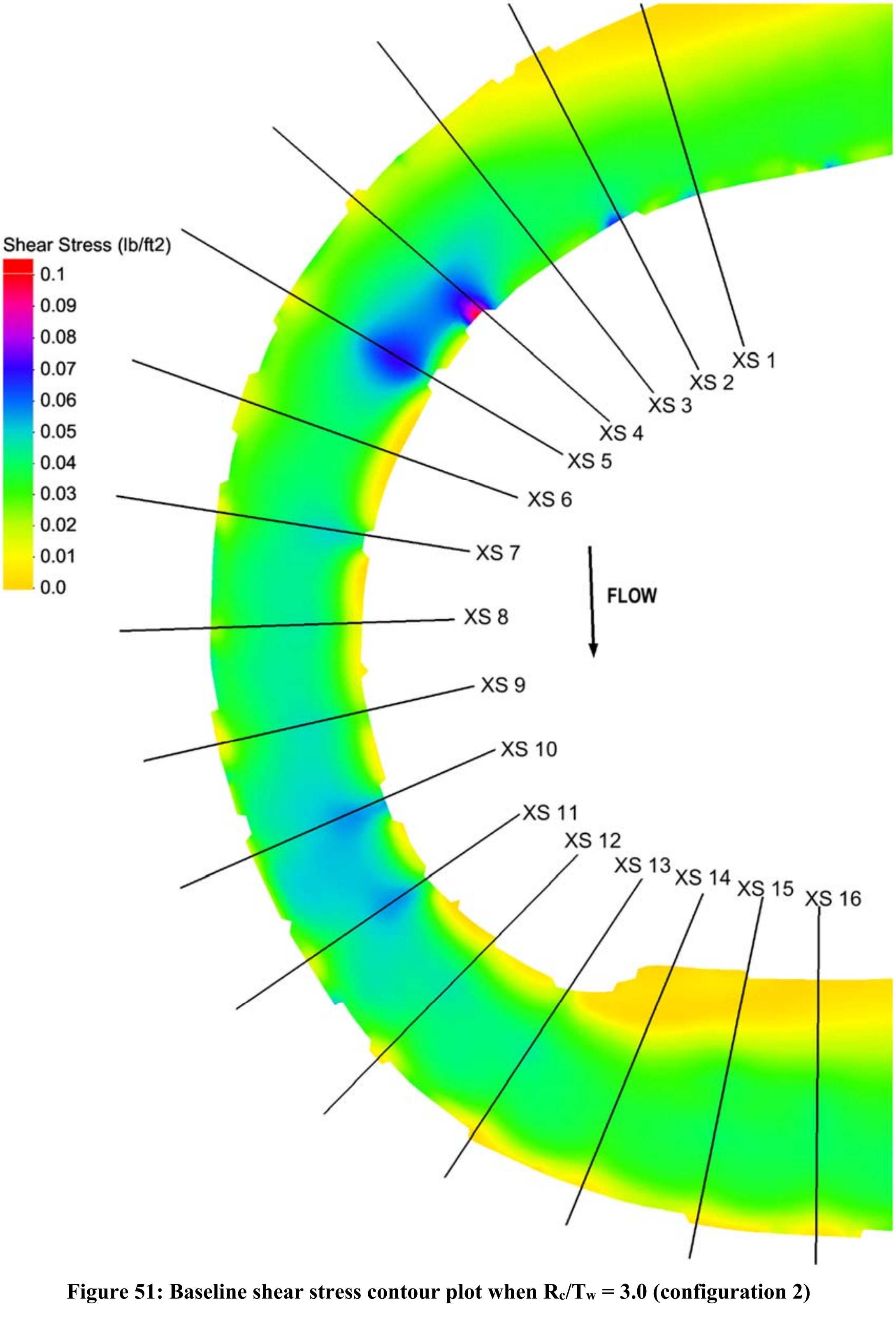

Figure 51: Baseline shear stress contour plot when $R_c/T_w = 3.0$ (configuration 2)

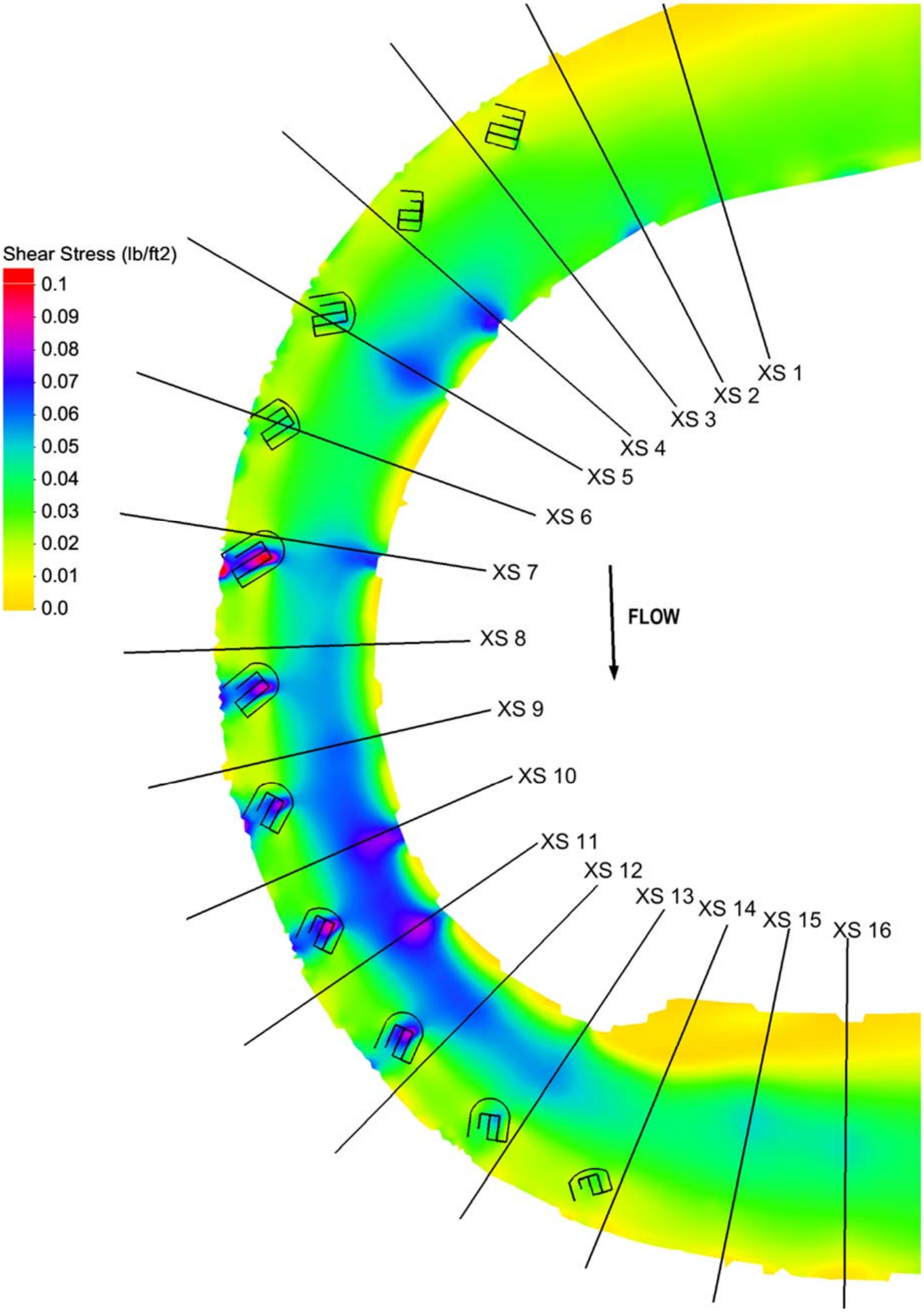

Figure 52: Bendway weir shear stress contour plot when $R_c/T_w = 3.0$ (configuration 1)

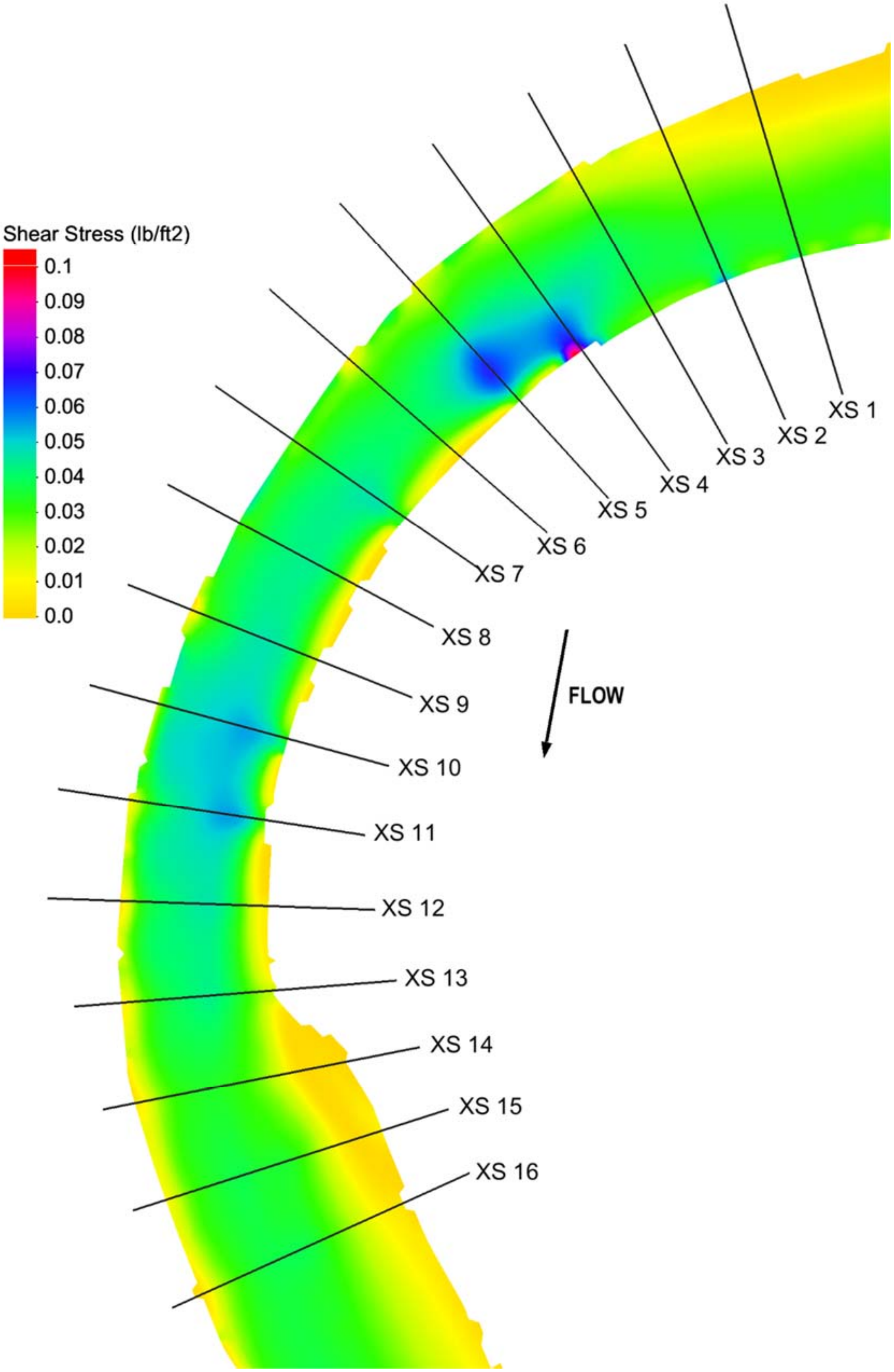

Figure 53: Baseline shear stress contour plot when $R_c/T_w = 5.0$ (configuration 4)

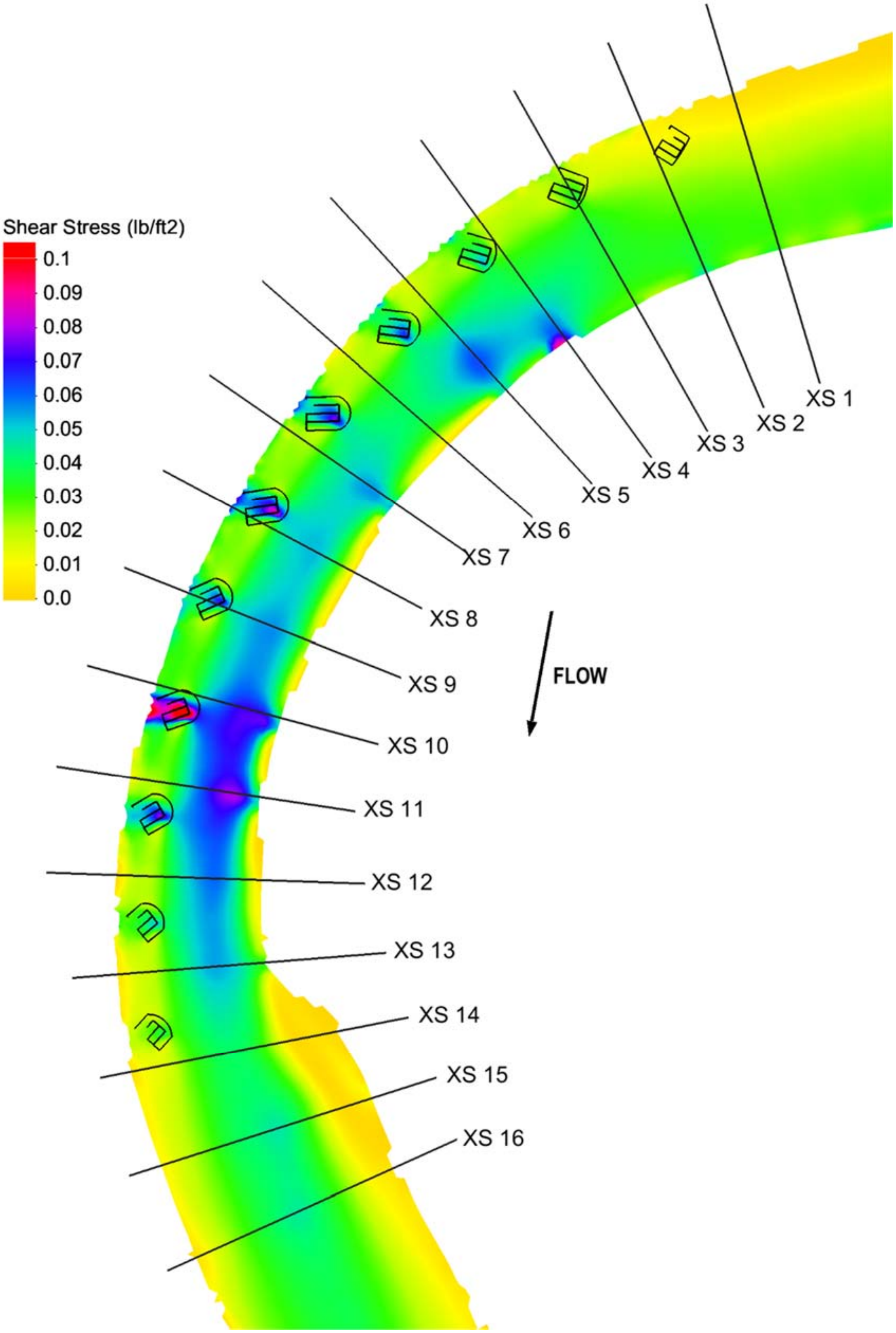

Figure 54: Bendway weir shear stress contour plot when $R_c/T_w = 5.0$ (configuration 3)

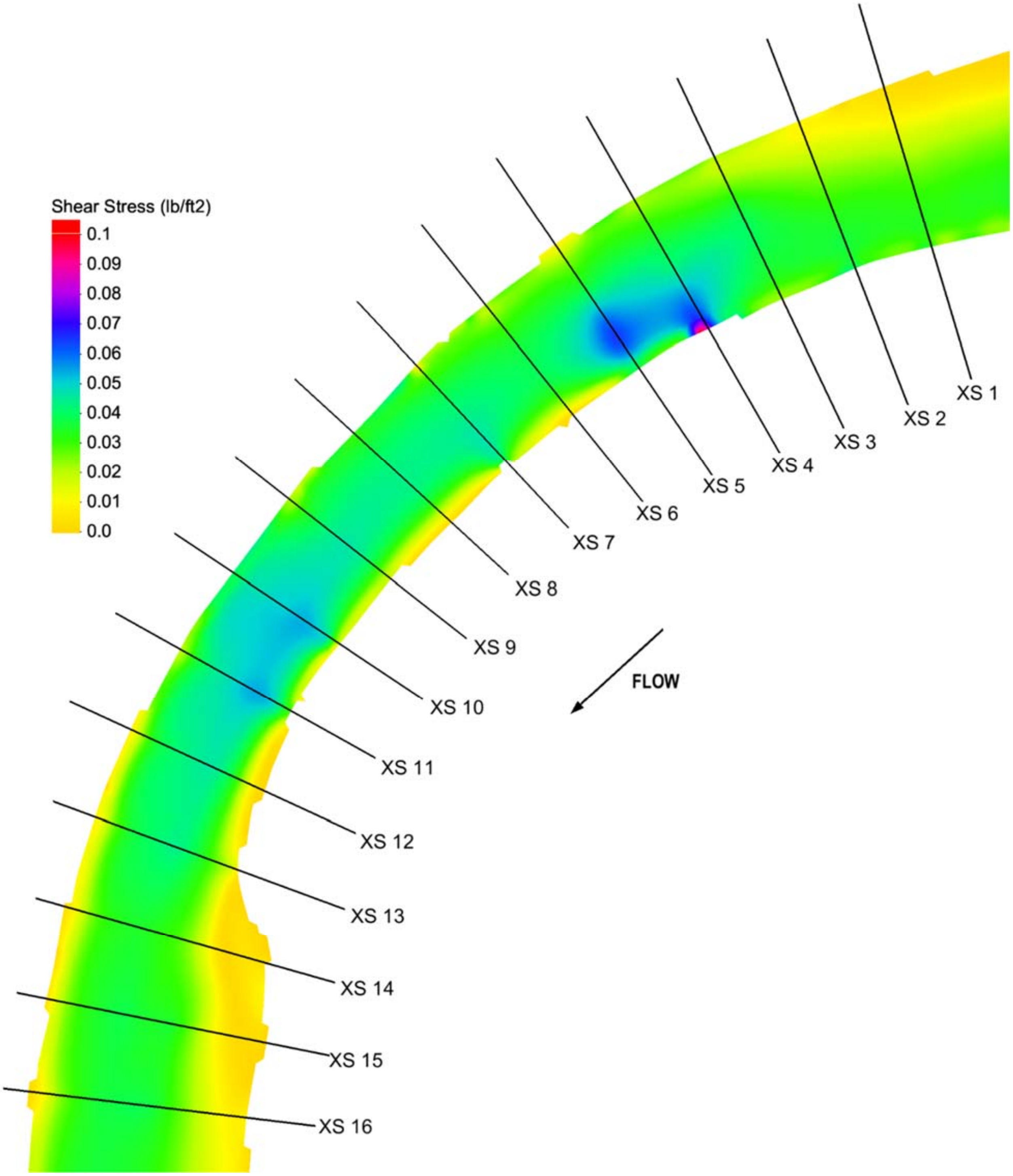

Figure 55: Baseline shear stress contour plot when R_c/T_w = 7.35 (configuration 6)

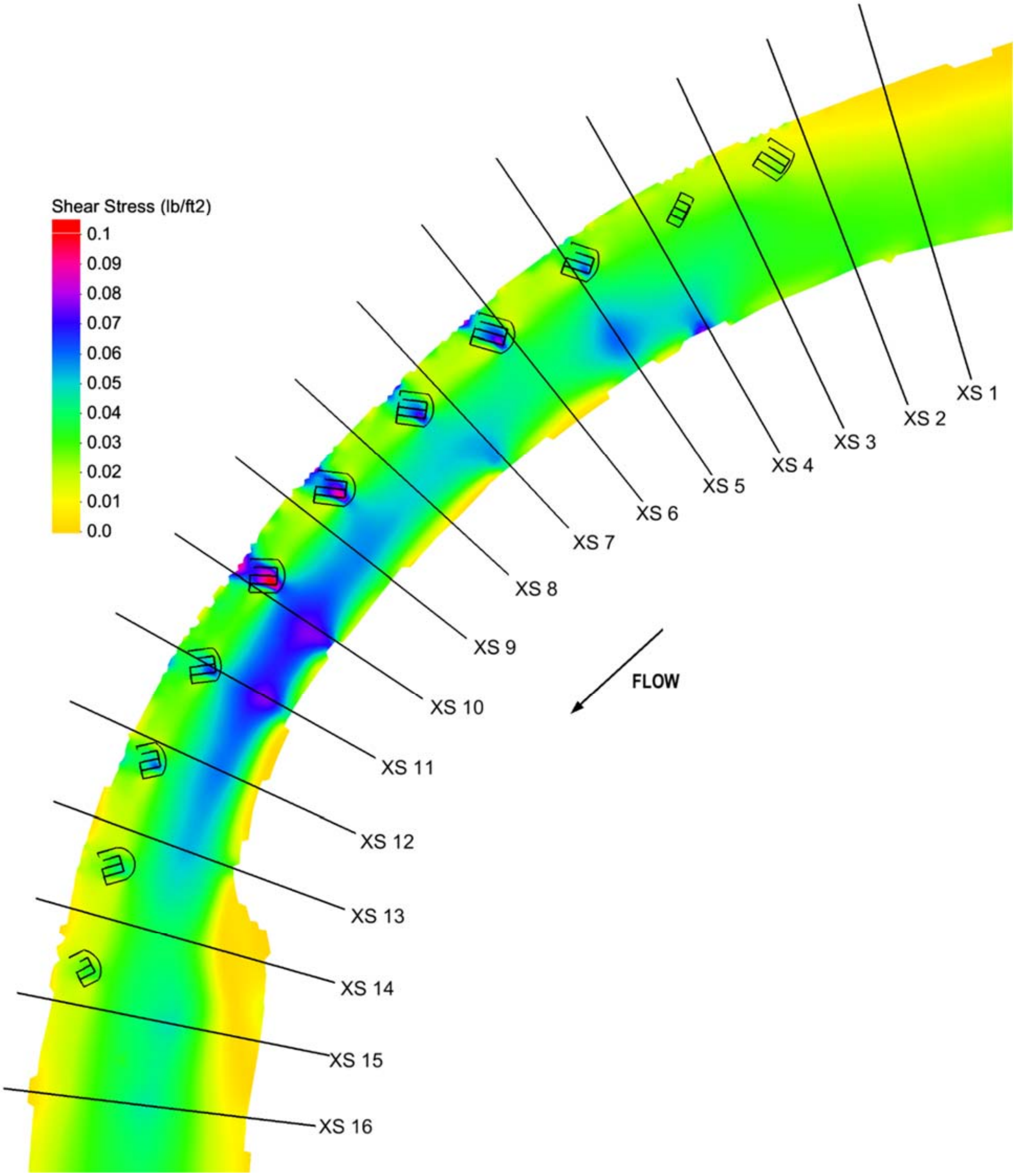

Figure 56: Bendway weir shear stress contour plot when R_c/T_w = 7.35 (configuration 5)

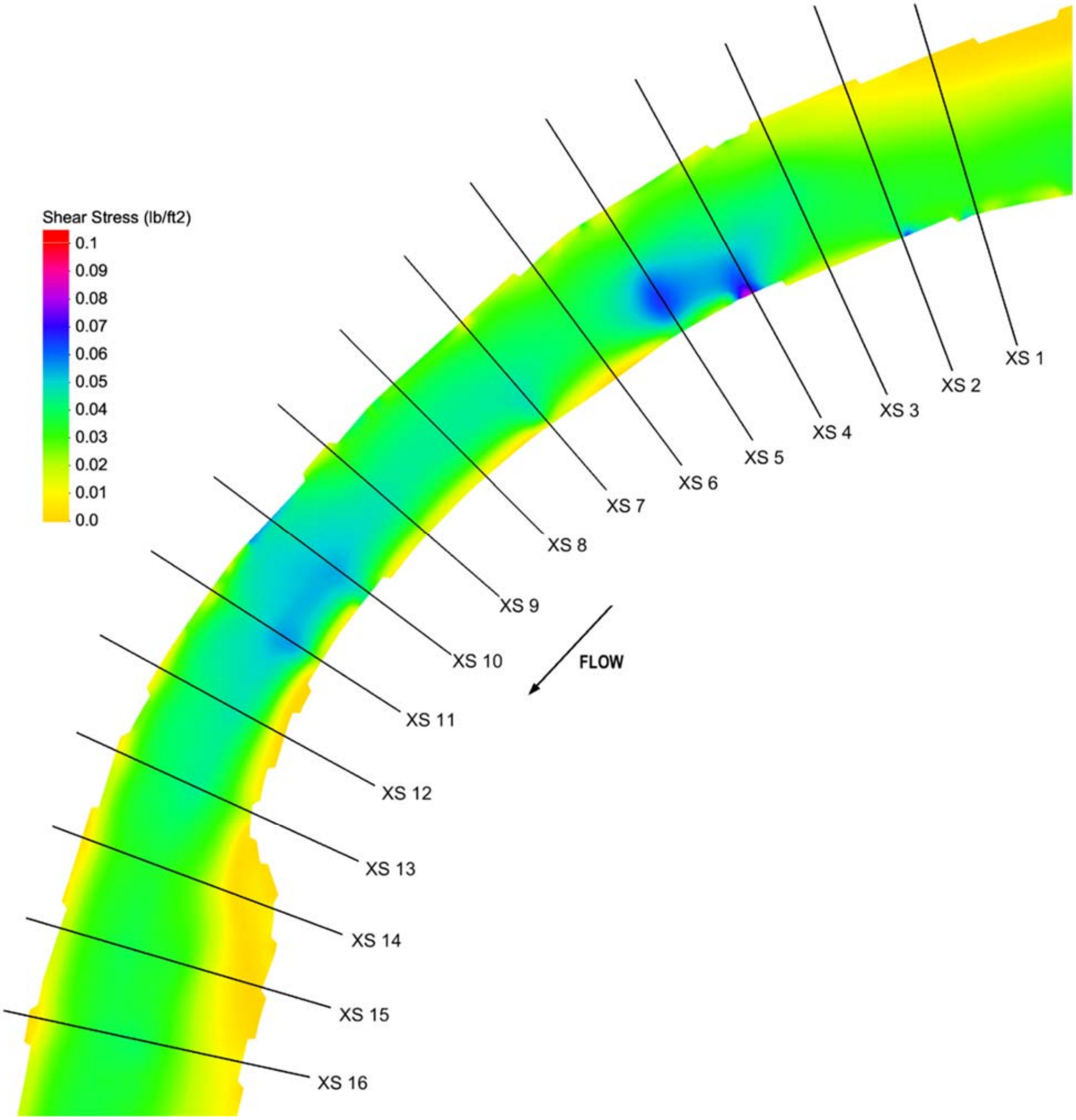

Figure 57: Baseline shear stress contour plot when R_c/T_w = 8.0 (configuration 8)

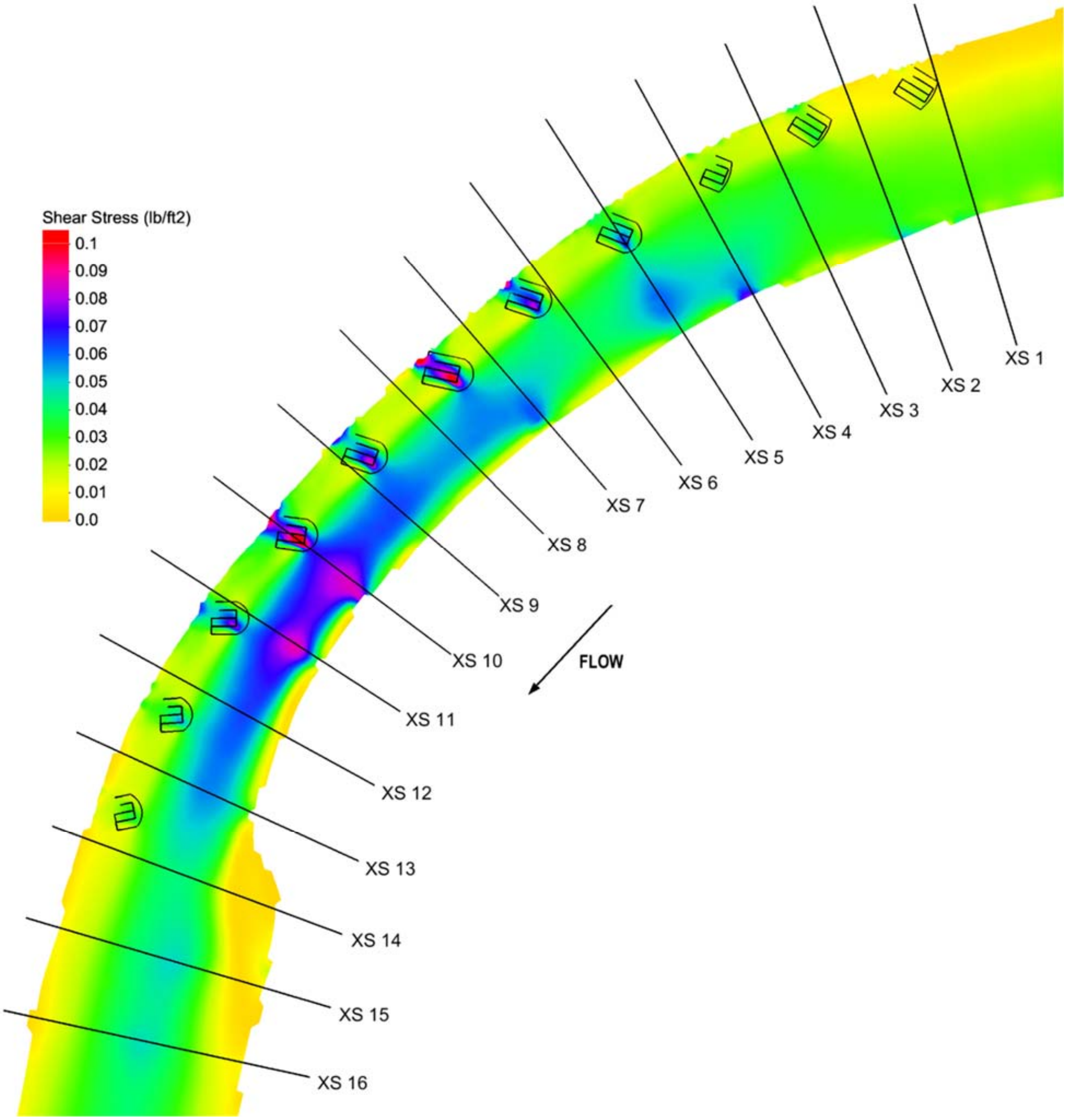

Figure 58: Bendway weir shear stress contour plot when $R_c/T_w = 8.0$ (configuration 7)

Trapezoidal Bathymetry

Use of the trapezoidal channel isolated the effects of the native bathymetry on the flow field and helped check if the trends and patterns observed in the native bathymetry were also observed in the trapezoidal channel. The velocity contour plots shown in Figure 59 through Figure

62 show that the velocity was evenly distributed when $R_c/T_w = 6.13$ and 2.3, for configurations 9 through 12. One important characteristic of the flow field to mention is that the high velocities in both bend radii were observed toward the inner bank of the bend in the baseline condition (configurations 10 and 12). High velocities toward the inner bank of a trapezoidal channel were also found by Pradhan et al. (2018) using a hydraulic model and a 2D numerical model. They showed that the combined effect of centrifugal acceleration, water surface super elevation, lateral pressure gradient, and secondary flows led to a lag between flow distribution and channel curvature. These factors contributed to higher inner bank velocities compared to the outer bank. Similar to the native bathymetry, installation of bendway weirs increased flow velocity in the channel center and inner bank regions, and decreased the velocity between bendway weirs, as expected. Both values of R_c/T_w showed similar velocity patterns with the presence of bendway weirs showing that the flow field patterns around the bendway weirs were not affected by the bend radius of curvature.

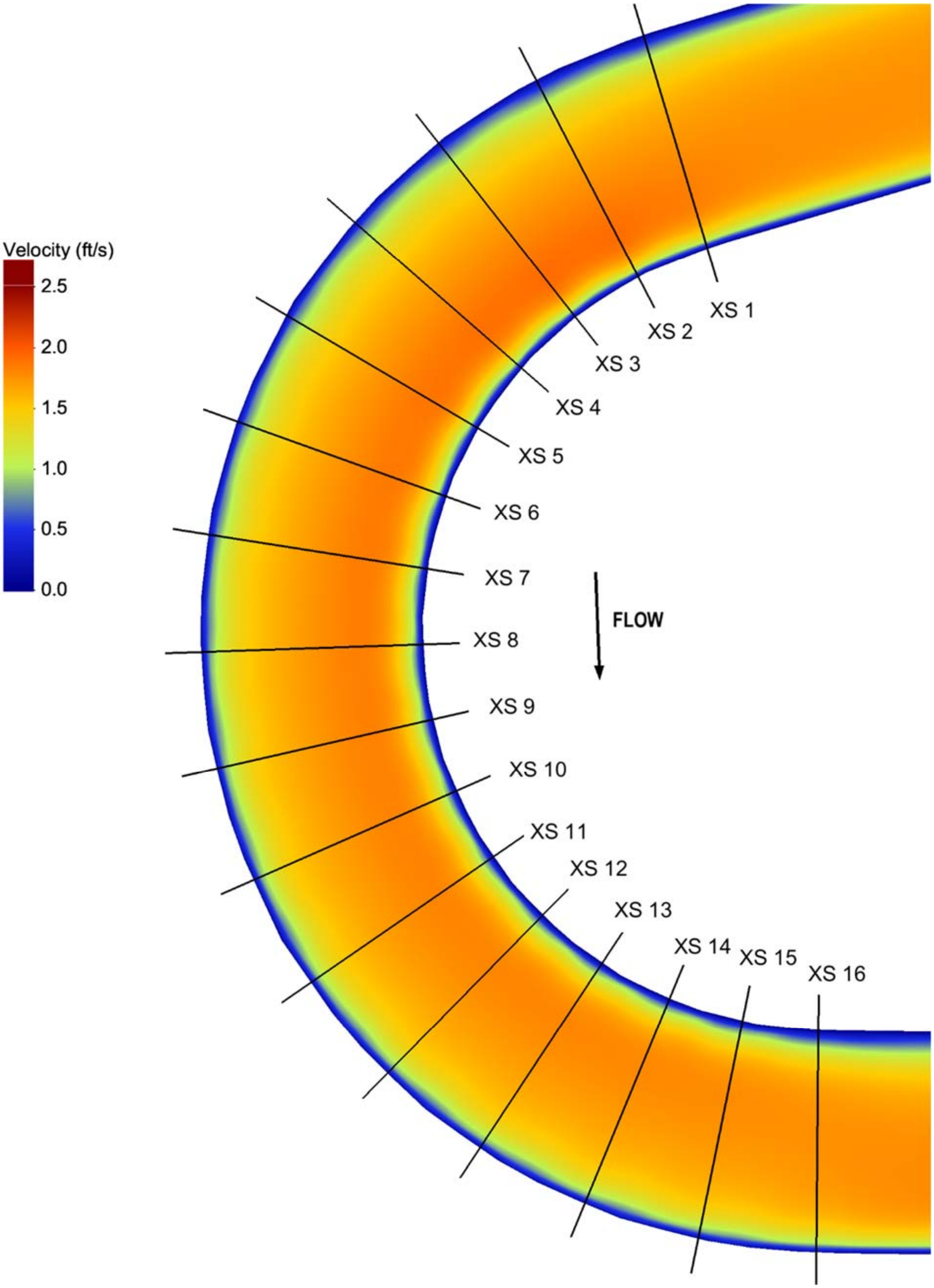

Figure 59: Baseline velocity contour plot when $R_c/T_w = 3.0$ (configuration 10)

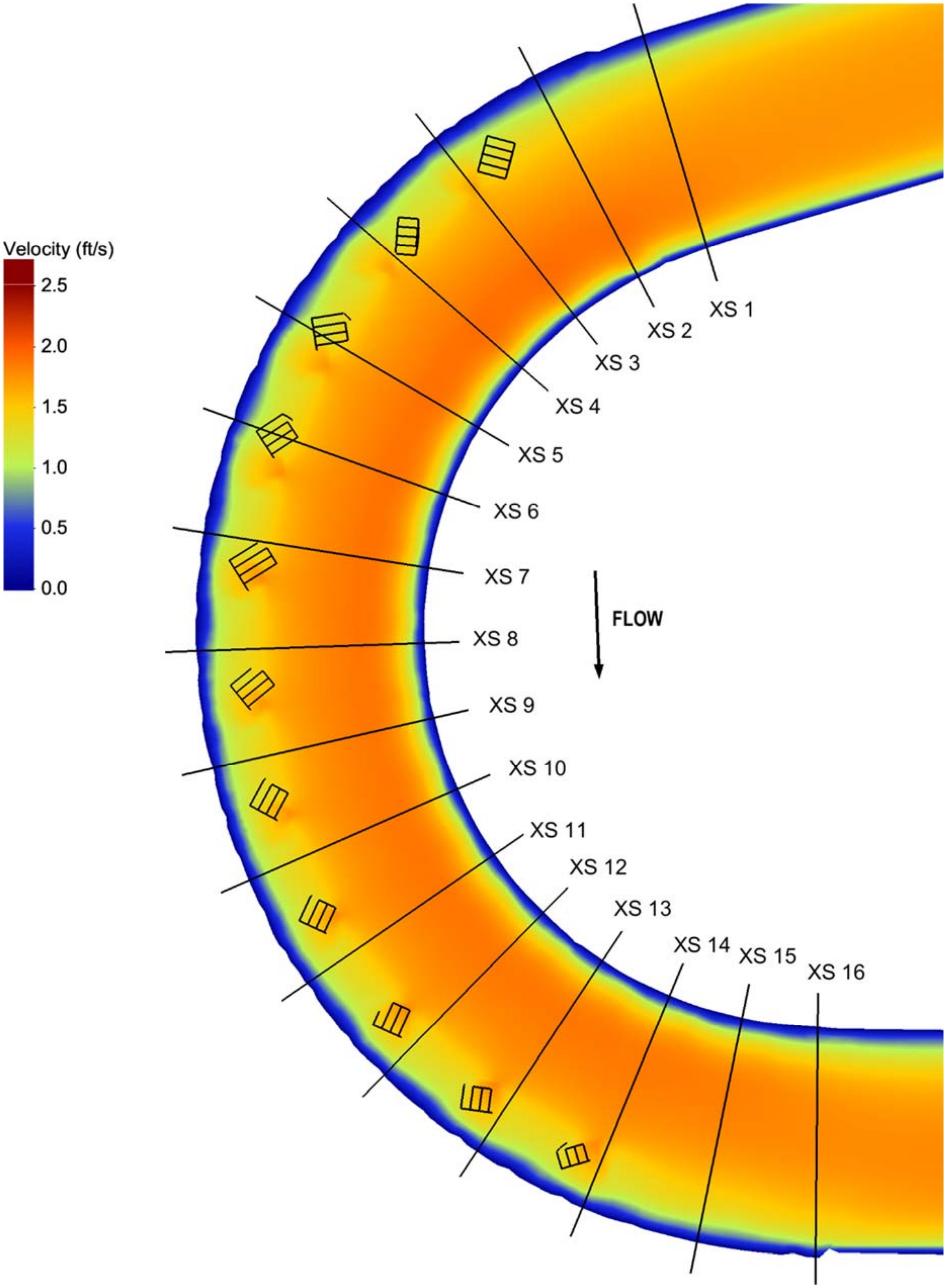

Figure 60: Bendway weir velocity contour plot when $R_c/T_w = 3.0$ (configuration 9)

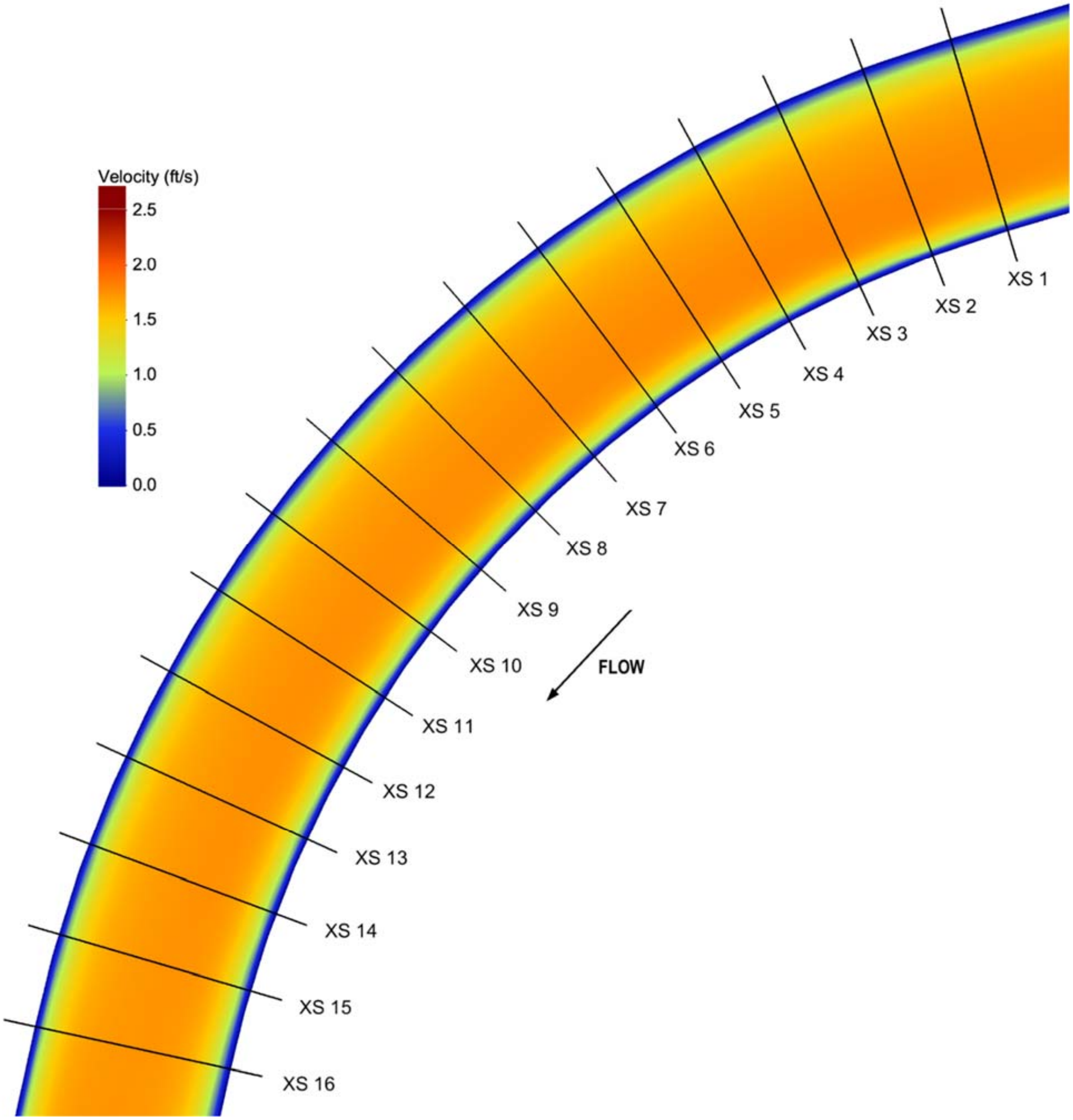

Figure 61: Baseline velocity contour plot when R_c/T_w = 8.0 (configuration 12)

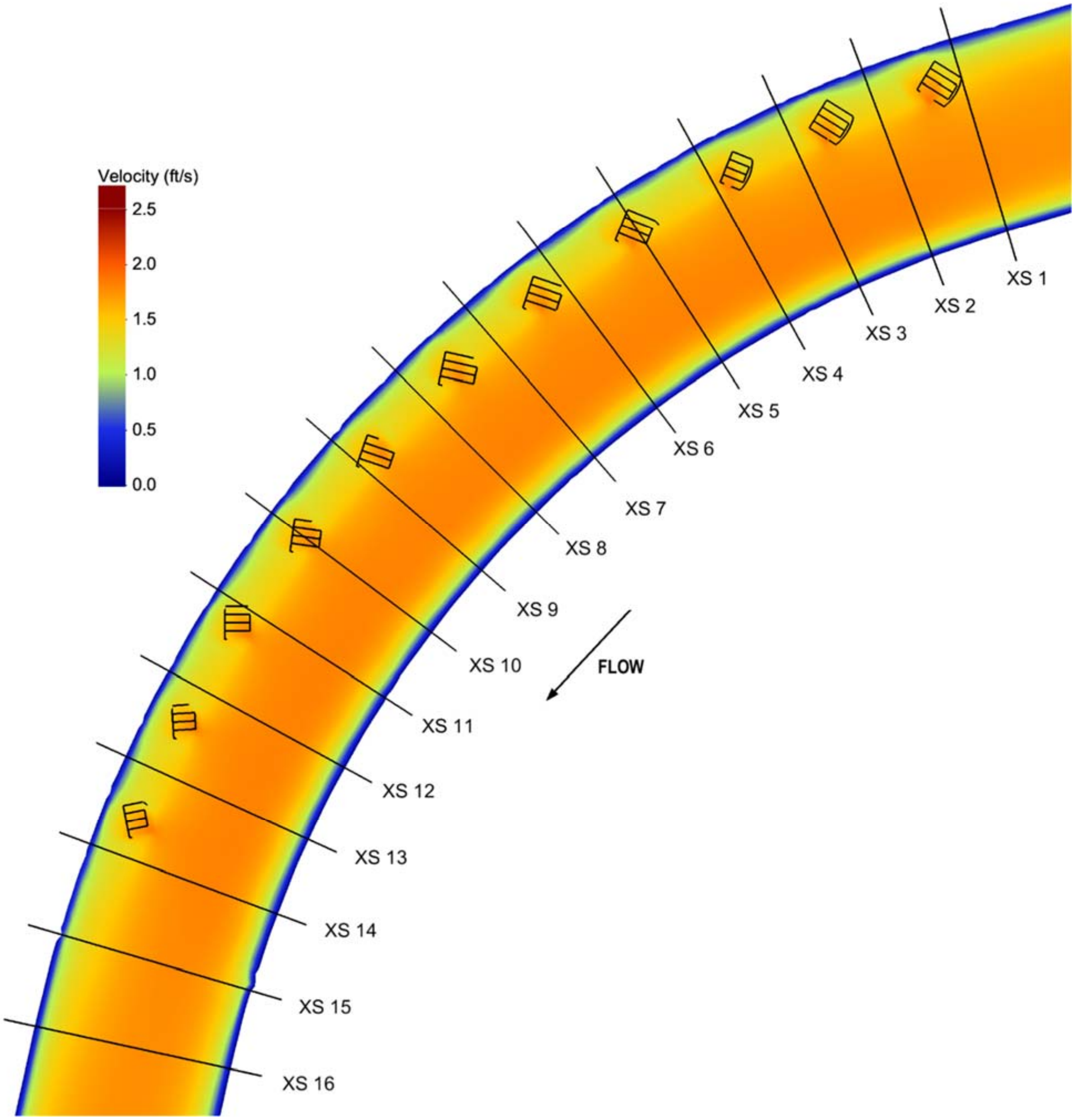

Figure 62: Bendway weir velocity contour plot when $R_c/T_w = 8.0$ (configuration 11)

In addition to the velocity contour plots, shear stress contour plots were also created for analysis. Shear stress plots shown in Figure 63 through Figure 66 for the trapezoidal channel helped identify specific patterns in the flow field, as the velocity field was very uniform between both values of R_c/T_w in the baseline and bendway weir case. Figure 63 and Figure 65 (configurations 10 and 12) show that the maximum shear stress in both values of R_c/T_w occurred near cross-section 2, but the maximum shear stress was greater when $R_c/T_w = 2.3$. In both bend radii cases, the installation of bendway weirs did not cause this area of maximum shear stress to move locations within the bend. Instead, the installation of bendway weirs increased the shear stress toward the middle to inner bank region due to flow contraction and increase of velocity in this region. Shear stress was increased throughout the bend where bendway weirs contracted the flow from about cross-sections 2 to 15. Shear stress between the weirs was found to be a minimum for both cases and magnitudes in the contour plots appeared to have very small differences between both bend radii.

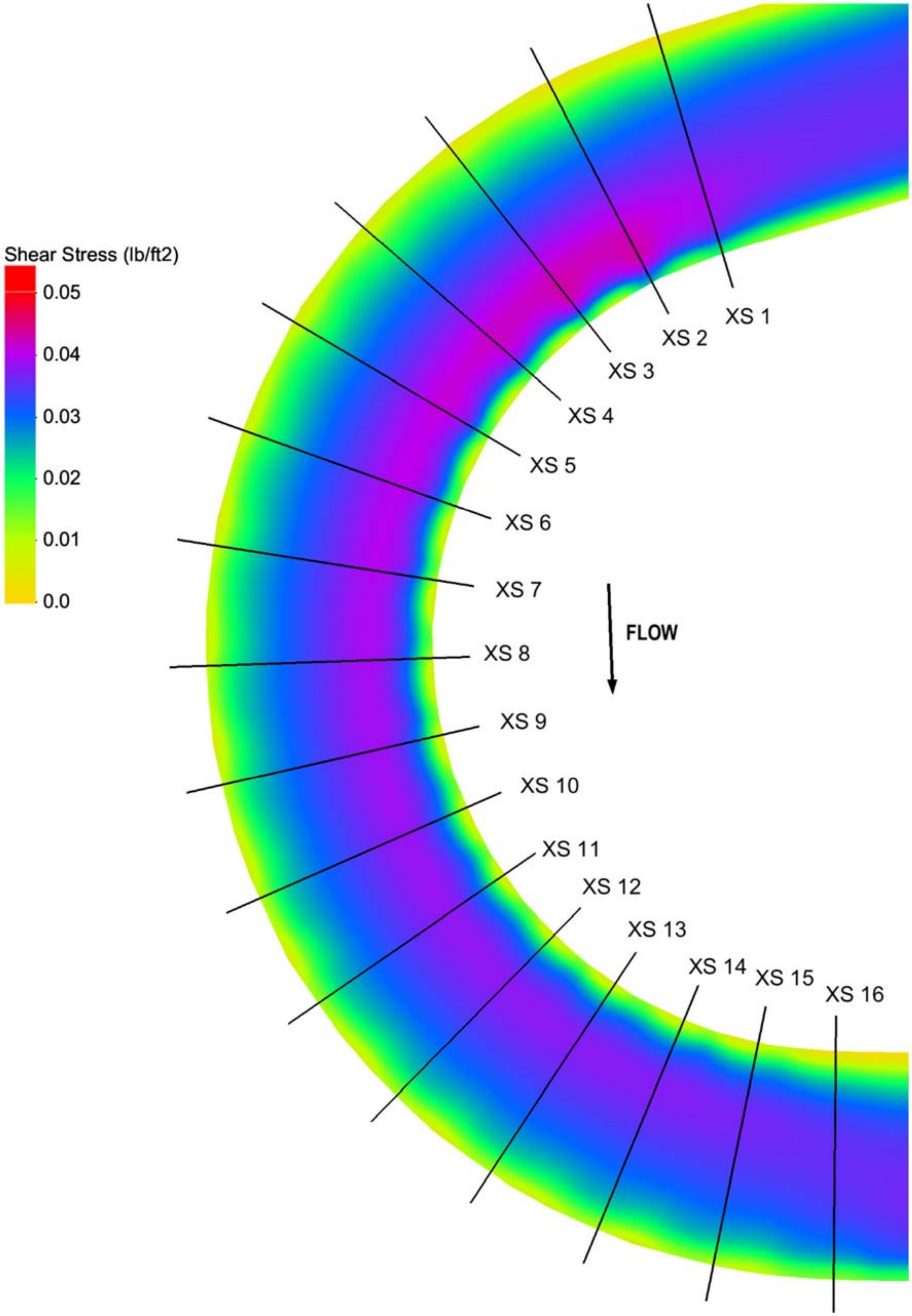

Figure 63: Baseline shear stress contour plot when $R_c/T_w = 3.0$ (configuration 10)

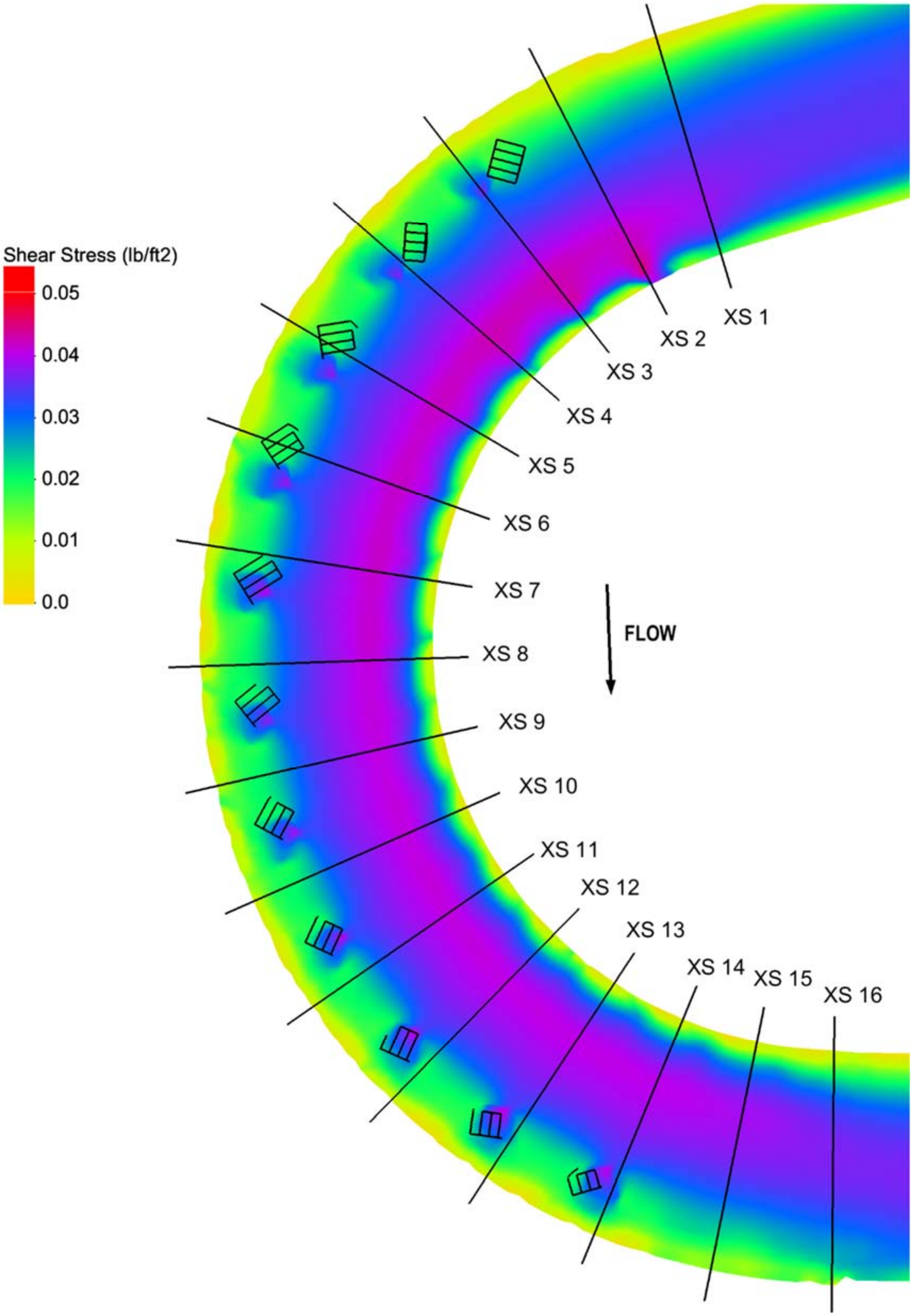

Figure 64: Bendway weir shear stress contour plot when $R_c/T_w = 3.0$ (configuration 9)

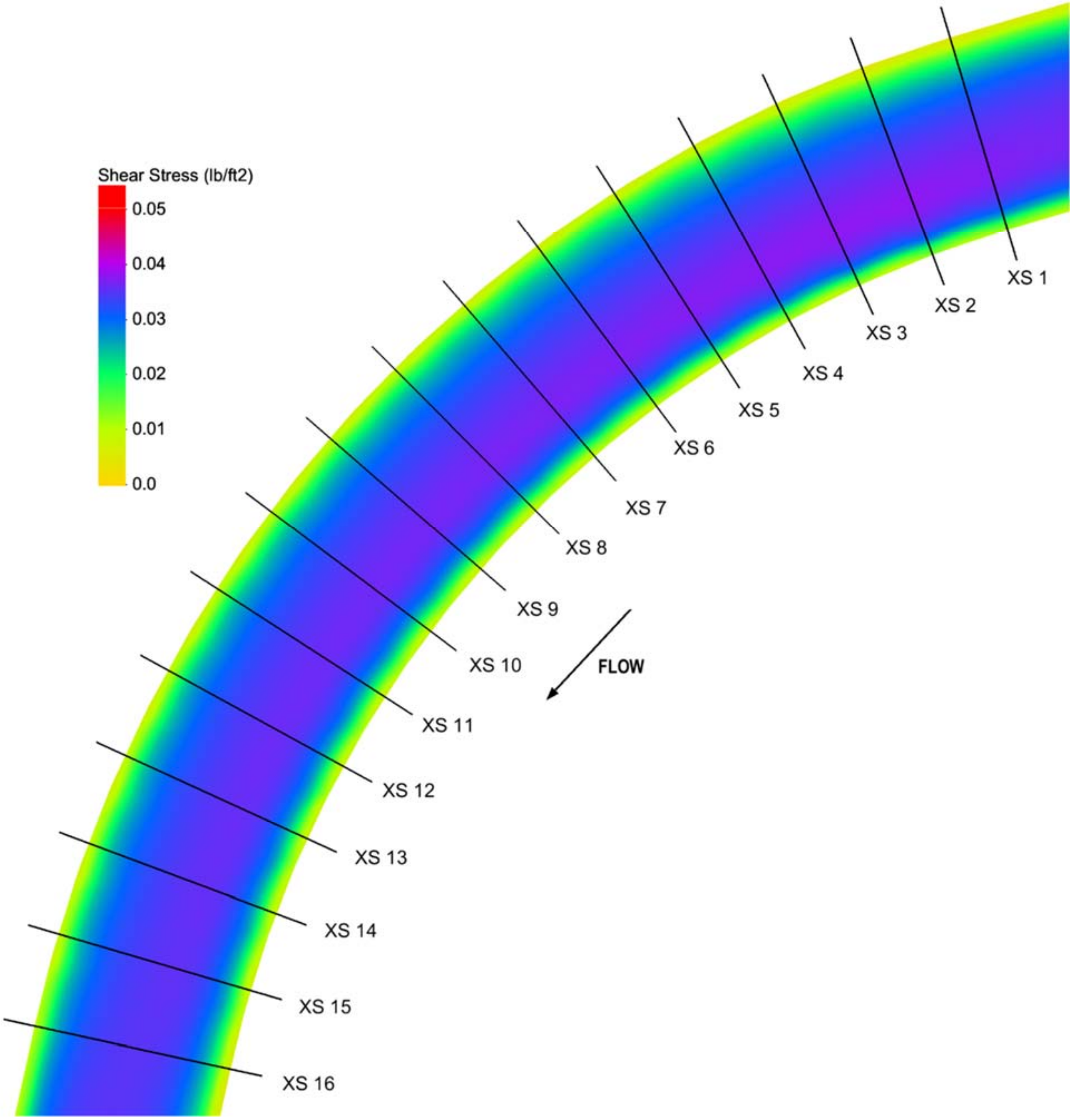

Figure 65: Baseline shear stress contour plot when $R_c/T_w = 8.0$ (configuration 12)

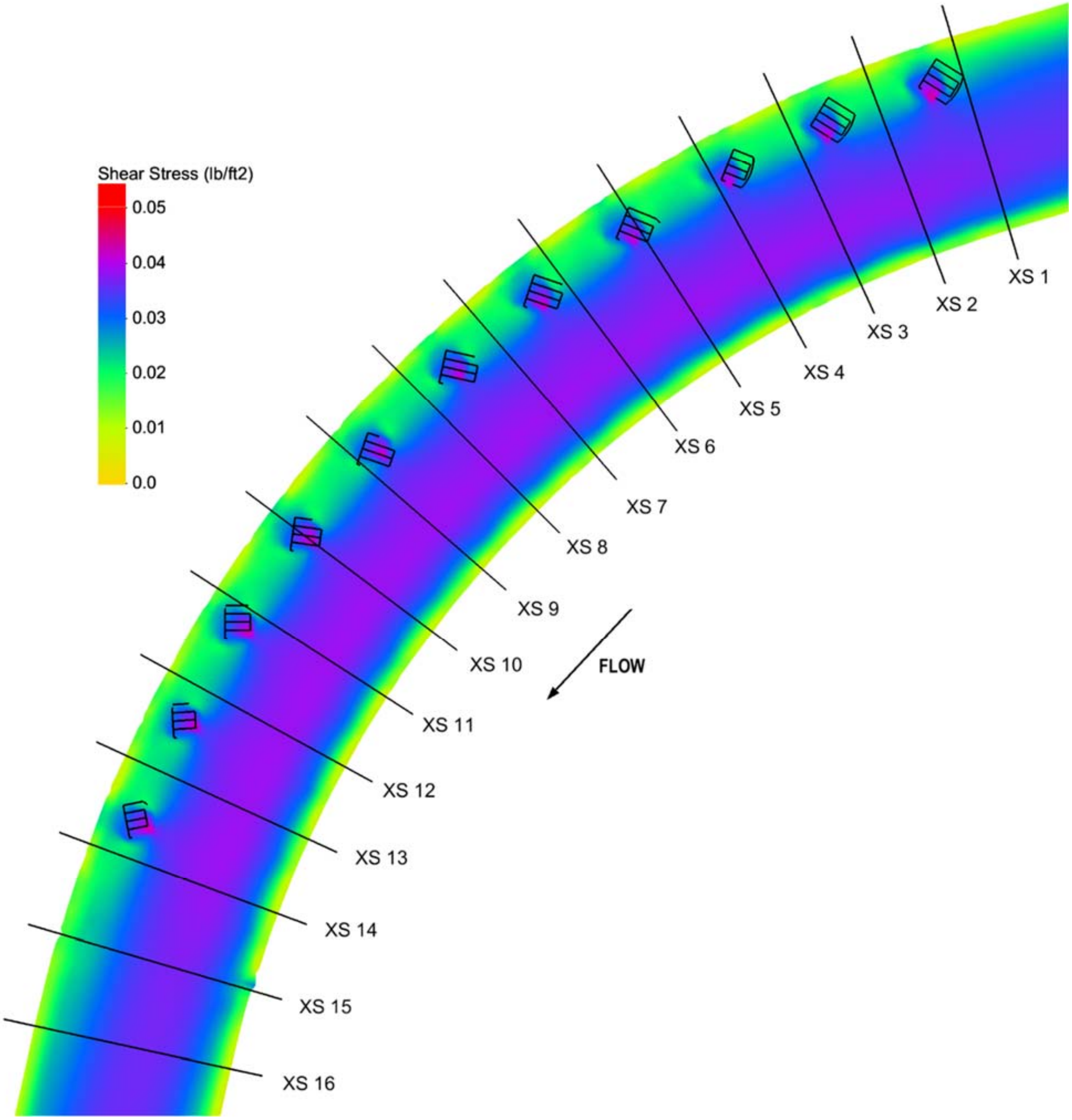

Figure 66: Bendway weir shear stress contour plot when R_c/T_w = 8.0 (configuration 11)

Cross-sectional Water Surface Elevation and Velocity

Native Bathymetry

Although contour plots show the spatial patterns of depth average velocity within the channel, cross-section plots of both velocity and WSE enable quantitative analysis of the flow field between the bends. Cross-sectional velocity and WSE distributions were extracted using the same 16 cross-sections that were used to form the bend geometry in each bend radius. Cross-sections were spaced at the same bend length in each bend and therefore, the flow traveled the same distance in each bend. Additionally, bathymetry and area of each cross-section were preserved as bend radius varied. Figure 47 through Figure 50 show the locations of the 16 cross-sections for each bend radius.

Plotting distributions of depth average velocity at the same cross-sections, facilitated direct comparisons of velocity distributions between each bend radius. Cross-sectional distributions of velocity were plotted for the baseline and bendway weir configurations for each bend radius. A complete set of cross-sectional velocity distribution plots can be found in Appendix B. However, Figure 67 and Figure 68 show two examples of these plots. These two figures give the distributions of depth average cross-sectional velocity at cross-section 9, located near the apex of the bend. This cross-section was located in the zone of relatively high velocity with and without bendway weirs.

Figure 67 shows that the velocity distribution in the baseline configuration for all bend radii remained the same, with negligible variations. Figure 68 shows that there was very little difference in velocity toward the inner bank between bend radii in the bendway weir configuration and in the contracted flow region created by the bendway weirs. There seemed to be more variation in depth average velocity when $R_c/T_w = 5.0$, especially toward the outer bank as shown in Figure 68, but the variation was due to flow passing over a bendway weir where the flow was contracted and velocity was increased, as shown in Figure 42. Flow velocity at the tip and top of bendway weirs was greater than that which occurred in the rest of the channel, such that the velocity values were not representative of the channel generally in this area. This result also occurred at other cross-sections. However, cross-section 7, 12, 13, 14, 15, and 16, represented cross-sections that did not intercept a bendway weir. Figure 69 through Figure 72 show the cross-sectional velocity distributions with and with bendway weirs for cross-sections 7 and 12. The velocity distributions at these cross-sections also indicated that the velocity distribution remained nearly identical for all R_c/T_w values with negligible differences. Therefore, these cross-sectional velocity plots show that R_c/T_w (specifically R_c) had little effect on the flow field in the native bathymetry channels fitted with bendway weirs.

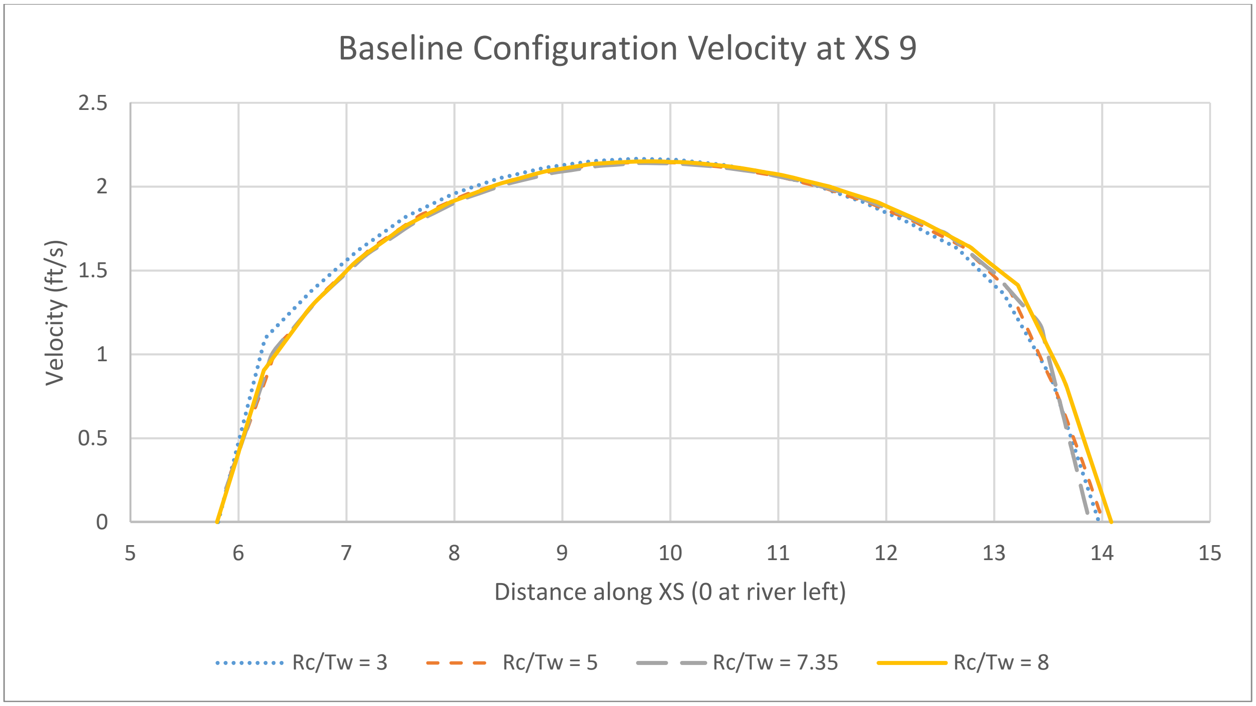

Figure 67: Baseline velocity distribution at cross-section 9

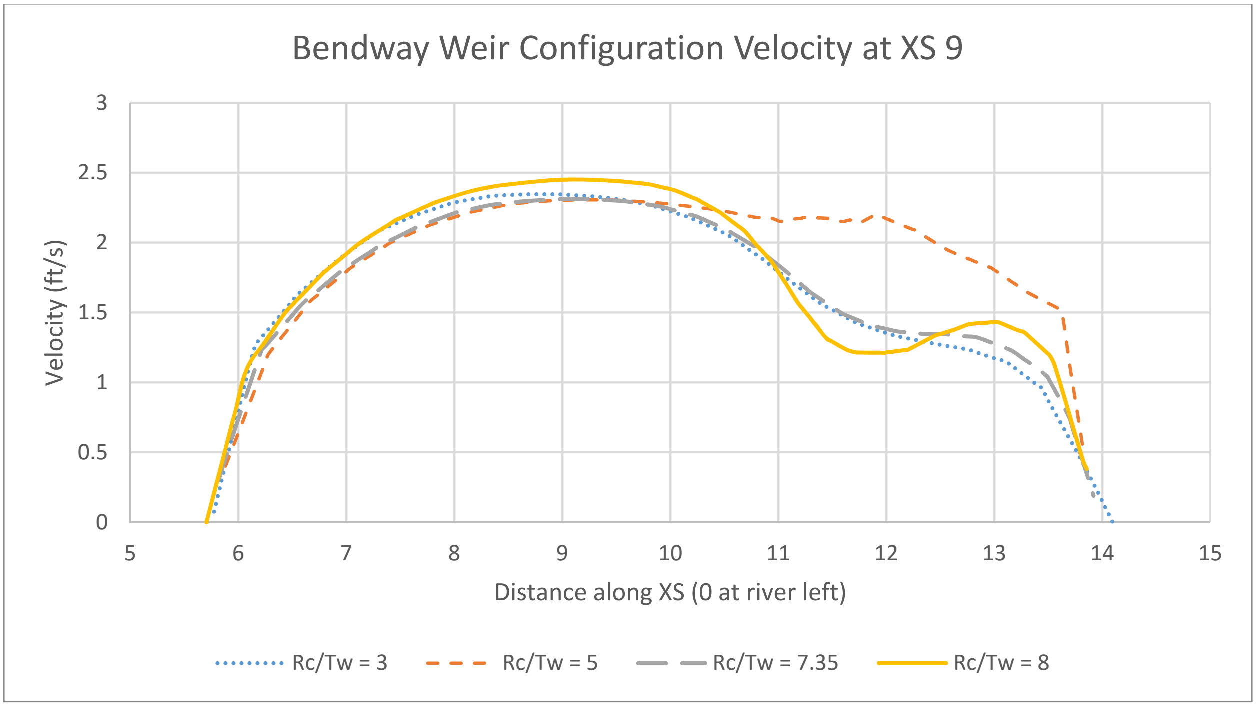

Figure 68: Bendway weir velocity distribution at cross-section 9

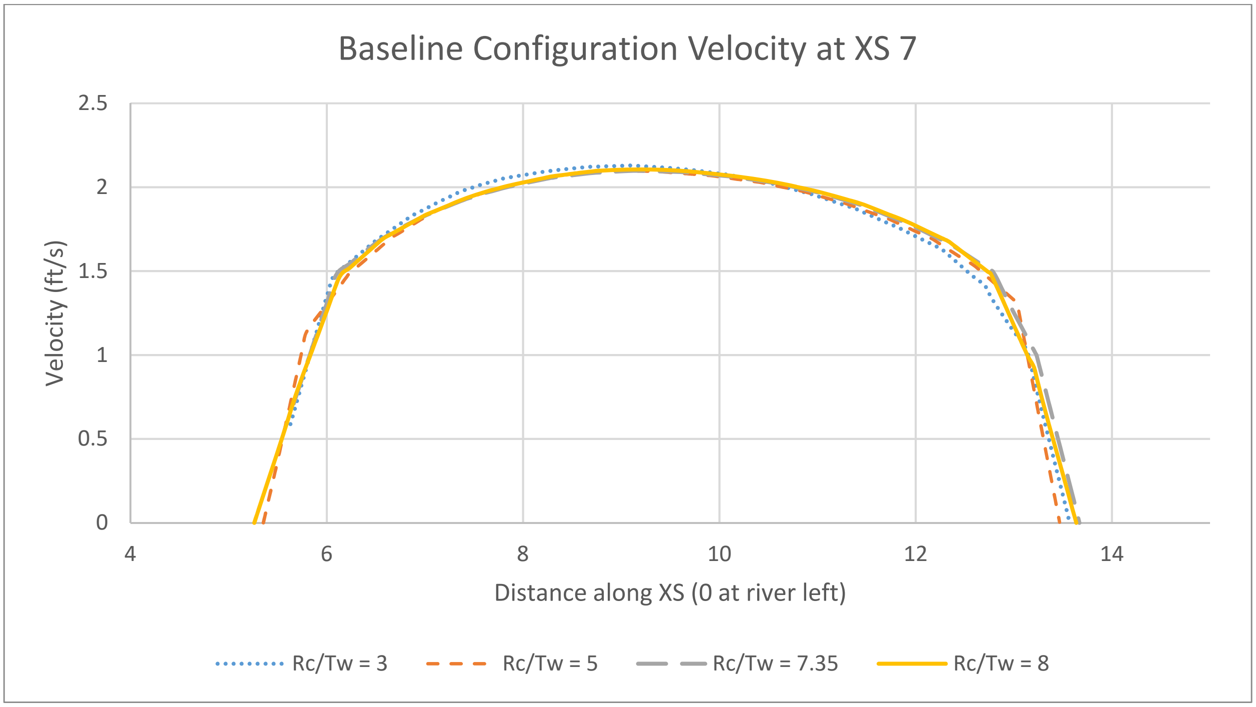

Figure 69: Baseline velocity distribution at cross-section 7

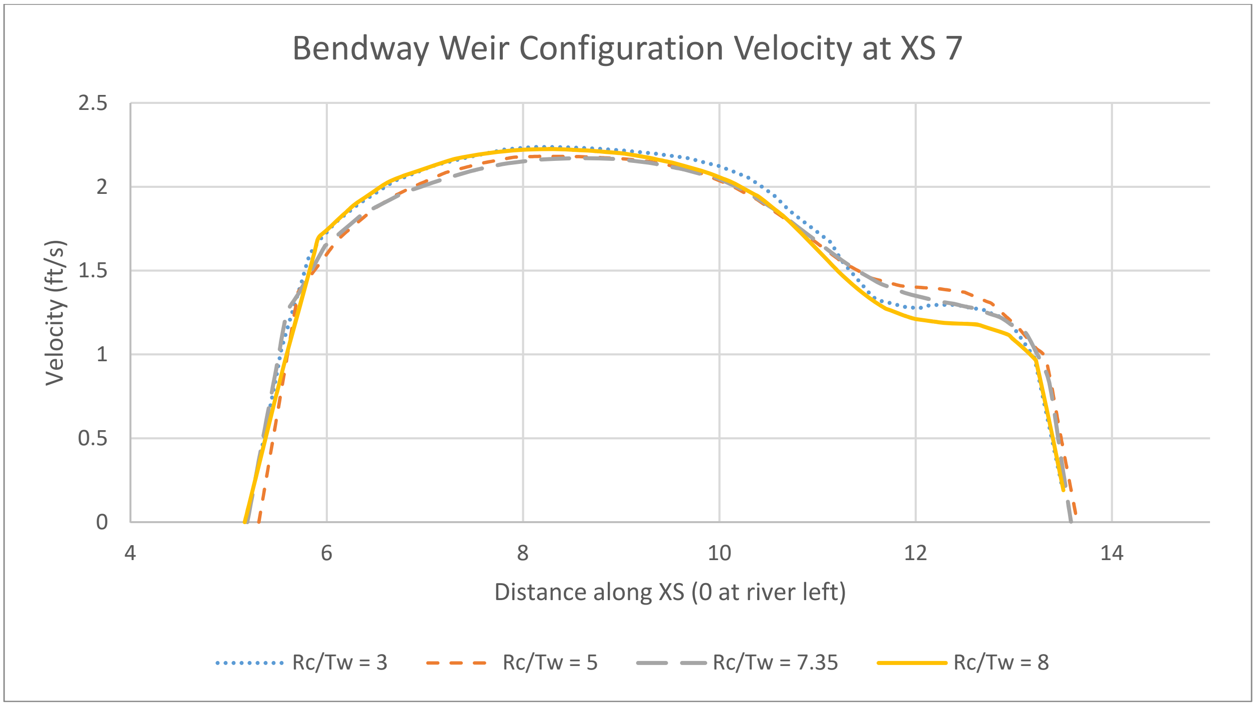

Figure 70: Bendway weir velocity distribution at cross-section 7

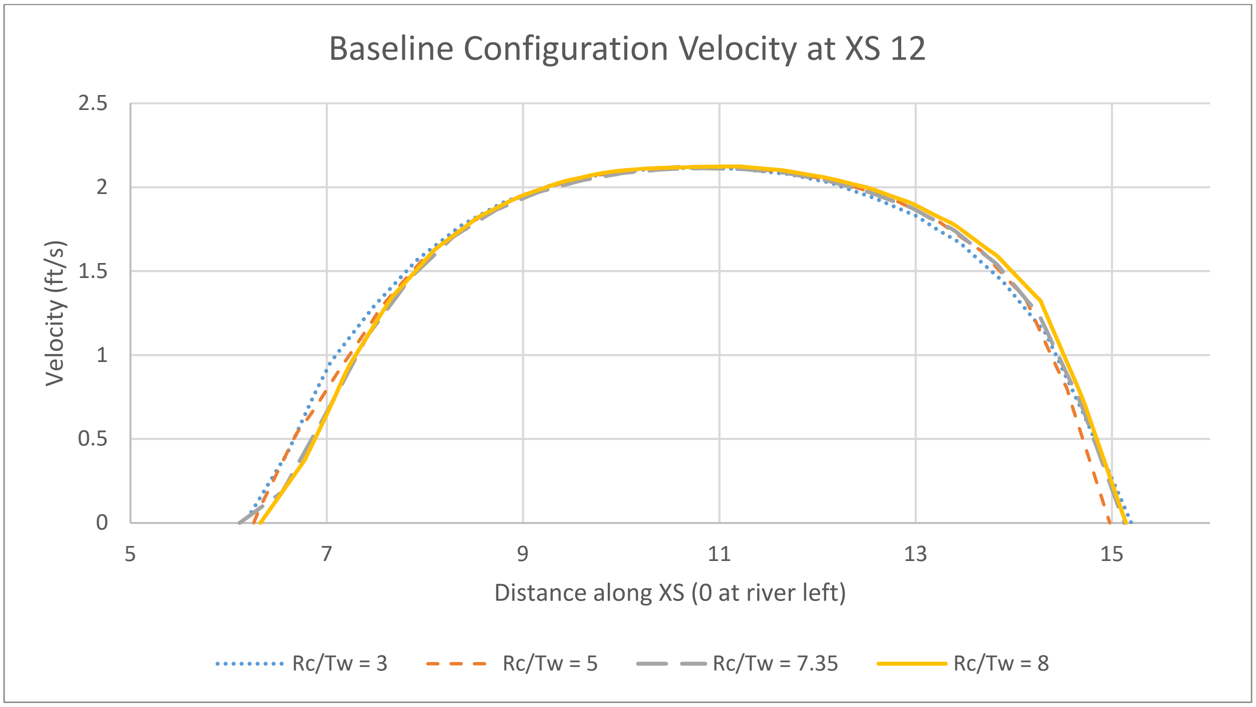

Figure 71: Baseline velocity distribution at cross-section 12

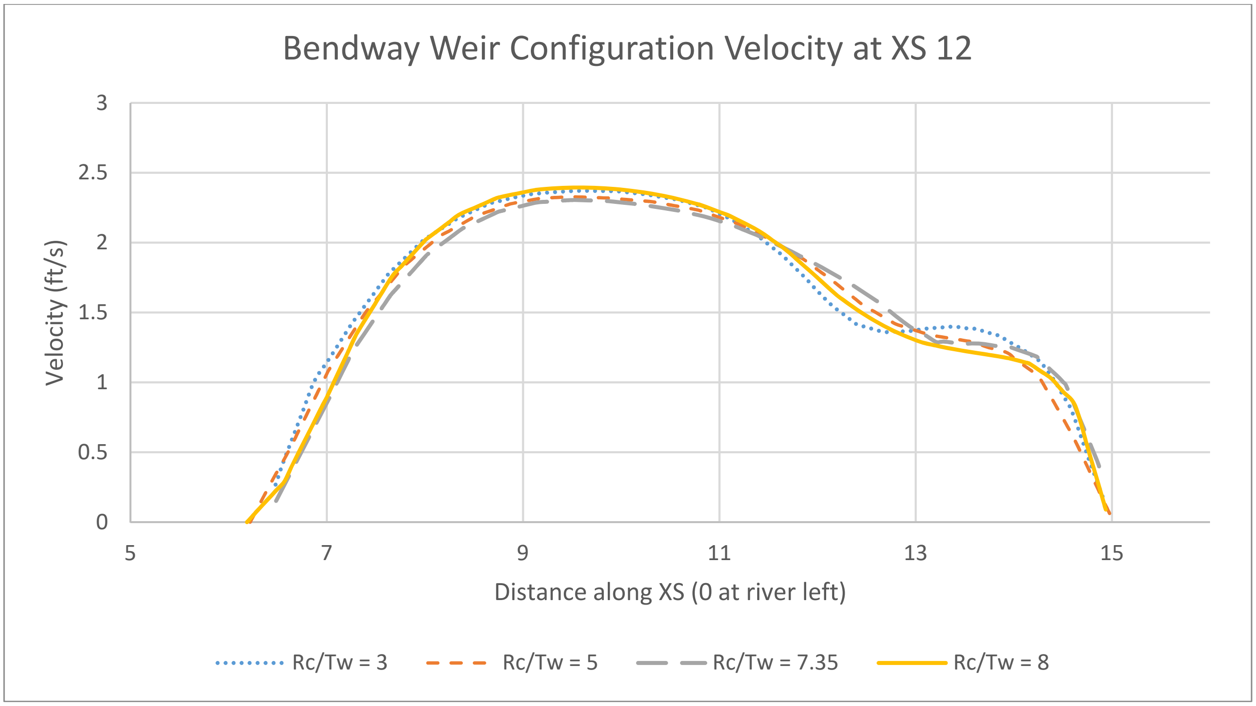

Figure 72: Bendway weir velocity distribution at cross-section 12

In addition to the cross-sectional plots of depth average velocity, water surface elevations associated with varying bend radii were also plotted for each of the 16 cross-sections. This was done to gain insight regarding how the WSE was affected by R_c/T_w when bendway weirs were present. Figure 155 to Figure 186 in Appendix C show the WSE plotted throughout the bend for each of the 16 cross-sections. Figure 73 and Figure 74 illustrate examples of these WSE plots for cross-section 9 and Figure 75 and Figure 76 illustrate WSE at cross-section 12. Similar to the distribution of depth average velocity for cross-section 9 in Figure 47, the WSE of flow in the baseline channel hardly varied for the entire cross-section. The maximum difference in WSE between the R_c/T_w values of 3.0 and 8.0 was 0.01 feet, which was negligibly small and within the model accuracy. The same difference was found for the bend fitted with the bendway weir configuration. The only exception observed was that the WSE associated with $R_c/T_w = 5.0$ dipped down near the outer bank. But, similar to the cross-sectional velocity plots, the cross-section intersected a bendway weir. It is important to mention that these WSE plots use the bed elevations from the $R_c/T_w = 3.0$ configuration and therefore, the bendway weirs were not always shown as part of the bed for other radii values unless the cross-section intersected a weir in the $R_c/T_w = 3.0$ configuration.

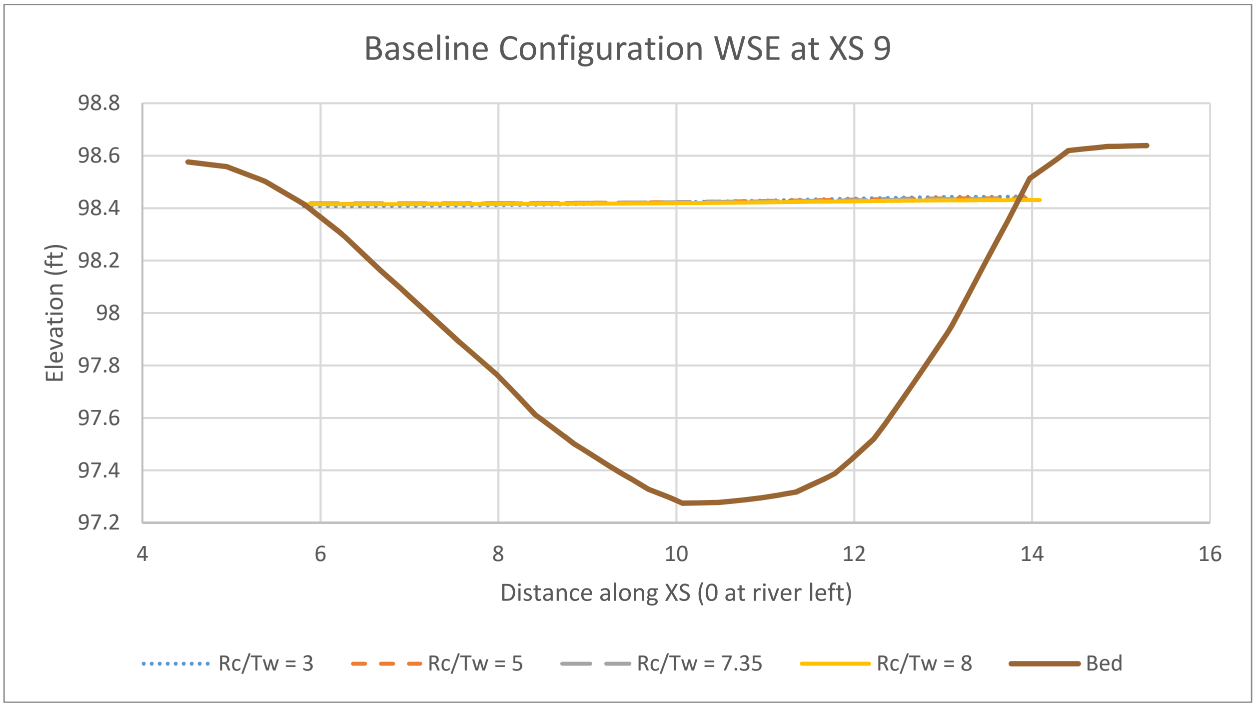

Figure 73: Baseline WSE at cross-section 9

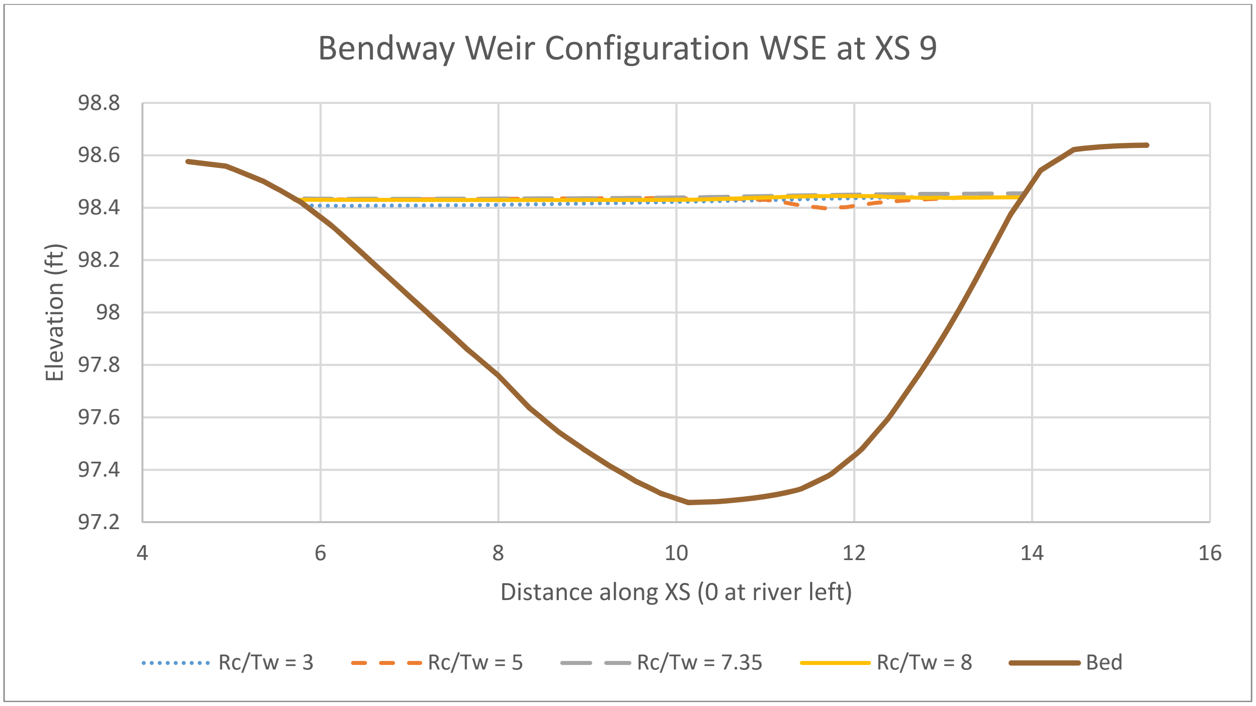

Figure 74: Bendway weir WSE at cross-section 9

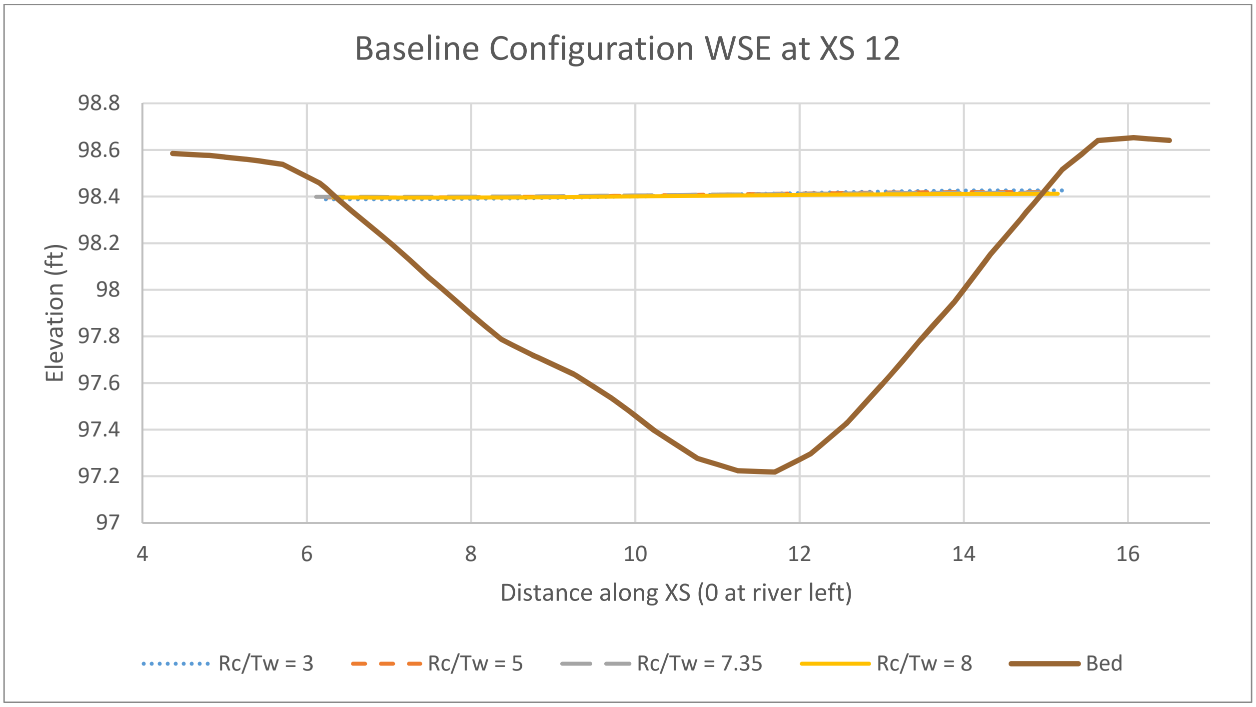

Figure 75: Baseline WSE at cross-section 12

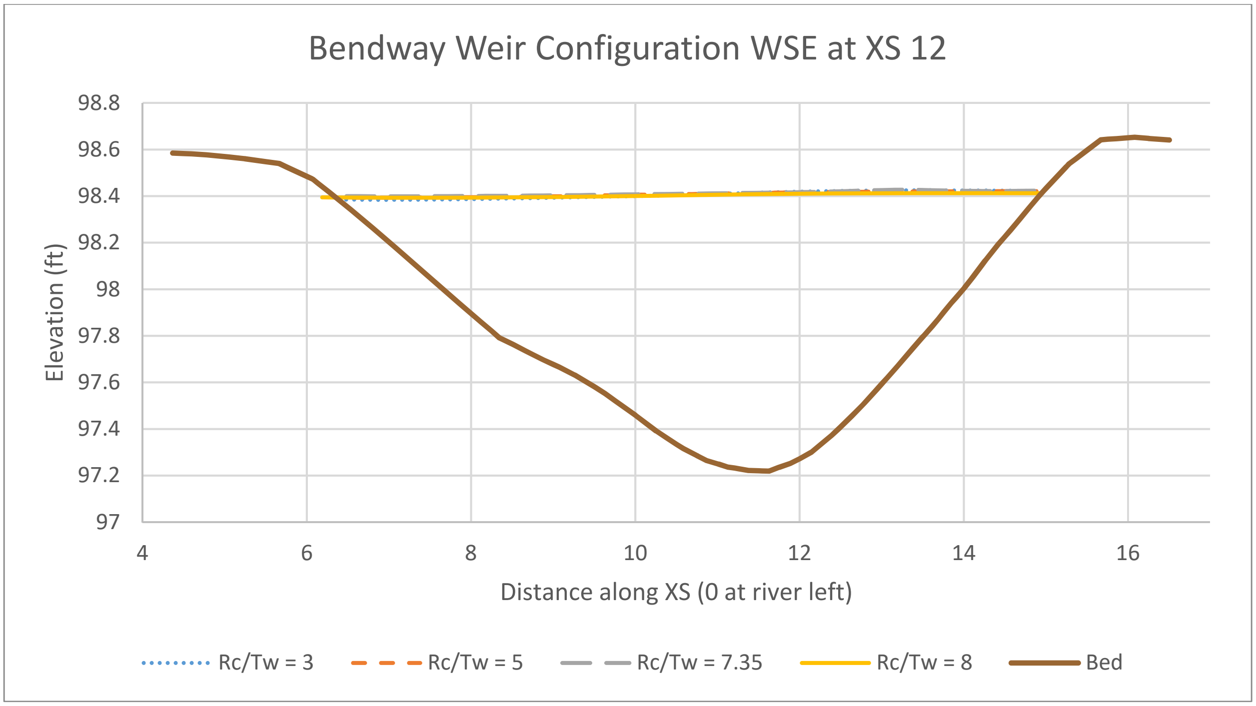

Figure 76: Bendway weir WSE at cross-section 12

Trapezoidal Bathymetry

As with the native bathymetry channel, data were extracted from the trapezoidal model at 16 cross-sections as shown in Figure 77. Cross-sections were located at the same longitudinal location as the native bathymetry cross-sections for consistent comparison. Cross-sectional velocity and WSE plots in the trapezoidal case allowed for the R_c/T_w = 2.3 and 6.13 cases to be compared without the effect of the native bathymetry. The thalweg in the native channel was located very close to the centerline of the channel and caused much of the flow velocity to be concentrated in the channel center. Additionally, the trapezoidal bathymetry showed very little super elevation of the water surface throughout the bend.

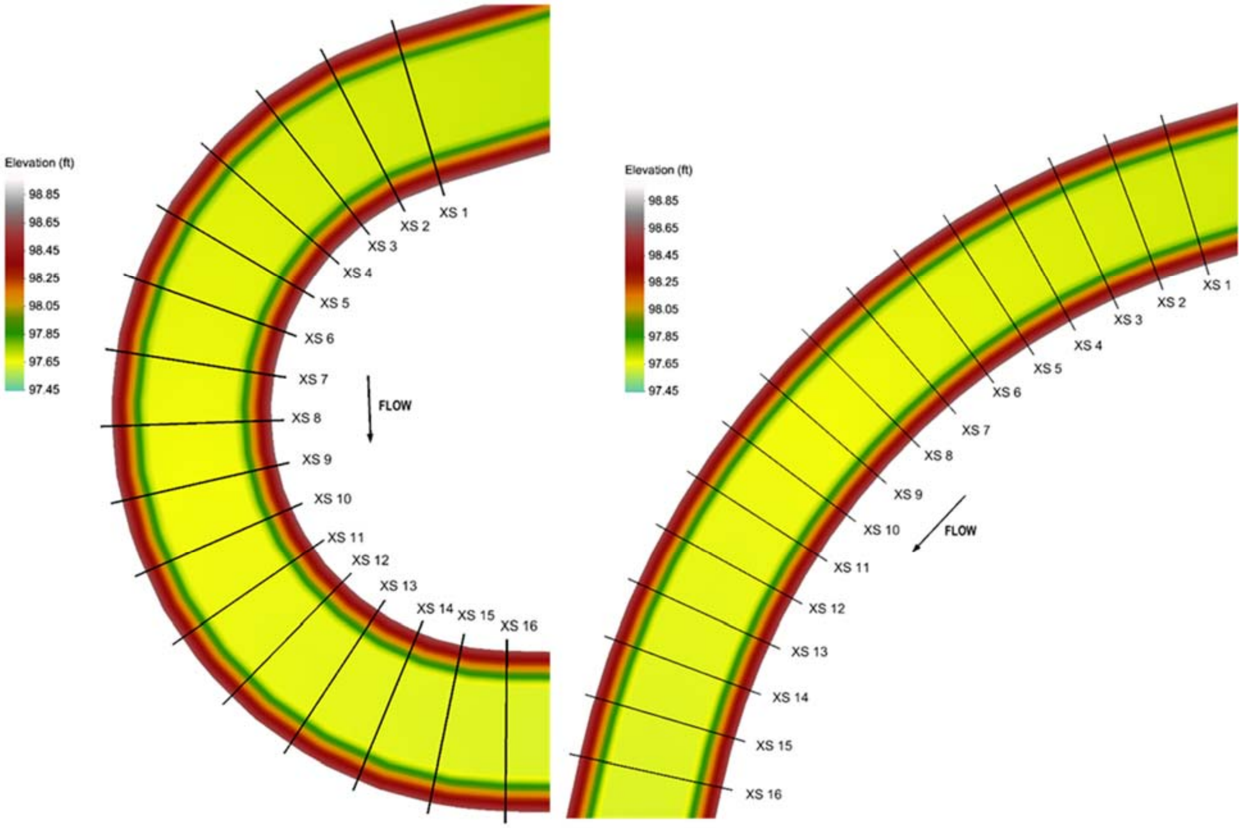

Figure 77: Trapezoidal cross-section locations with elevation contours for (a) $R_c/T_w = 3.0$ and (b) $R_c/T_w = 8.0$

The complete set of cross-sectional plots depth average velocity along the trapezoidal channel is shown in Figure 187 through Figure 218 in Appendix C. Figure 78 and Figure 79 give an example of the velocity distributions at cross-section 9 of the channel. Cross-section 9 is located just after the apex of the bend. Both figures show that the depth average velocity was greater by approximately 0.1 ft/s near the inner bank in the baseline and bendway weir configuration when $R_c/T_w = 2.3$. The outer bank of the baseline and bendway weir configuration showed that the value $R_c/T_w = 6.31$ had a higher velocity compared to when $R_c/T_w = 2.3$. This trend continued for every cross-section throughout the bend. Cross-section 1 showed that the velocity difference near the inner and outer bank was the greatest and as the flow progressed through the bend the difference between the two decreased. The differences between the flow velocities for both bend radii were the same in the inner and outer bank with and without the bendway weirs present. This result showed that on a cross-sectional scale, the bendway weirs had very little effect on the flow field, except locally in the vicinity of a bendway weir.

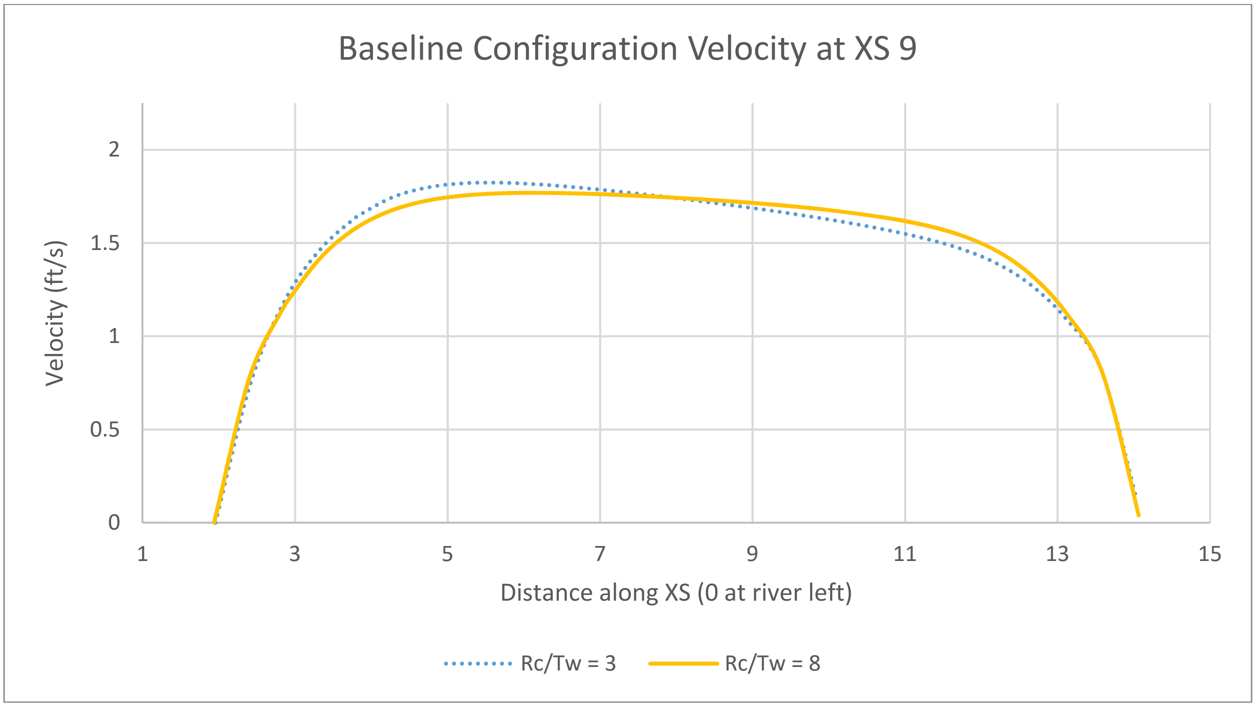

Figure 78: Velocity distribution at cross-section 9 for the baseline configuration

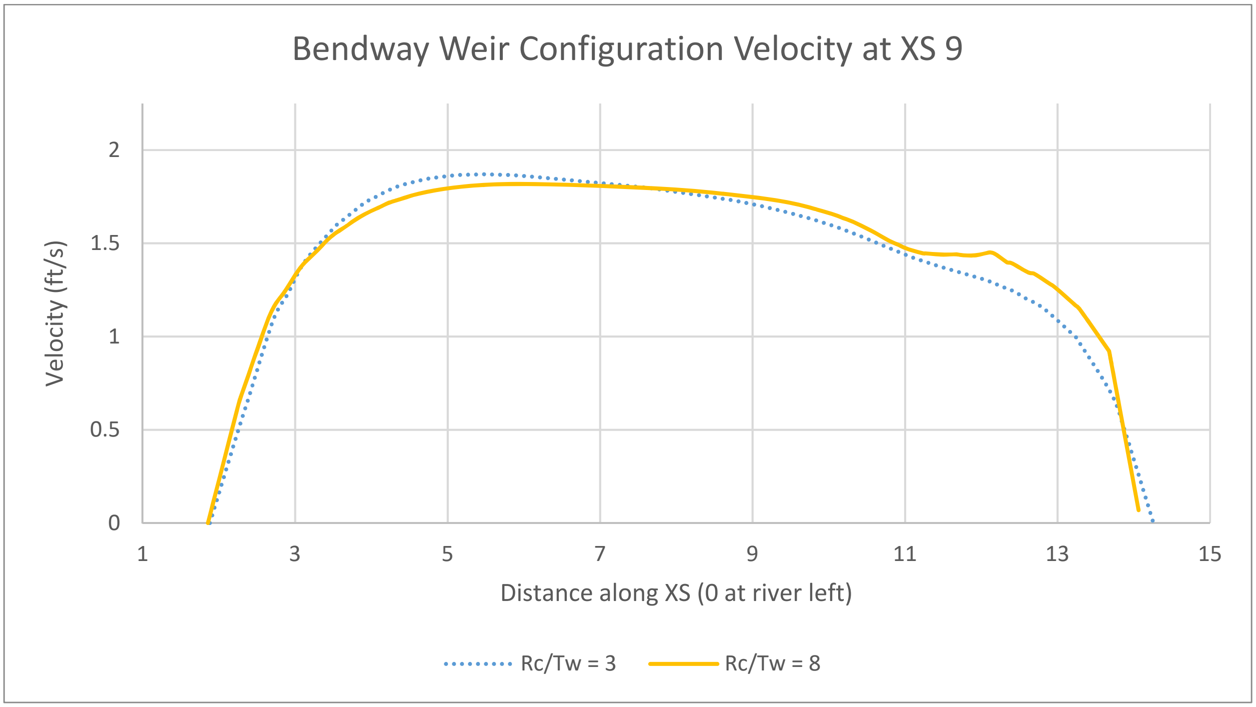

Figure 79: Velocity distribution at cross-section 9 for the bendway weir configuration

In addition to the velocity cross-sectional plots, the WSE and bed elevations were also plotted for both values of R_c/T_w. The complete set of plots is shown in Figure 219 through Figure 250 of Appendix D. Figure 80 and Figure 81 give an example of the WSE plots at cross-section 9 of the baseline and bendway weir configuration. Figure 80 and Figure 81 show that there was slightly more super elevation of the water surface when $R_c/T_w = 2.3$ with and without bendway weirs at cross-section 9. This difference of super elevation between the values of $R_c/T_w = 2.3$ and 6.31 remained constant throughout the bend as well as between the baseline and bendway weir configuration. Although the value of $R_c/T_w = 2.3$ resulted in a lower WSE toward the inner bank and a higher WSE toward the outer bank, the profile did not significantly change from the baseline to bendway weir case. This result showed that the R_c/T_w affected the WSE but this effect did not change with the installation of bendway weirs.

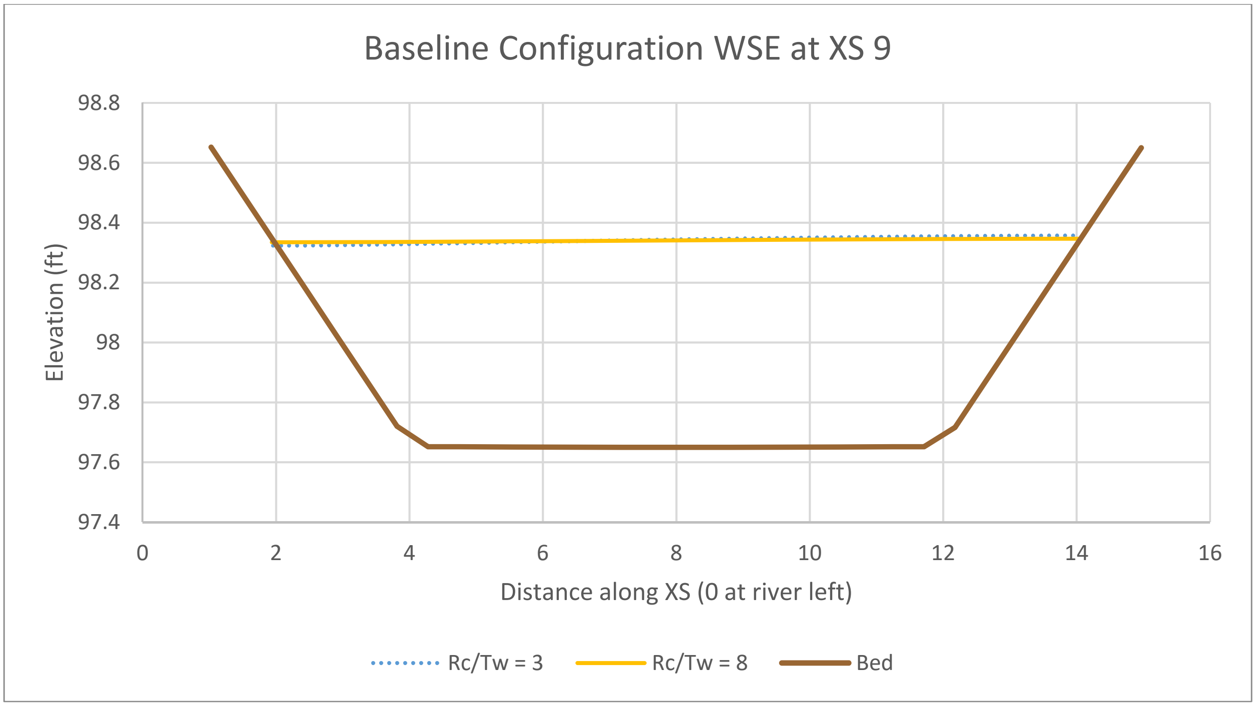

Figure 80: WSE at cross-section 9 for the baseline configuration

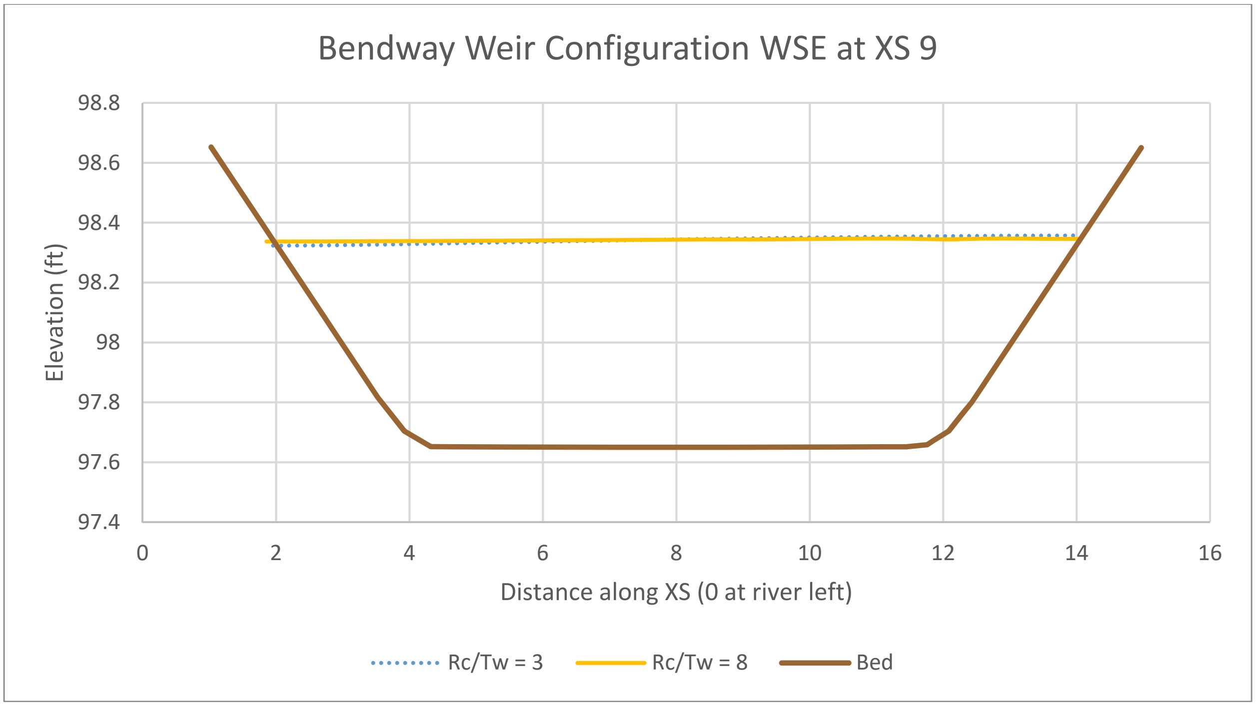

Figure 81: WSE at cross-section 9 for the bendway weir configuration

Cross-Sectional Maximum Velocity

Native Bathymetry

Results in this section used Equation 7 to compute the ratio of maximum velocity per cross-section to the average velocity at the entrance of the bend.

$$MVR_{XS} = (\max XS\ velocity)/(average\ bend\ entrance\ velocity) \qquad (6)$$

There were 16 cross-sections for which plots of cross-section distribution of depth average velocity were made. These cross-sections were also the same cross-sections that were used in the cross sectional velocity and WSE plots in the previous section. The ratio in Equation 6 was calculated for each of the 16 cross sections in the baseline and bendway weir configuration and then plotted to show how the ratio varied throughout the bend for each radius of curvature.

Figure 82 relates that the maximum value of depth average cross-sectional velocity to the cross-sectional average velocity at the bend entrance. Baseline condition results were nearly identical for each of the bend radii. The largest difference was at cross-section 5 where the MVR_{XS} ratio was about 6% greater for $R_c/T_w = 3.0$ than that of 8.0. There were negligible differences in the ratios for the remaining cross-sections in the bend.

The results obtained for the bendway weir configurations were comparable to those for the baseline condition except the MVR_{XS} ratio increased by a maximum of about 36% at cross-section 10. There was negligible difference between the ratios for each of the cross-sections, as Figure 83 indicates, though there was a spike in the ratio when $R_c/T_w = 8.0$ at cross-section 10, but this was due to the cross-section intersecting the bendway weir tip and thus extracting a much higher velocity compared to the rest of the channel. The general trend of the ratio for each of the bend radii shows that even with the bendway weirs installed, bend radius had little effect on the distribution of depth average velocity distribution throughout the bend.

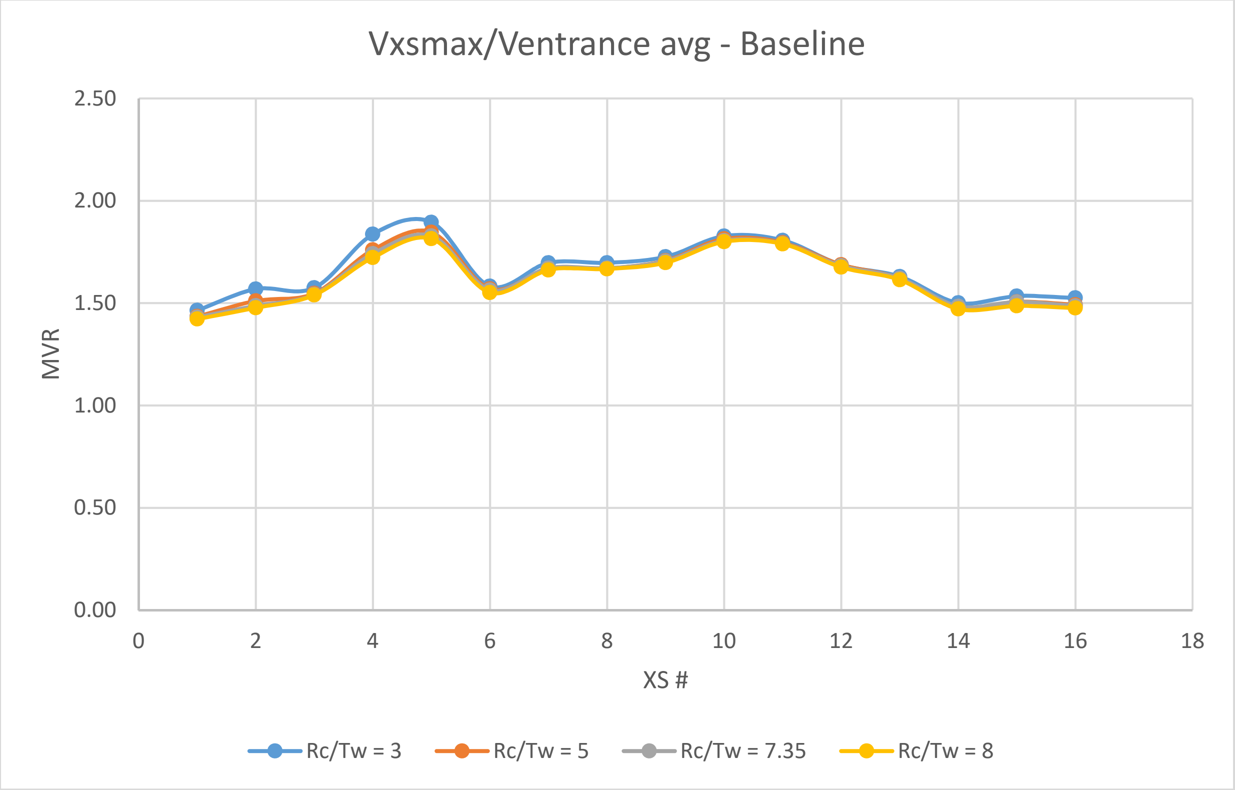

Figure 82: Ratio of maximum velocity at each cross-section to average cross-sectional bend entrance velocity in the baseline channel

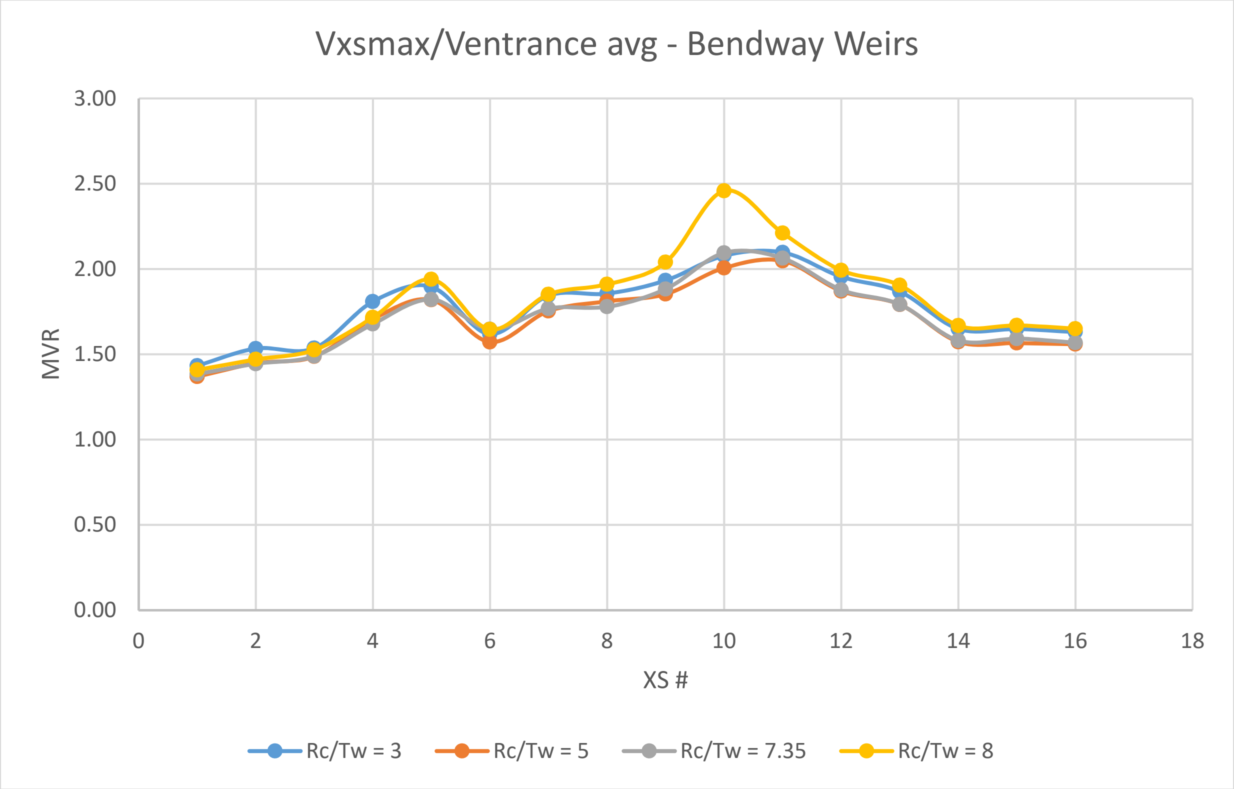

Figure 83: Ratio of maximum velocity at each cross-section to average cross-sectional bend entrance velocity in the bendway weir channel

Trapezoidal Bathymetry

As with the analysis of flow along the bend with the native bathymetry channel, the maximum cross-sectional velocity was also computed for the trapezoidal channel to gain insight regarding how R_c/T_w affected the maximum values of depth average cross-sectional velocity in the baseline and bendway weir configurations. On average, the bendway weirs when $R_c/T_w = 2.3$ caused a 3% increase in maximum velocity in the channel. When $R_c/T_w = 6.13$ the increase was only about a 0.2% in maximum channel velocity. When $R_c/T_w = 2.3$ there was an increase of 2.8% higher maximum velocity when compared to $R_c/T_w = 6.13$. This change was very small and was not indicative that the flow velocity changes in the presence of bendway weirs with varying radius of curvature.

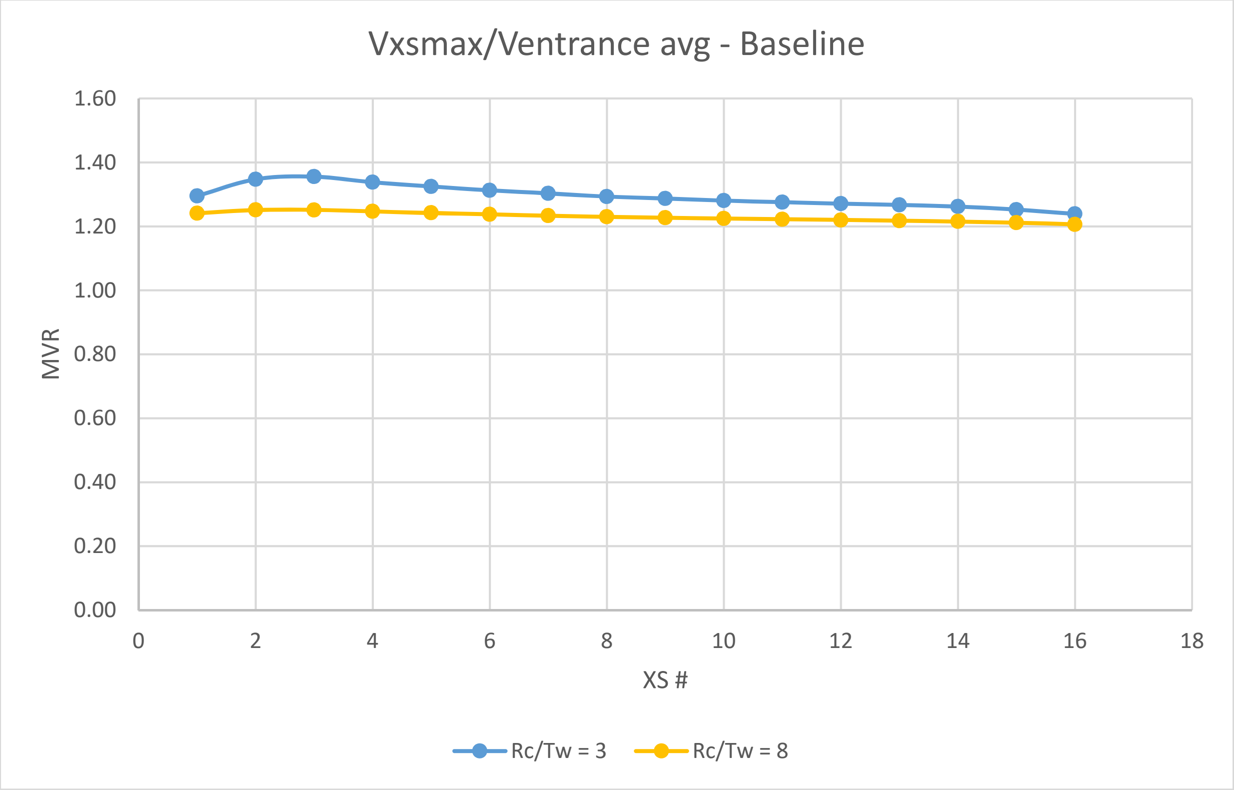

Figure 84: Baseline maximum cross-section velocity to average bend entrance velocity

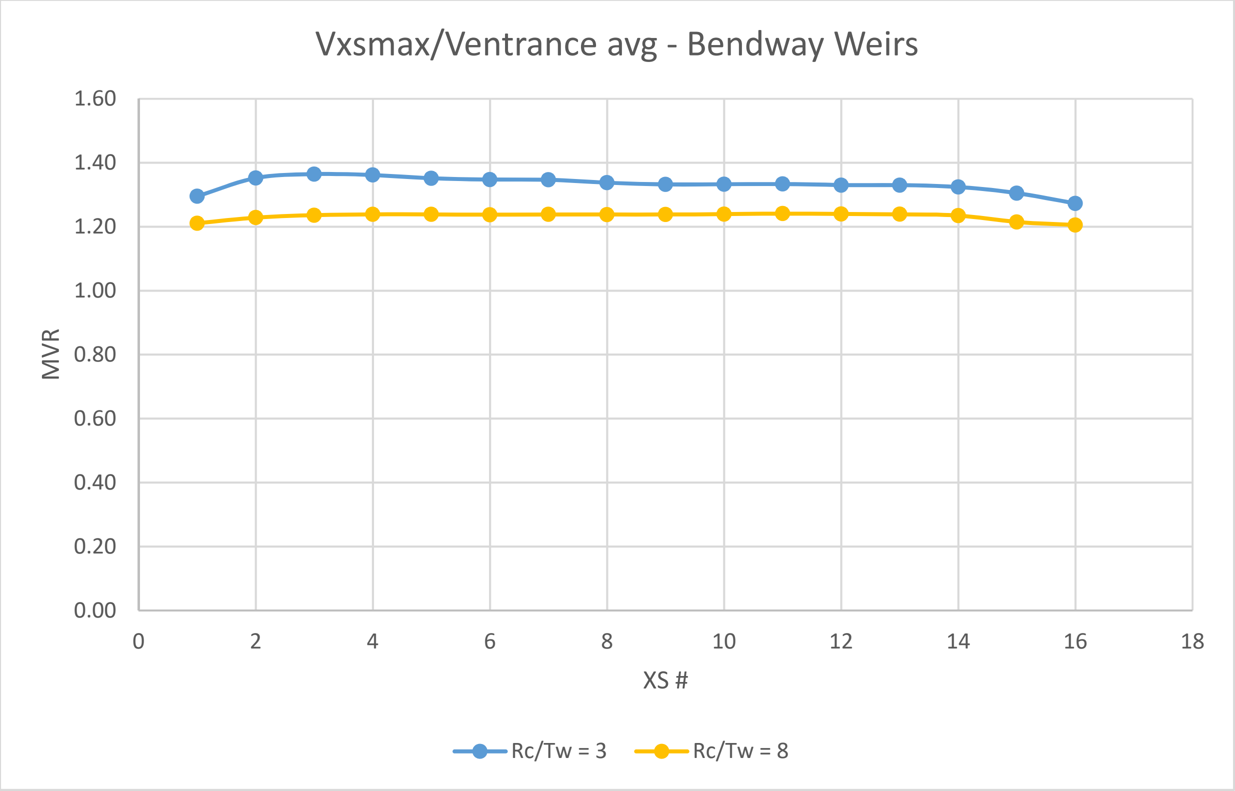

Figure 85: Bendway weir maximum cross-section velocity to average bend entrance velocity

Maximum Velocity Compared in Lateral Sections of the Channel Width

Native Bathymetry

In addition to contour and cross-sectional plots of velocity and WSE, the maximum and average velocities were calculated for 3 lateral sections (inner $T_w/3$, middle $T_w/3$ and outer $T_w/5$) in each of the 16 cross-sections shown in Figure 86. Because bendway weirs significantly affect the flow field around the bend, it was important to evaluate how the velocity changed for the inner bank, channel center, and outer bank sections of the bends. This information indicated how much the presence of bendway weirs increased the velocity in the inner and middle third of the channel width, and how much the velocity was decreased with the presence of bendway weirs in the outer fifth of the channel width.

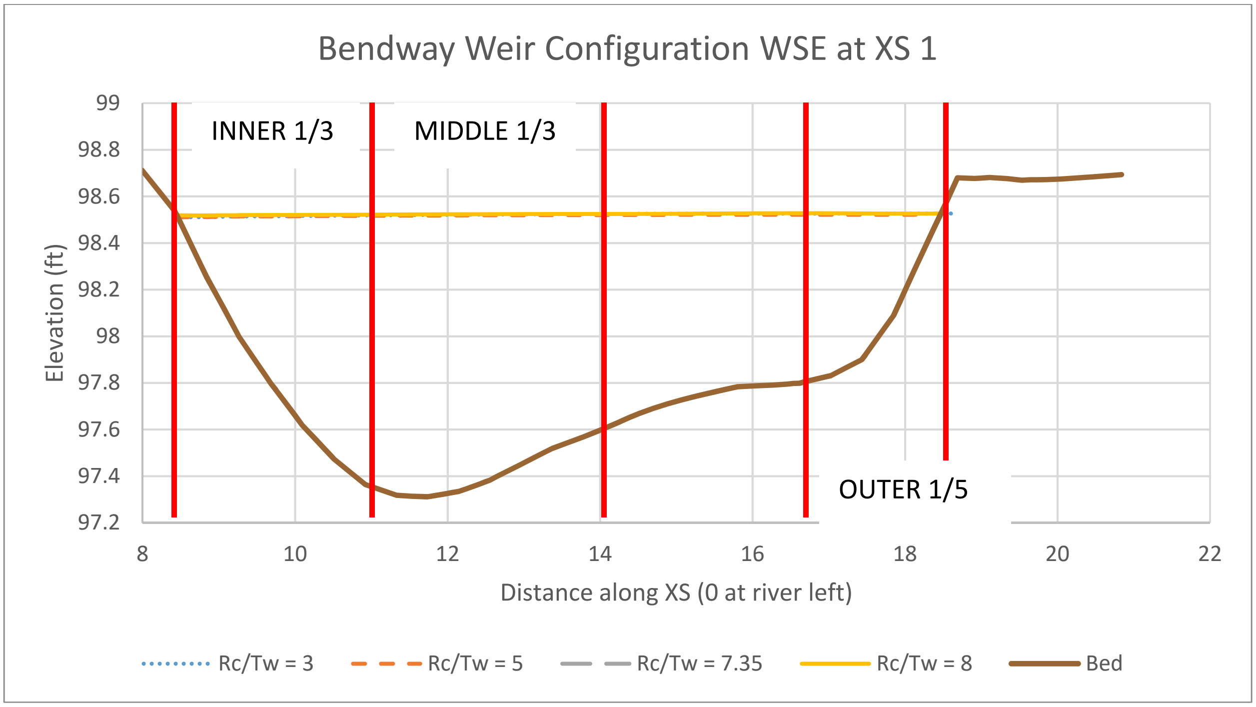

Figure 86: Maximum and average velocity lateral sections used in the velocity distribution analysis (example using cross-section 1)

The maximum velocity of the inner and middle third of the channel width for the entire bend changed little for the R_c/T_w values considered. Figure 87 through Figure 90 show nearly the same maximum velocity in the cross sections throughout the bend for the values of R_c/T_w considered. Figure 90 shows that when $R_c/T_w = 8$, there was a much greater maximum velocity than the other bend radii. Similar to previous results, this was again due to the intersection of the cross-section with the tip of a bendway weir where a very high velocity was located.

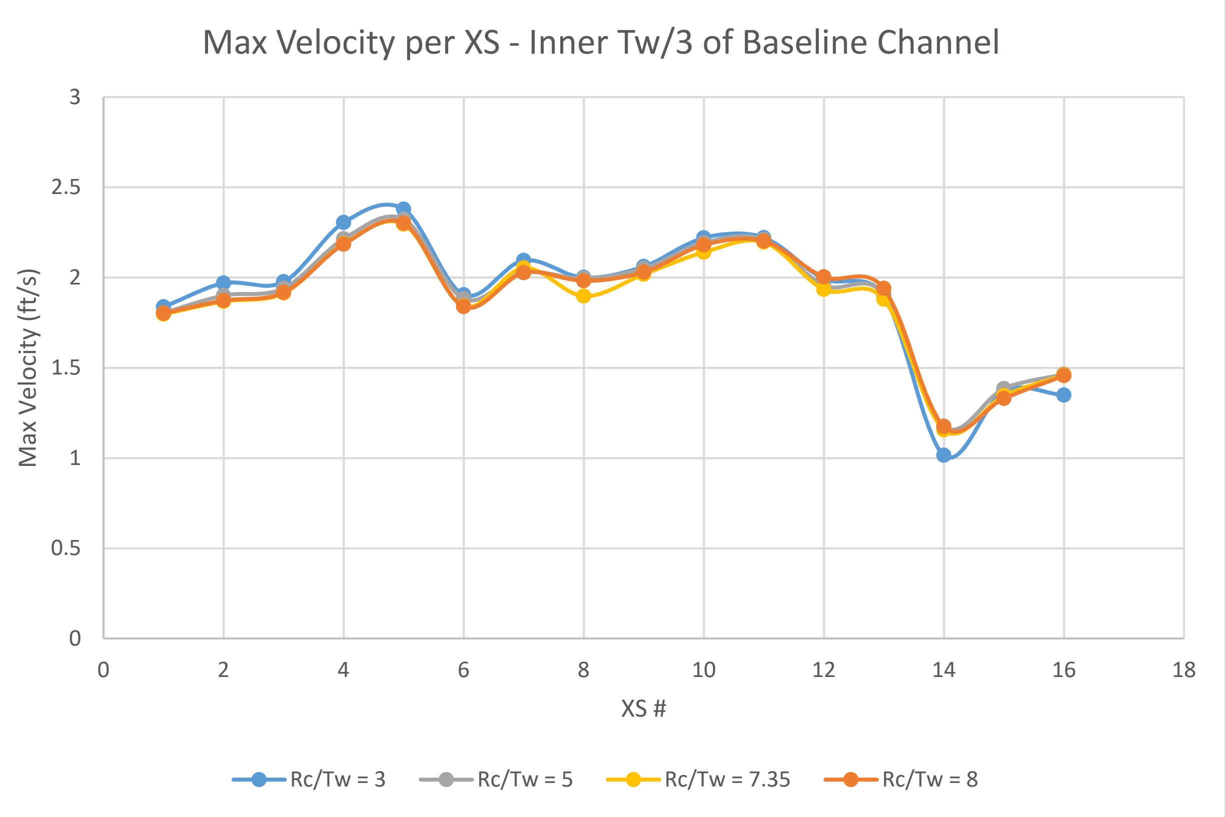

Figure 87: Max velocity in the inner third of the baseline channel

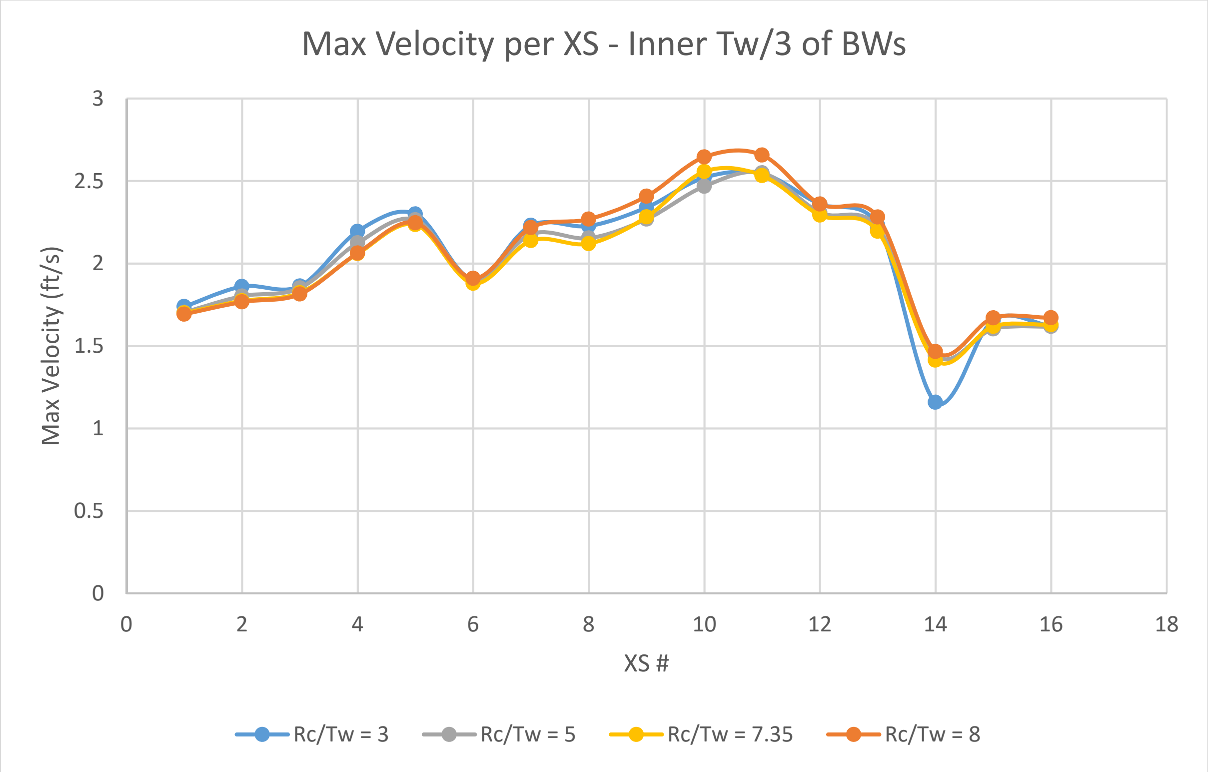

Figure 88: Max velocity in the inner third channel width of the BW channel

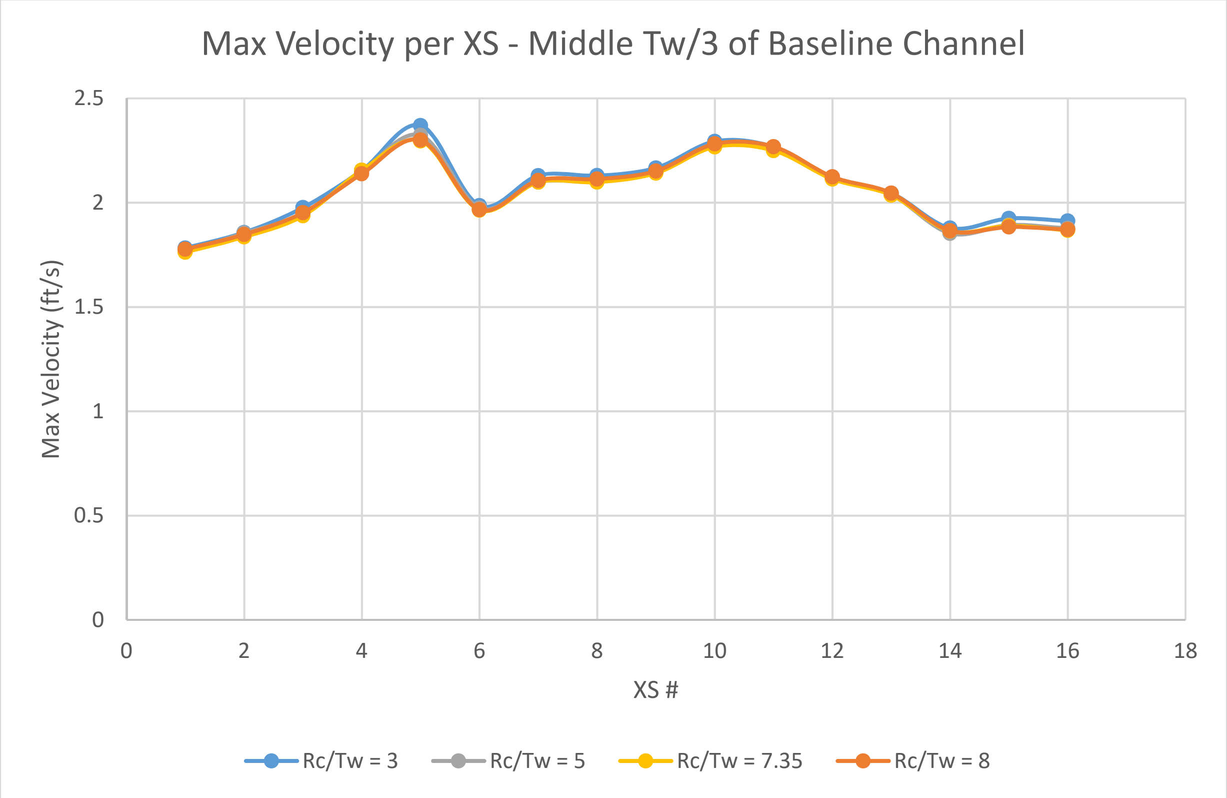

Figure 89: Max velocity in the middle third channel width of the baseline channel

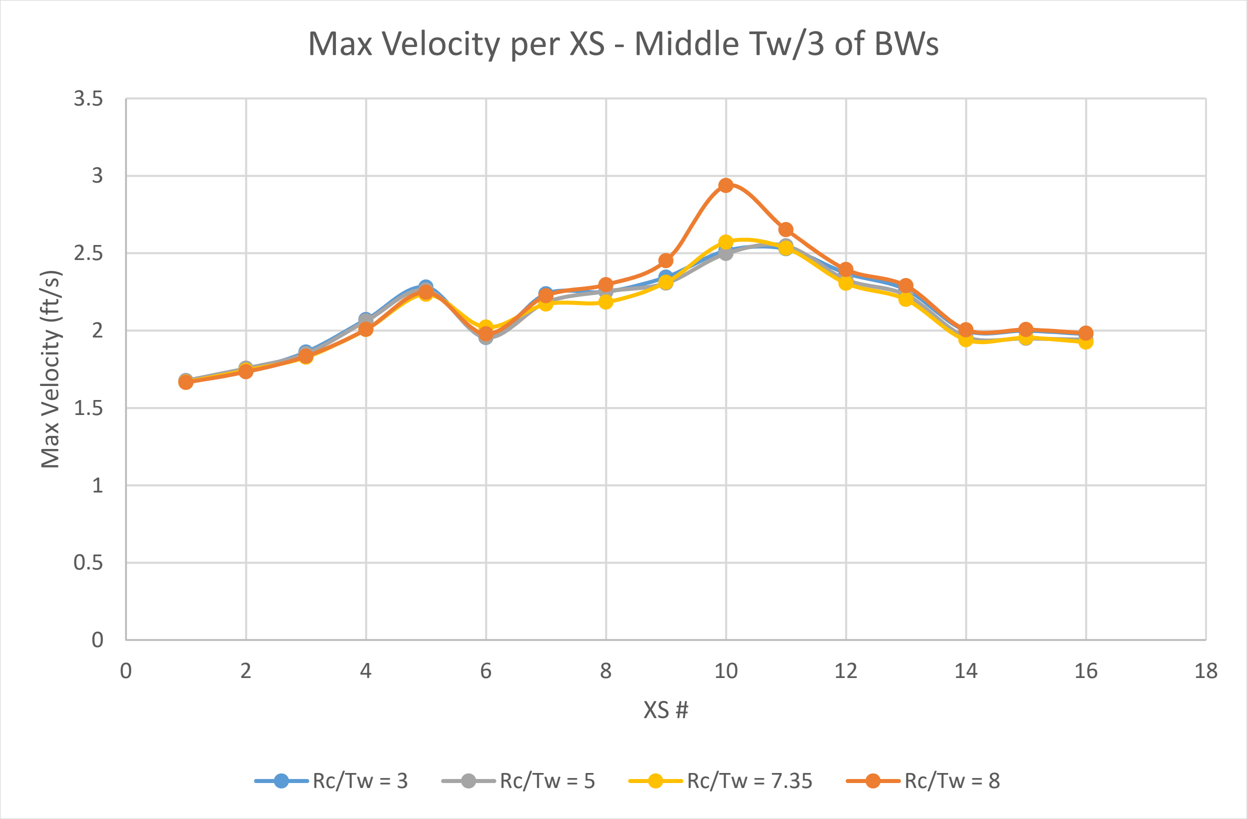

Figure 90: Max velocity in the middle third channel width of the BW channel

The variation of average values of depth average velocity in the inner and middle sections of the channel's width are essentially the same as for the maximum velocities. Figure 91 shows that the maximum depth average velocities in the inner third channel width of the baseline channel were very similar between the R_c/T_w values and differed by less than 0.1 ft/s. Figure 92 shows that the maximum velocities of the inner third channel width in the bendway weir channel when $R_c/T_w = 8.0$ were higher between cross-sections 1 through 6 in this inner bank region than when $R_c/T_w = 3.0$. The difference between the two values of R_c/T_w decreased in the channel's center third width between cross-section 6-13 and neither value of Rc/T_w was observed to have a clear higher maximum velocity.

Along the middle of the channel, Figure 93 and Figure 94 show that the average velocity of the middle third of the channel width did not change with R_c/T_w, as the average velocity did not change at each cross-section when changing bend radius. The only outlier was cross-section 10 when $R_c/T_w = 8.0$. The average velocity for this situation was affected by the high velocity at a bendway weir tip.

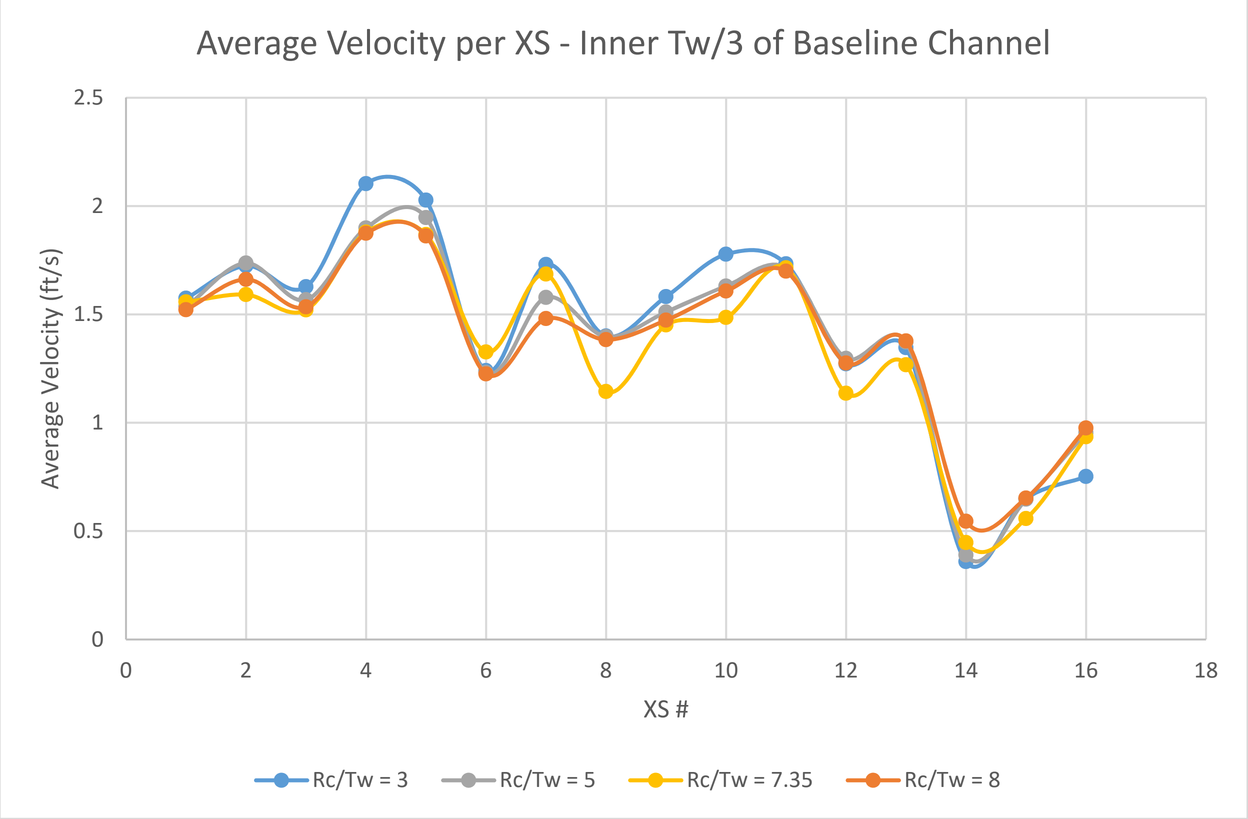

Figure 91: Average velocity in the inner third channel width of the baseline channel

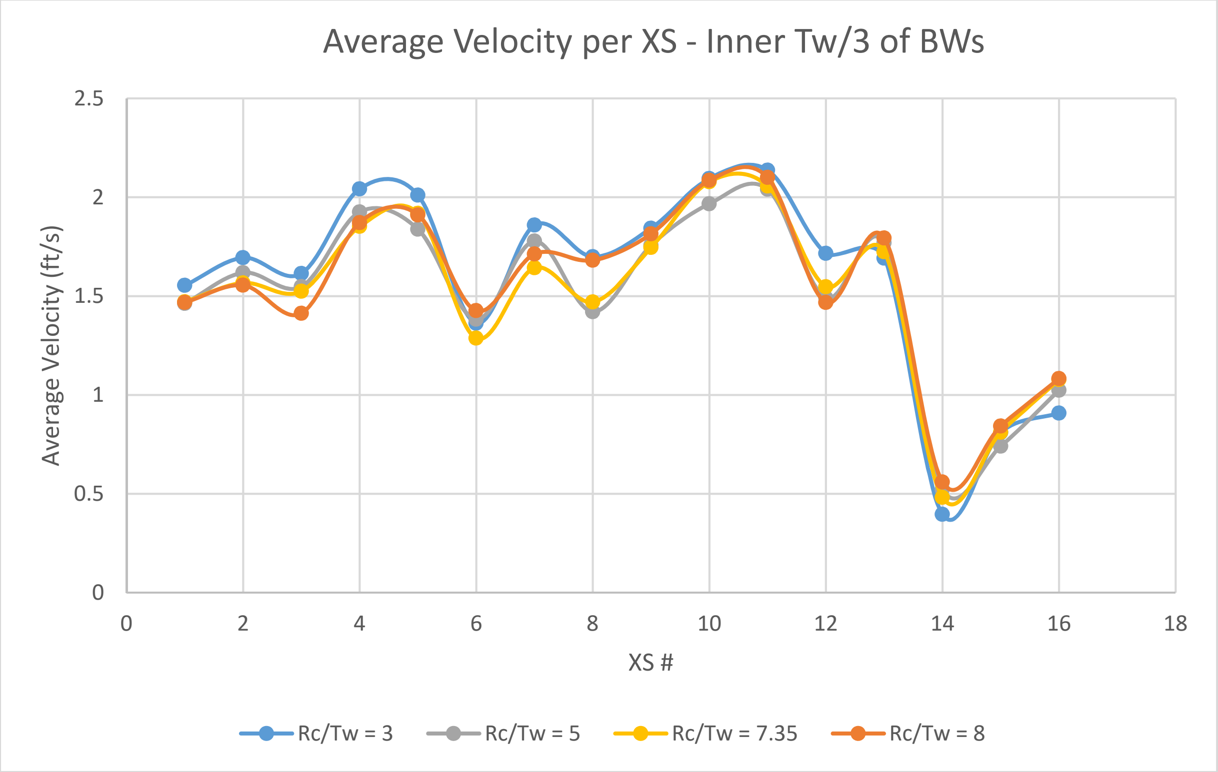

Figure 92: Average velocity in the inner third channel width of the bendway weir channel

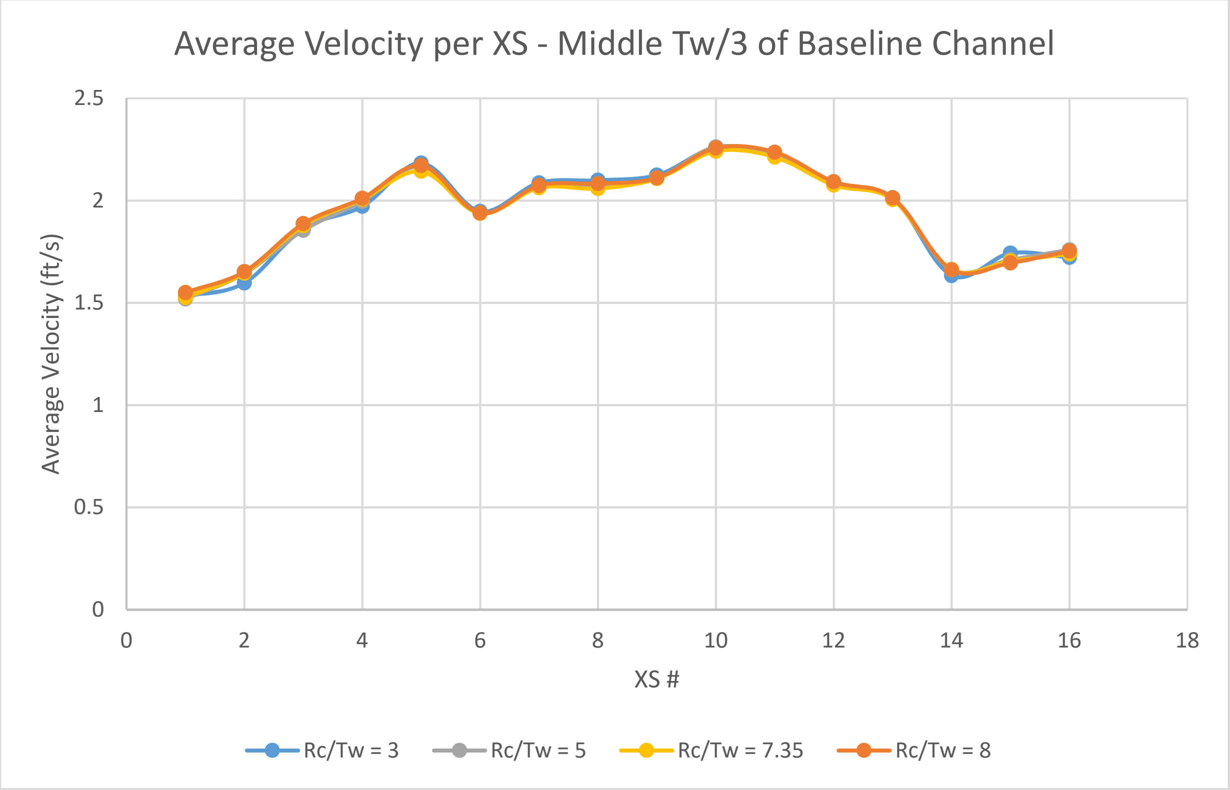

Figure 93: Average velocity in the middle third channel width of the baseline channel

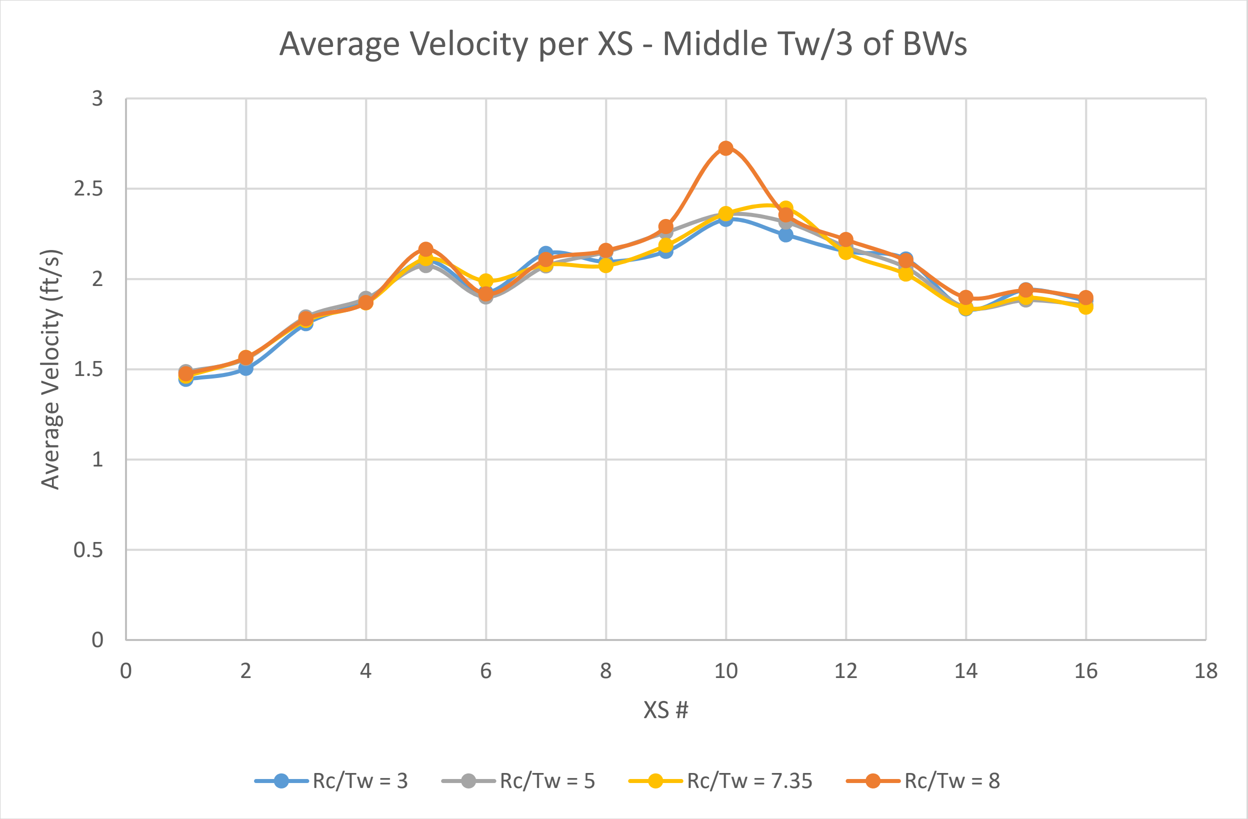

Figure 94: Average velocity in the middle third channel width of the bendway weir channel

The inner and middle third sections of the channel showed very little difference in maximum velocity between the varying values of R_c/T_w. This trend continued for the outer fifth of the baseline channel but not for the channel fitted with bendway weirs. The max velocity in the outer fifth of the baseline channel remained the same at cross sections between varying R_c/T_w as shown in Figure 95. But, the max velocity in the outer fifth seemed to be much more unstable for the bendway weir configuration and showed that the max velocity was similar for all bend radii at the start and end of the bend (cross-sections 1 through 4 and 12 through 16) as seen in Figure 96. If the large spikes are removed from the plot in Figure 96, the general trend seems to show that the maximum velocity does not change with bend radii but this can only be speculated as there was significant instability in this region induced by the bendway weirs. In this regard, the limitations of numerical modeling using a depth average flow model become evident. As this model is not configured to address flow situations involving three-dimensional and unsteady flows, the modeling results should be vied with due caution.

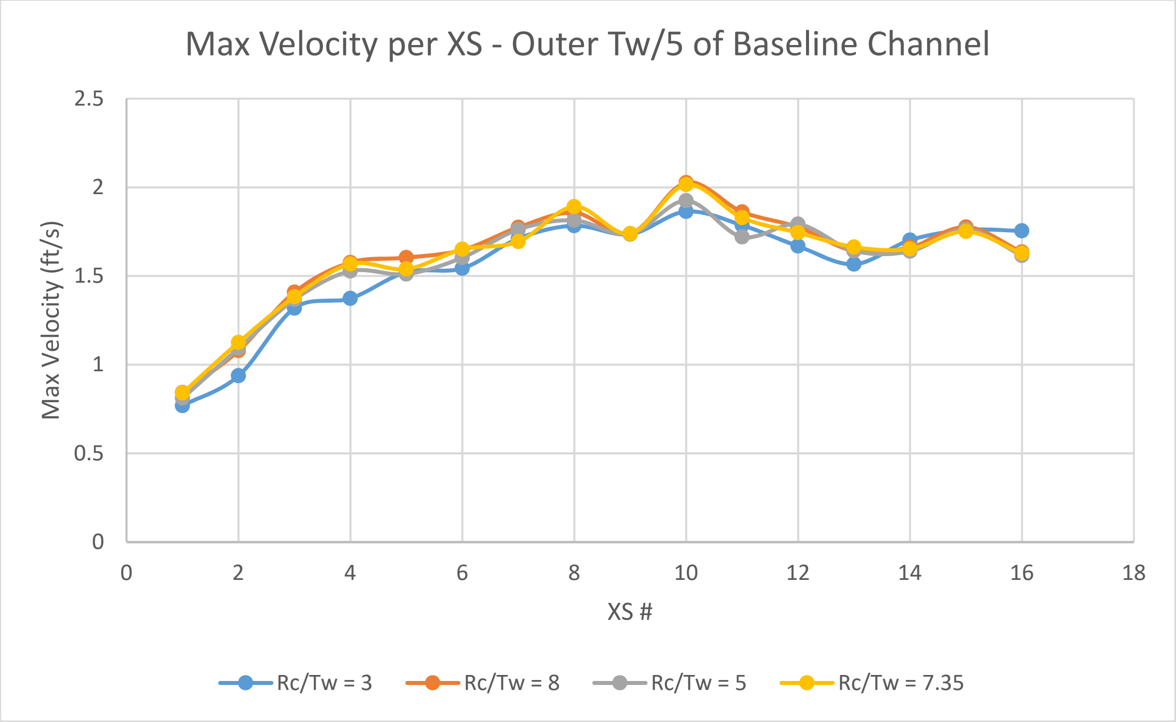

Figure 95: Max velocity in the outer fifth channel width of the baseline channel

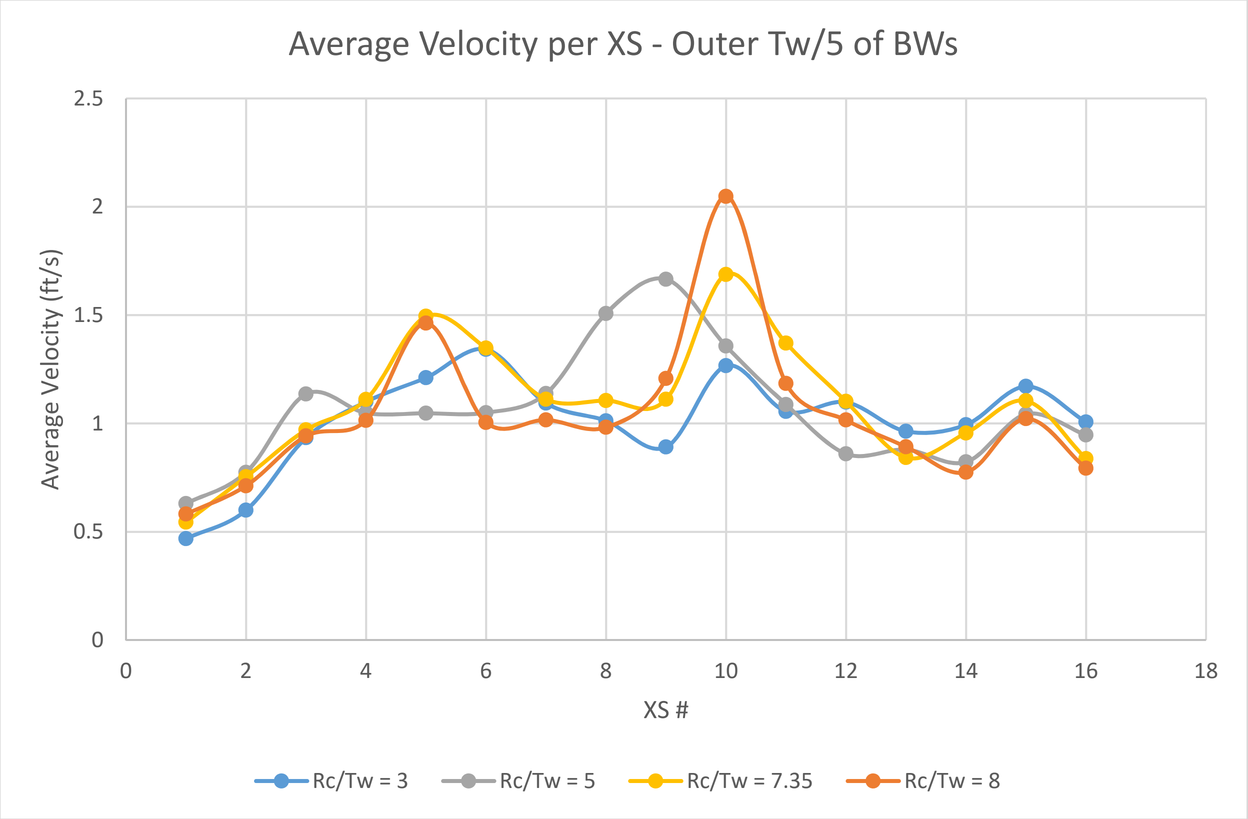

Figure 96: Max velocity in the outer fifth channel width of the bendway weir channel

Average velocities in the outer fifth of the channel width were variable for the baseline and bendway weir configuration. However, Figure 97 and Figure 98 show that the average velocities for all bend radii followed the same trend and only slightly differed in magnitude for select cross-sections. Variability was reduced between cross-sections 1-4 and 12-16 for the baseline and bendway weir configurations.

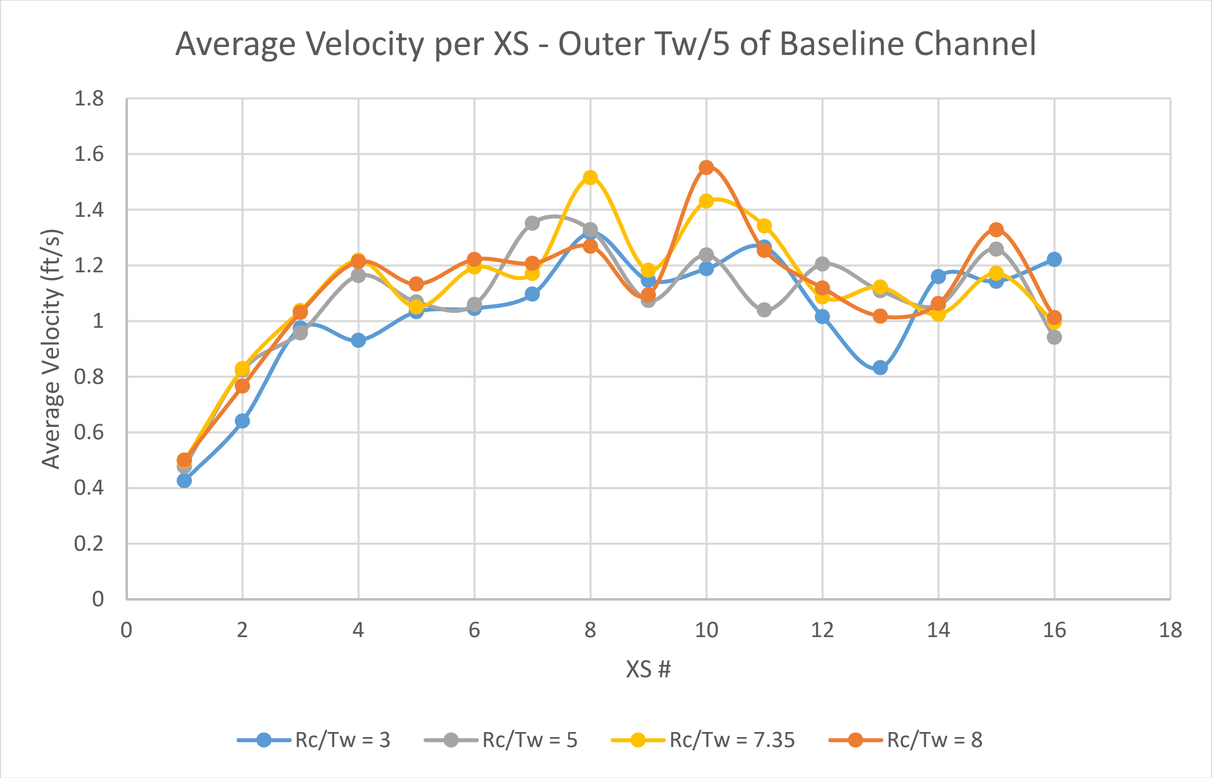

Figure 97: Average velocity in the outer fifth channel width of the baseline channel

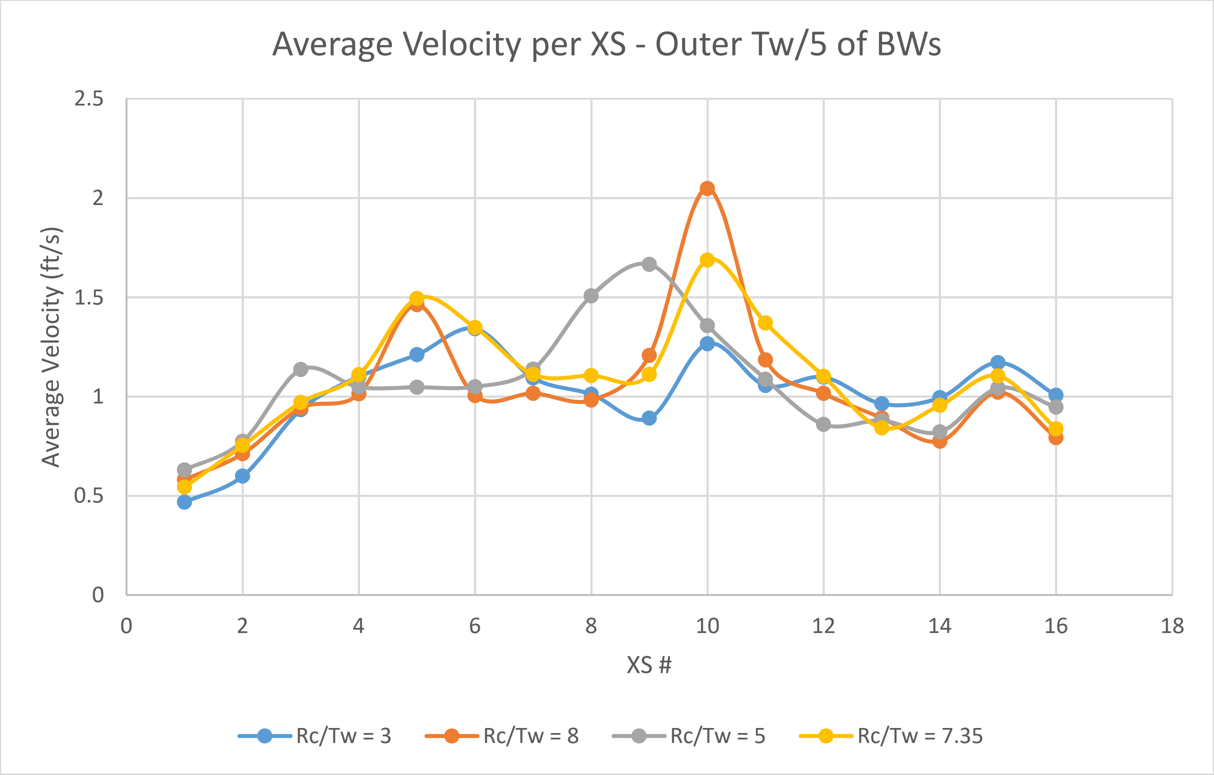

Figure 98: Average velocity in the outer fifth channel width of the bendway weir channel

In addition to zonal analysis, percentage of increased or decreased maximum velocity from the baseline condition to the bendway weir condition was a valuable analysis tool to evaluate the flow field changes. The analysis was completed for the 3 lateral zones in the 16 cross sections (inner third, middle third, and outer fifth). Figure 99 shows that the maximum velocity was decreased from the baseline to bendway weir configuration between cross-sections 1-6 and then increased to a maximum of 20% higher velocities in all bend radii at the end of the bend at cross-sections 14 through 16. After cross-section 6, the bendway weirs caused the largest increase of maximum velocity in the $R_c/T_w = 8.0$. The maximum velocity in the $R_c/T_w = 8.0$ bend compared to 3.0 was about 8% higher at cross-section 10 (close to bend apex). Alternatively, the velocity increase was the same for all bend radii in the middle third of the channel, throughout the bend as shown in Figure 100. Similar to the inner third of the bend, the bendway weirs deceased the maximum velocity in the middle third of the channel between cross-section1-6 and then increased the maximum velocity from cross-section 6 throughout the rest of the bend. The maximum velocity was increased for all bend radii a maximum of about 12% at cross-section 12 from the baseline to bendway weir configuration. The outer fifth of the channel again proved to be variable but trends that weren't affected by spikes in maximum velocity (due to intersecting a bendway weir) show that the value $R_c/T_w = 8.0$ generally had the greatest reduction of maximum velocity along the outer fifth of the channel. The general trend also shows that the value $R_c/T_w = 3.0$ generally had the least reduction of maximum velocity along the outer fifth of the channel.

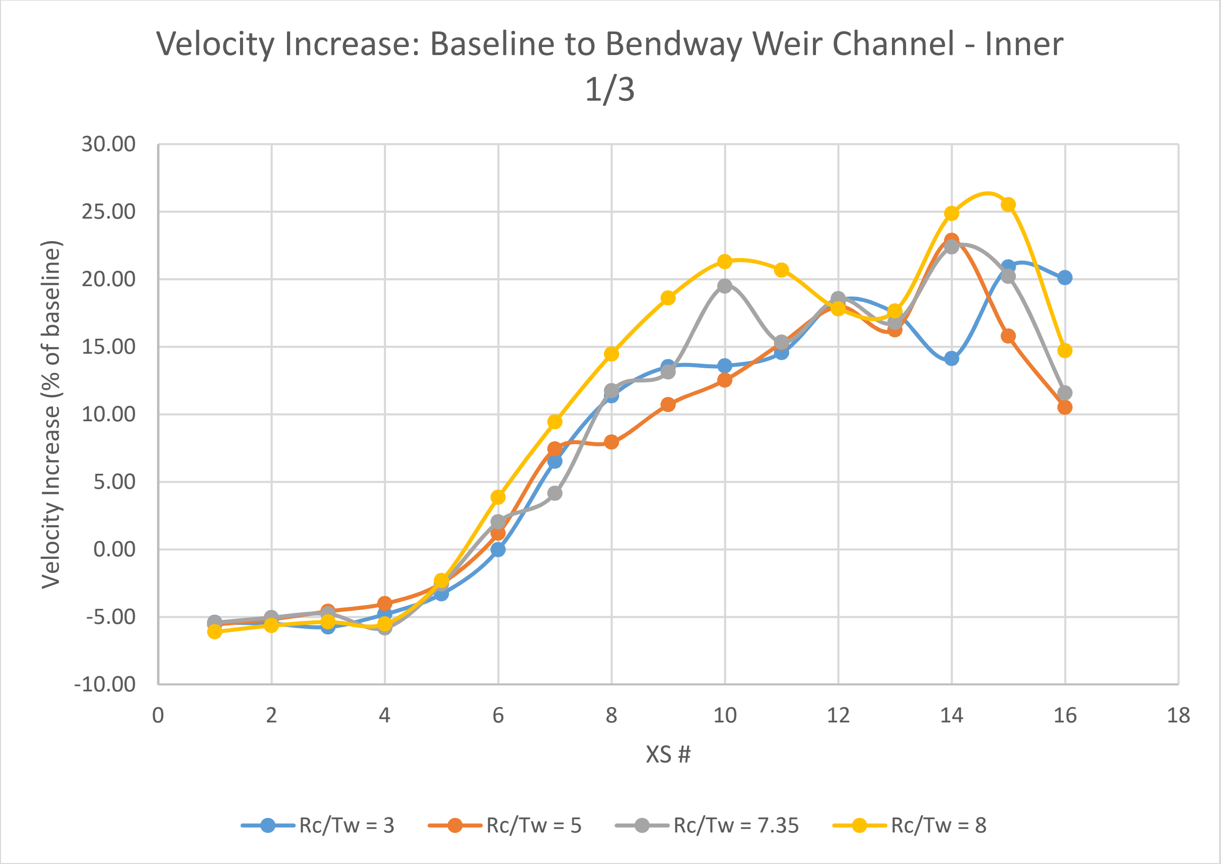

Figure 99: Velocity change from baseline to bendway weirs for the inner 1/3 channel width

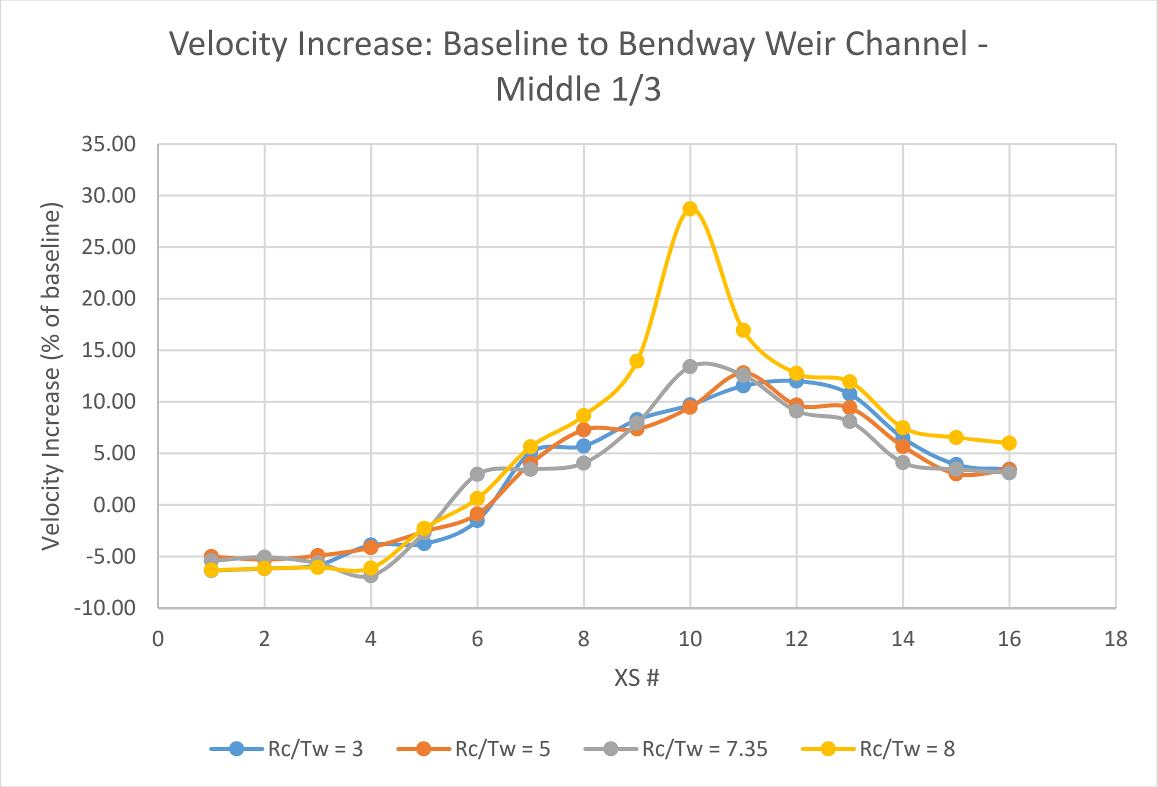

Figure 100: Velocity change from baseline to bendway weirs for the middle 1/3 channel width

Trapezoidal Bathymetry

Maximum and average values of depth average velocities were also analyzed for the trapezoidal channel using three lateral sections within the 16 data extraction cross-sections in the model. This analysis method enabled the flow field to be more carefully evaluated in the trapezoidal channel. Figure 101 shows the three lateral sections that were used for the evaluation.

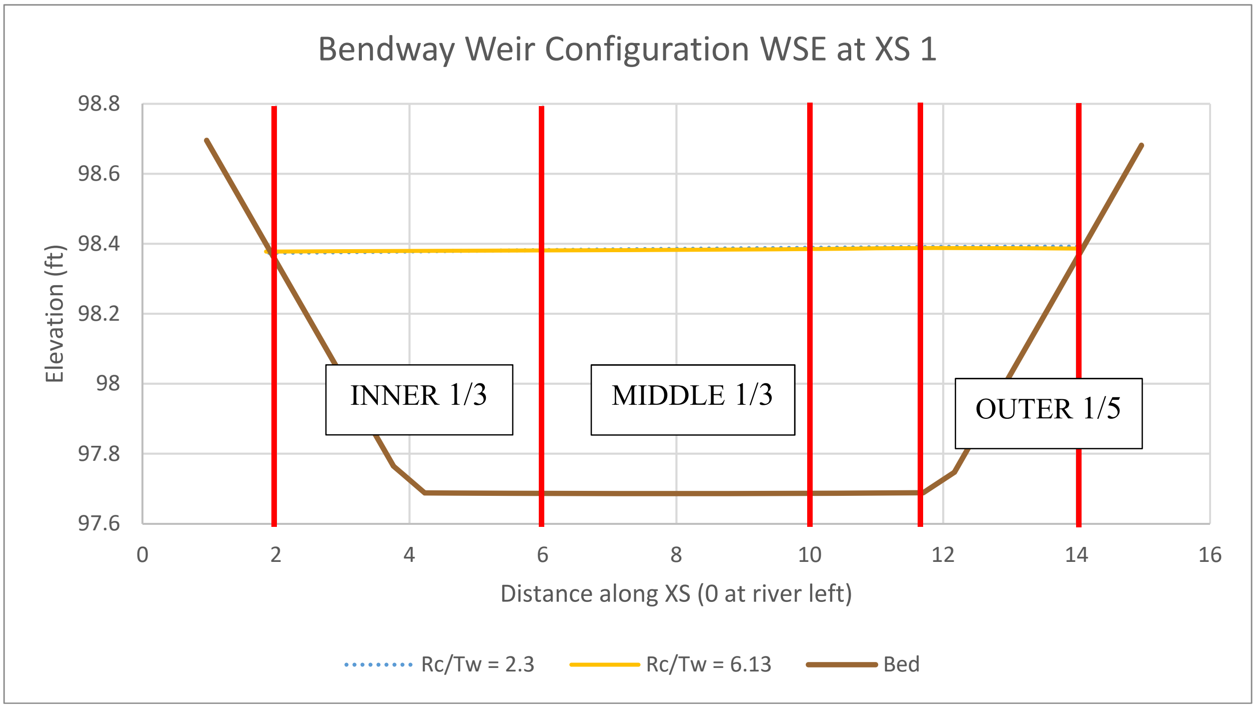

Figure 101: Maximum and average velocity lateral sections used in the velocity distribution analysis (example using cross-section 1)

The maximum velocity in the inner third of the trapezoidal channel resulted in a very similar state at the native bathymetry channel. Figure 102 and Figure 103 show that the maximum velocity observed at each cross-section throughout the bend remains fairly constant before and after the installation of bendway weirs in both bend radii. Bendway weirs caused an average of 2.1% increase of velocity when $R_c/T_w = 2.3$, and an increase of approximately 2.2% when $R_c/T_w = 6.13$. The bendway weirs caused only 0.1% difference in maximum velocity between the two values of R_c/T_w, thereby showing that the bend radius had minimal effect on the flow field.

The average velocities in Figure 104 and Figure 105 did not show as much of a pattern compared to the maximum velocity plots but they do show that the average velocities of both values of R_c/T_w increase by about 4% when the bendway weirs were installed. The effect of both bend radii on the on average velocity in the presence of bendway weirs remained the same in both cases.

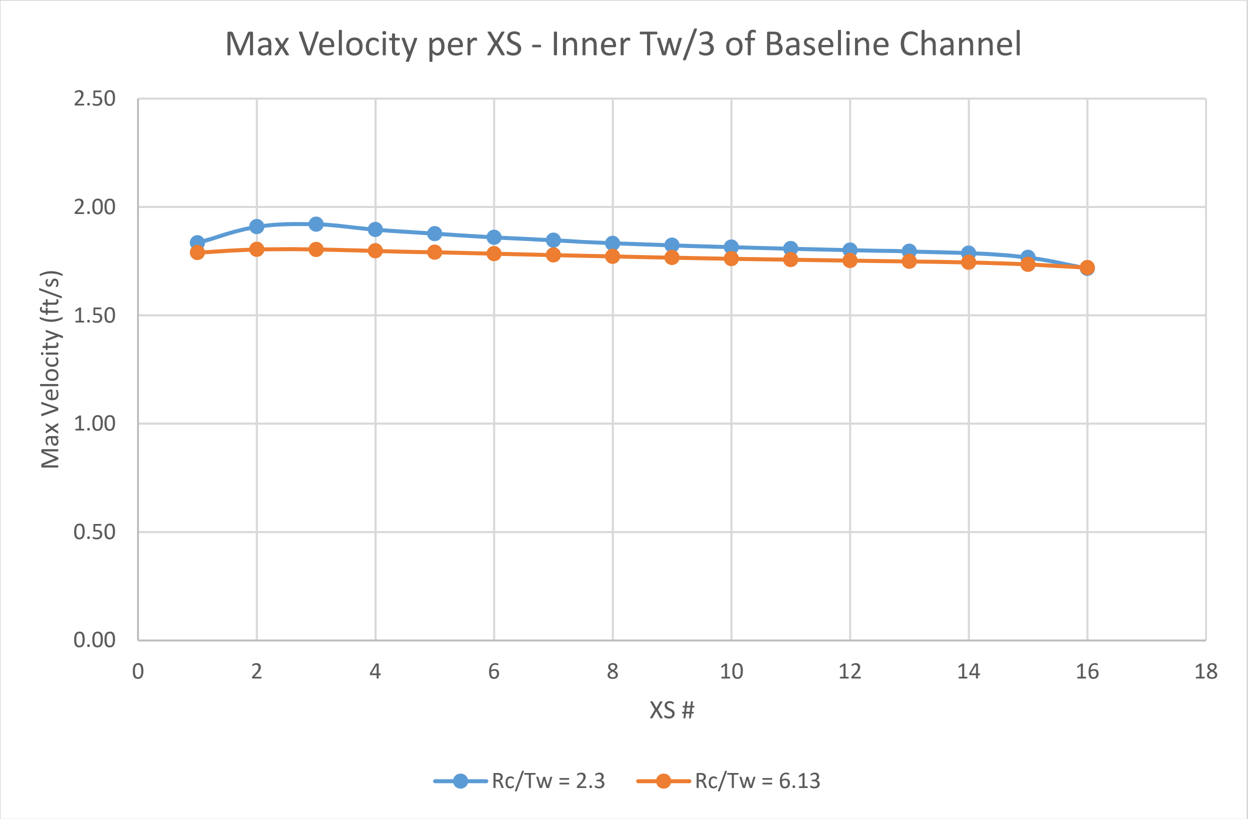

Figure 102: Max velocity in the inner third channel width of the baseline channel

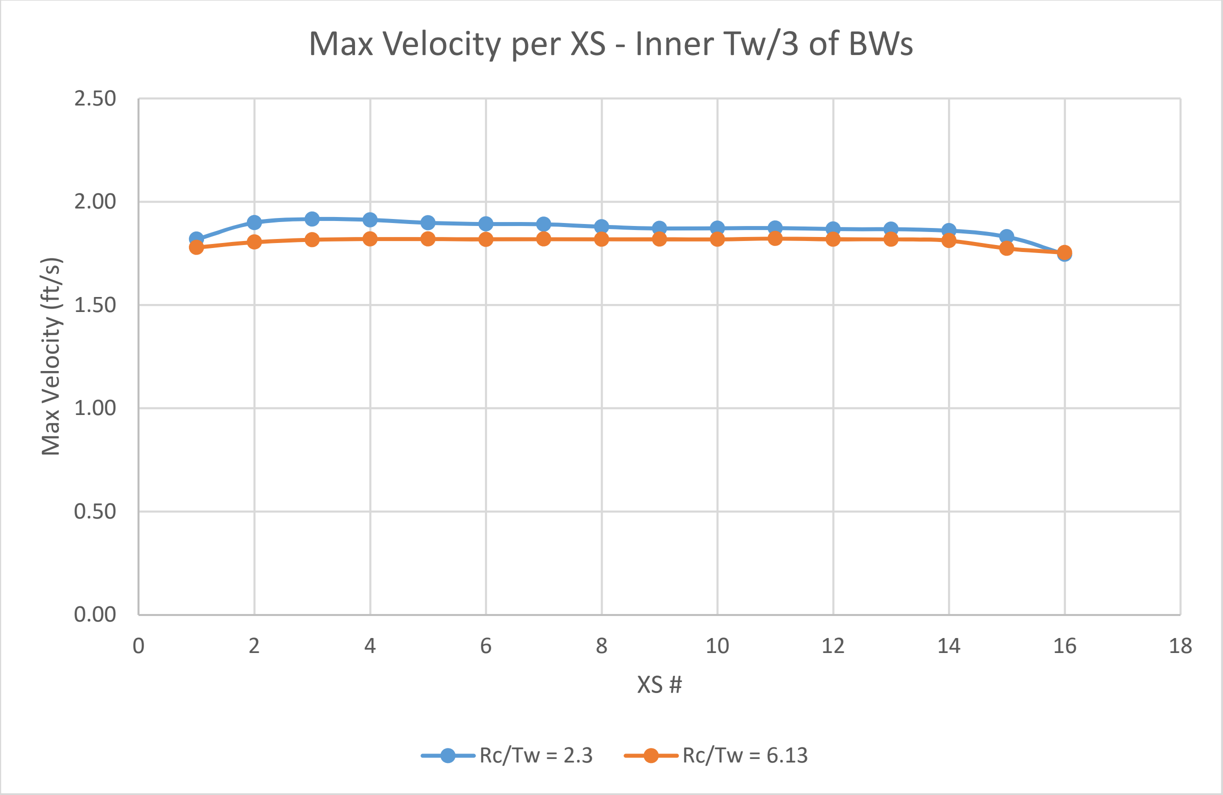

Figure 103: Max velocity in the inner third channel width of the bendway weir channel

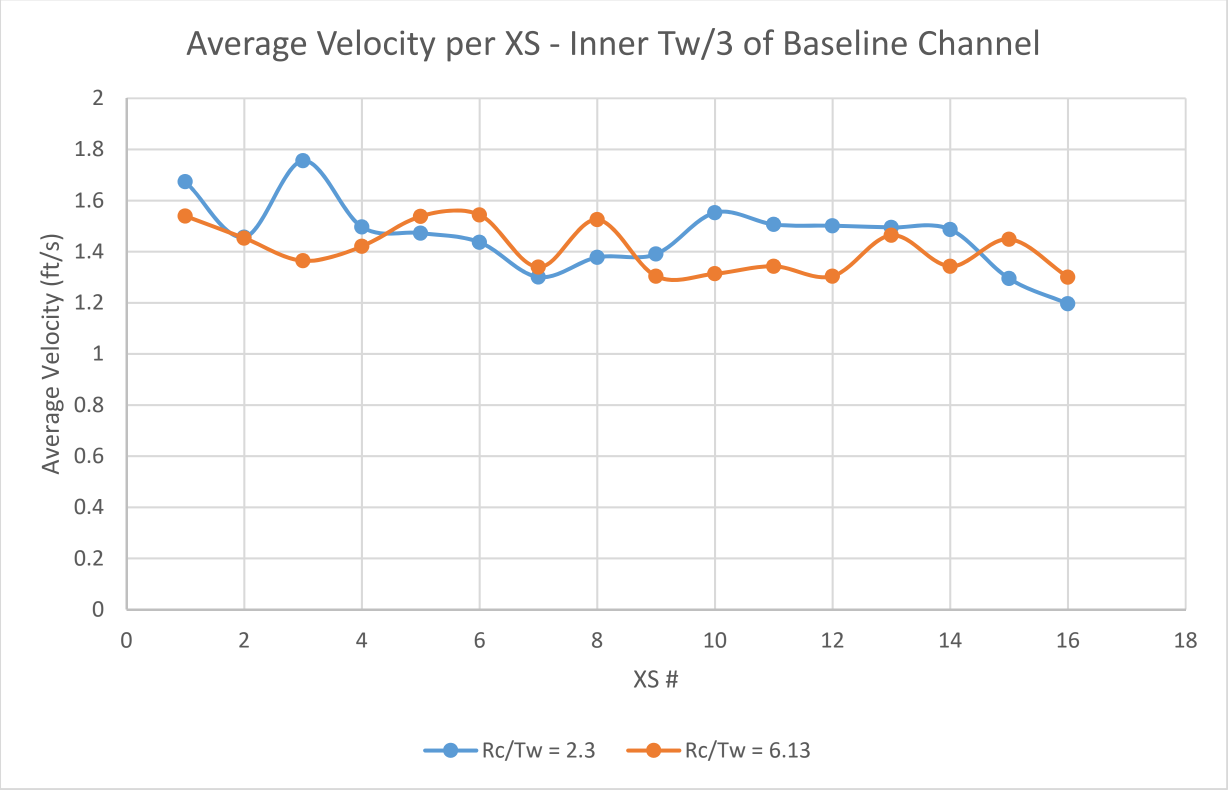

Figure 104: Average Velocity in the inner third channel width of the baseline channel

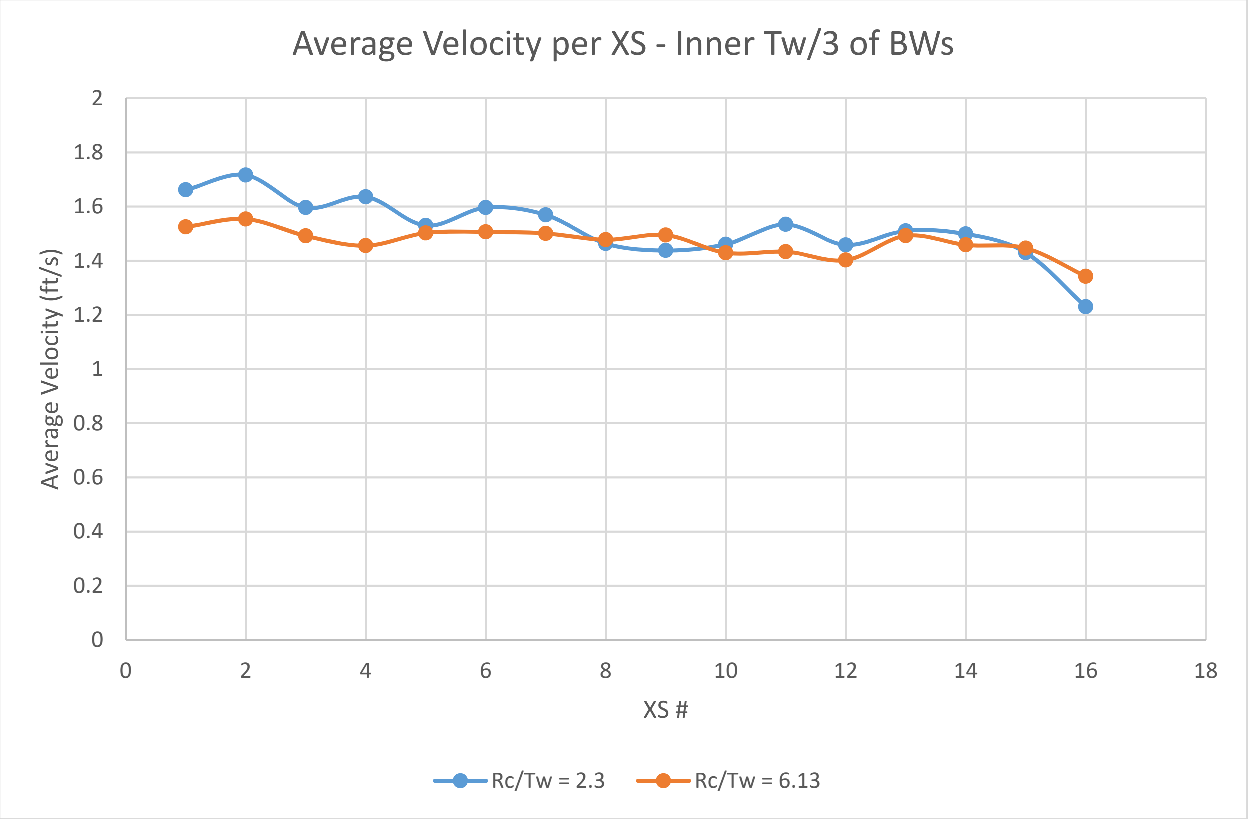

Figure 105: Average velocity in the inner third channel width of the bendway weir channel

The middle third of the channel width also saw little difference in the effect of the bendway weirs on the average and maximum velocities for both values of R_c/T_w. The middle third of the channel experienced on average a 1.8% maximum velocity increase when $R_c/T_w = 2.3$ and a 2.1% increase when $R_c/T_w = 6.13$ as shown in Figure 106 and Figure 107. Change of bend radius only caused a 0.3% difference in the change of maximum velocities between the two values. Average velocities shown in Figure 108 and Figure 109 also show that the average values of depth average velocity for both values of R_c/T_w varied the same amount from the baseline to bendway weir configuration.

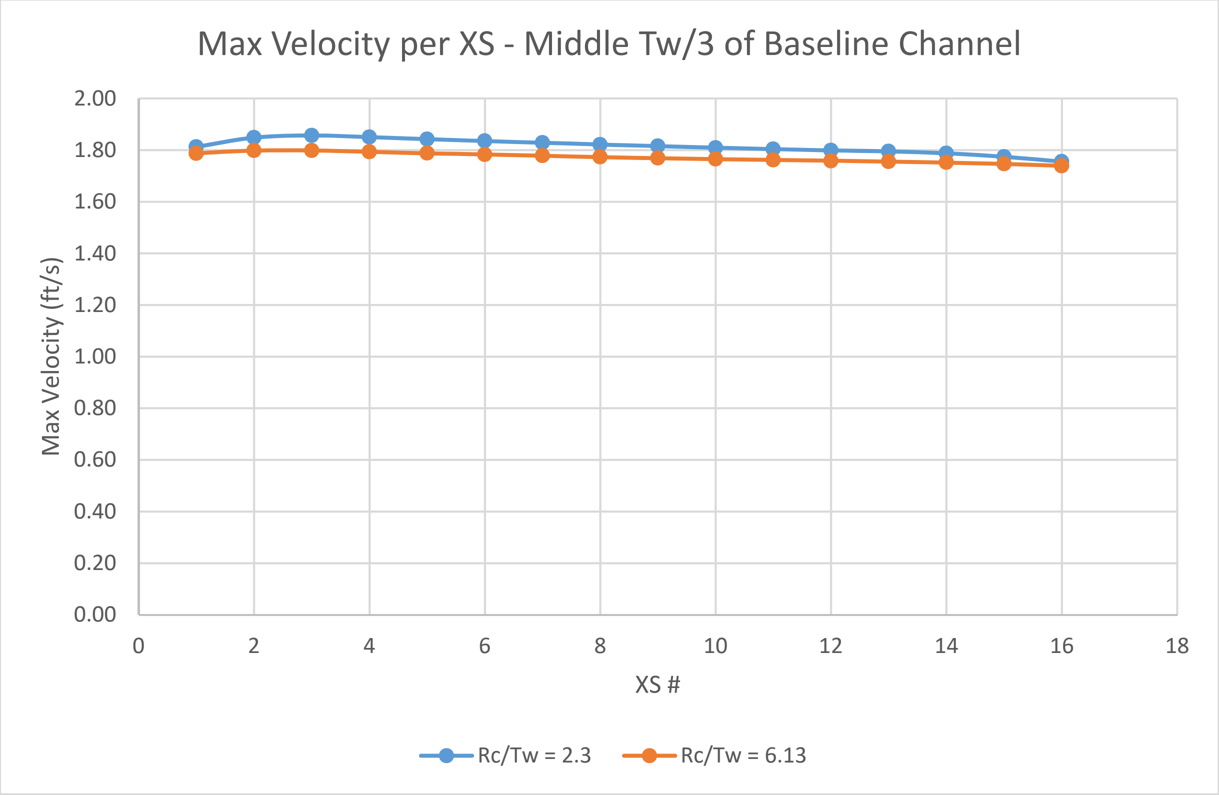

Figure 106: Maximum velocity in the middle third channel width of the baseline channel

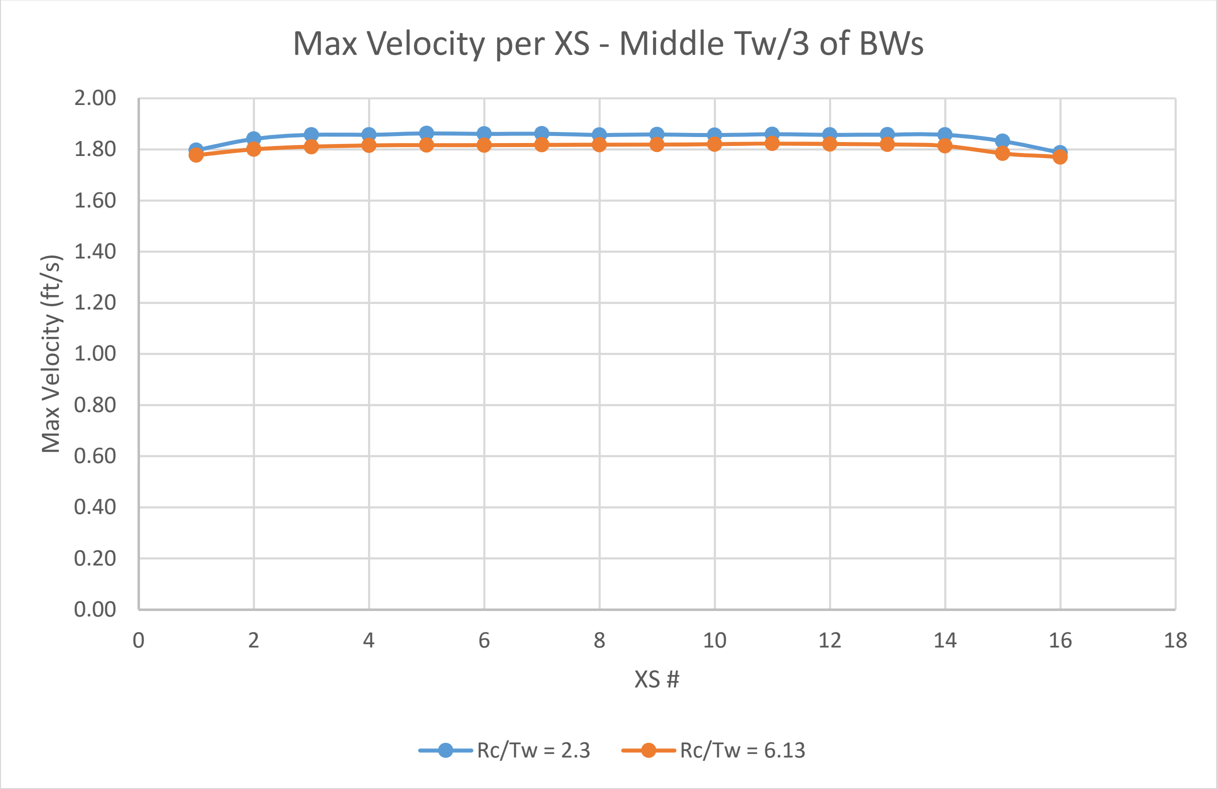

Figure 107: Maximum velocity in the middle third channel width of the bendway weir channel

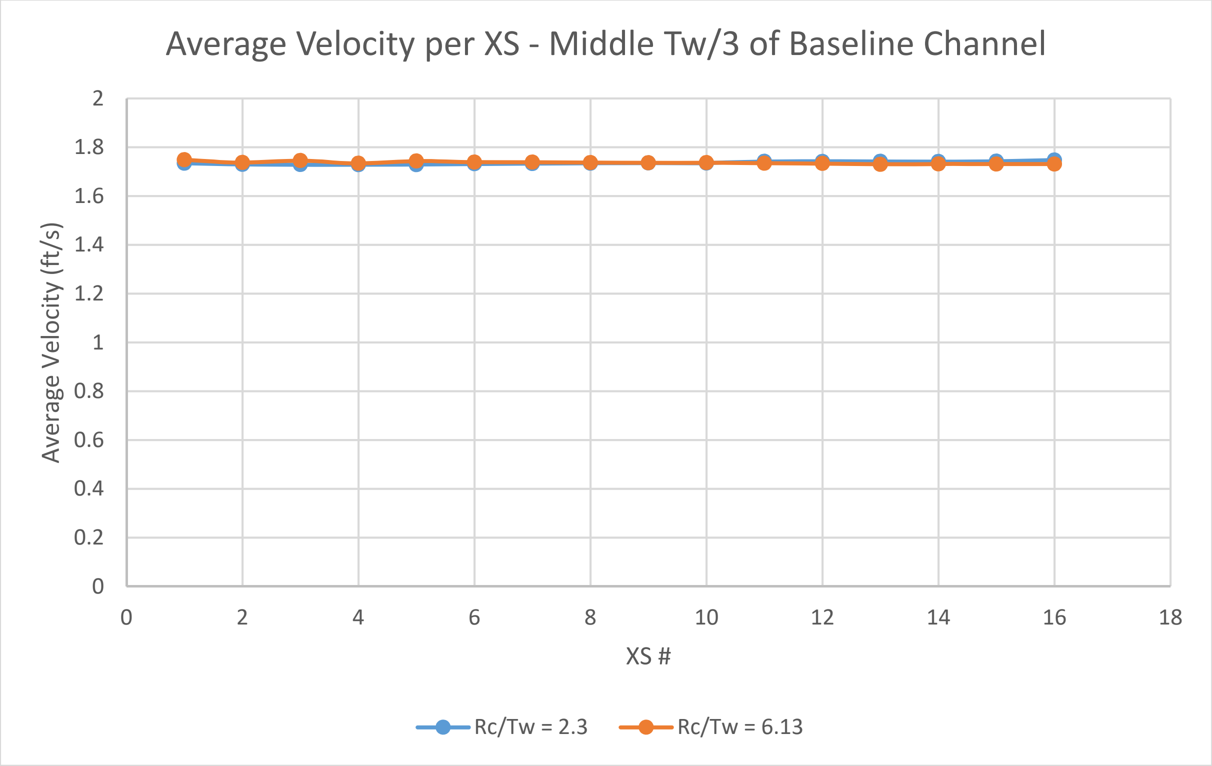

Figure 108: Average velocity in the middle third channel width of the baseline channel

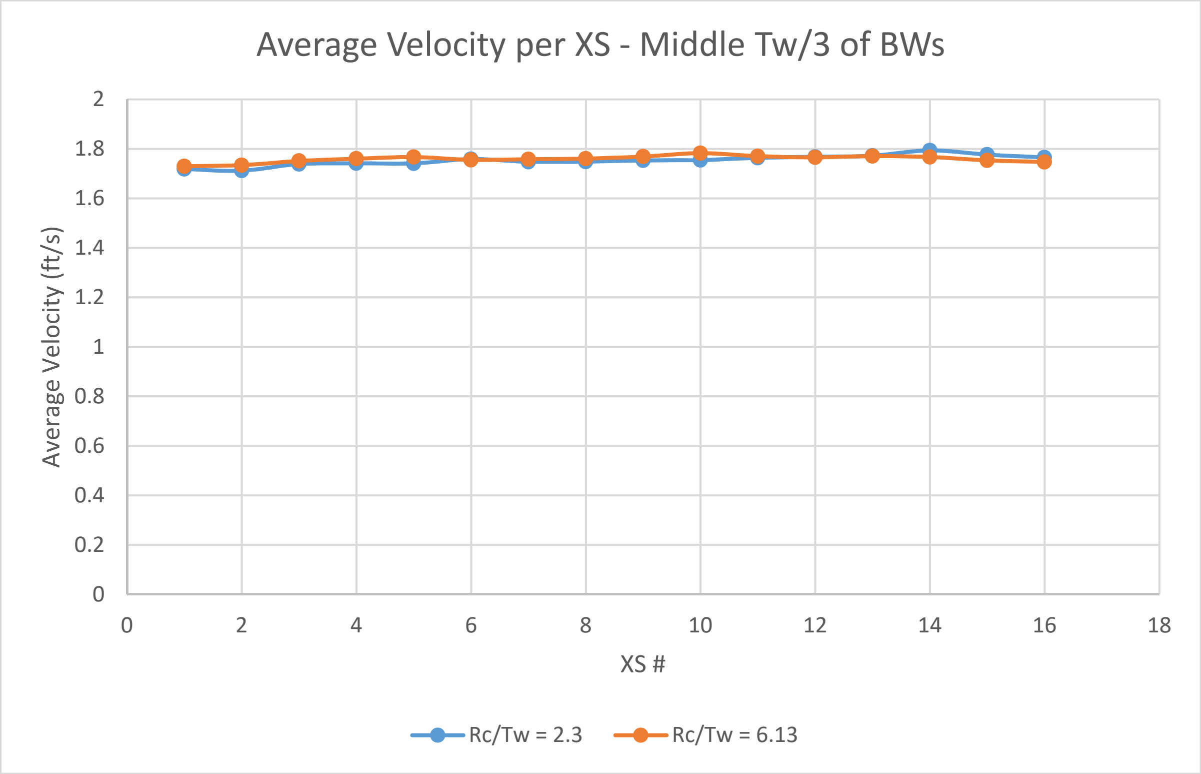

Figure 109: Average velocity in the middle third channel width of the bendway weir channel

Flow in the outer fifth of the channel width showed very similar behavior compared to the flow in the middle and inner thirds of the channel. Figure 110 and Figure 111 show that the maximum velocity from the baseline to bendway configuration decreased on average 6% when R_c/T_w = 2.3 and 5.9% when R_c/T_w = 6.13. Maximum depth average velocity in the outer fifth channel width of both bends was effectively reduced the same amount by the bendway weirs for the two values of R_c/T_w.

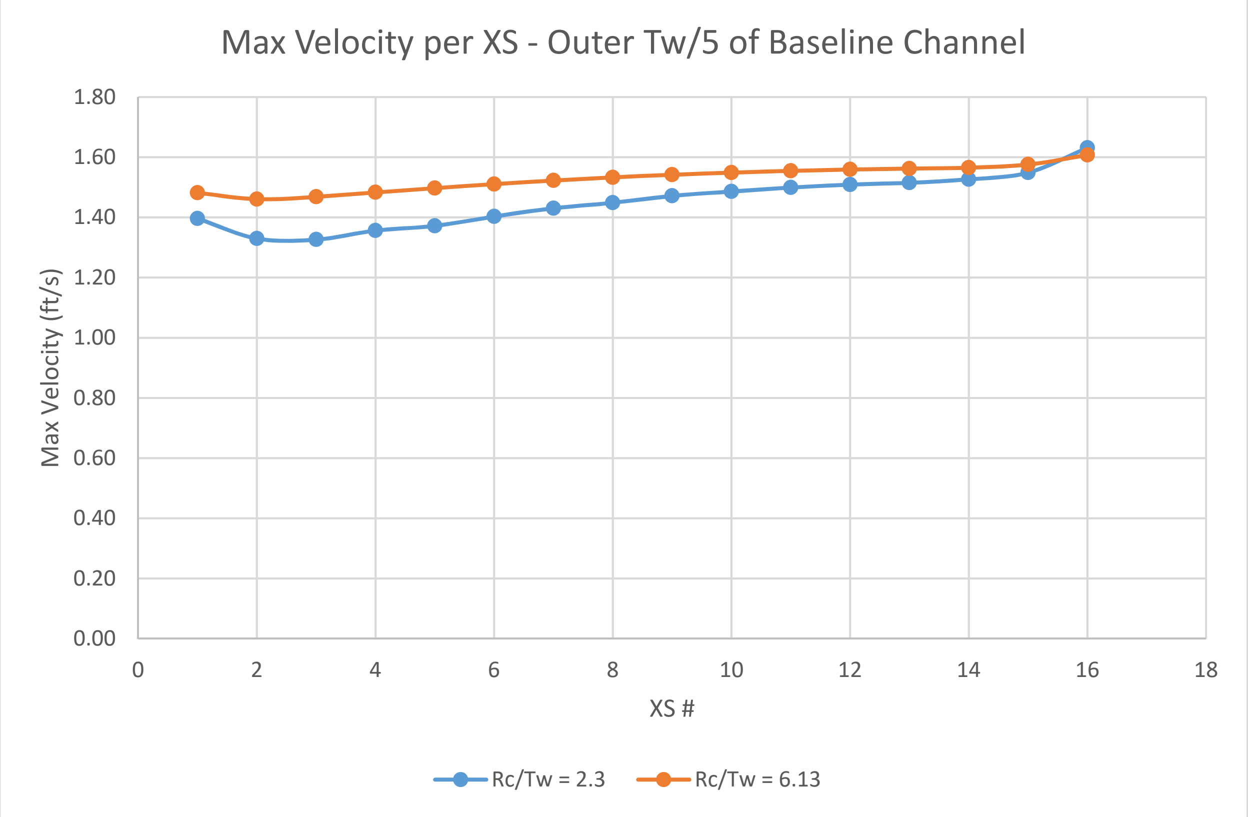

Figure 110: Maximum velocity in the outer fifth channel width of the baseline channel

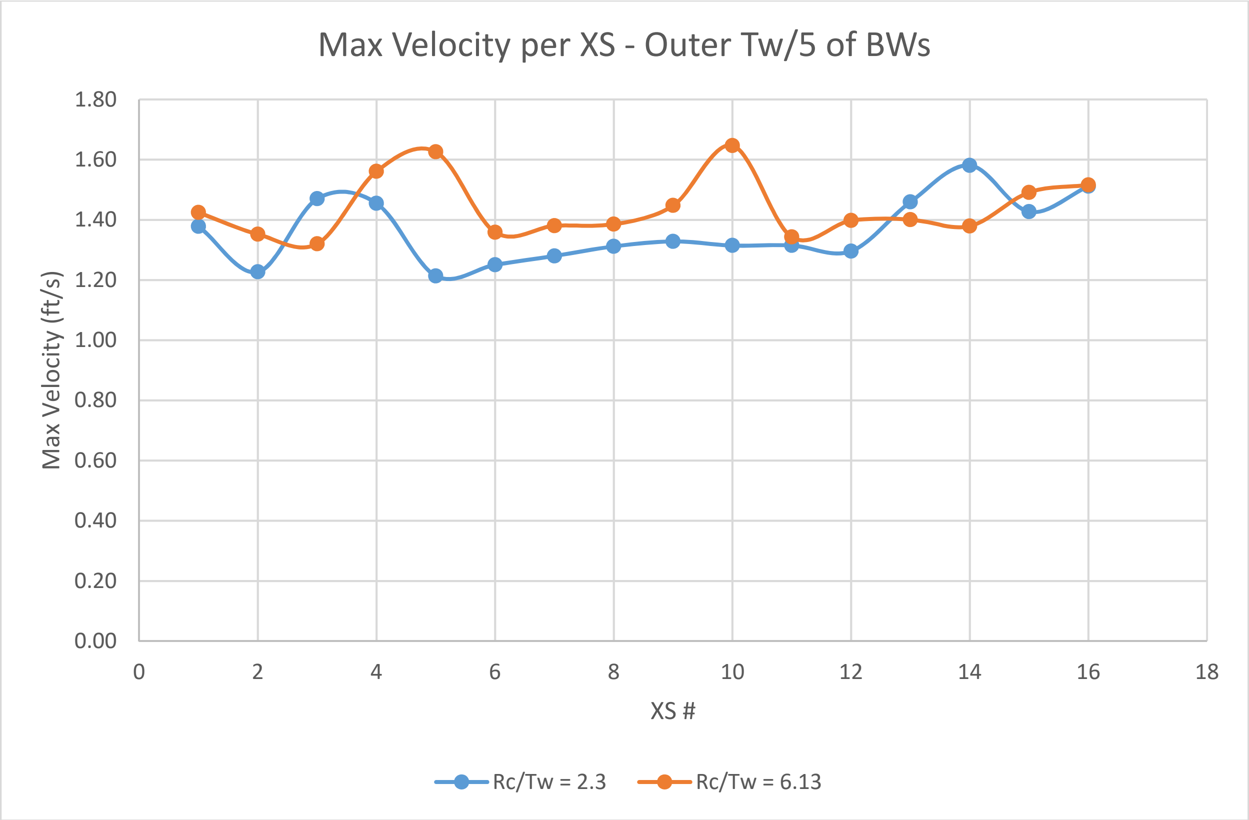

Figure 111: Maximum velocity in the outer fifth channel width of the bendway weir channel

CHAPTER 7. CONCLUSIONS AND RECOMMENDATIONS

This study used the depth average 2D numerical model SRH-2D to examine the effect of bend radius of curvature on the flow field around bendway weirs. Bend radius was cast in terms of the non-dimensional parameter R_c/T_w for a value of T_w suitably representative of the Middle reach of the Rio Grande River.

The numerical model was calibrated and validated using laboratory data from a hydraulic model of a double bend of the Rio Grande River. The calibrated numerical model had an average depth error of 6.15% and velocity error of 20.70% compared to date measured in the hydraulic model. These errors were deemed acceptable for achieving the primary objective of the present study

Conclusions

The main conclusions from the study are as follows:

1. For bends characteristic of the native Rio Grande bathymetry, and for the trapezoidal bathymetry modeled, bend radius (expressed non-dimensionally as R_c/T_w) negligibly affected the flow field around a bend fitted with a configuration of bendway weirs.
2. The influences of the parameter R_c/T_w on bend morphology (e.g. point bars and location of deepest flow) were averted in this study by use of a fixed, trapezoidal channel to represent the effects of centrifugal acceleration on bend flow field.
3. Channel morphology such as thalweg location and lateral channel contractions play a large role in determining the flow field around an alluvial bend. The study showed

that native bathymetry of the two bends of specific interest along the Middle Rio Grande affect the location of zones of high velocity in those bends.

4. Zones of high velocity and shear stress were essentially identical in their location and magnitude between the varying degrees of R_c/T_w.
5. For the bend with native bathymetry or trapezoidal bathymetry, the ratio of maximum value of depth average cross-sectional velocity to average bend entrance velocity remained relatively constant between the values of R_c/T_w.
6. For the bend fitted with a configuration of bendway weirs, the ratio of the maximum value of depth average velocity (at a cross-section) to average bend entrance velocity remained relatively constant between the varying values of R_c/T_w.
7. The flow field toward the inner bank experienced negligible differences in both maximum and average values of depth average velocity for flows in the presence of bendway weirs and variable R_c/T_w. The water surface elevation along the inner bank was lower when $R_c/T_w = 3.0$ than when $R_c/T_w = 8.0$ due to stronger influence of centrifugal acceleration caused by the former value of R_c/T_w.
8. The middle third of the channel width also experienced negligible differences in maximum and average values of depth average velocity for the range of R_c/T_w tested. Additionally, the water surface elevation in the middle third of the channel was practically constant for the range of R_c/T_w values.
9. Flow velocities near the outer bank of the channel fitted with bendway weirs were difficult to evaluate with the 2D model, as this region was highly turbulent between the bendway weirs. In general, the model indicated that the velocities of the outer bank were not substantially affected by the values of R_c/T_w used in this study.

Recommendations

The results of this study reveal useful effects of bend radius (and the parameter R_c/T_w) on bendway weir flow fields. However, they also suggest the need for the following additional studies:

1. For the present study, the variable T_w in the non-dimensional parameter R_c/T_w was held constant at a value representative of the Middle Rio Grande River. A further study could vary T_w for constant values of R_c/T_w.
2. Use numerical modeling to include sediment transport and bed morphodynamics enabling the bed to change and form more natural and representative geometry associated with the bend radius.
3. Obtain and analyze field data of bendway weirs in varying bend radii to again gain additional data indicative of natural conditions in alluvial channels.
4. Identify if different bendway weir designs are more susceptible to effects of bend radius of curvature

REFERENCES

Cox, A. L. (2005). *A Study of In-stream Rehabilitation Structures in Sand-bed Channels*. M.S. Thesis, Colorado State University, Department of Civil Engineering, Fort Collins, CO.

Darrow, J. D. (2004). *Effects of Bendway Weir Characteristics on Resulting Flow Conditions.* Fort Collins, CO: Colorado State University.

Garfield, M. (2019). *The Effects of Scour on the Flow Field at a Bendway Weir*. M.S. Thesis, Colorado State University, Department of Civil Engineering, Fort Collins, CO.

Heintz, M. L. (2002). *Investigation of Bendway Weir Spacing.* Fort Collins, CO: Colorado State University.

Holste, N. (2016). "Bend Geometry Modification for 3D Numerical Modeling." Technical Report No. SRH-2016-24. U.S. Department of the Interior Bureau of Reclamation Technical Service Center, Denver, CO.

Julien, P. Y., & Duncan, J. R. (2003). *Optimal Design Criteria of Bendway Weirs from Numeircal Simulations and Physical Model Studies.* Fort Collins, CO: Colorado State University.

Kashyap, Shalini, et al. (2012) *Influence of Channel Aspect Ratio and Curvature on Flow, Secondary Circulation, and Bed Shear Stress in a Rectangular Channel Bend*. 12th ed., vol. 138, Journal of Hydraulic Engineering

Kasper, K. E. (2005). *Accuracy of HEC-RAS to Calculated Flow Depths and Total Energy Loss With and Without Bendway Weirs in a Meander Bend*. M.S. Thesis, Colorado State University, Department of Civil Engineering, Fort Collins, CO.

Kinzli, K. (2005). *Effects of Bendway Weir Characteristics on Resulting Eddy and Channel Flow Conditions*. M.S. Thesis, Colorado State University, Department of Civil Engineering, Fort Collins, CO.

Lagasse, P. F., Clopper, P. E., Pagán-Ortiz, J. E., Zevenbergen, L. W., Arneson, L. A., Schall, J. D., & Girard, L. G. (2009). *Bridge Scour and Stream Instability Countermeasures.* Washington, D.C.: Federal Highway Administration.

Lai, Yong G. (2008) *SRH-2D Version 2: Theory and User's Manual*. Bureau of Reclamation, *SRH-2D Version 2: Theory and User's Manual*.

McCullah, J. A., & Gray, D. (2005). *Environmentally Sensitive Channel- and Bank- Protection Measures.* Washington, D.C.: Transportation Research Board, National Academies of Science.

Natural Resources Conservation Service. (2007). *Technical Supplement 14H Flow Changing Techniques Part 654 National Engineering Handbook.* United States Department of Agriculture.

Pradhan, Arpan, et al. (2018) *Variation of Velocity Distribution in Rough Meandering Channels*. vol. 2018, Hindawi, *Variation of Velocity Distribution in Rough Meandering Channels*.

Richard, G. (2001). *Quantification and Prediction of Lateral Channel Adjustments Downstream from Cochiti Dam, Rio Grande, NM.* Fort Collins, CO: Colorado State University.

Schmidt, P. G. (2005). *Effects of Bendway Weir Field Geometric Characteristics on Channel Flow Conditions*. M.S. Thesis, Colorado State University, Department of Civil Engineering, Fort Collins, CO.

Sclafani, P. (2010). *Methodology for Predicting Maximum Velocity and Shear Stress in a Sinuous Channel with Bendway Weirs Using 1-D Hec-Ras Modeling Results.* Fort Collins, CO: Colorado State University.

Scurlock, S. M., Cox, A. L., Thornton, C. I., & Abt, S. R. (2014). *Calibration and validation of a numerical model forevaluation of transverse in-stream structure research.* Denver, CO: Bureau of Reclamation.

Scurlock, S. M., Thornton, C. I., & Abt, S. R. (2014). *Evaluation of bendway-weir structures within the native topography channel.* Denver, CO: Bureau of Reclamation.

Shin, K., Ettema, R., & Thornton, C. I. (2018). *Native Channel Topography and Rock-Weir Structure Channel-Maintenance Techniques.* Fort Collins, CO: Colorado State University.

Thornton, C. I., James, M., & Shin, K. (2016). *Testing of instream vane structures within the native-topography channel.* Fort Collins, CO: Colorado State University.

Walker, K. G. (2009). *Comparison of a Generalized Trapezoidal Hydraulic Model to a Native Topography Patterned Bed Surface Model of the Rio Grande*. M.S. Thesis, Colorado State University, Department of Civil and Environmental Engineering, Fort Collins, CO.

APPENDIX A. BENDWAY WEIR DESIGN CROSS SECTIONAL PLOTS

The following cross-sectional plots show a cross-sectional view of the bed profile and the bendway weir on top of the bed profile. These plots are taken from the design spreadsheets that were used to design the bendway weirs in each of the models completed in this study. The bendway weirs are labeled with the furthest upstream weir being weir #1 and are labeled consecutively progressing downstream. The following plots are included from the R_c/T_w = 7.35 configuration and are representative of the designs in the remaining configurations. Only a few examples of the trapezoidal weir designs are given as they are repetitive.

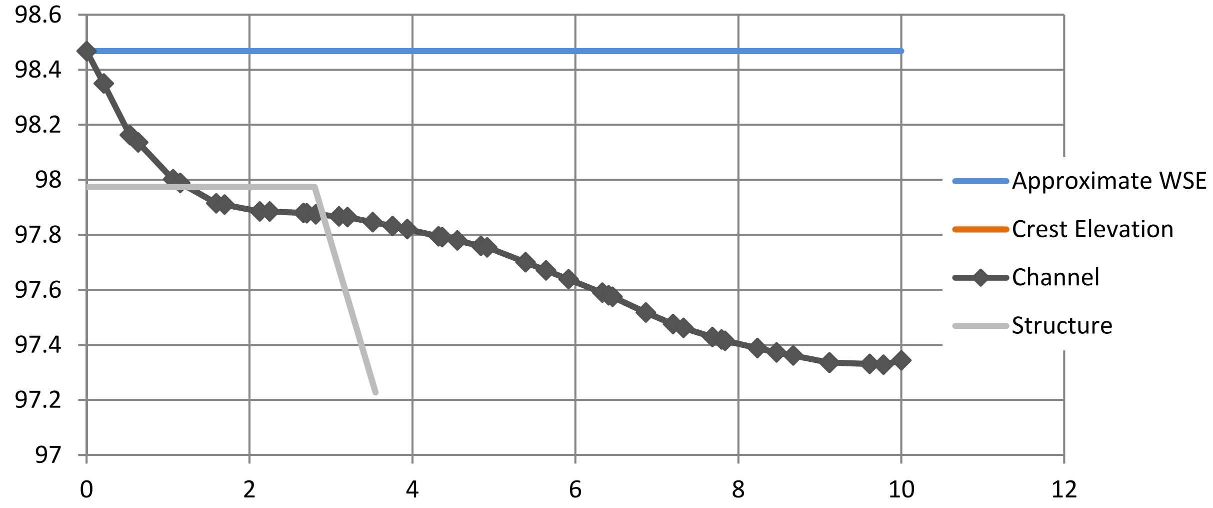

Figure 112: Weir 1 design

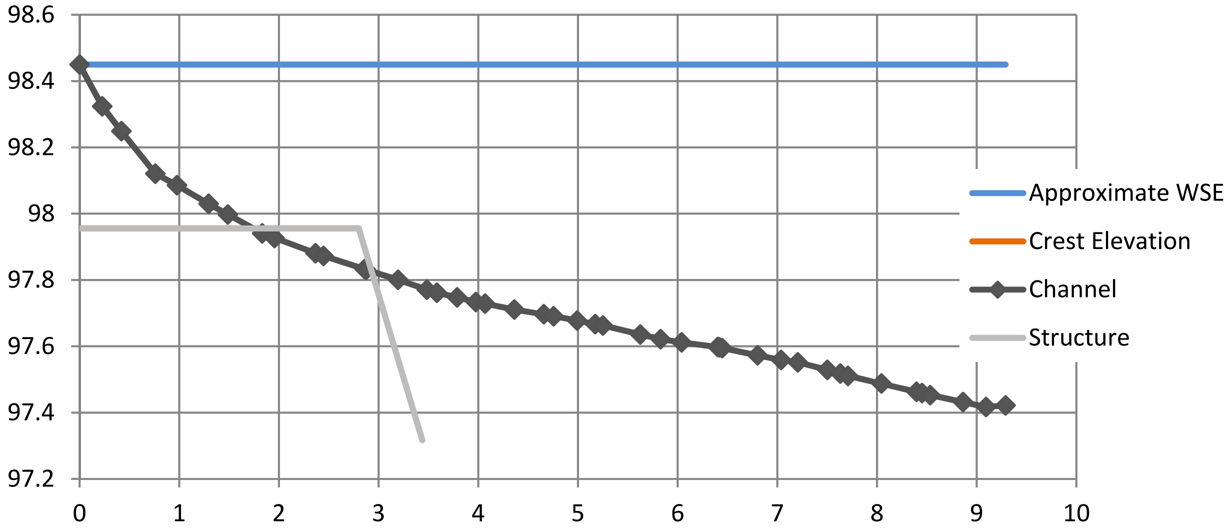

Figure 113: Weir 2 design

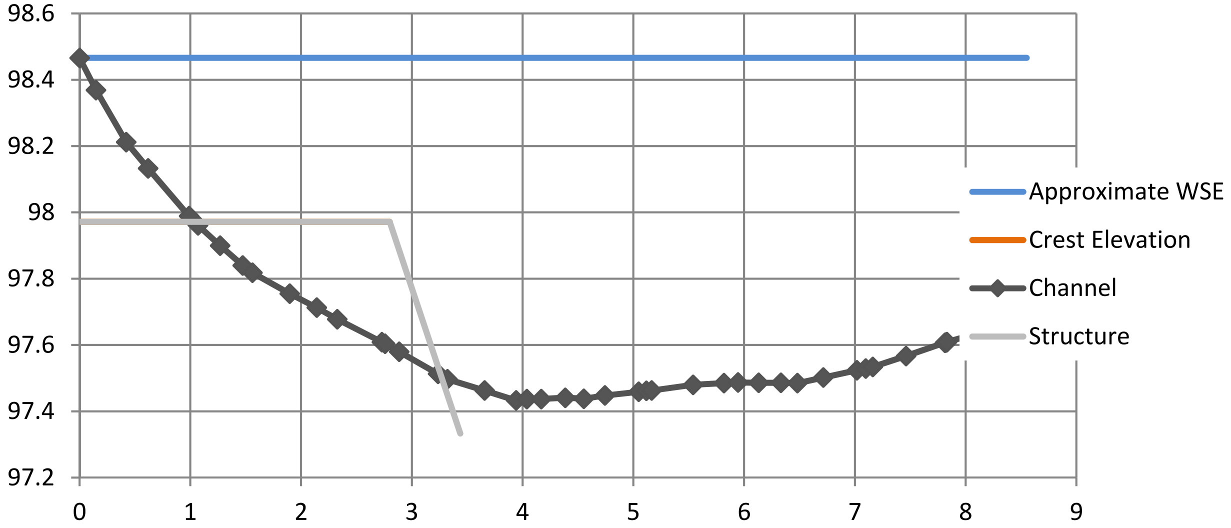

Figure 114: Weir 3 design

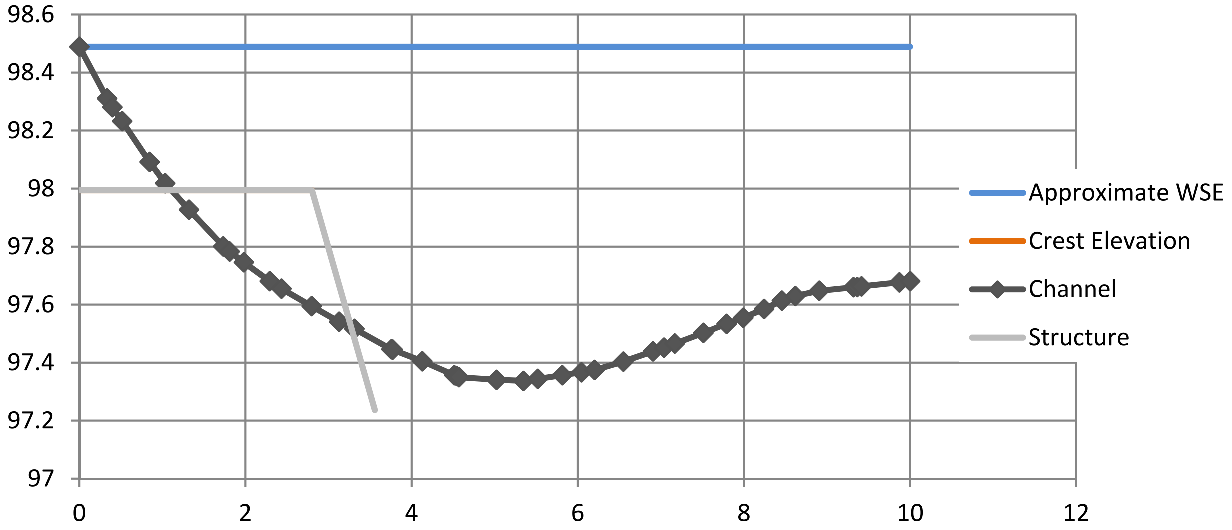

Figure 115: Weir 4 design

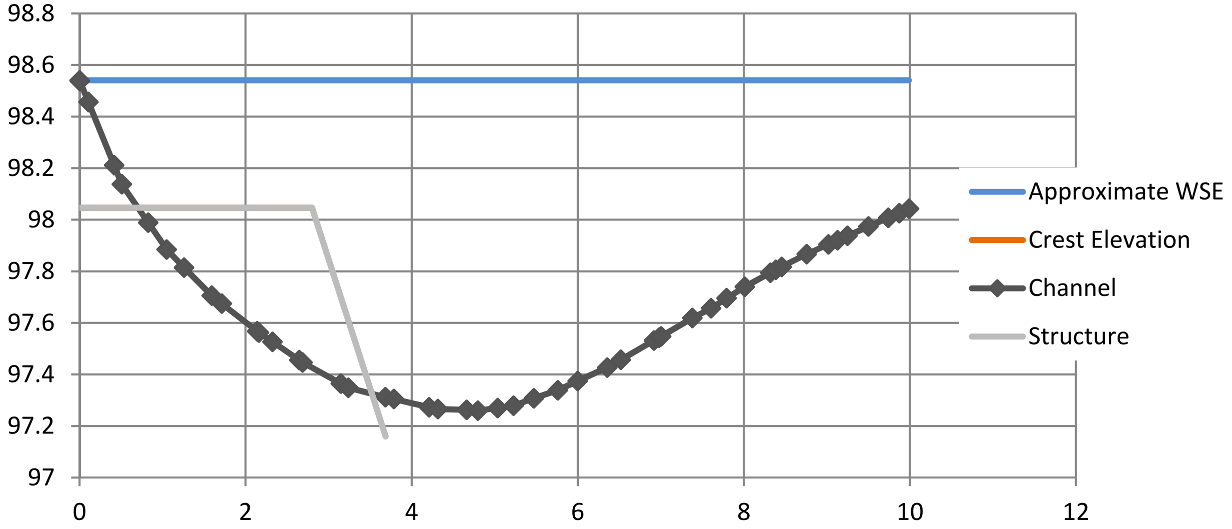

Figure 116: Weir 5 design

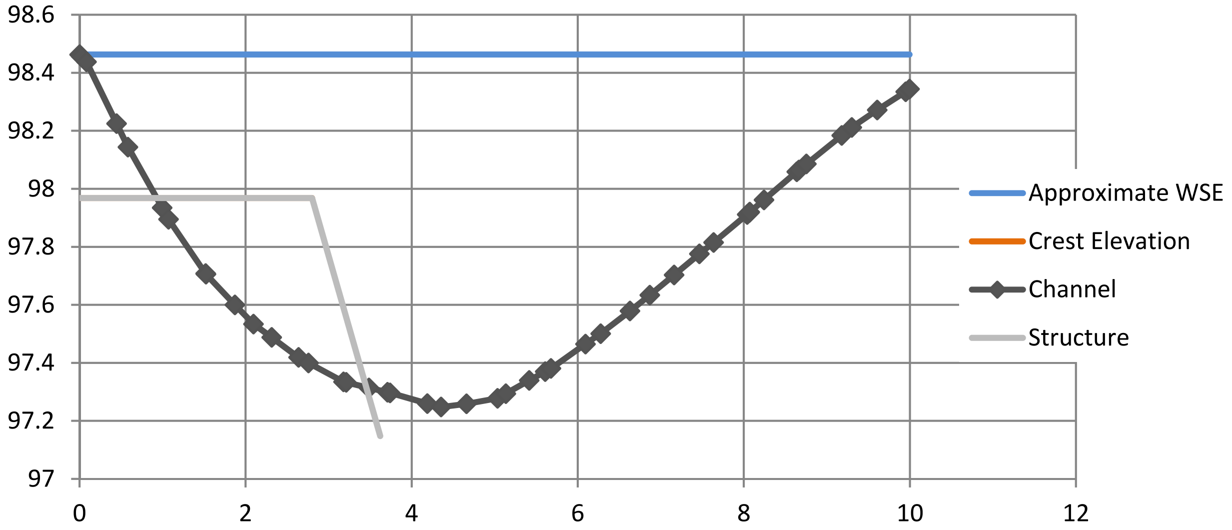

Figure 117: Weir 6 design

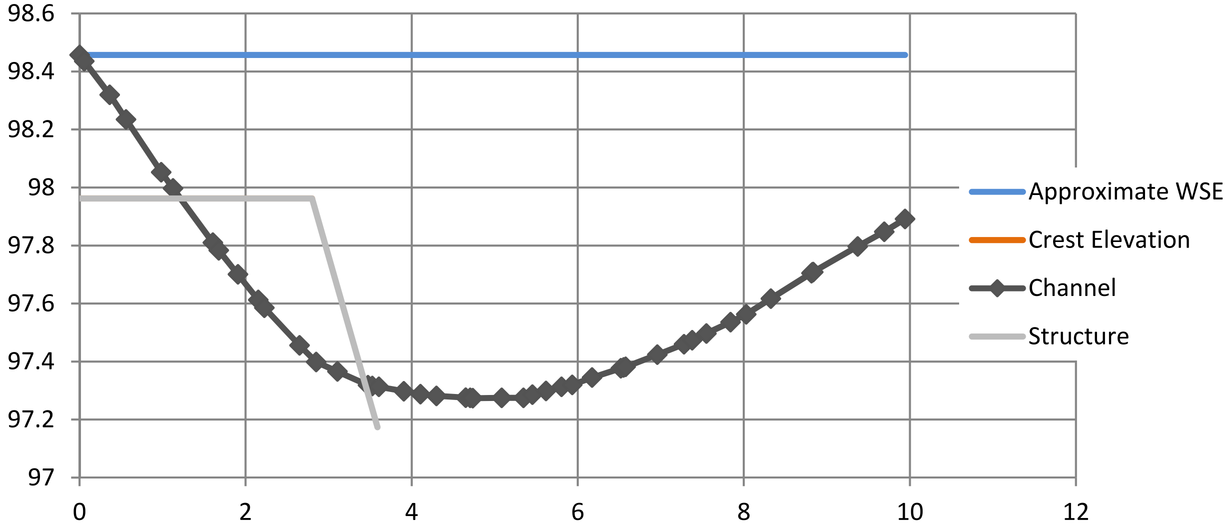

Figure 118: Weir 7 design

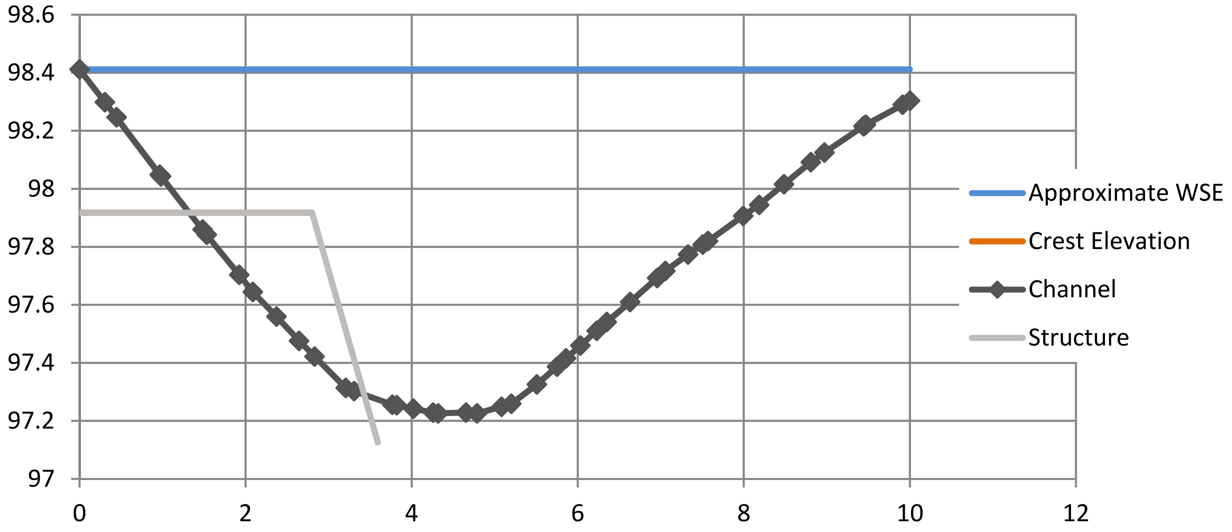

Figure 119: Weir 8 design

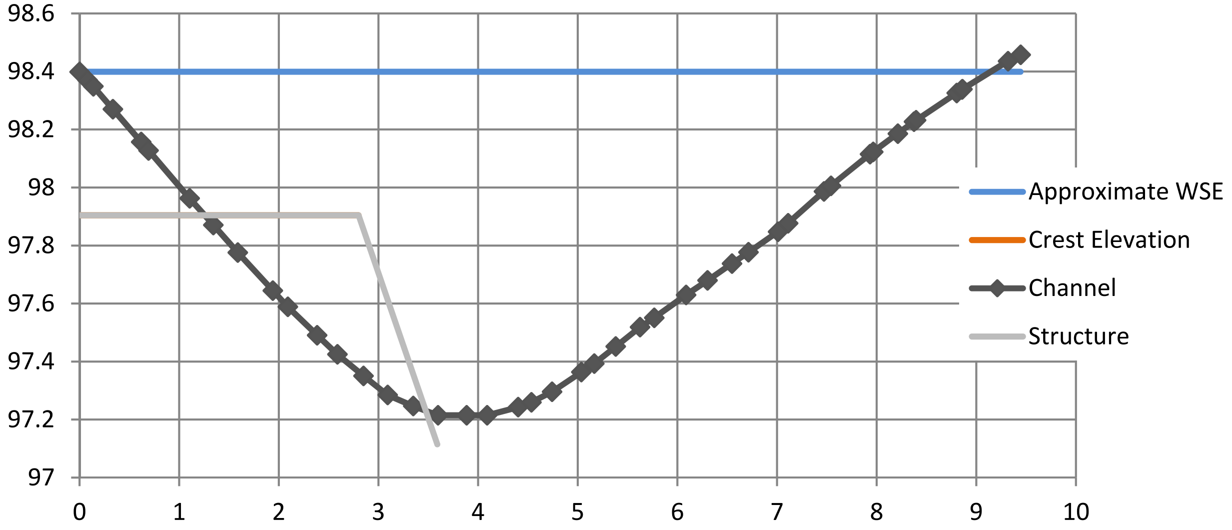

Figure 120: Weir 9 design

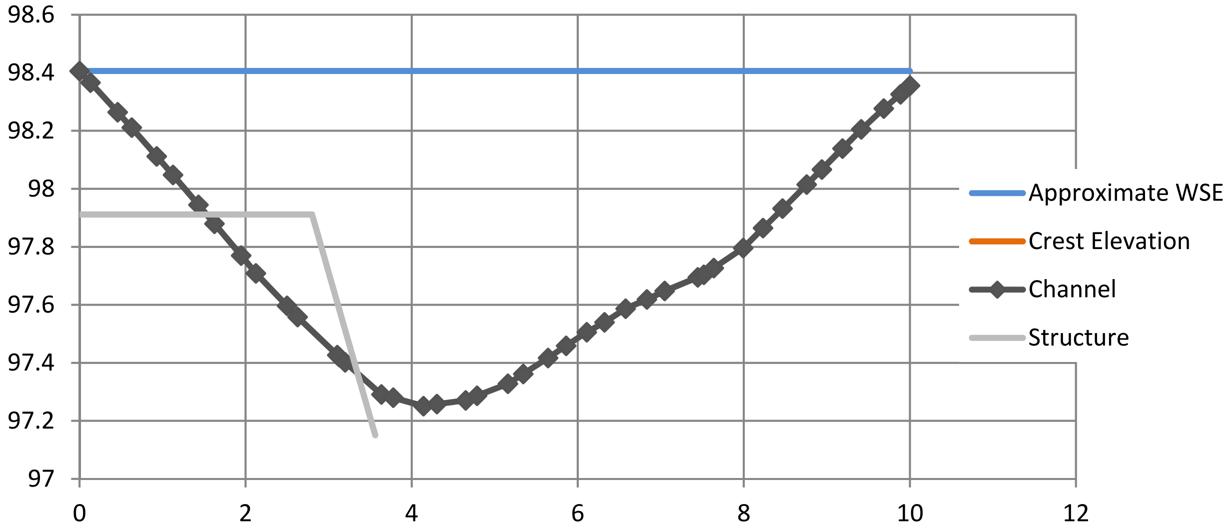

Figure 121: Weir 10 design

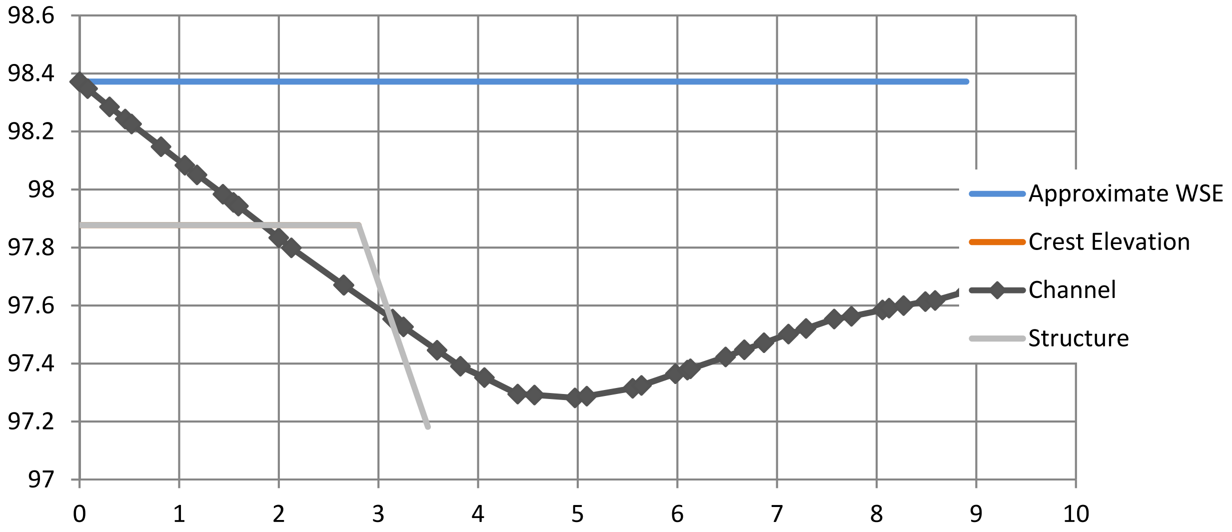

Figure 122: Weir 11 design

APPENDIX B. CROSS-SECTIONAL PLOTS OF WATER SURFACE ELEVATION AND VELOCITY – NATIVE BATHYMETRY

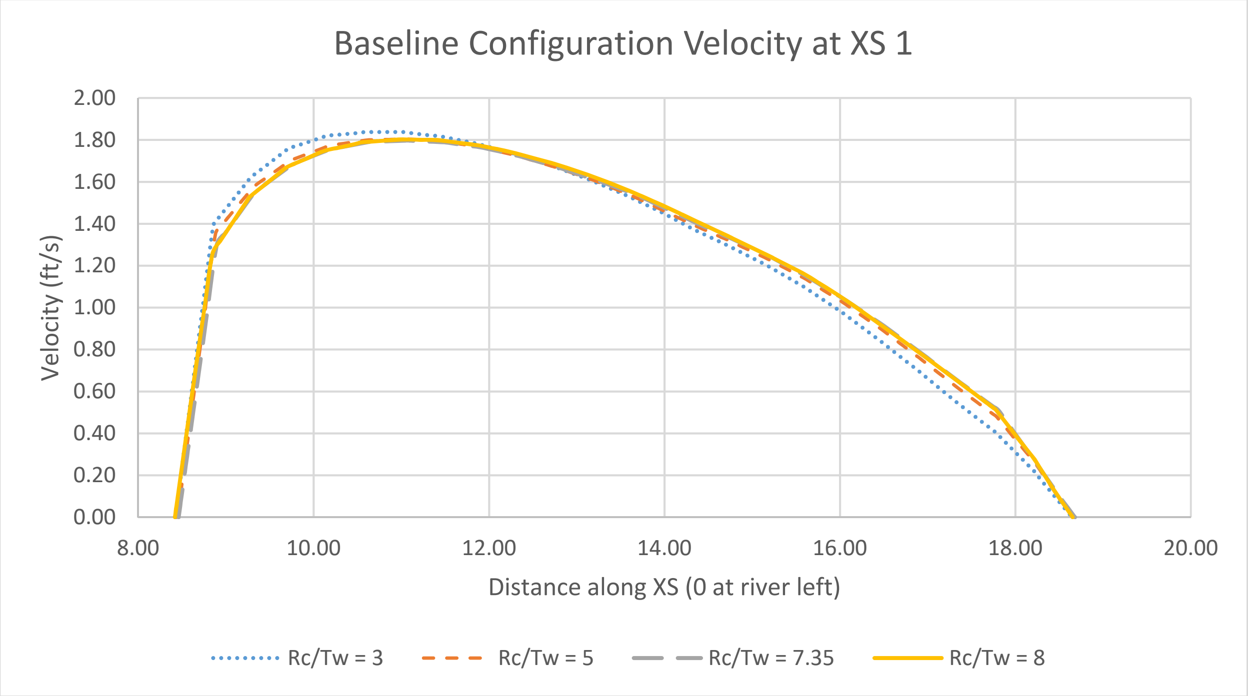

Figure 123: Velocity across XS 1 in the baseline configuration

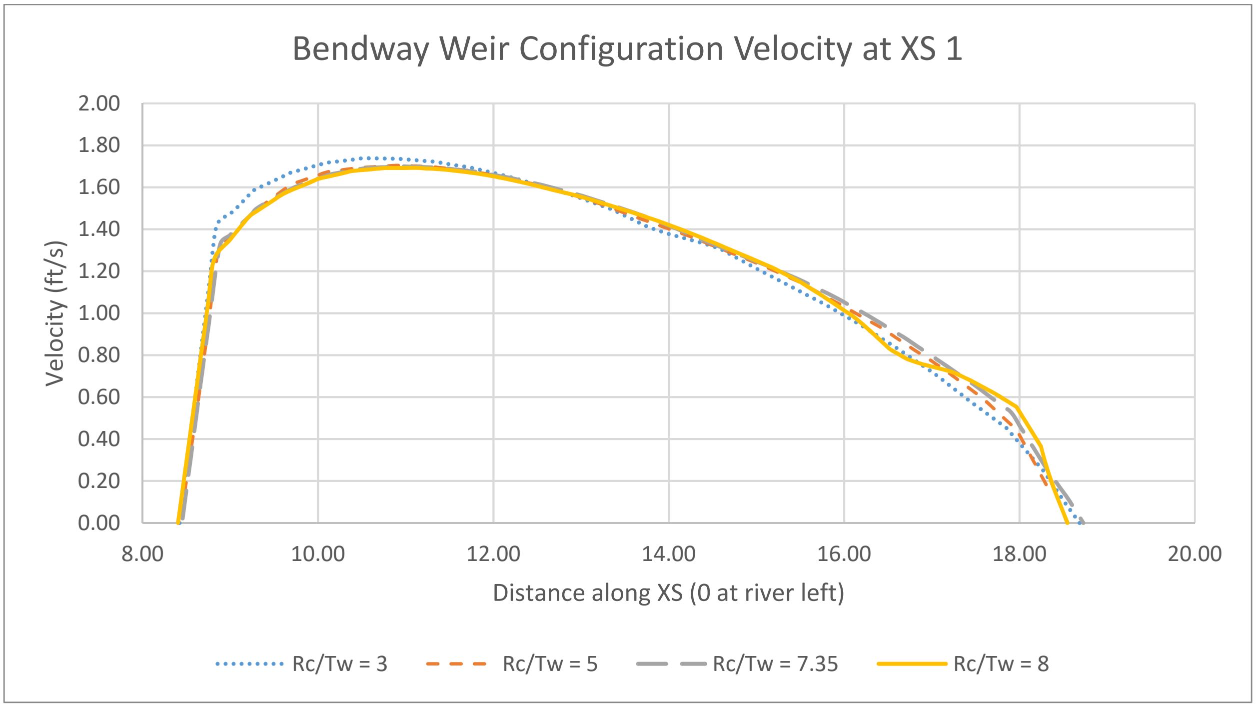

Figure 124: Velocity across XS 1 in the bendway weir configuration

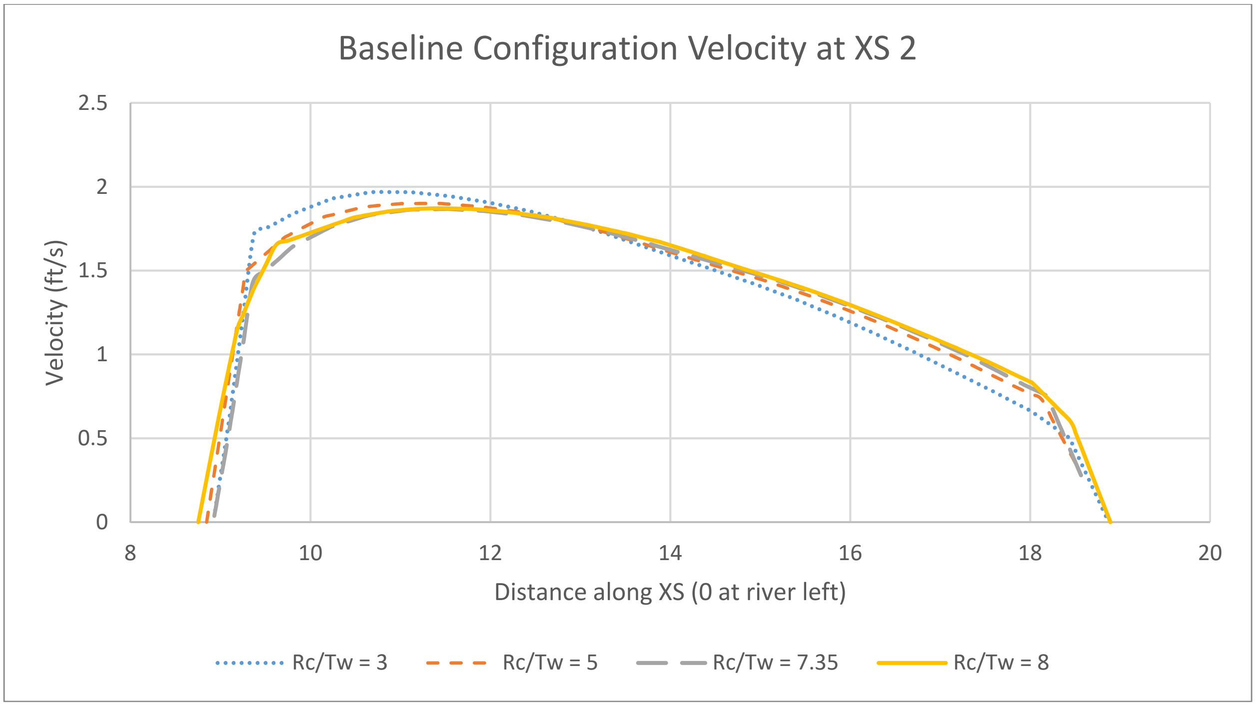

Figure 125: Velocity across XS 2 in the baseline configuration

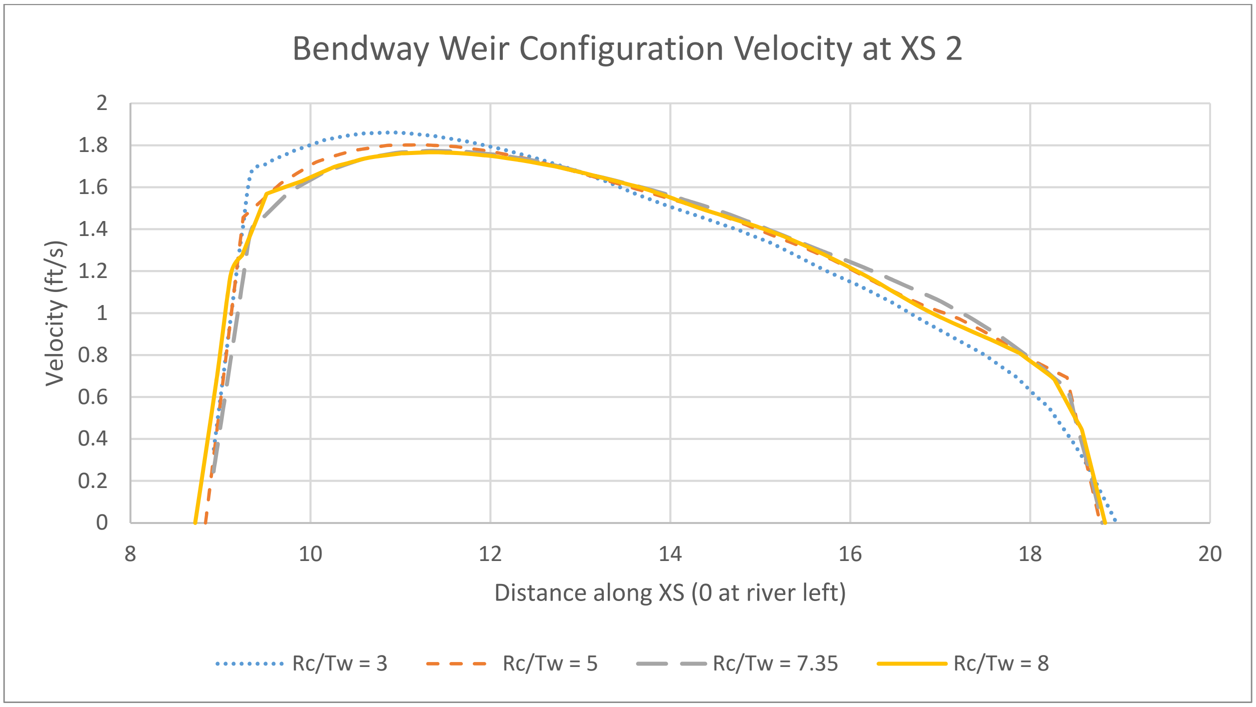

Figure 126: Velocity across XS 2 in the bendway weir configuration

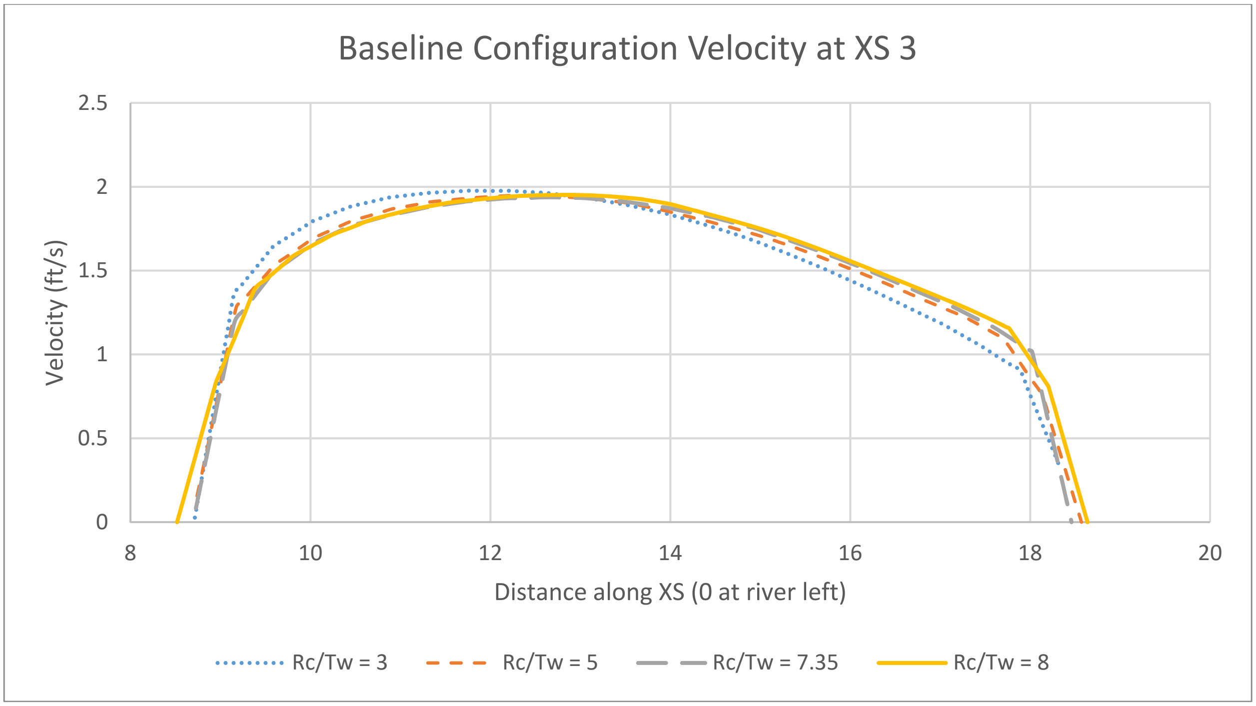

Figure 127: Velocity across XS 3 in the baseline configuration

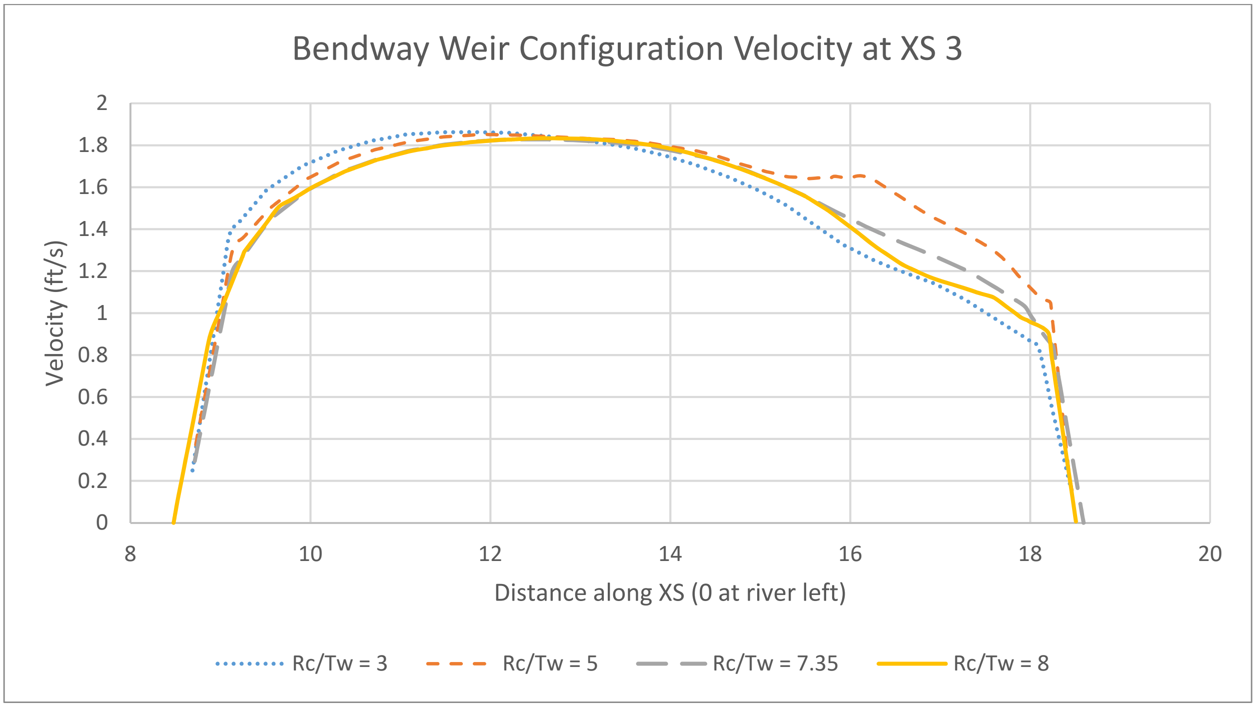

Figure 128: Velocity across XS 3 in the bendway weir configuration

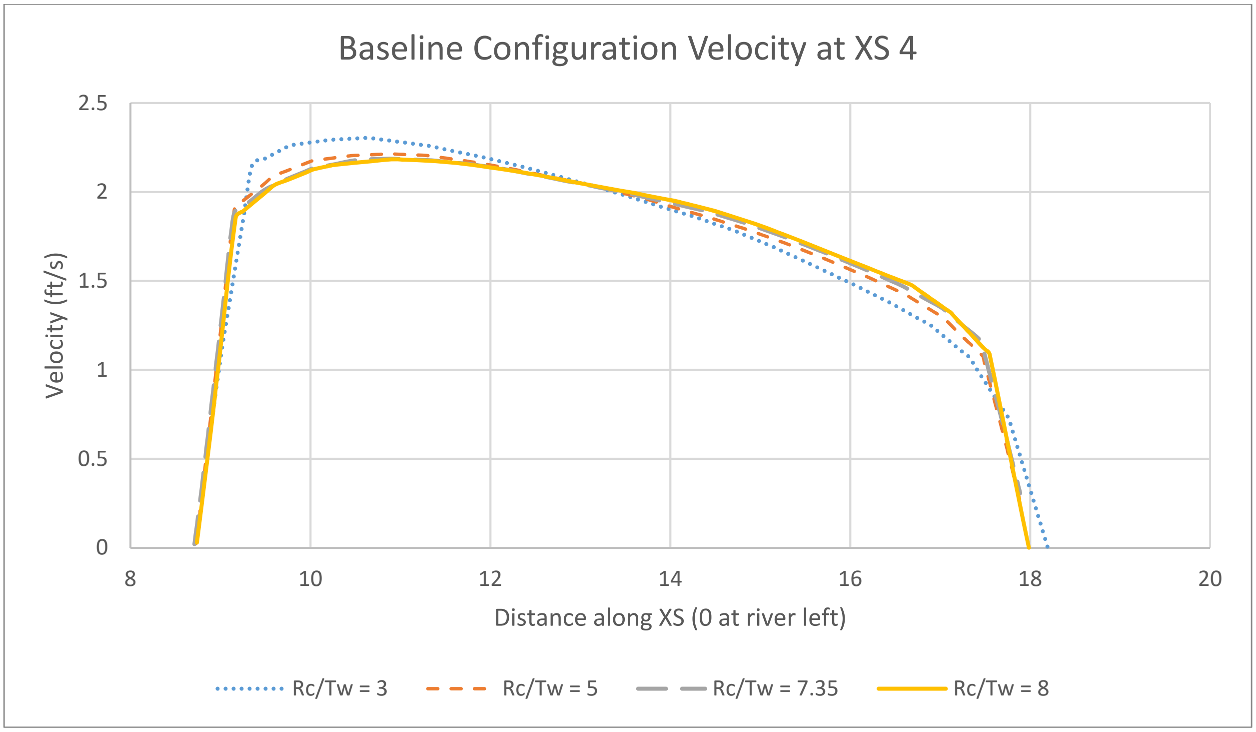

Figure 129: Velocity across XS 4 in the baseline configuration

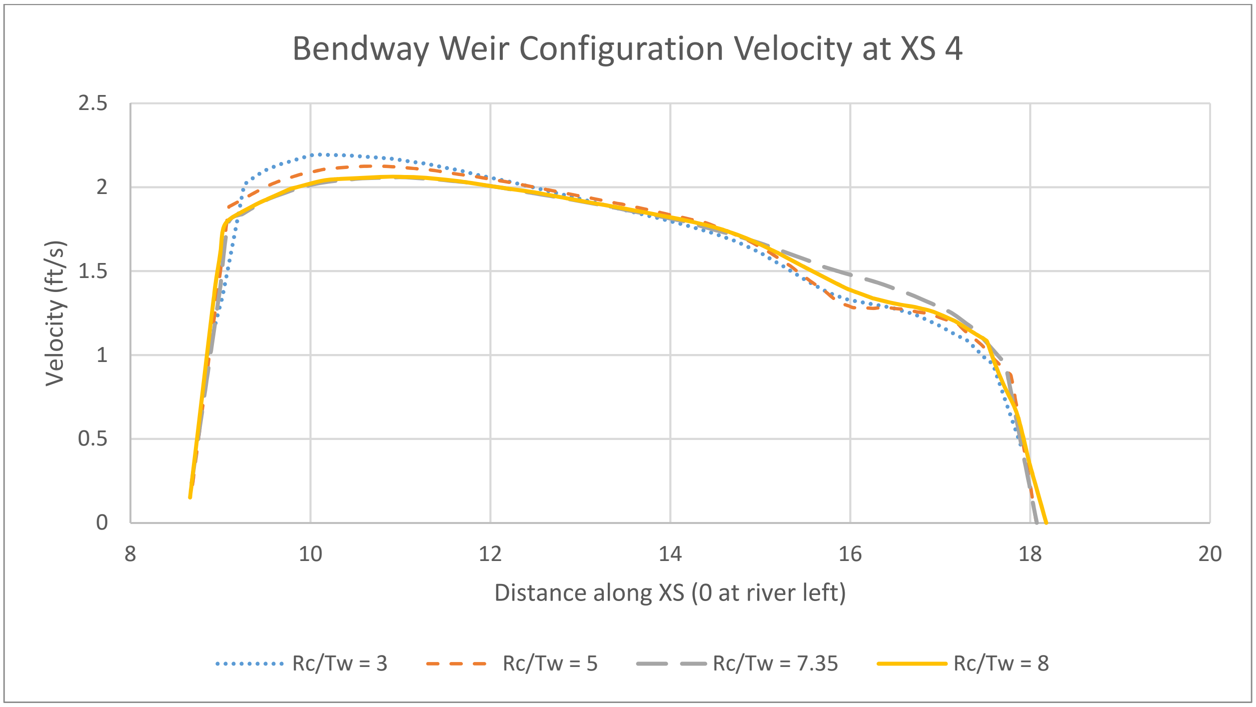

Figure 130: Velocity across XS 4 in the bendway weir configuration

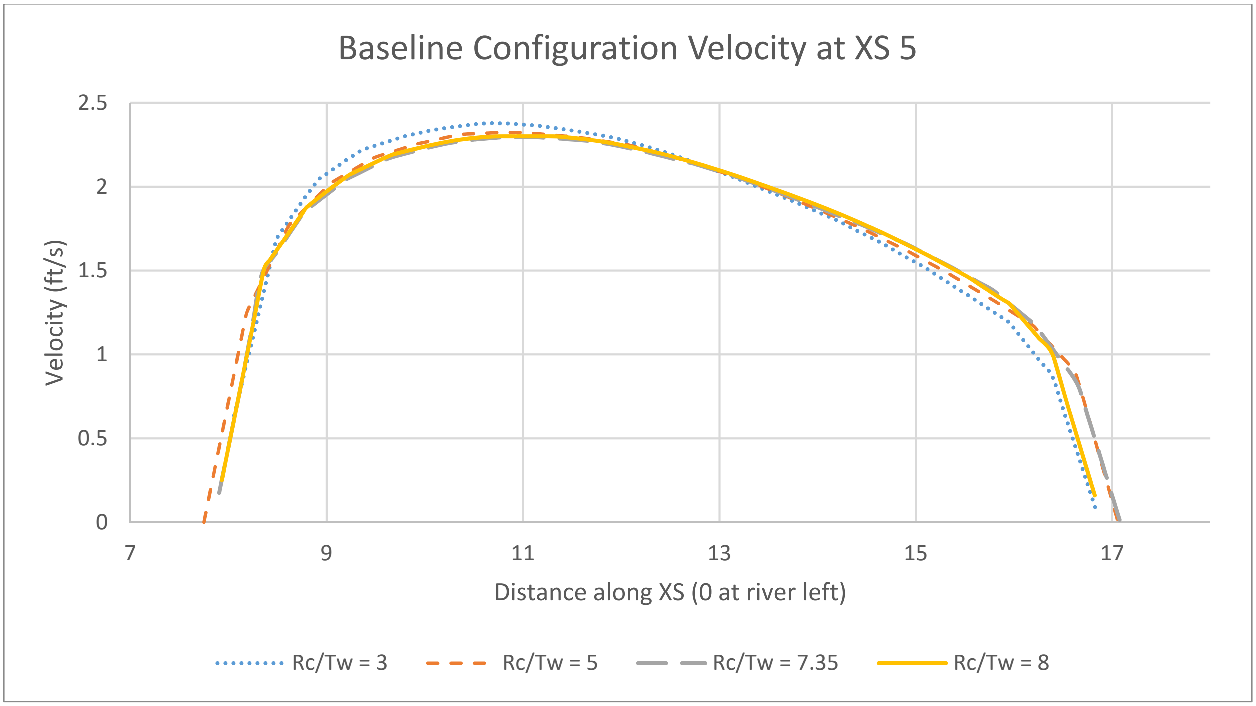

Figure 131: Velocity across XS 5 in the baseline configuration

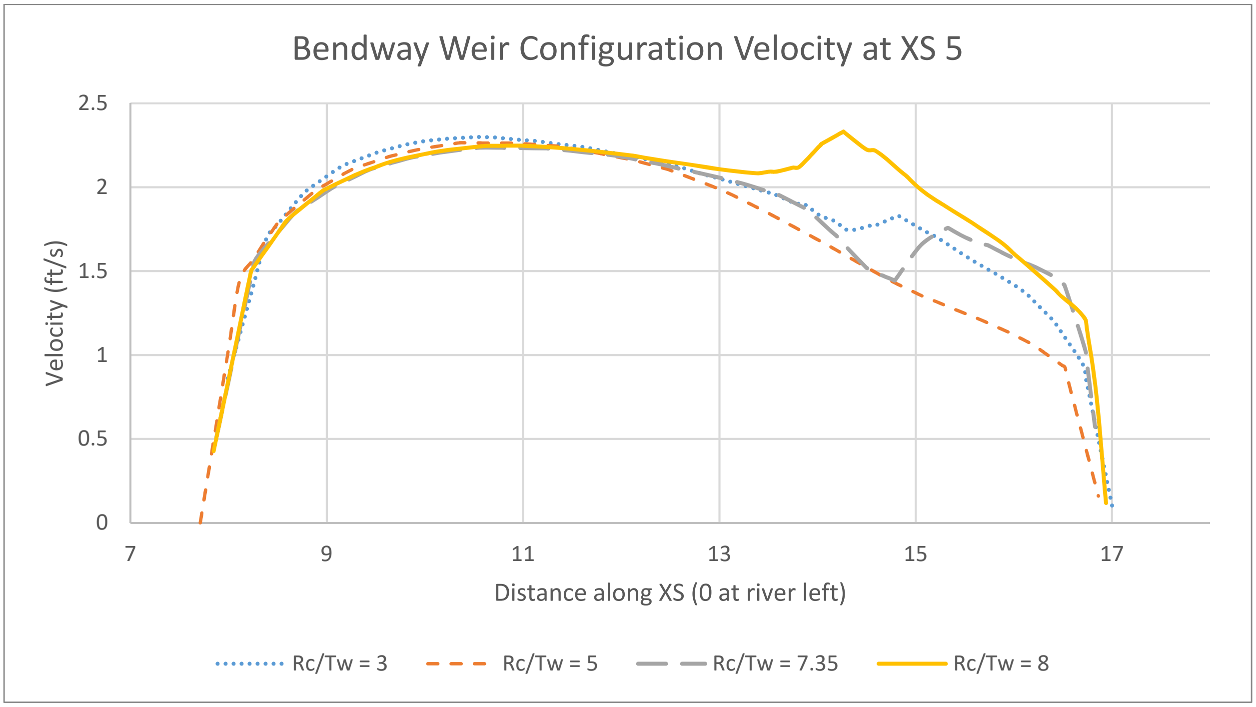

Figure 132: Velocity across XS 5 in the bendway weir configuration

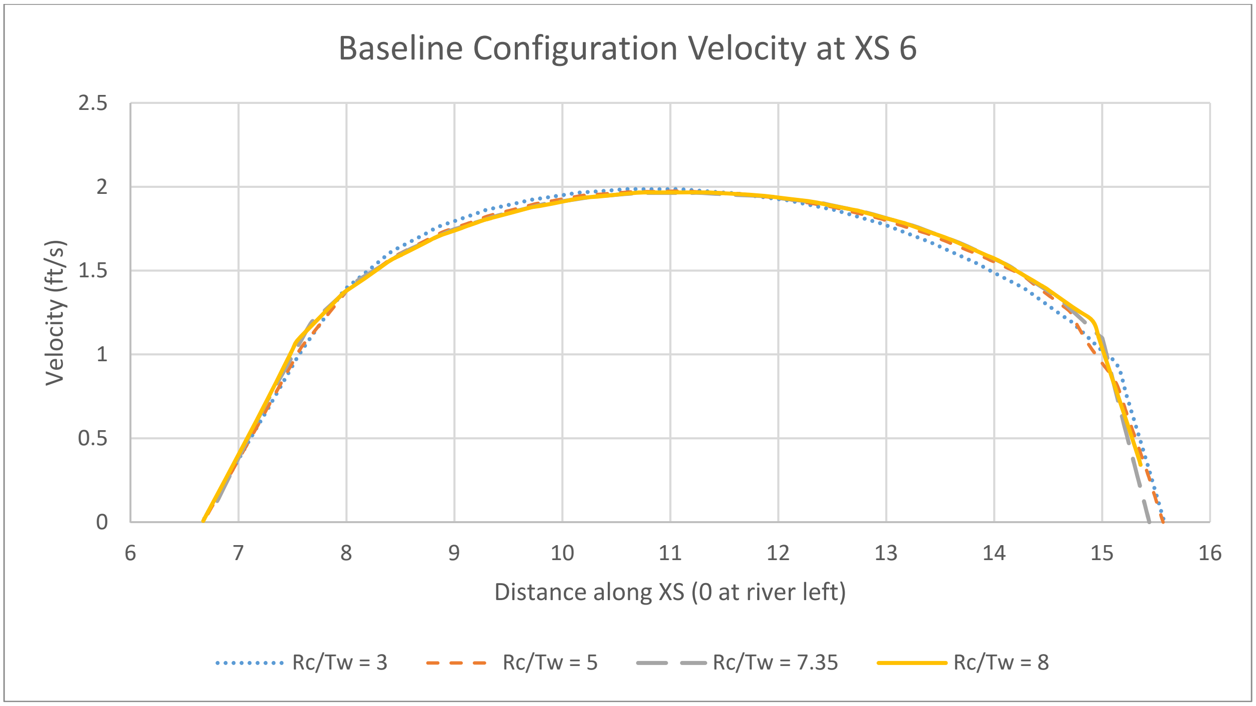

Figure 133: Velocity across XS 6 in the baseline configuration

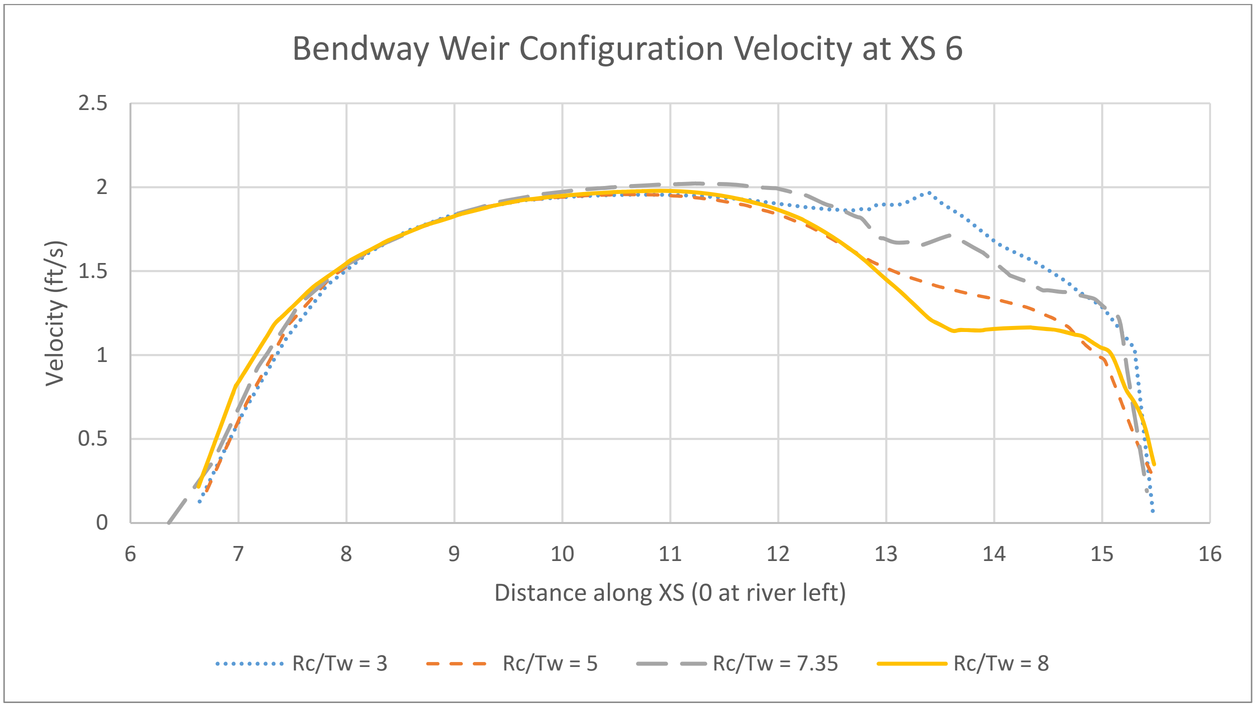

Figure 134: Velocity across XS 6 in the bendway weir configuration

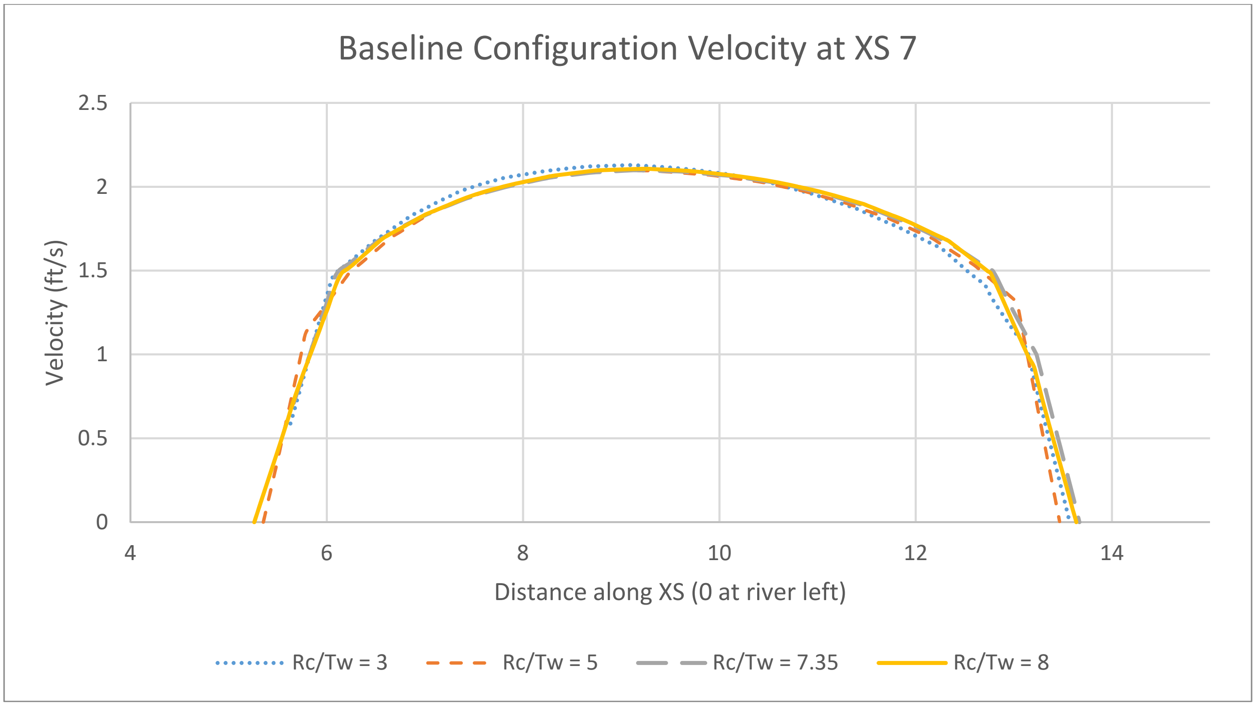

Figure 135: Velocity across XS 7 in the baseline configuration

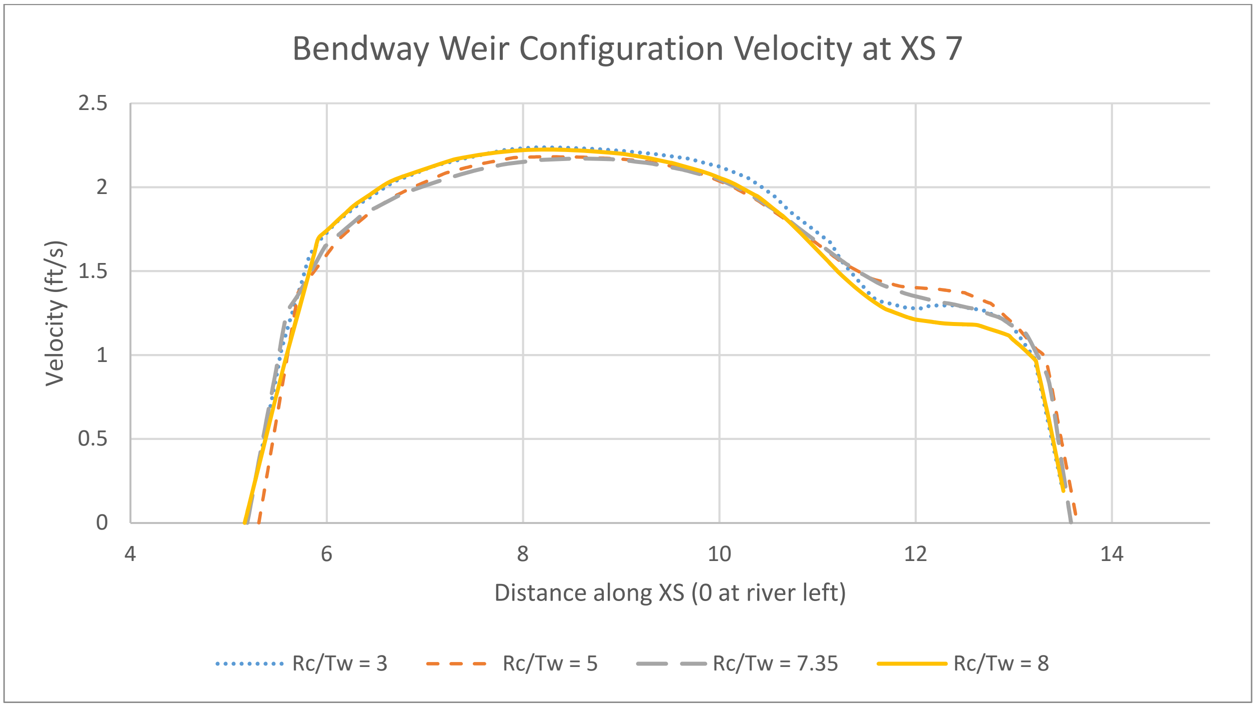

Figure 136: Velocity across XS 7 in the bendway weir configuration

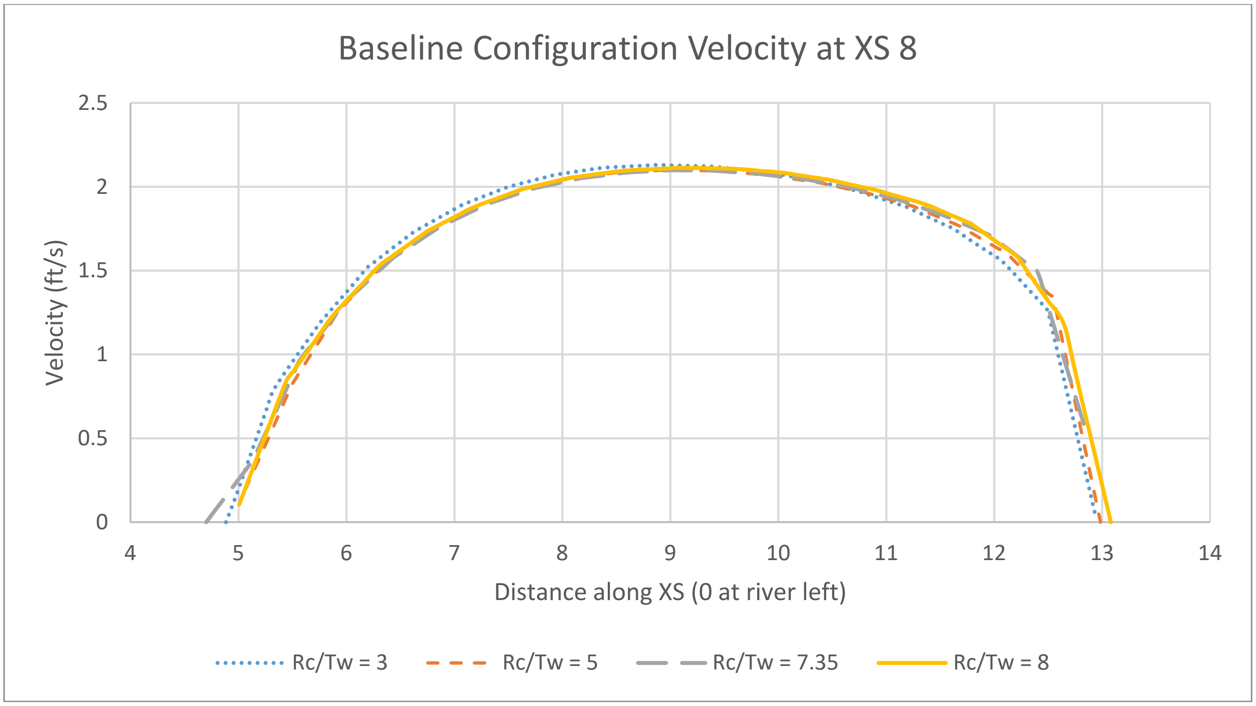

Figure 137: Velocity across XS 8 in the baseline configuration

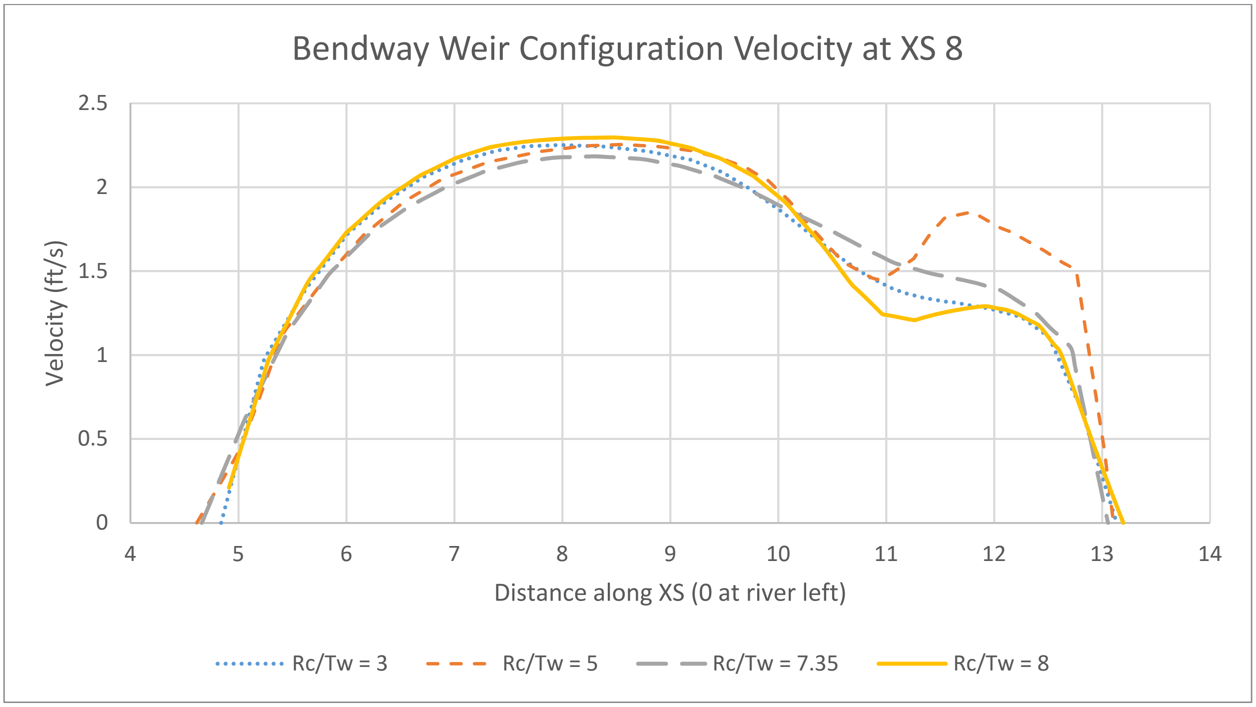

Figure 138: Velocity across XS 8 in the bendway weir configuration

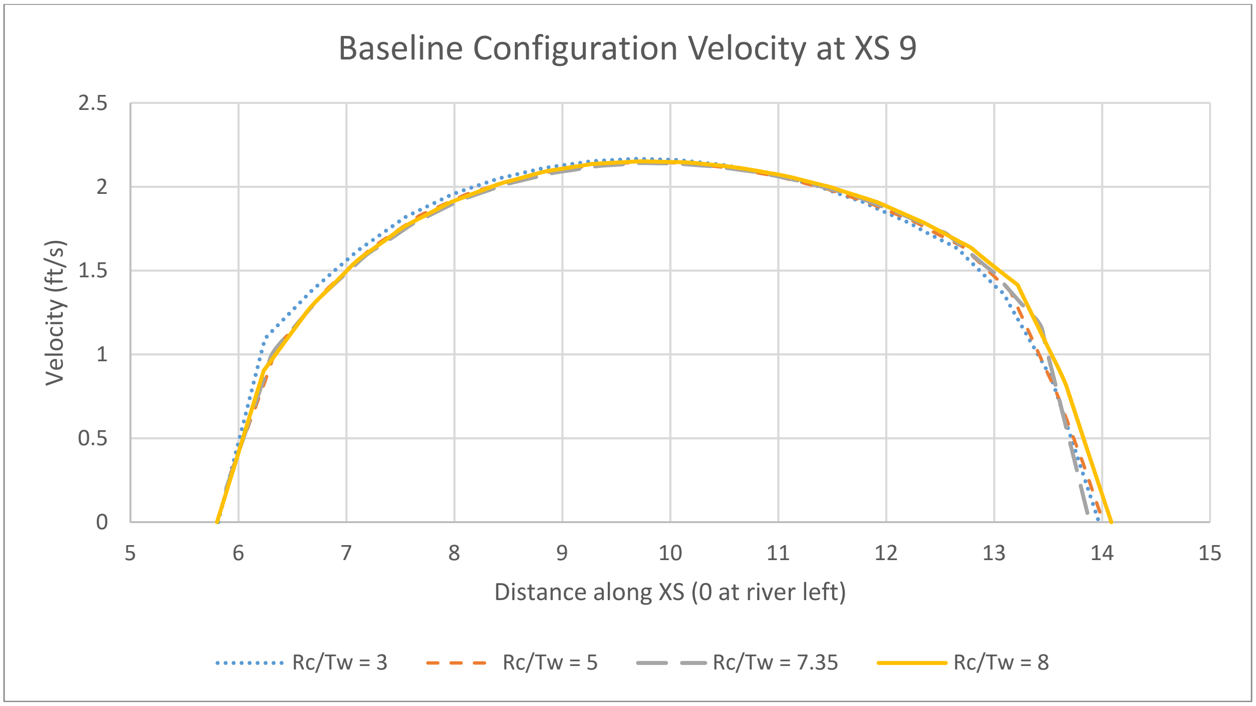

Figure 139: Velocity across XS 9 in the baseline configuration

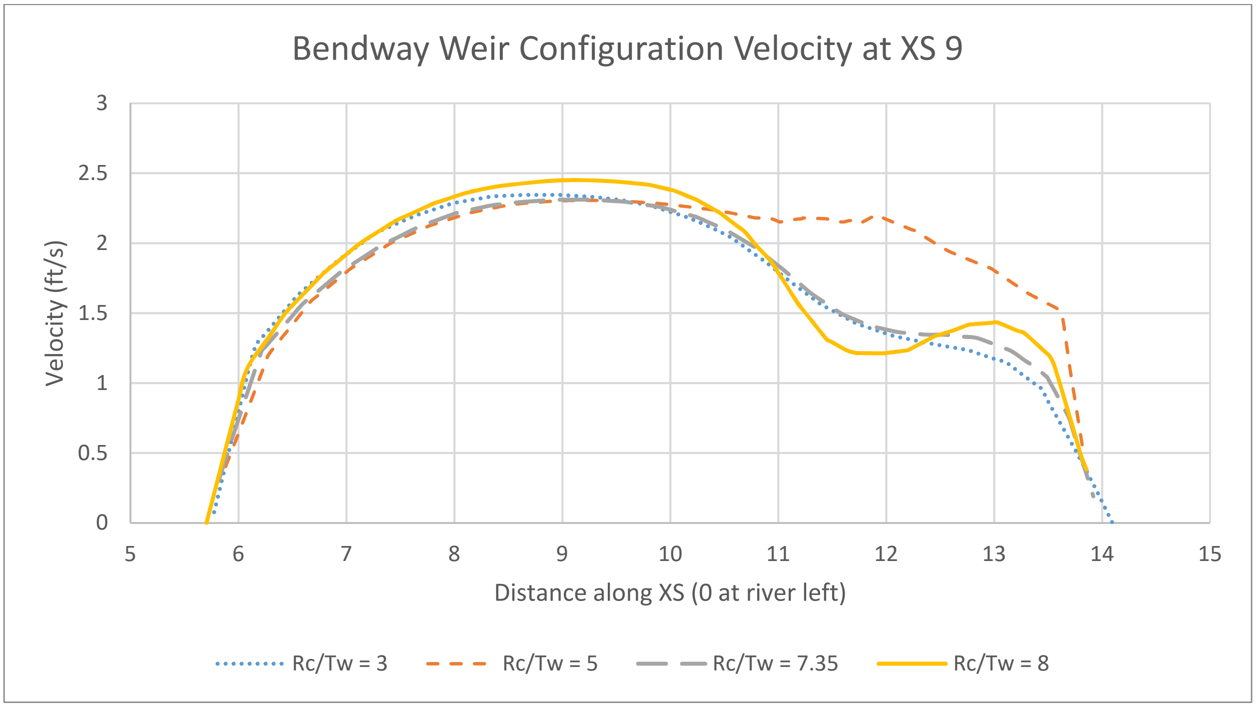

Figure 140: Velocity across XS 9 in the bendway weir configuration

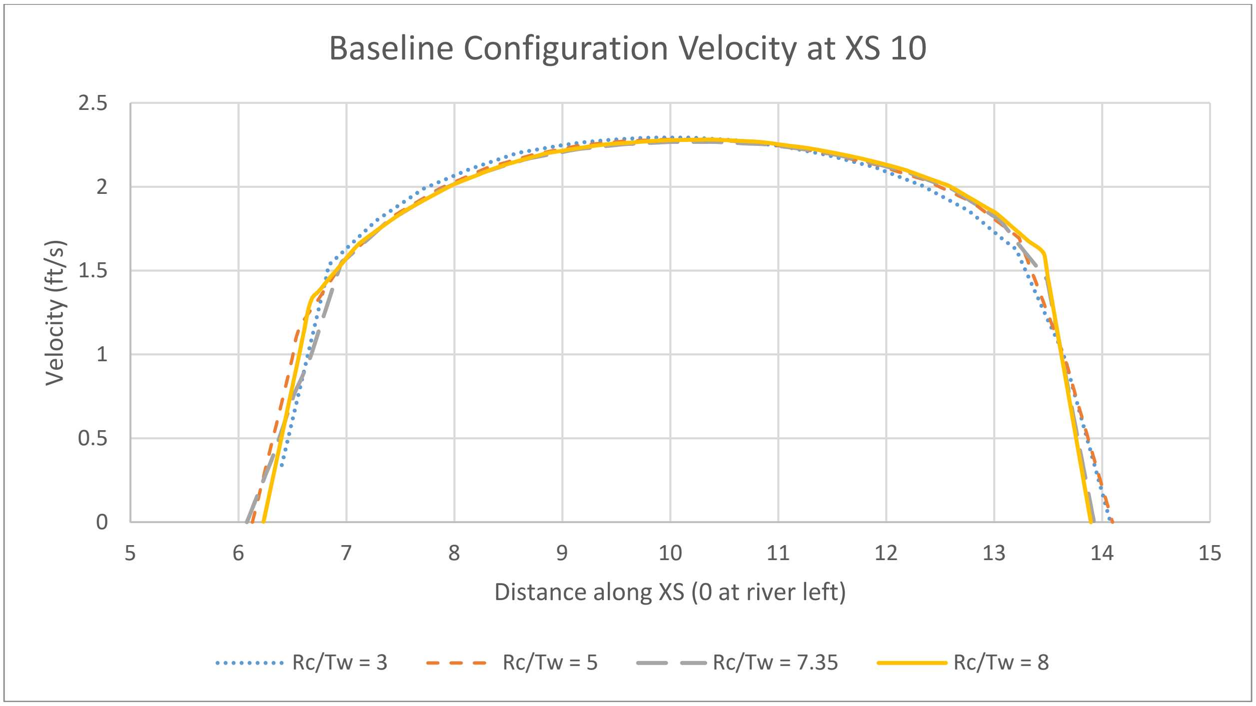

Figure 141: Velocity across XS 10 in the baseline configuration

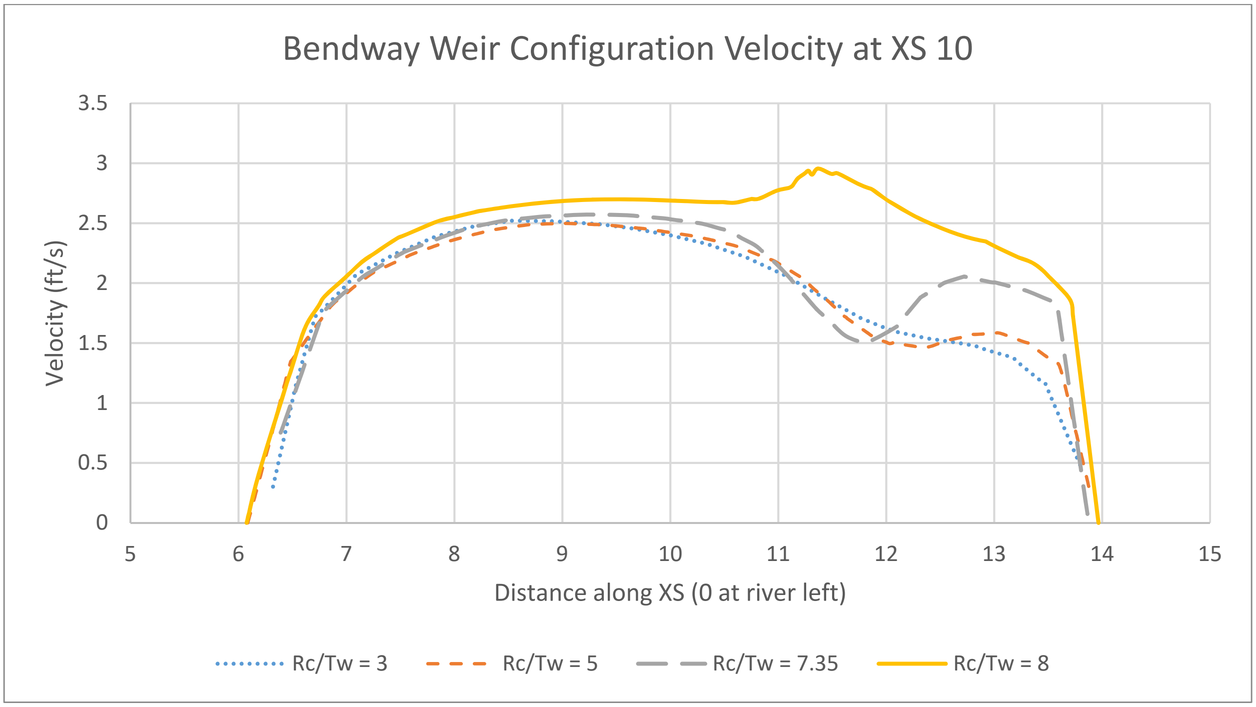

Figure 142: Velocity across XS 10 in the bendway weir configuration

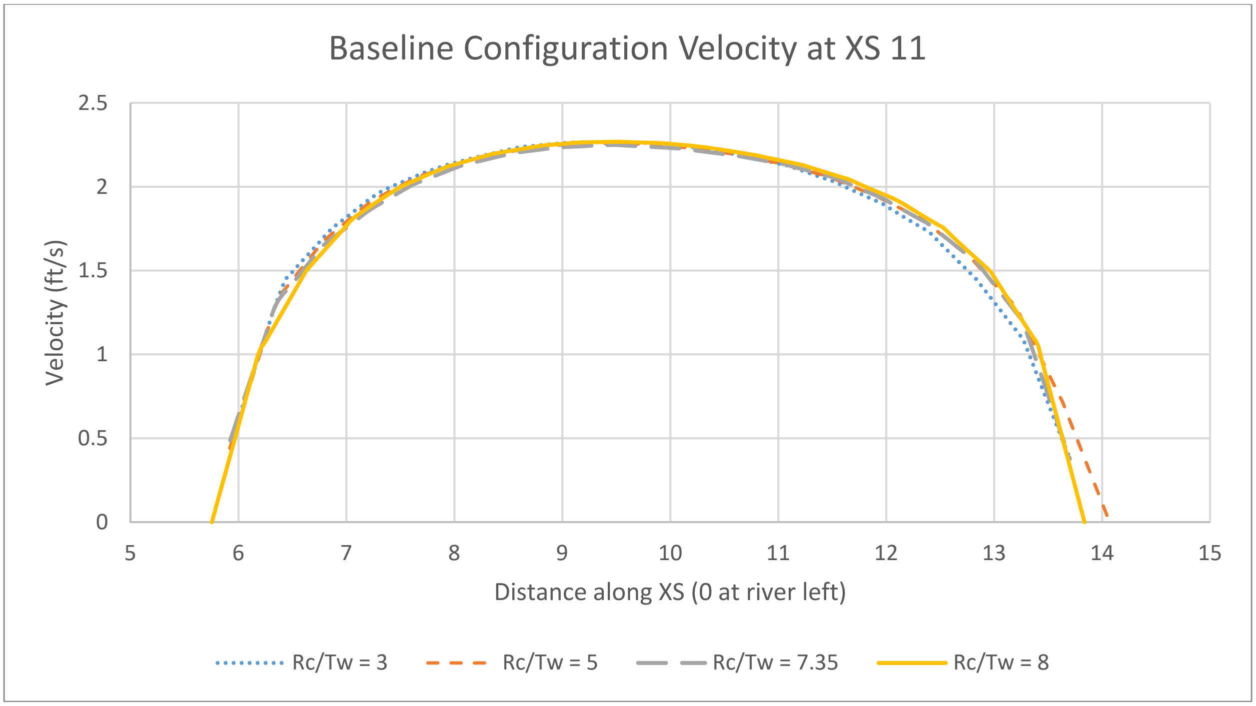

Figure 143: Velocity across XS 11 in the baseline configuration

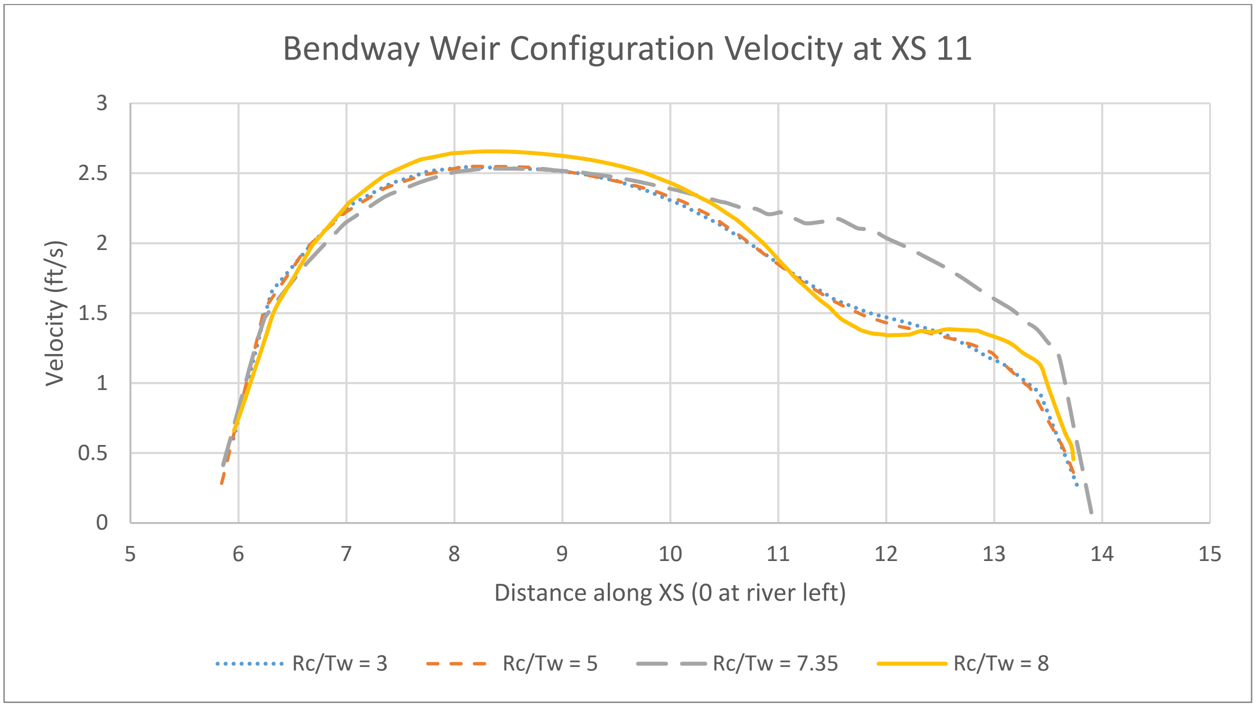

Figure 144: Velocity across XS 11 in the bendway weir configuration

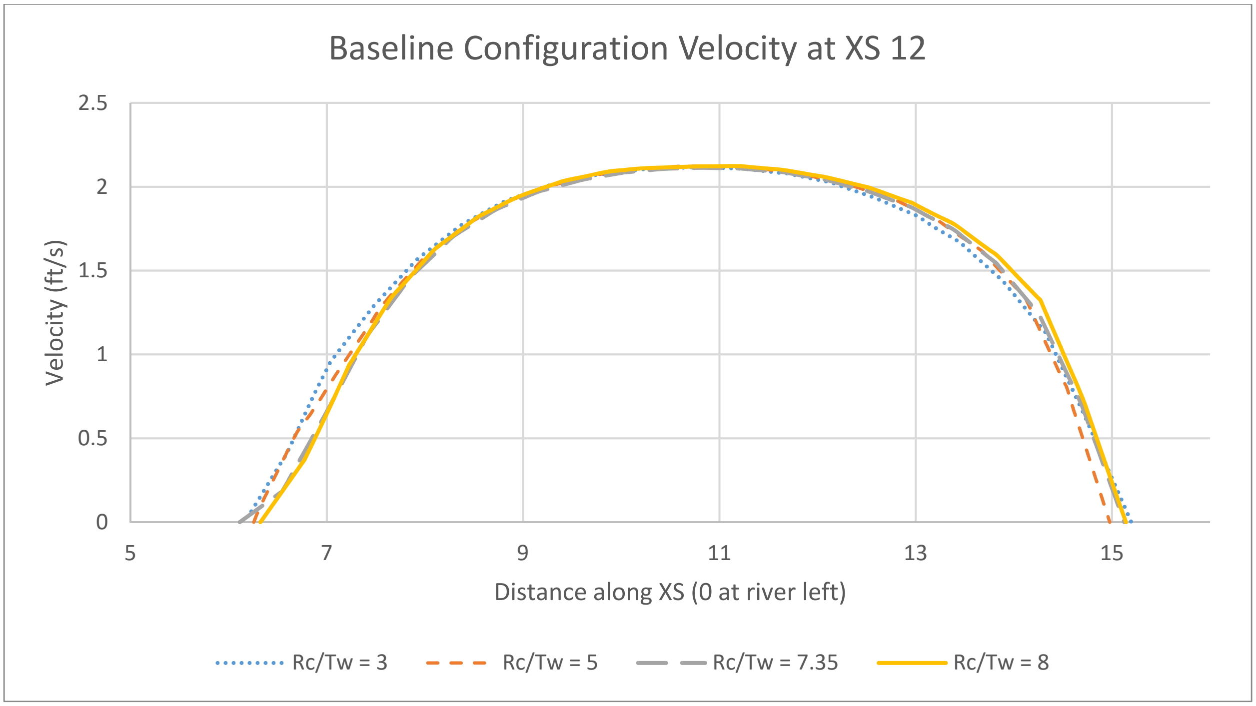

Figure 145: Velocity across XS 12 in the baseline configuration

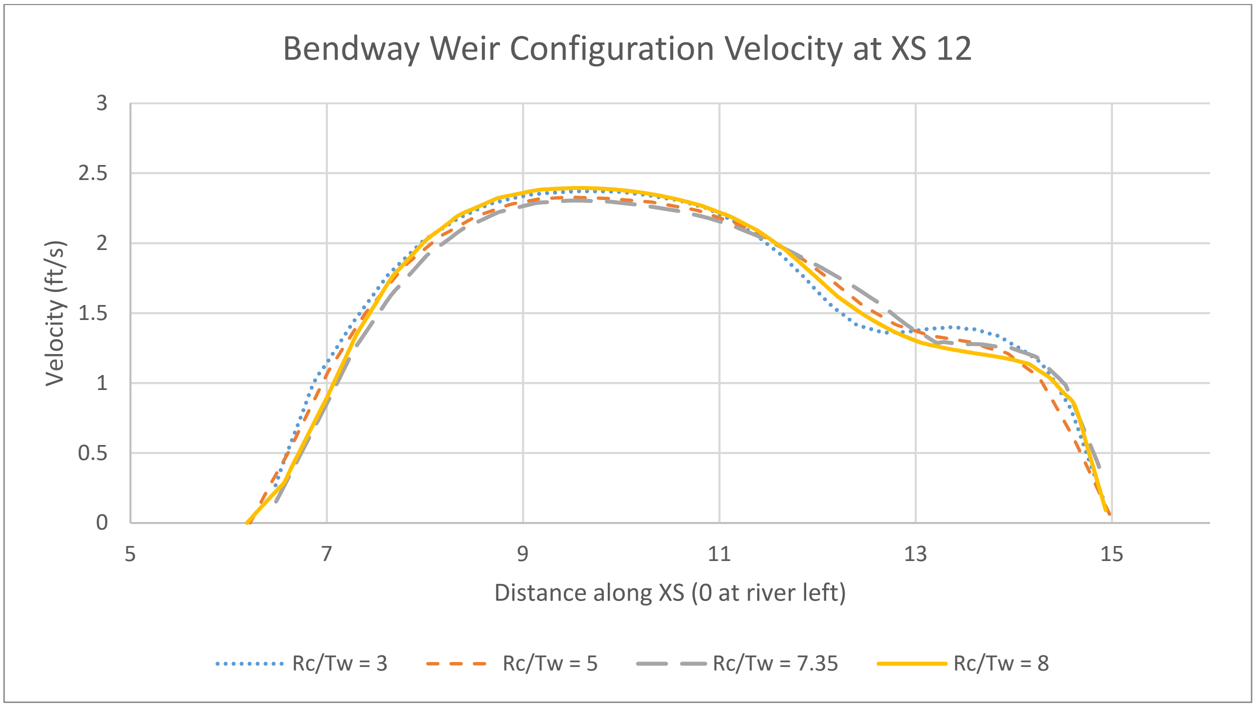

Figure 146: Velocity across XS 12 in the bendway weir configuration

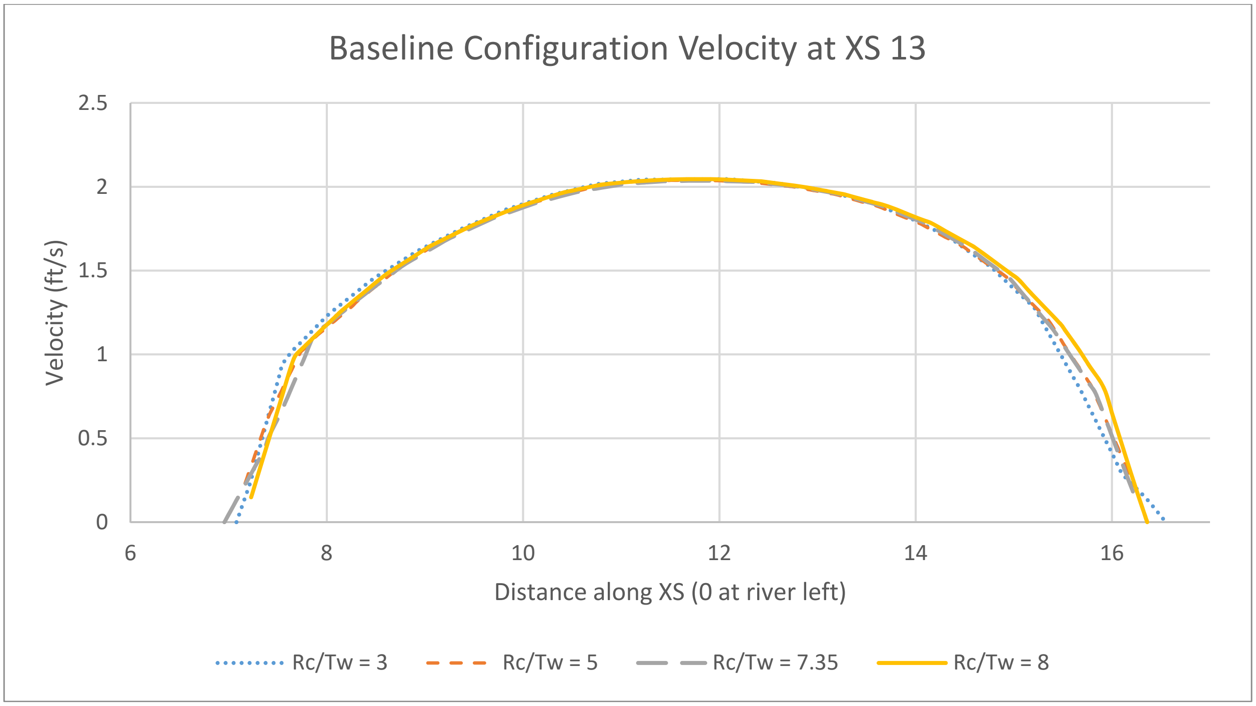

Figure 147: Velocity across XS 13 in the baseline configuration

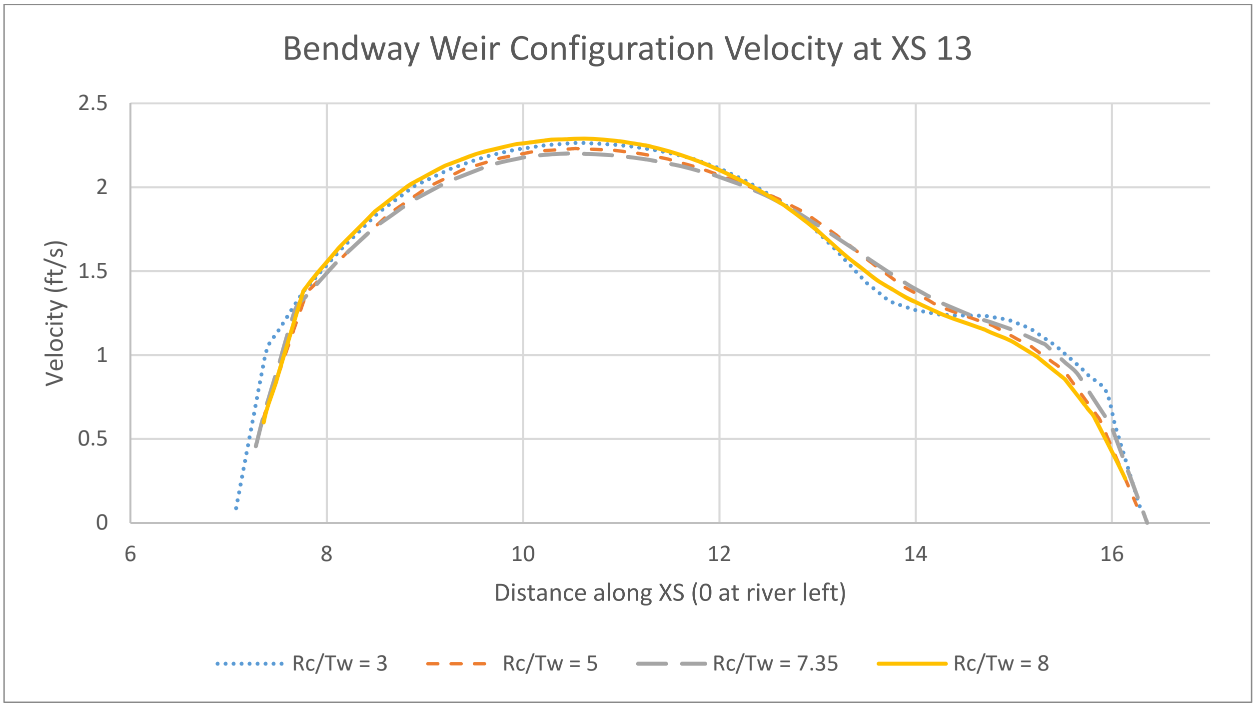

Figure 148: Velocity across XS 13 in the bendway weir configuration

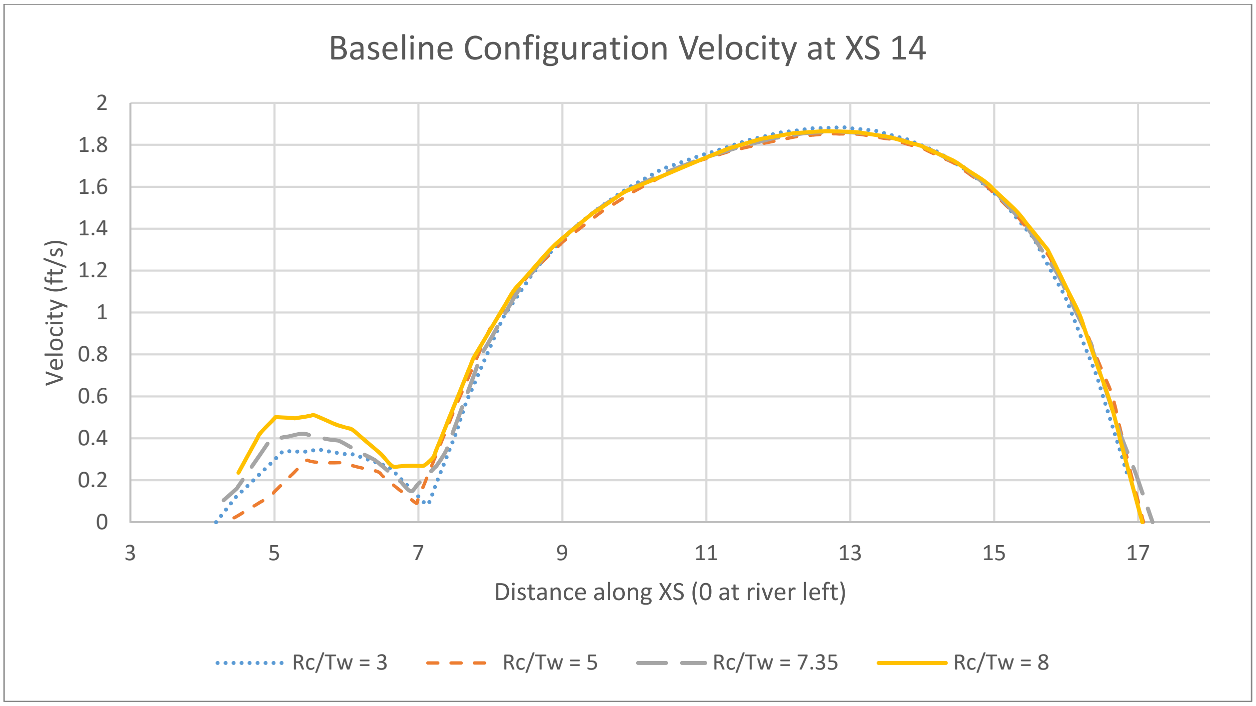

Figure 149: Velocity across XS 14 in the baseline configuration

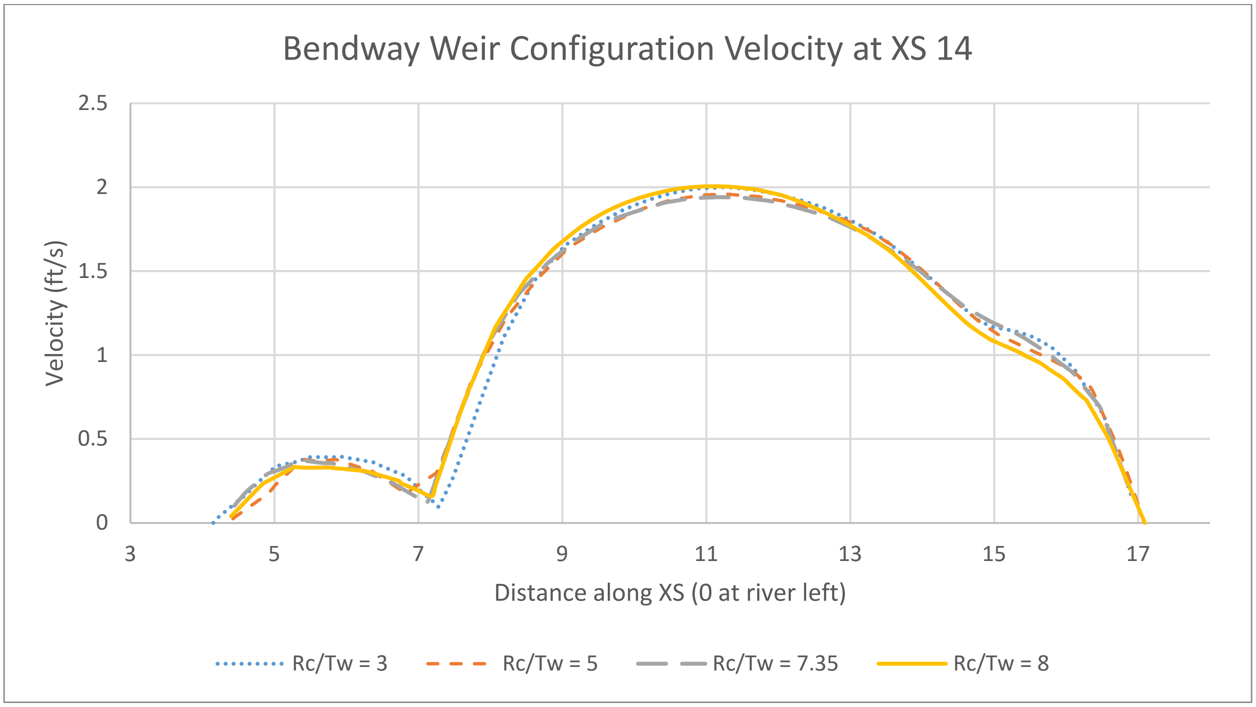

Figure 150: Velocity across XS 14 in the bendway weir configuration

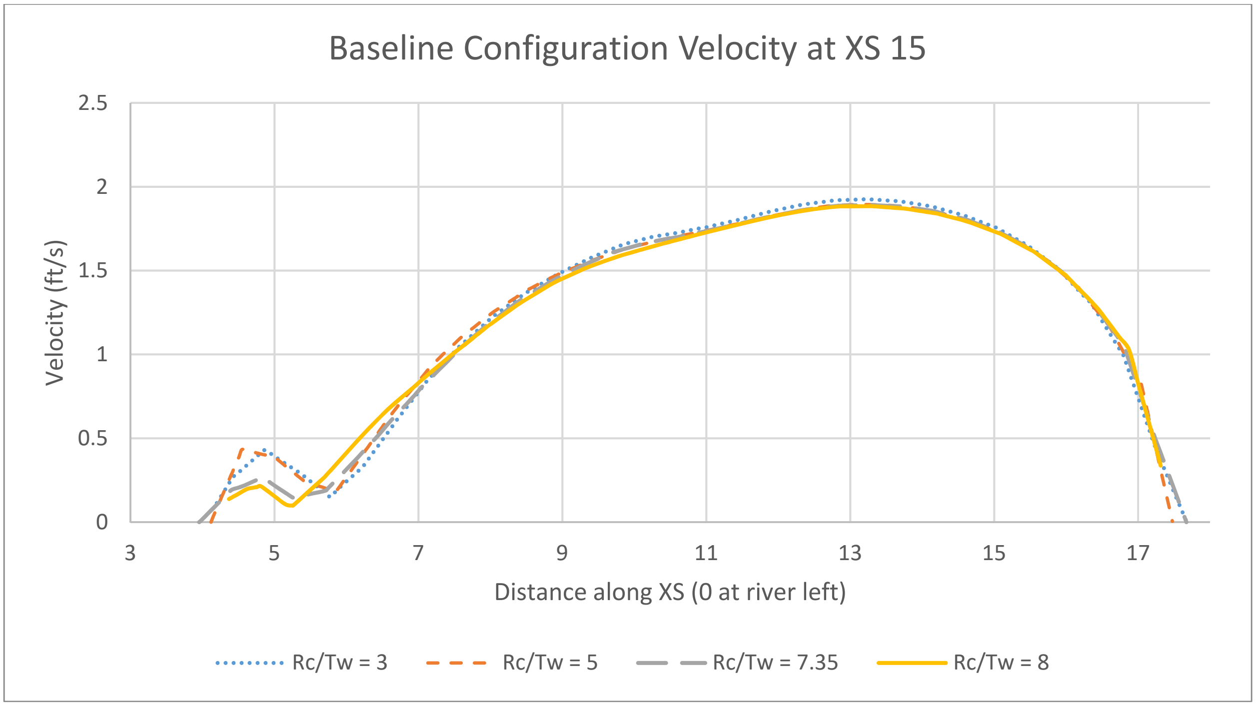

Figure 151: Velocity across XS 15 in the baseline configuration

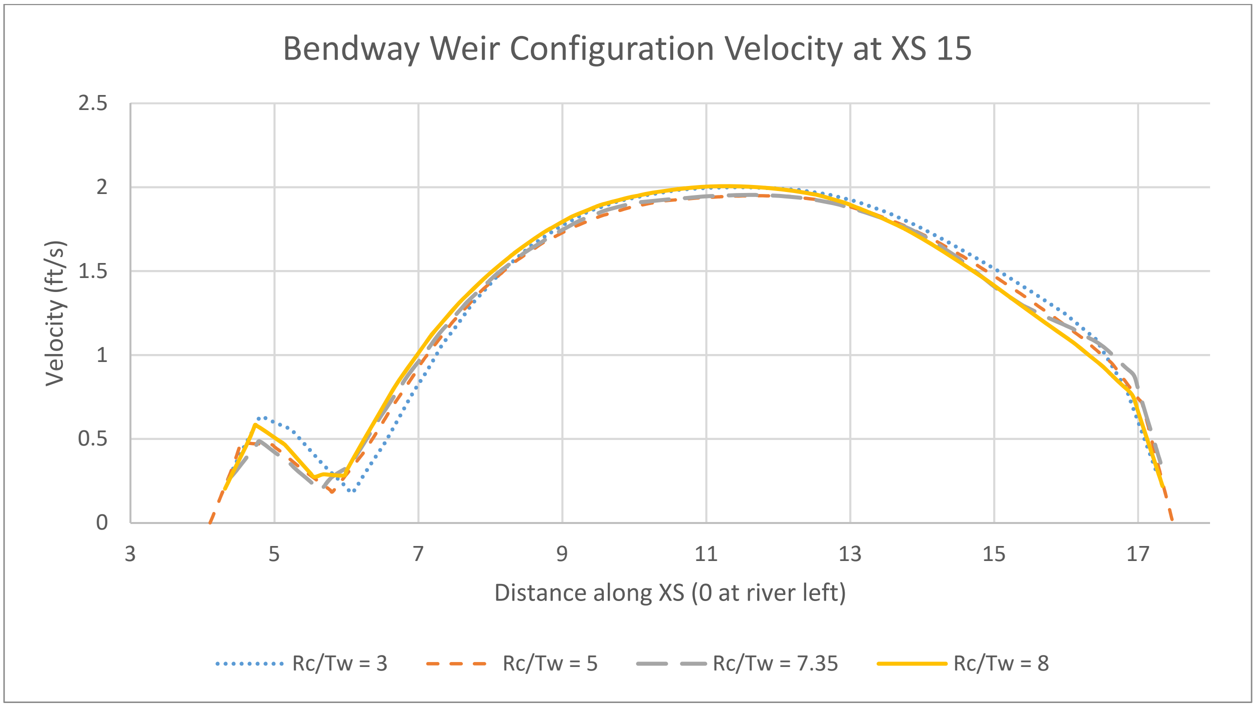

Figure 152: Velocity across XS 15 in the bendway weir configuration

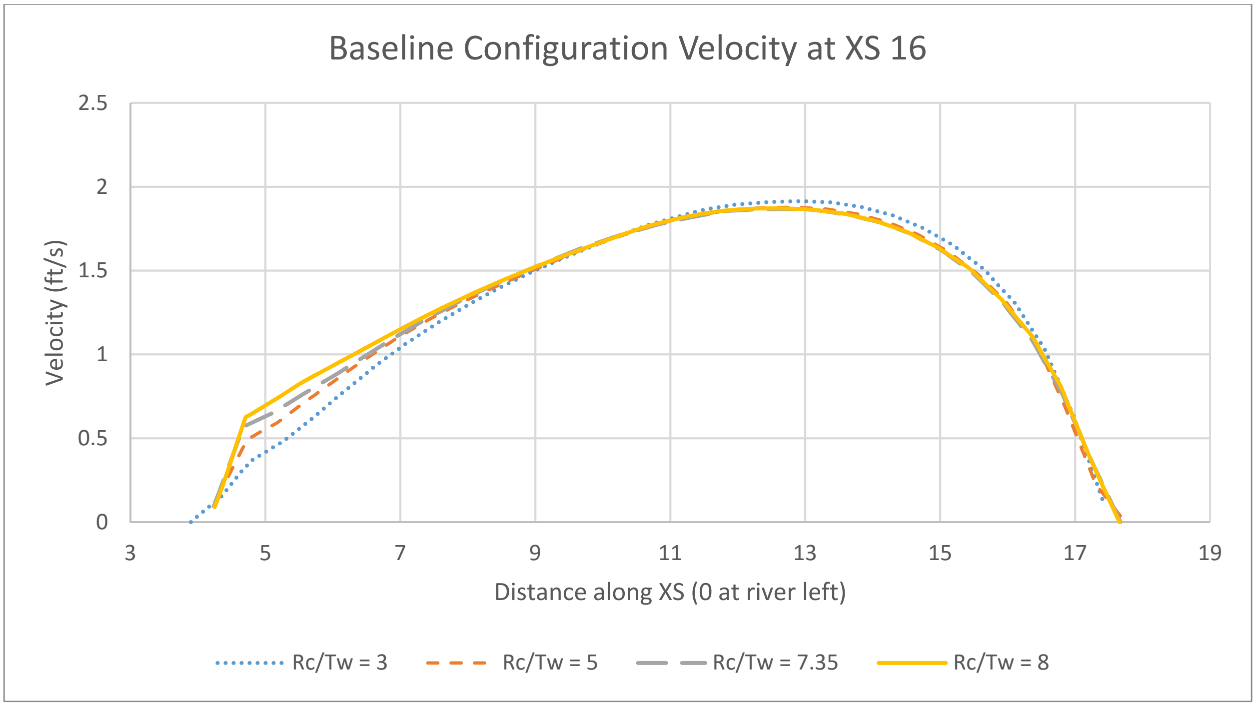

Figure 153: Velocity across XS 16 in the baseline configuration

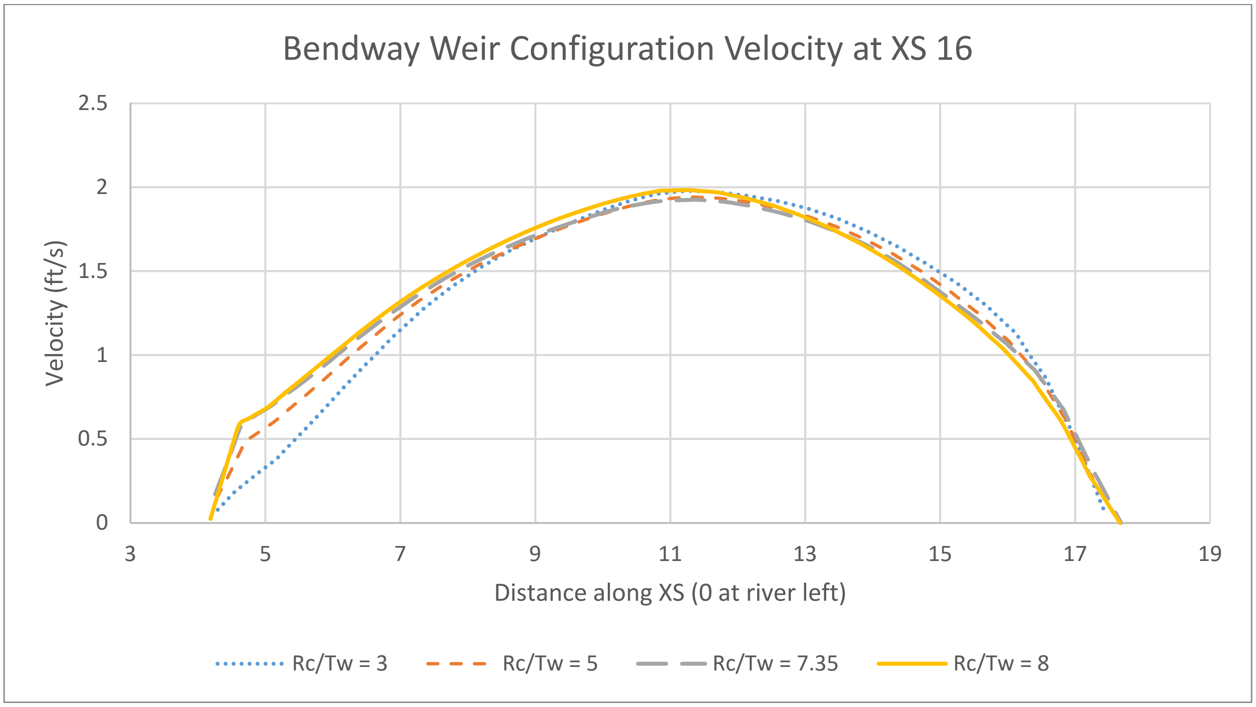

Figure 154: Velocity across XS 16 in the bendway weir configuration

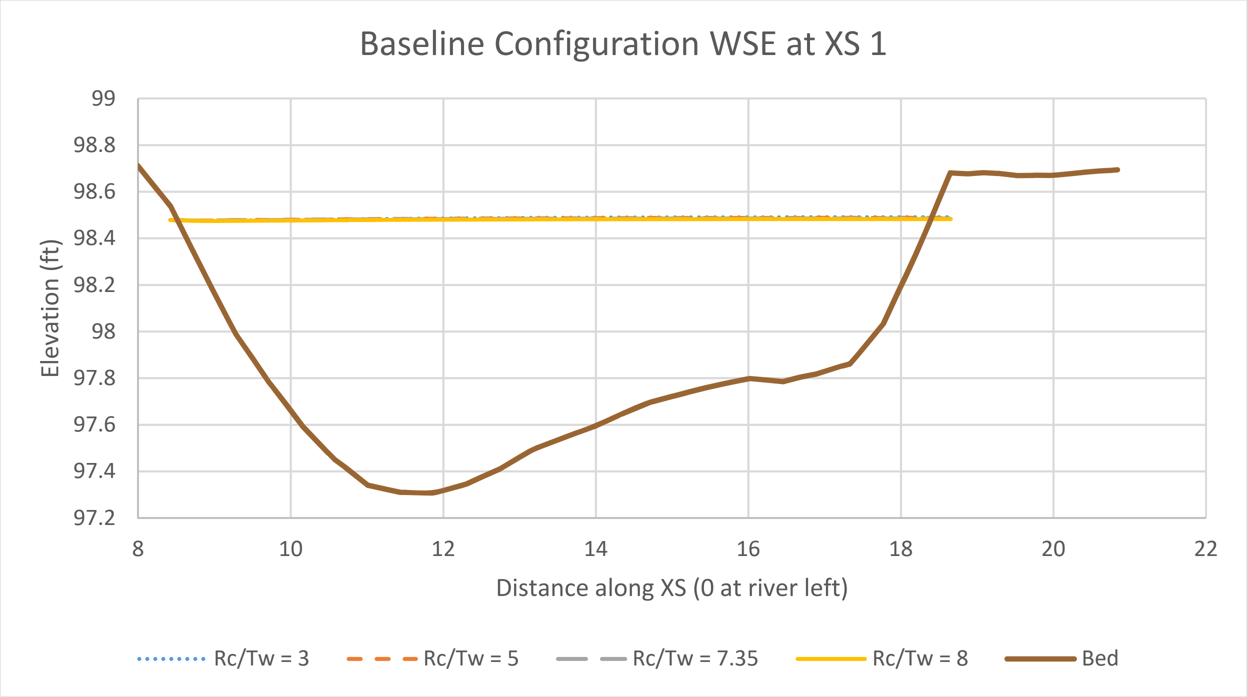

Figure 155: WSE across XS 1 in the baseline configuration

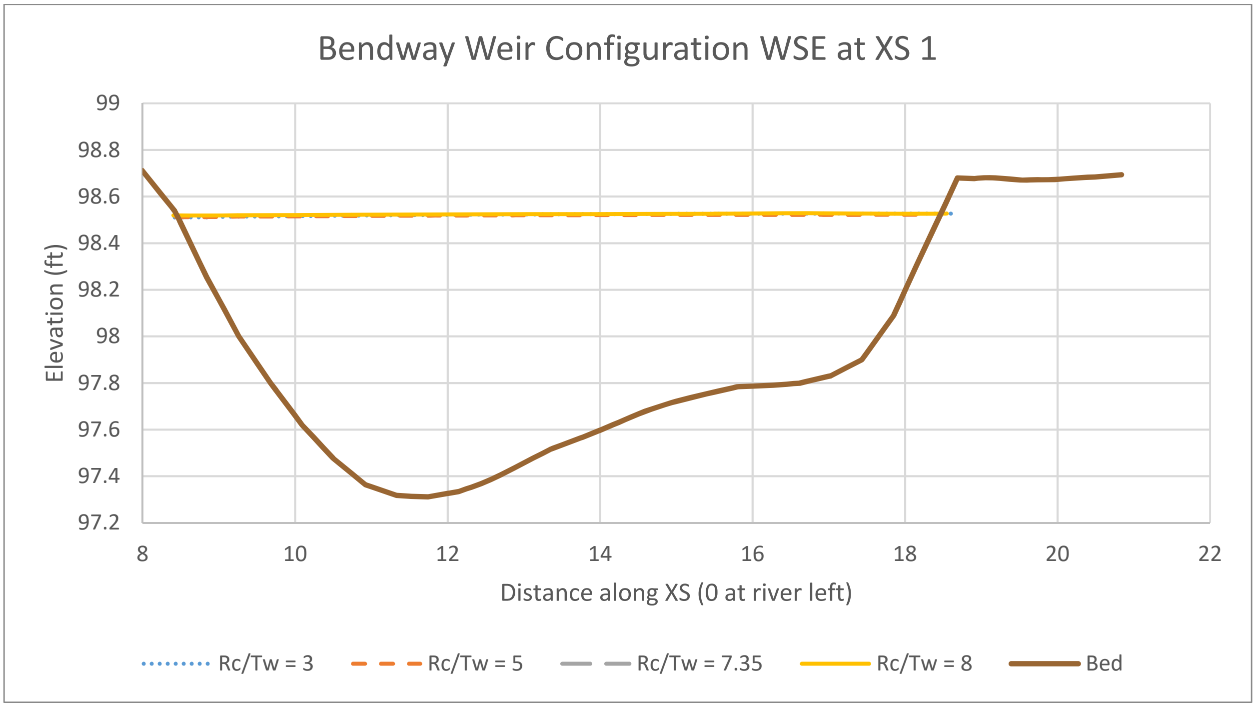

Figure 156: WSE across XS 1 in the bendway weir configuration

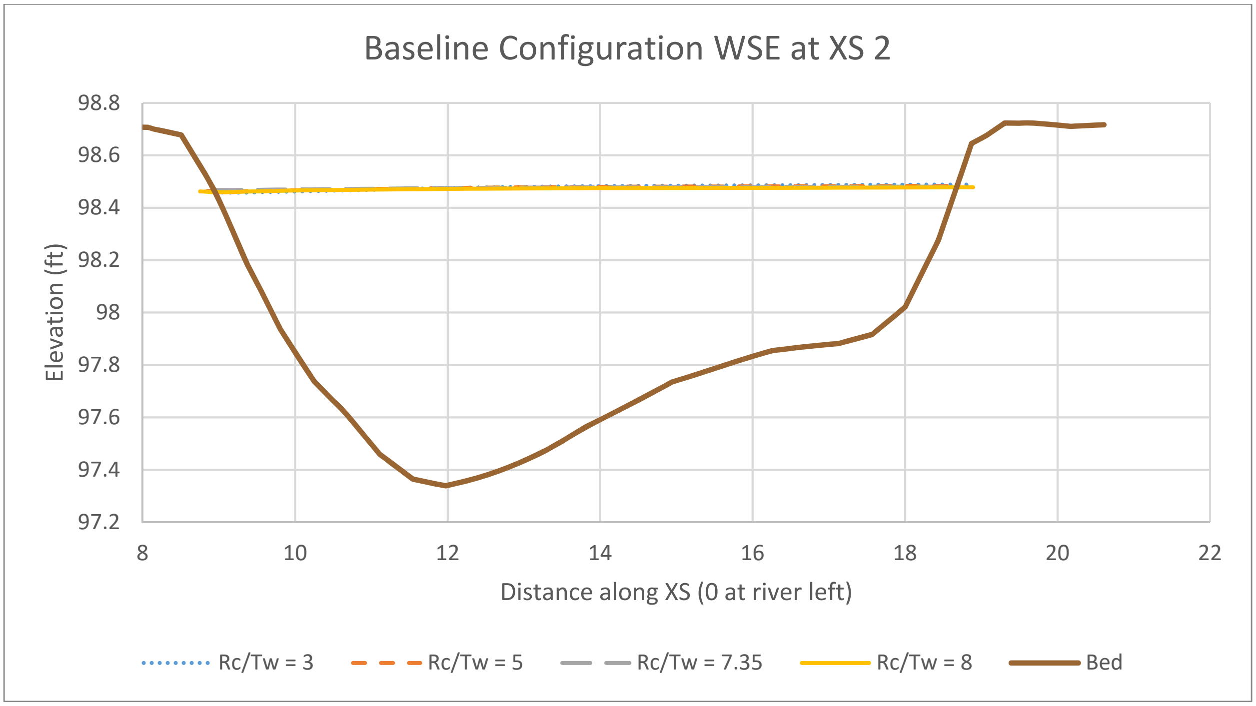

Figure 157: WSE across XS 2 in the baseline configuration

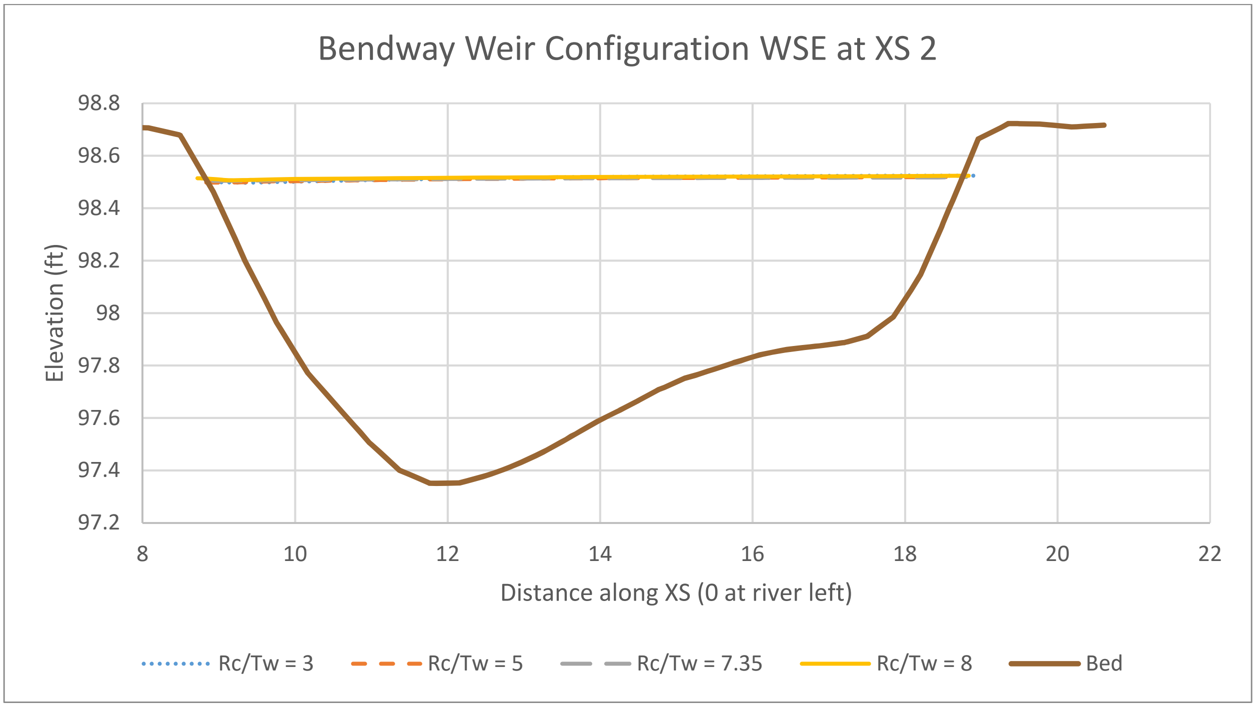

Figure 158: WSE across XS 2 in the bendway weir configuration

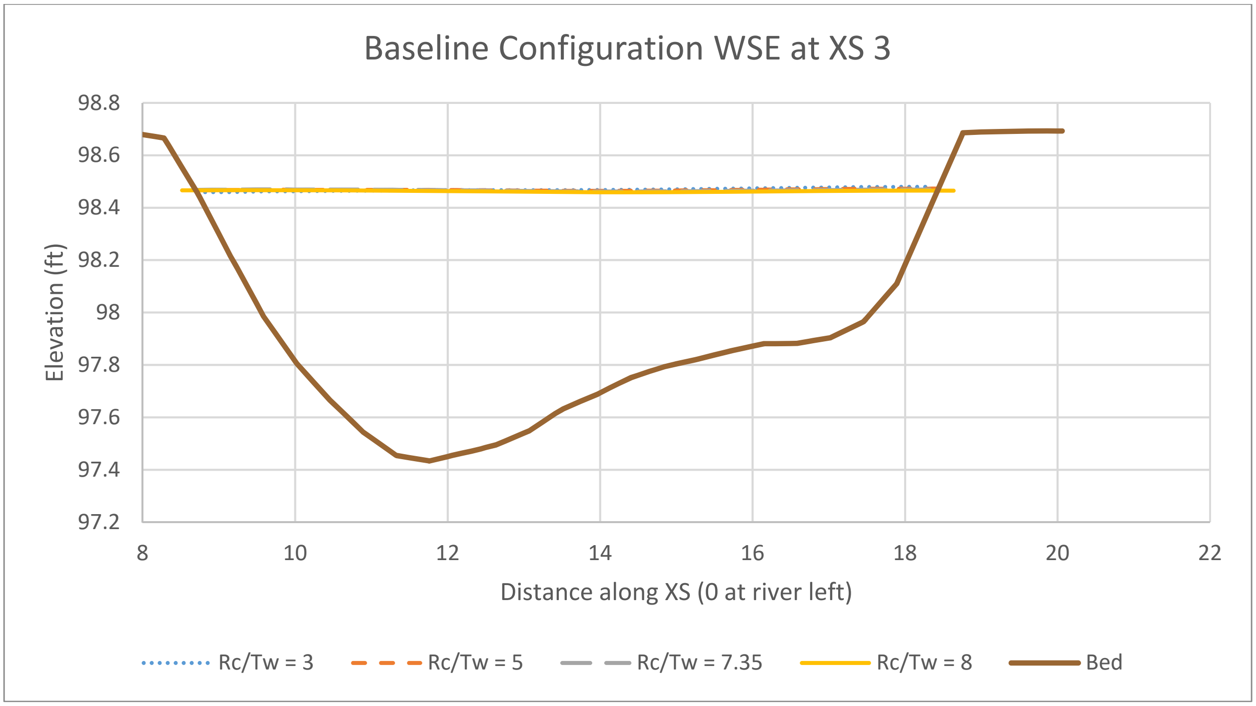

Figure 159: WSE across XS 3 in the baseline configuration

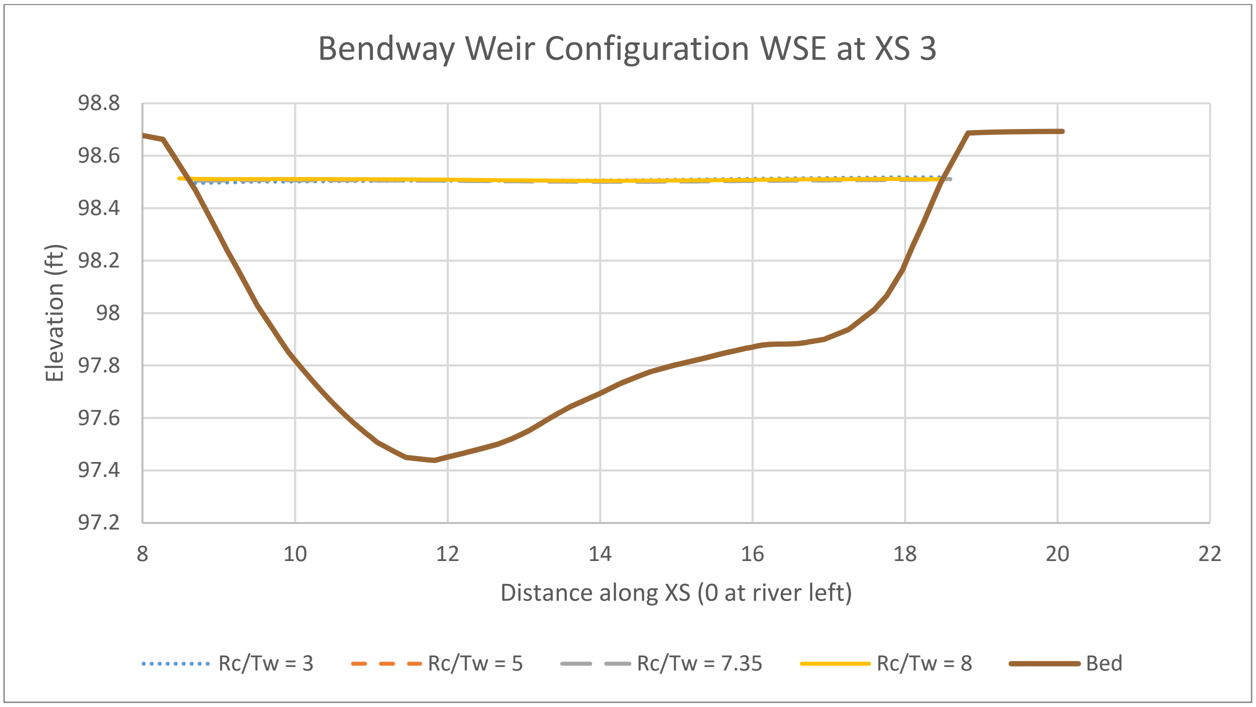

Figure 160: WSE across XS 3 in the bendway weir configuration

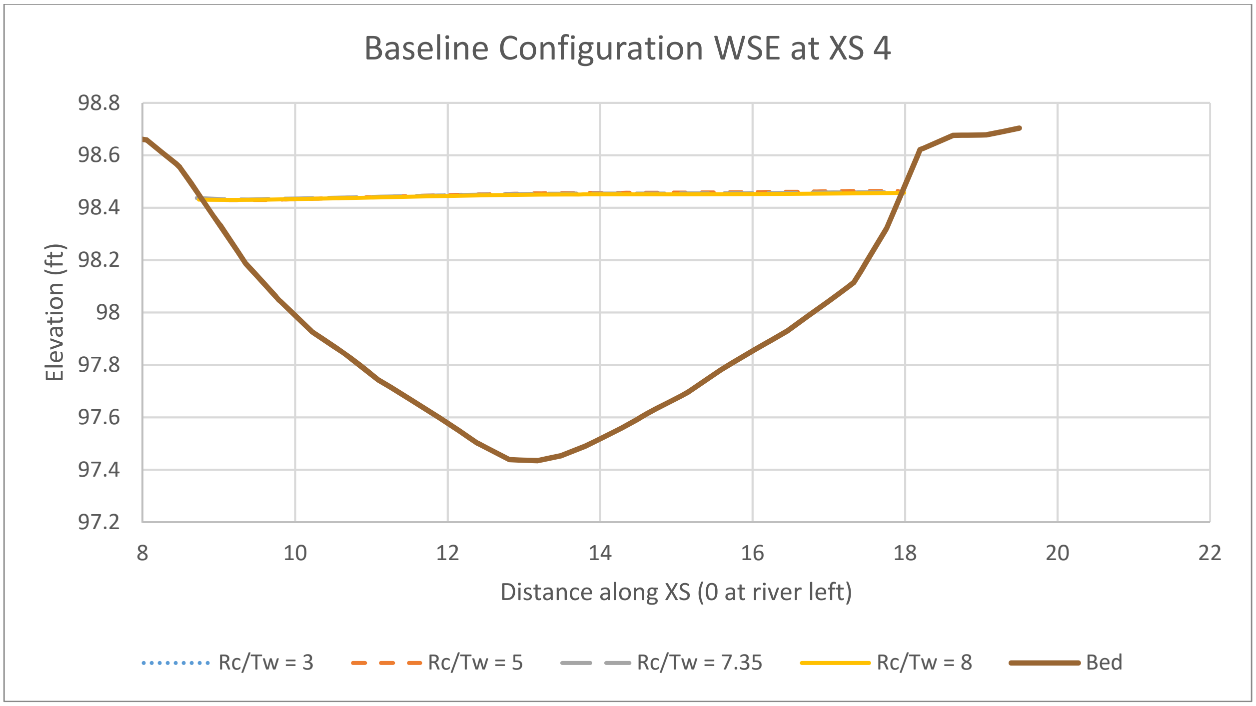

Figure 161: WSE across XS 4 in the baseline configuration

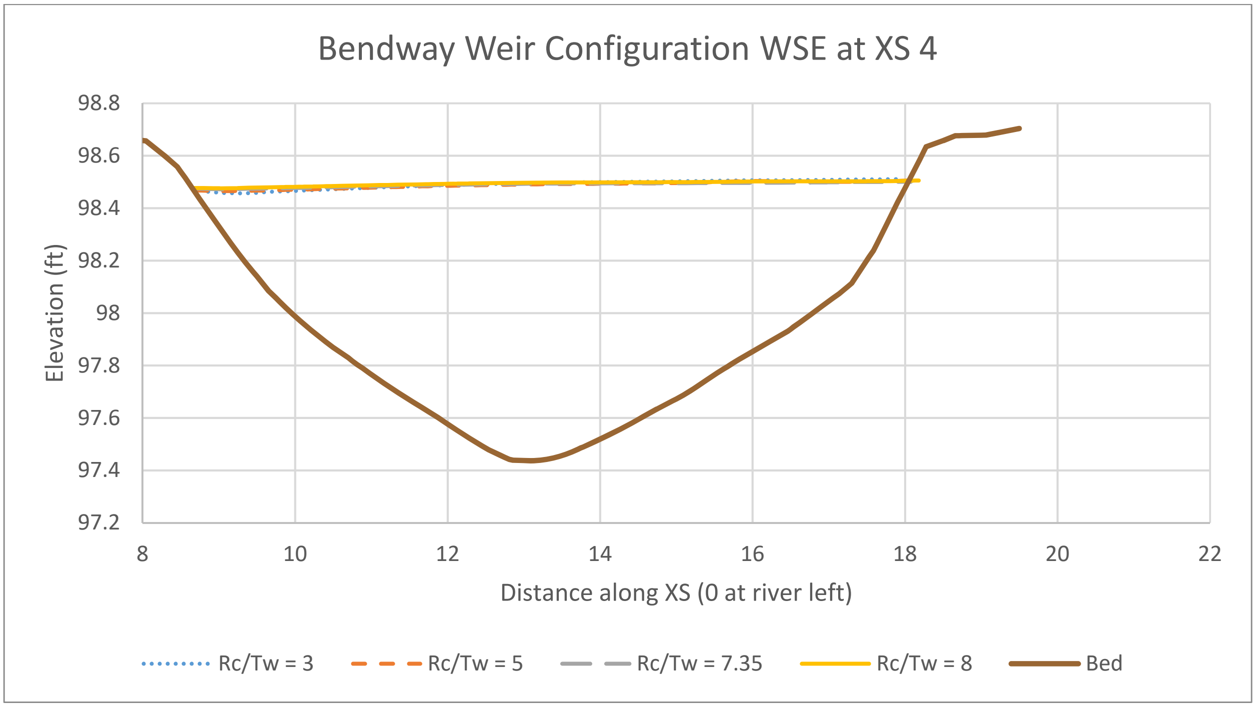

Figure 162: WSE across XS 4 in the bendway weir configuration

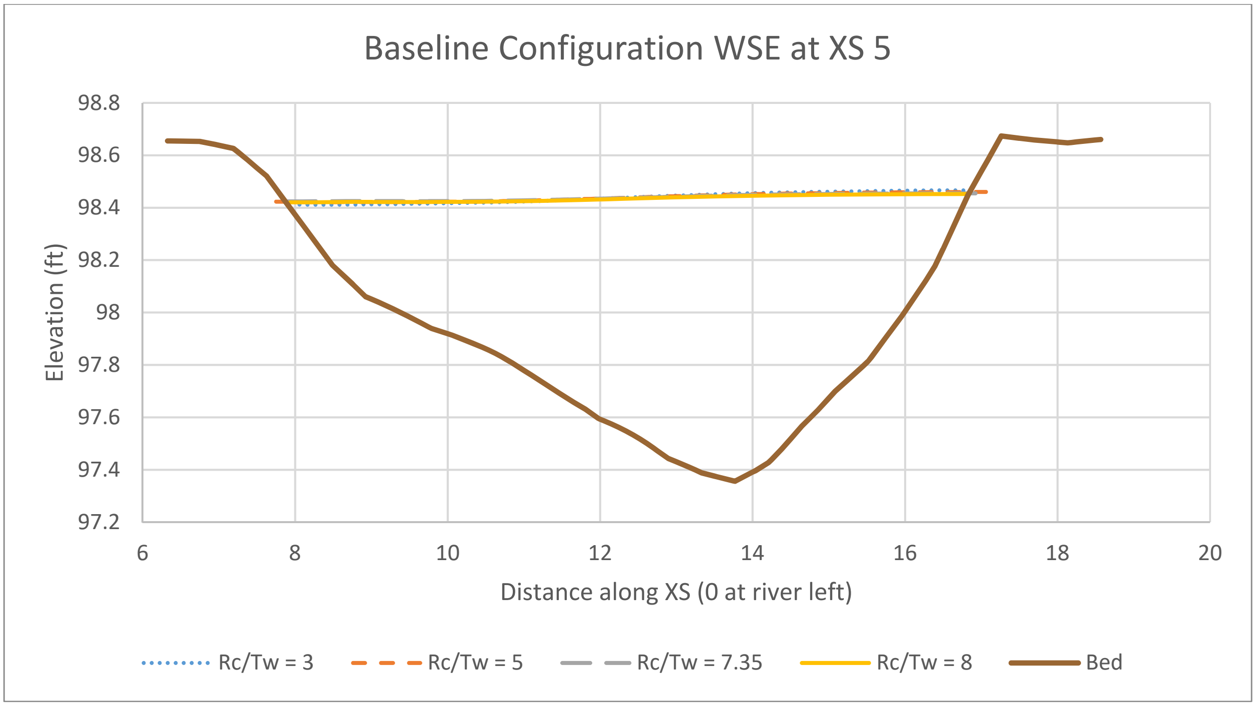

Figure 163: WSE across XS 5 in the baseline configuration

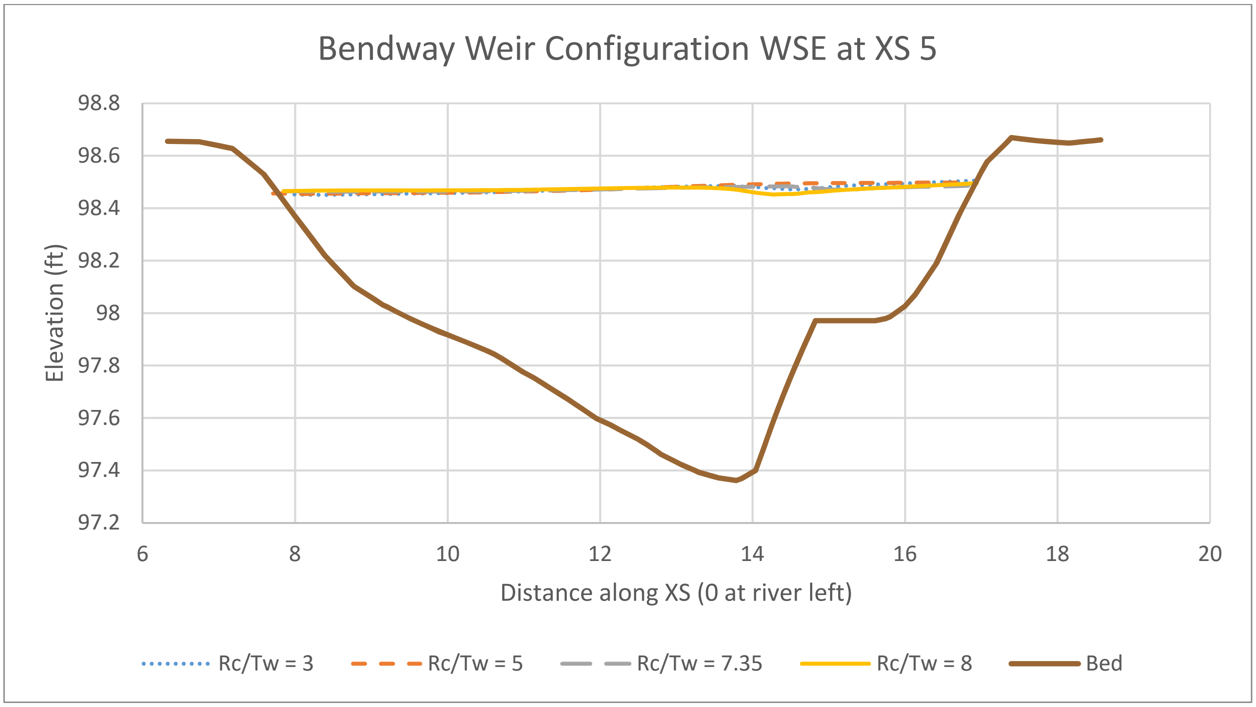

Figure 164: WSE across XS 5 in the bendway weir configuration

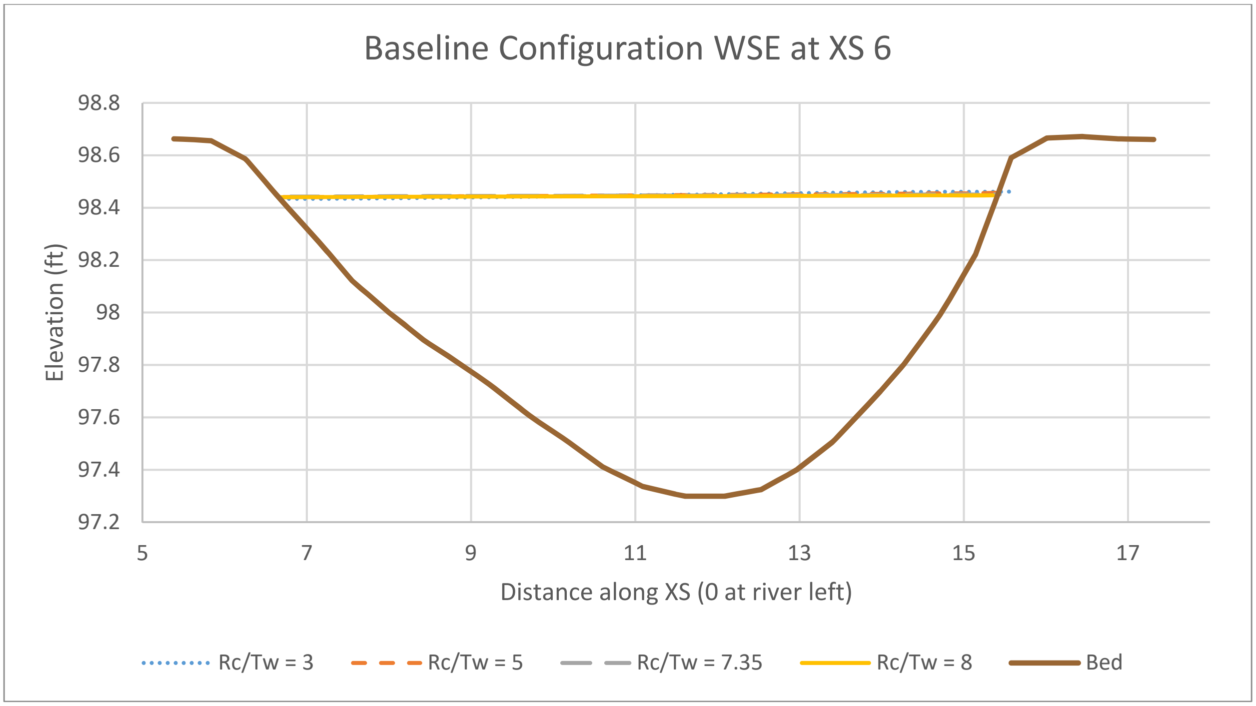

Figure 165: WSE across XS 6 in the baseline configuration

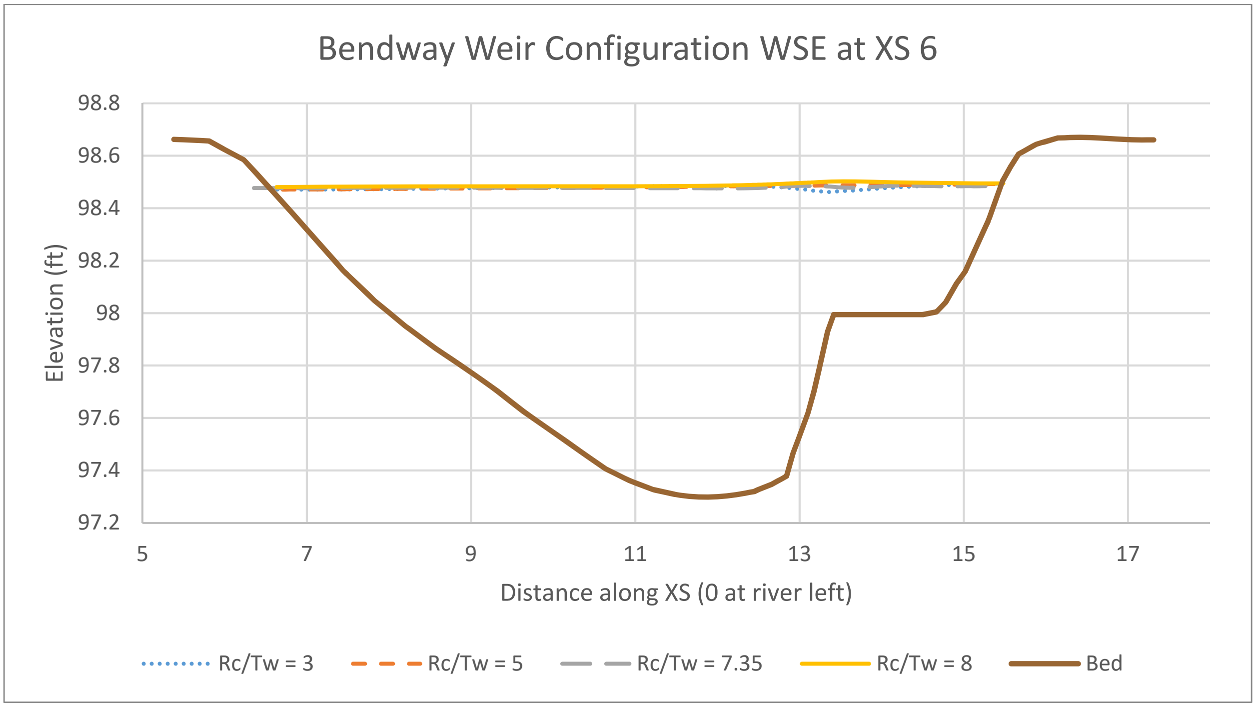

Figure 166: WSE across XS 6 in the bendway weir configuration

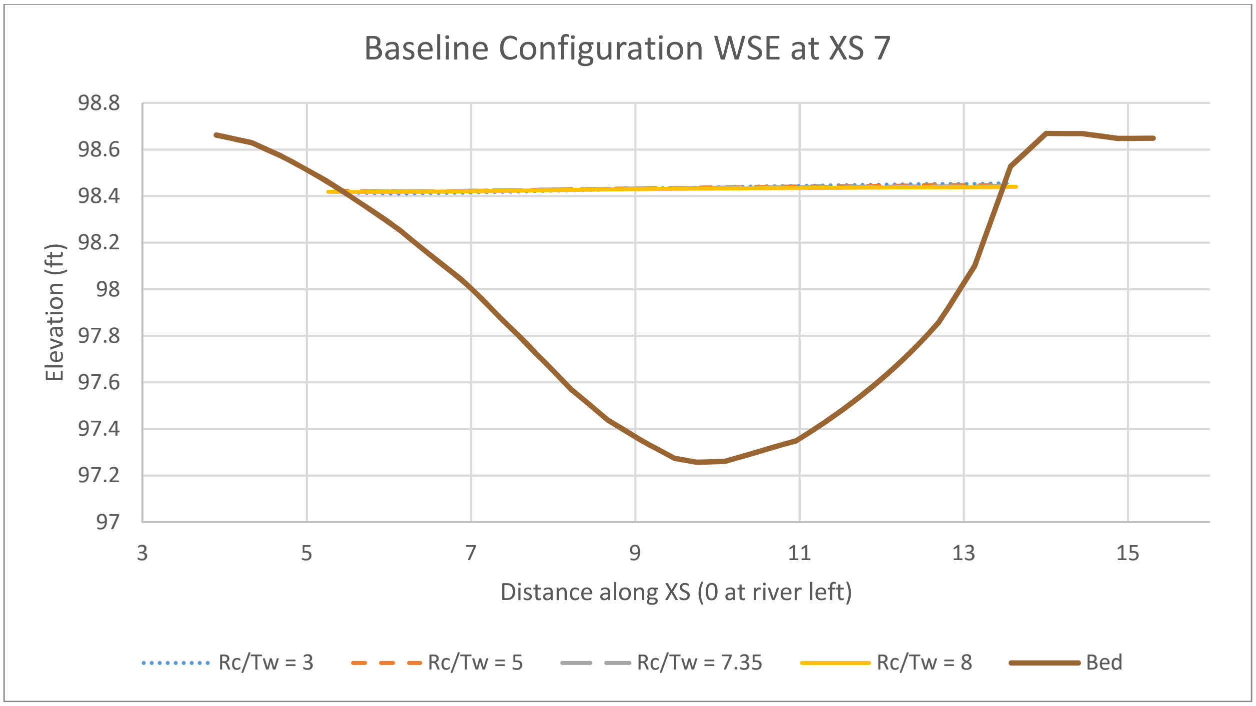

Figure 167: WSE across XS 7 in the baseline configuration

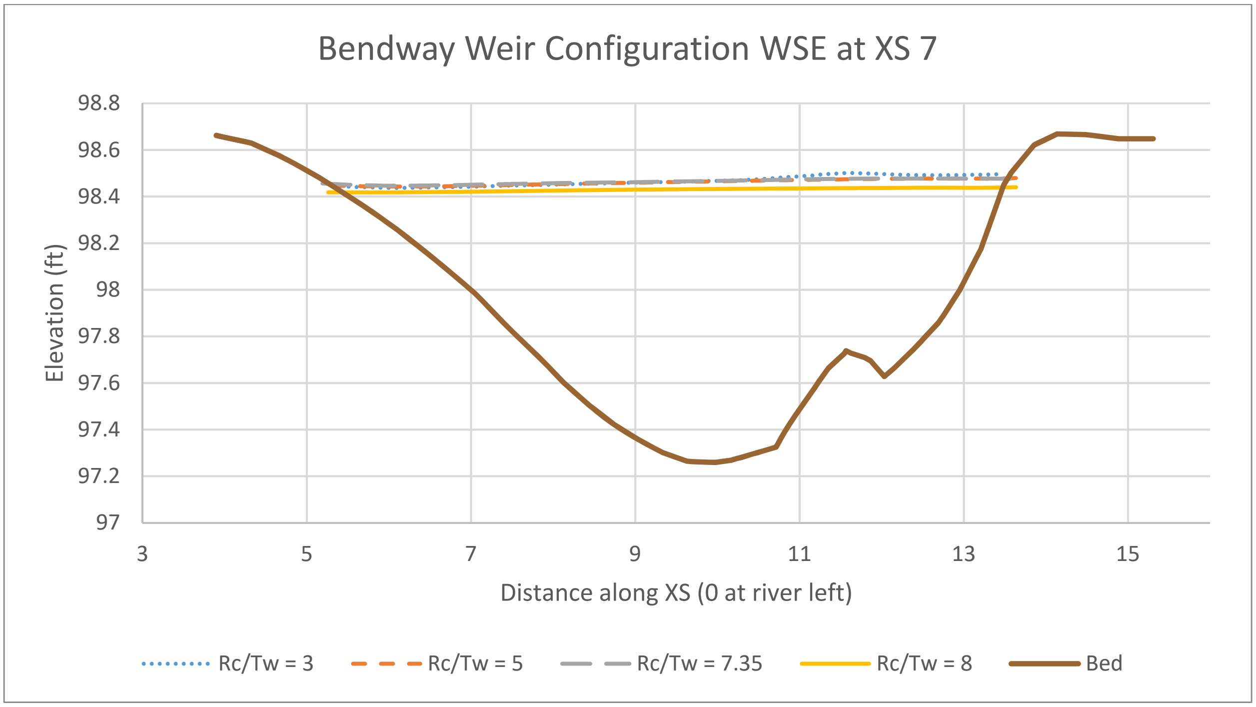

Figure 168: WSE across XS 7 in the bendway weir configuration

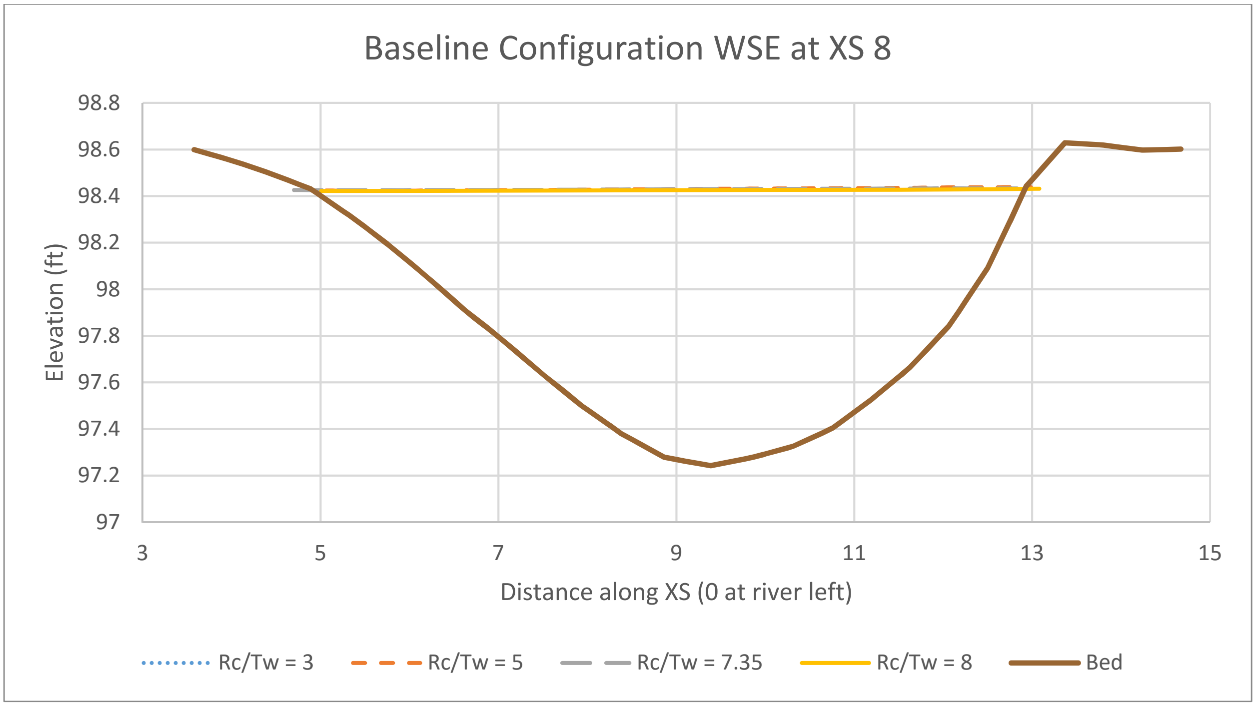

Figure 169: WSE across XS 8 in the baseline configuration

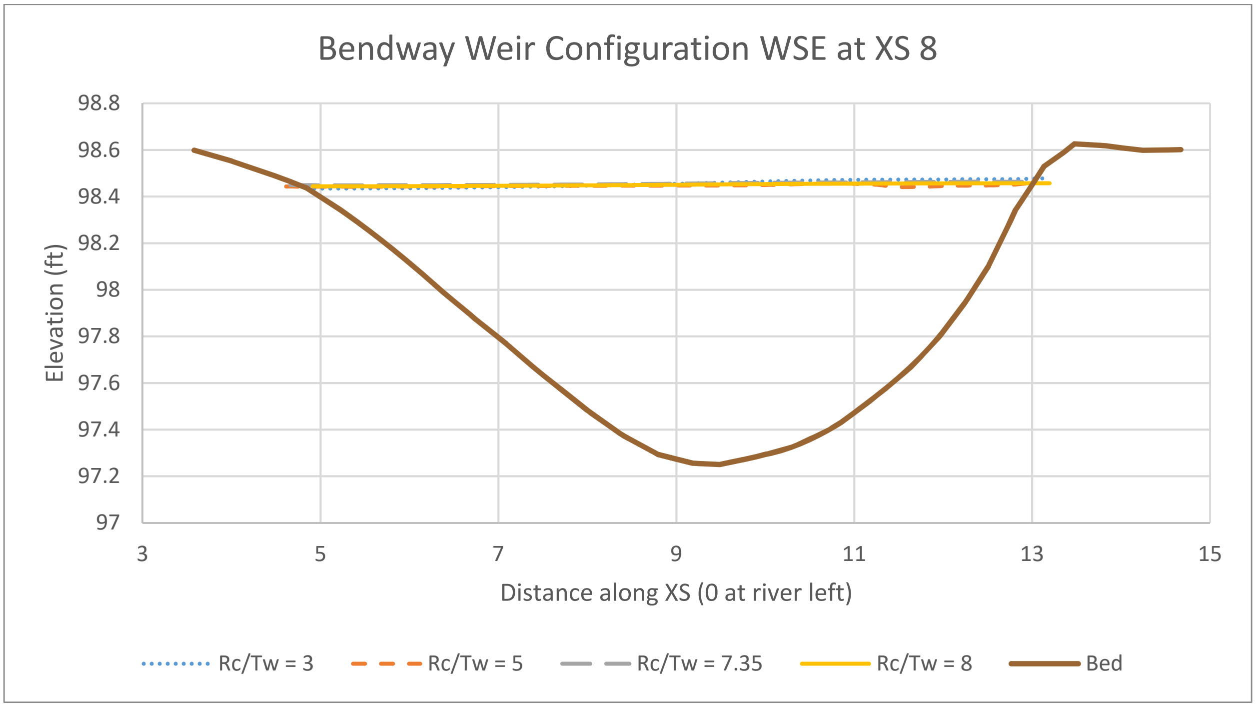

Figure 170: WSE across XS 8 in the bendway weir configuration

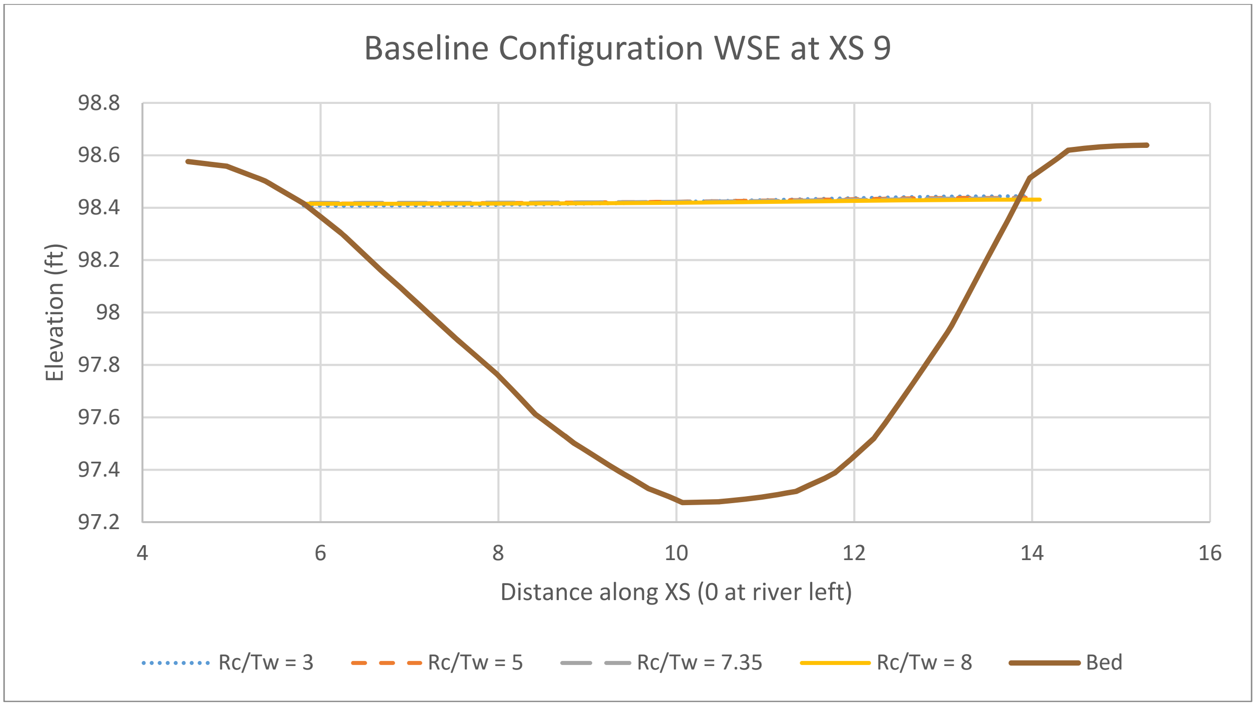

Figure 171: WSE across XS 9 in the baseline configuration

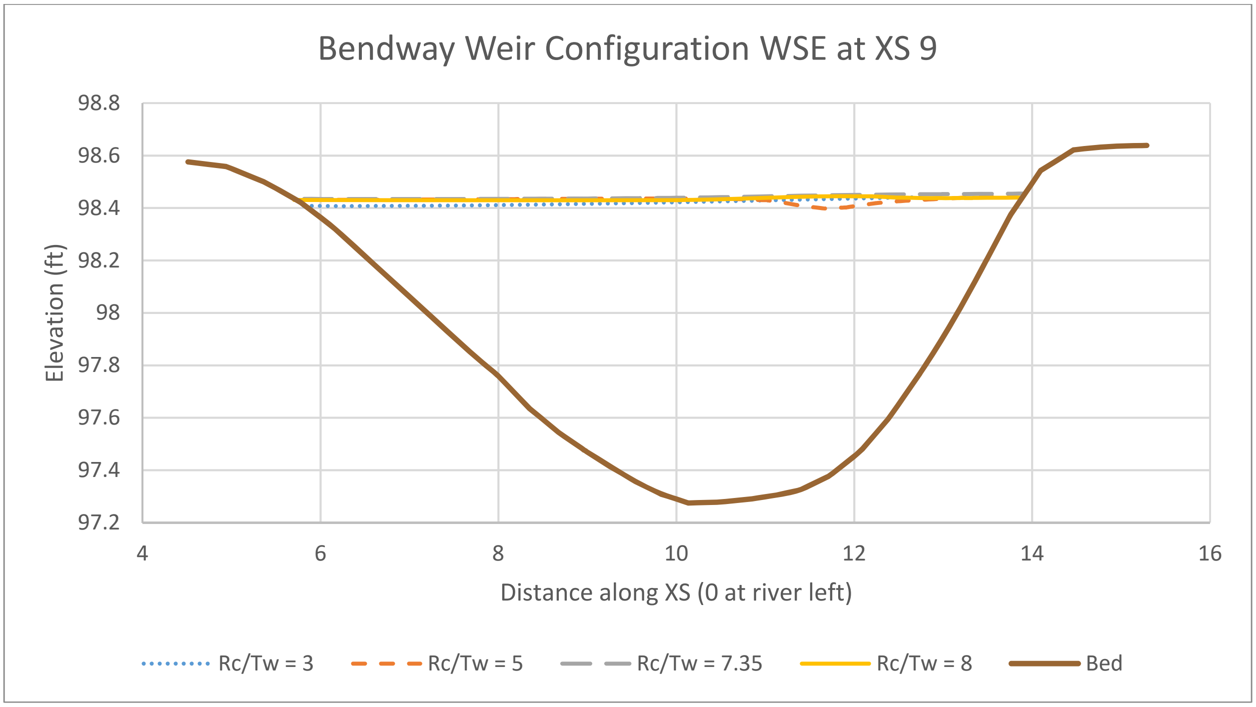

Figure 172: WSE across XS 9 in the bendway weir configuration

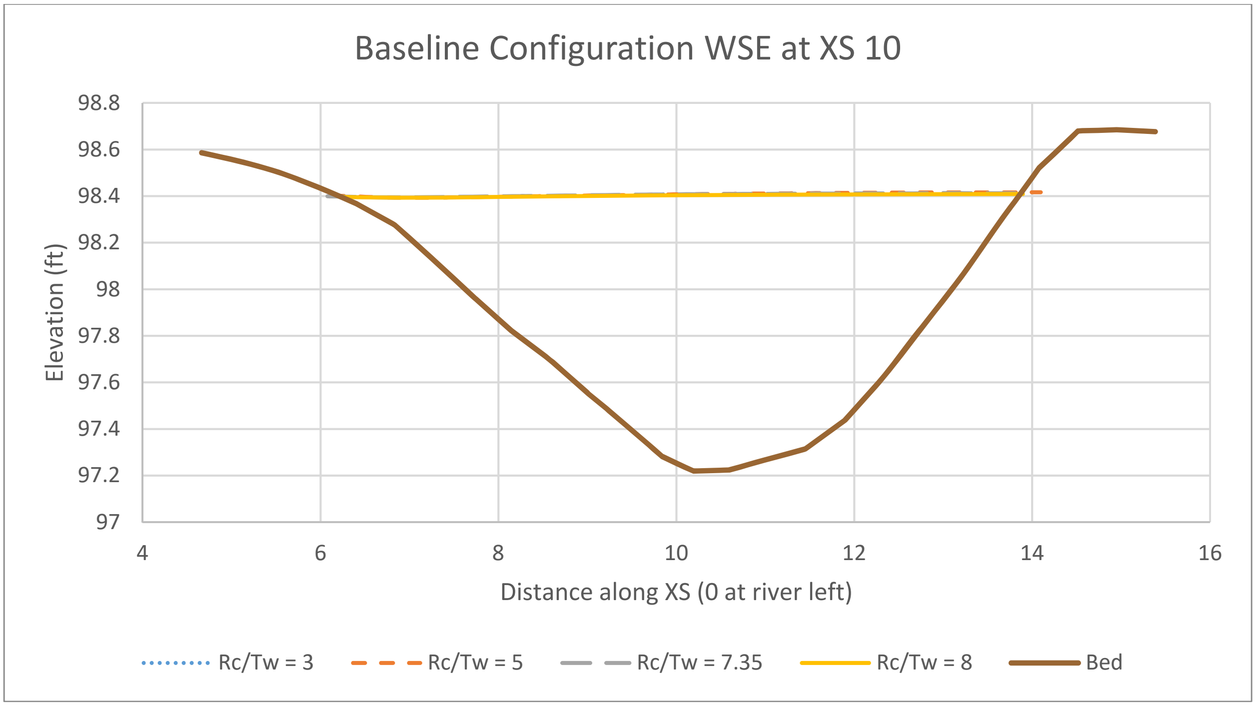

Figure 173: WSE across XS 10 in the baseline configuration

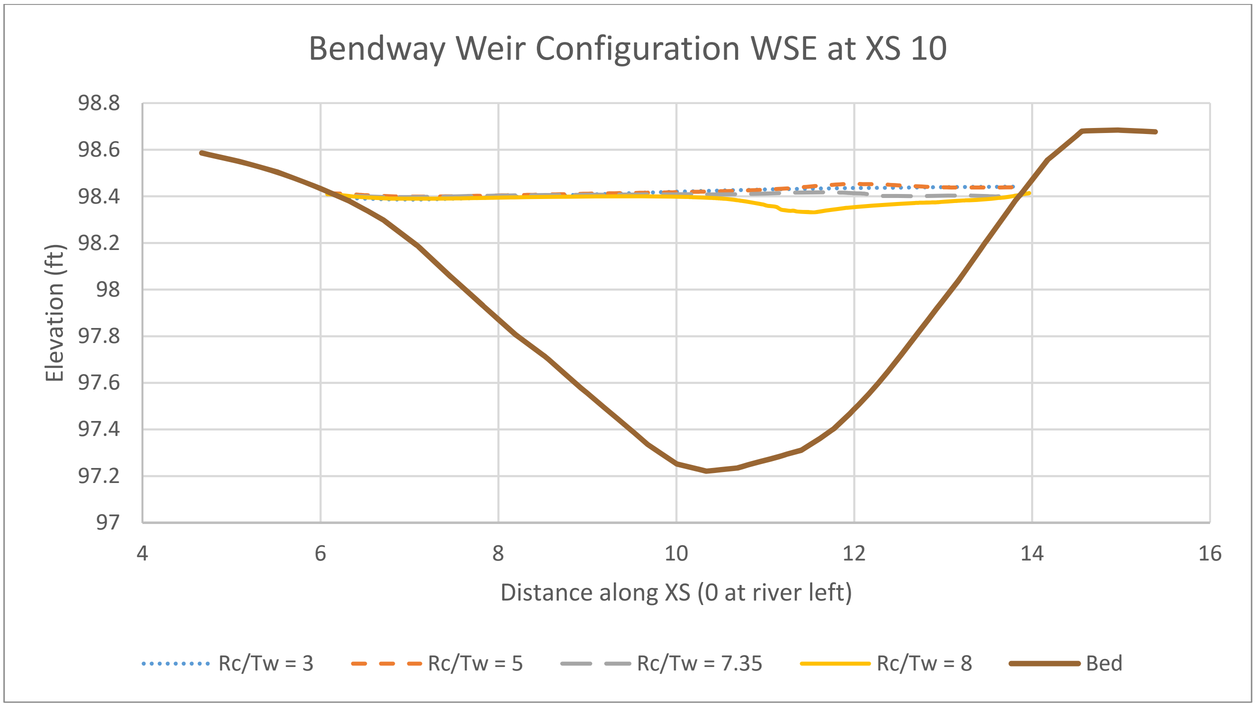

Figure 174: WSE across XS 10 in the bendway weir configuration

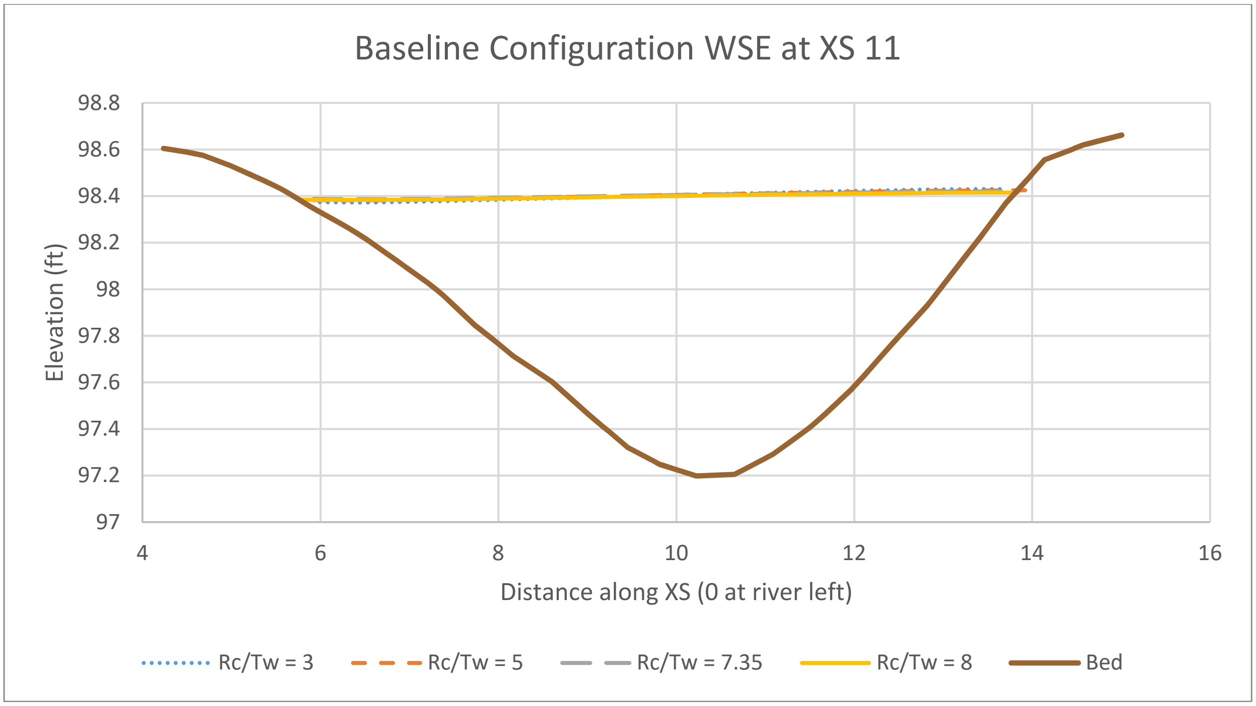

Figure 175: WSE across XS 11 in the baseline configuration

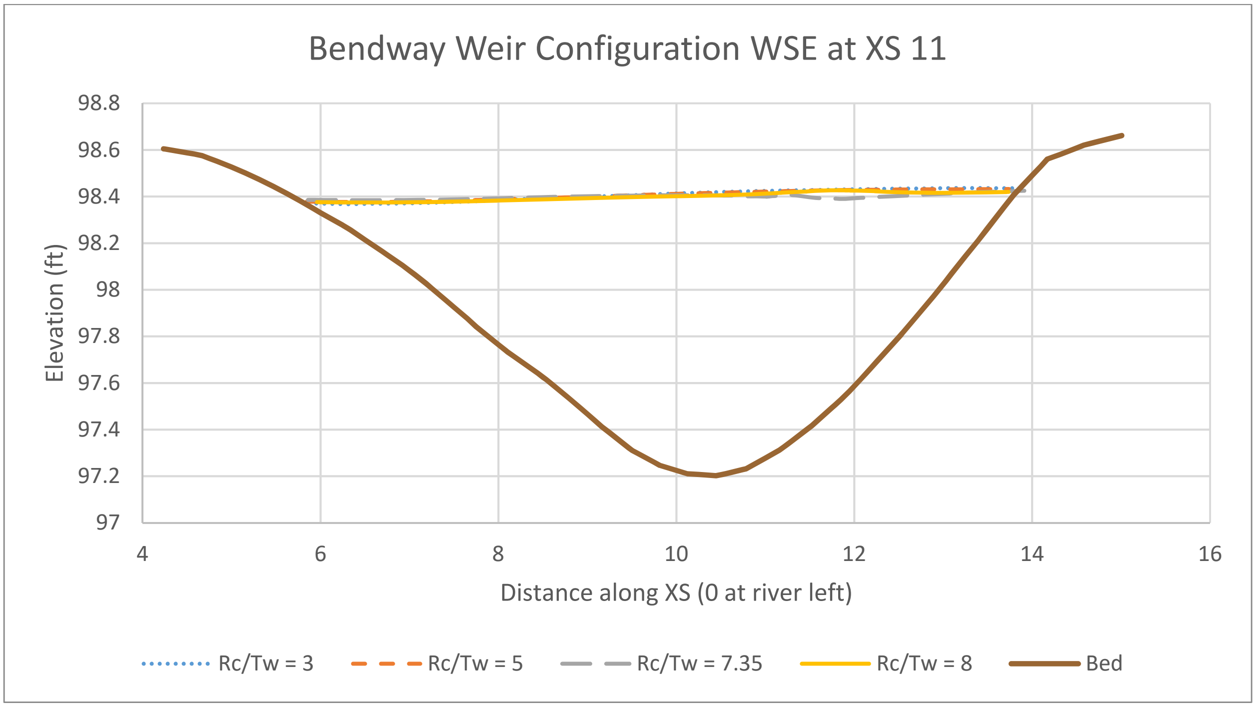

Figure 176: WSE across XS 11 in the bendway weir configuration

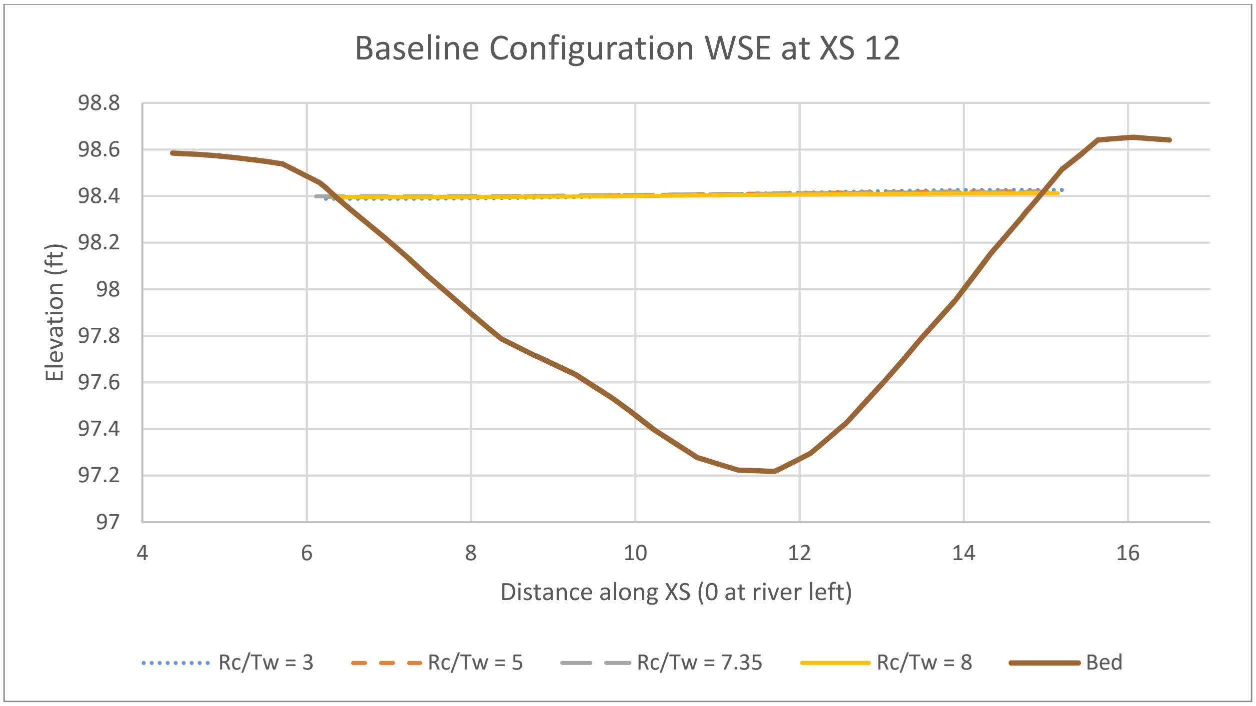

Figure 177: WSE across XS 12 in the baseline configuration

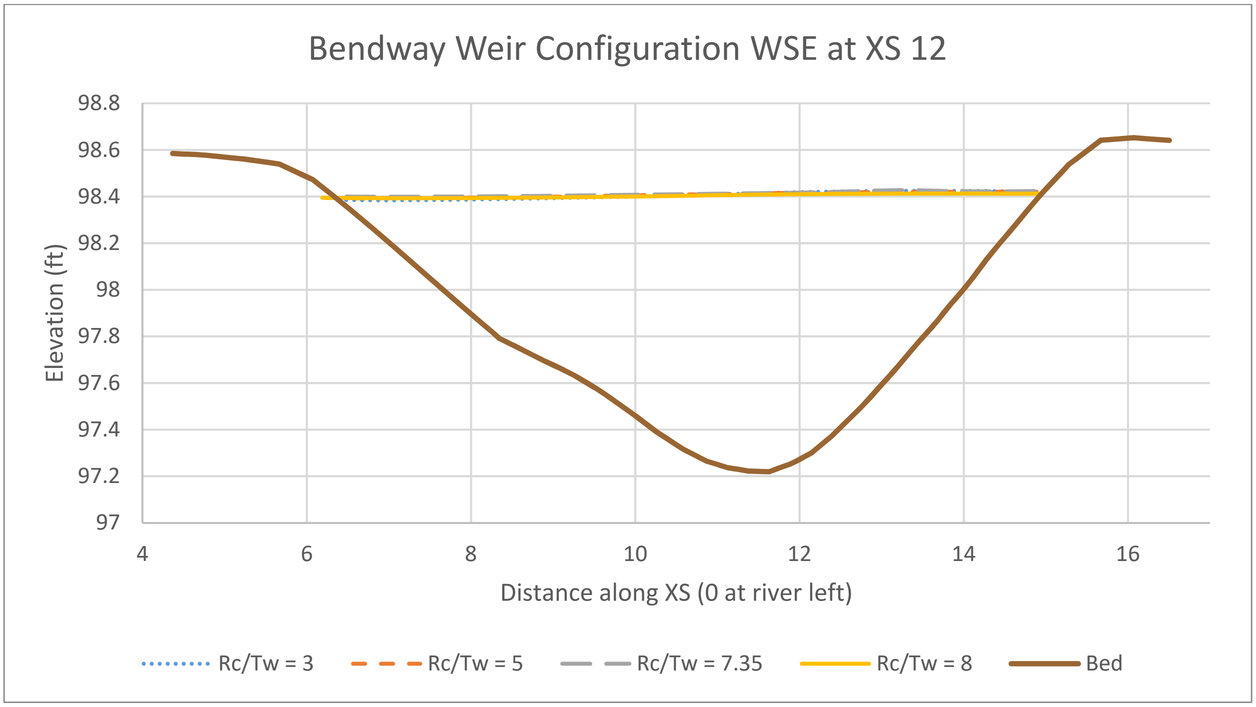

Figure 178: WSE across XS 12 in the bendway weir configuration

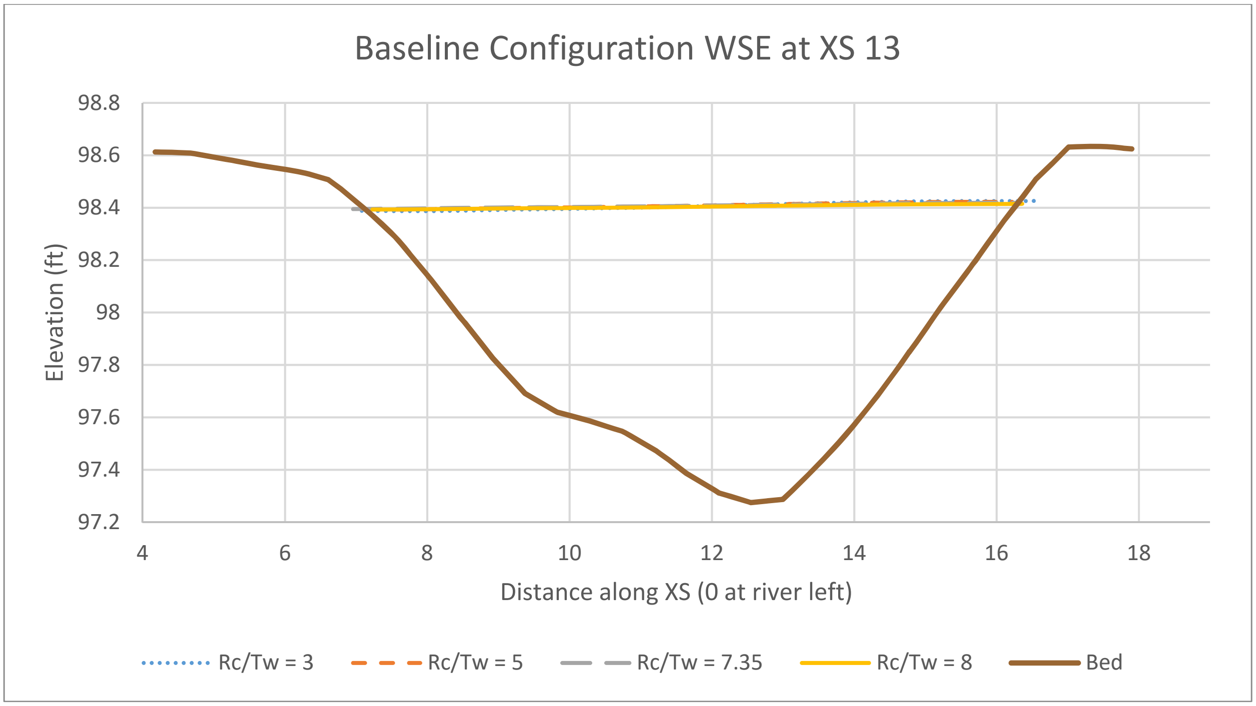

Figure 179: WSE across XS 13 in the baseline configuration

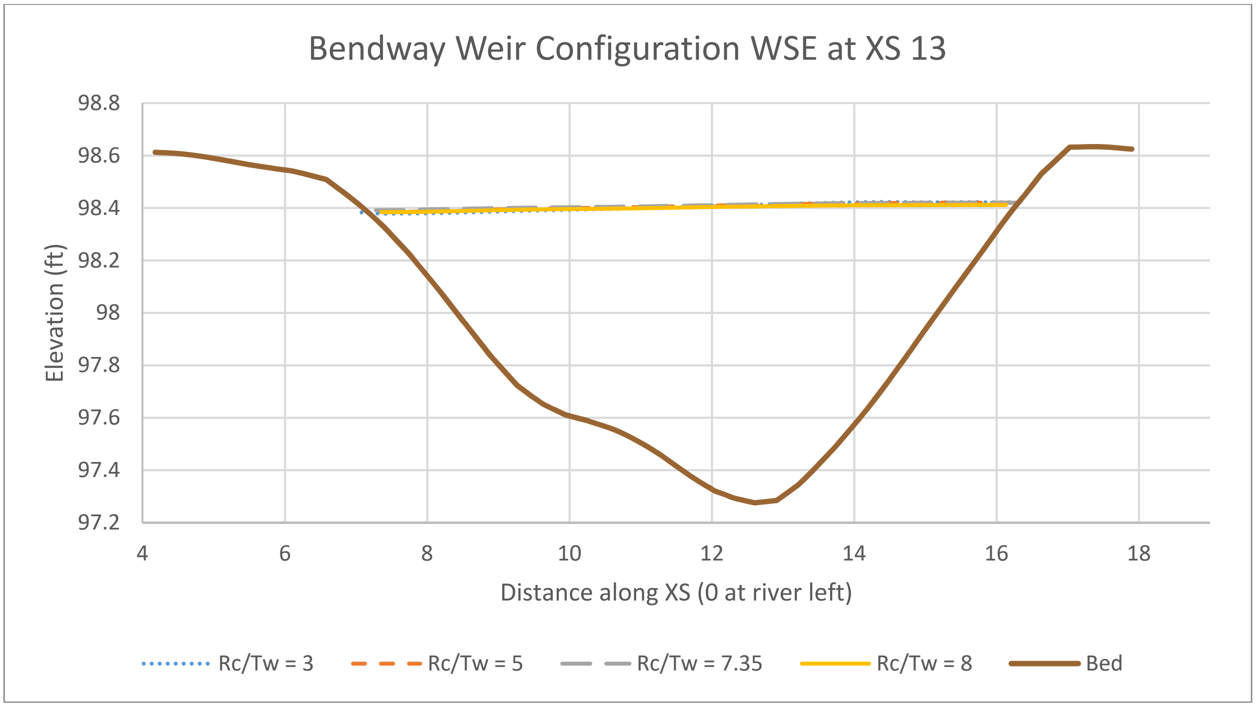

Figure 180: WSE across XS 13 in the bendway weir configuration

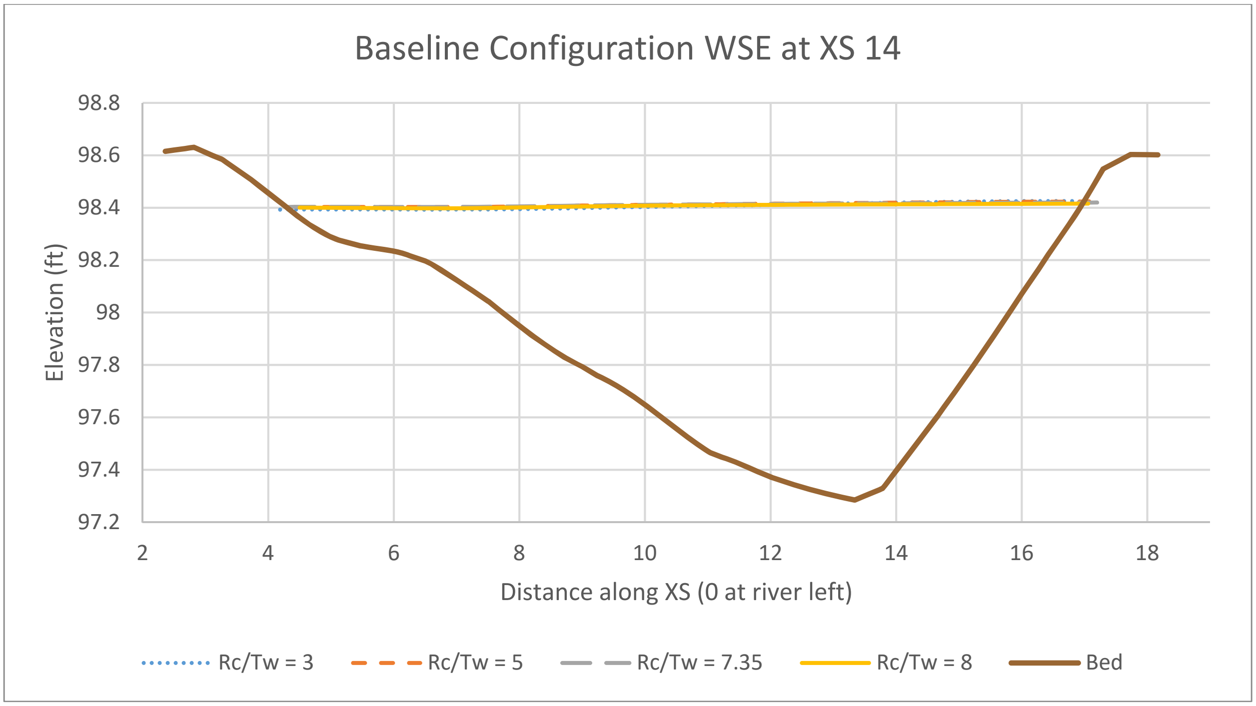

Figure 181: WSE across XS 14 in the baseline configuration

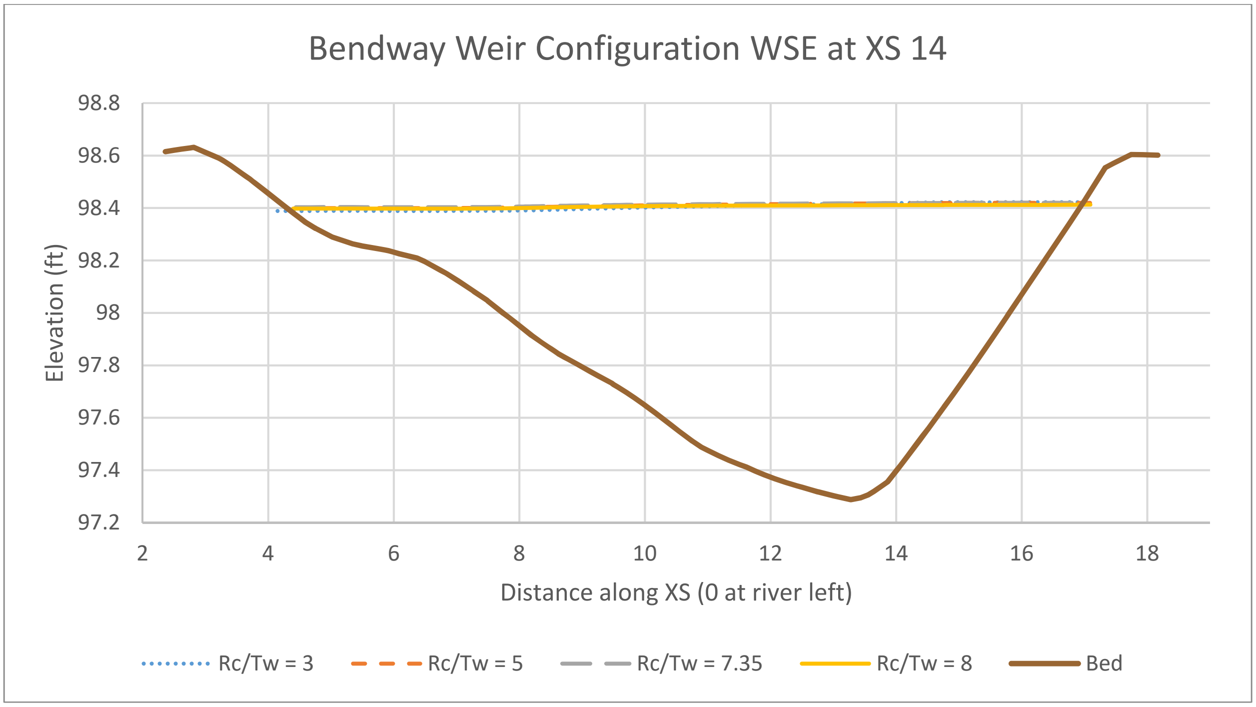

Figure 182: WSE across XS 14 in the bendway weir configuration

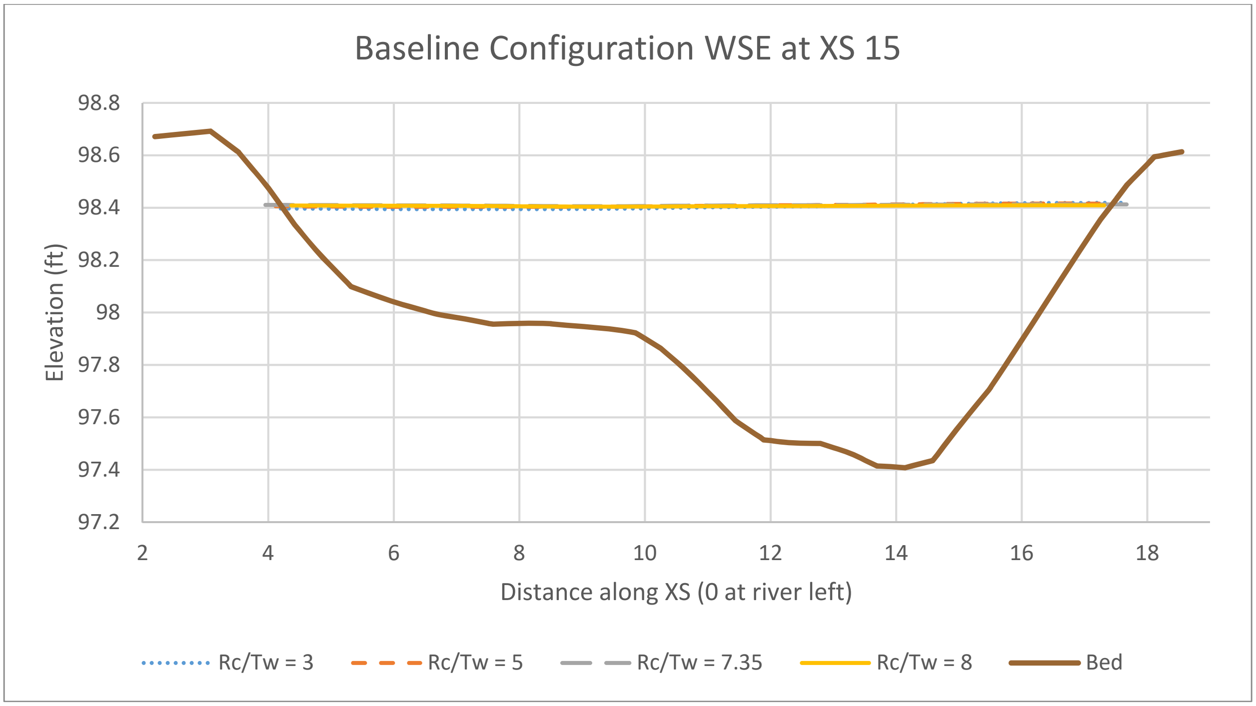

Figure 183: WSE across XS 15 in the baseline configuration

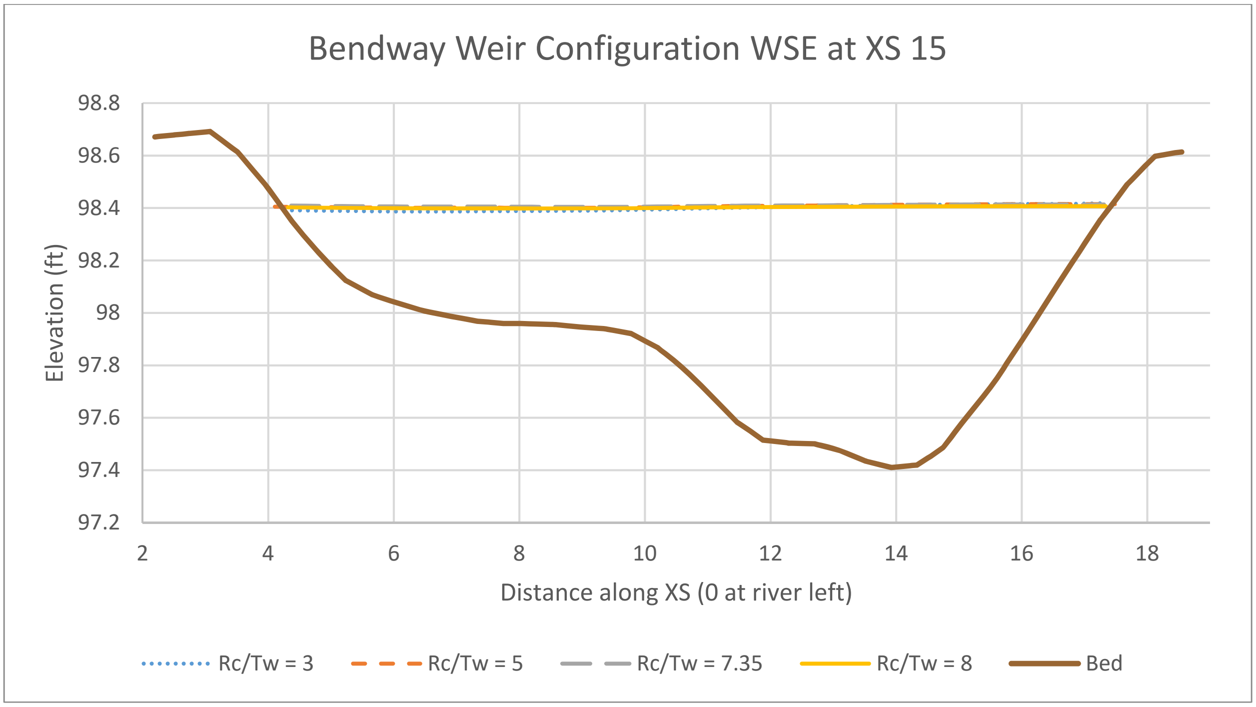

Figure 184: WSE across XS 15 in the bendway weir configuration

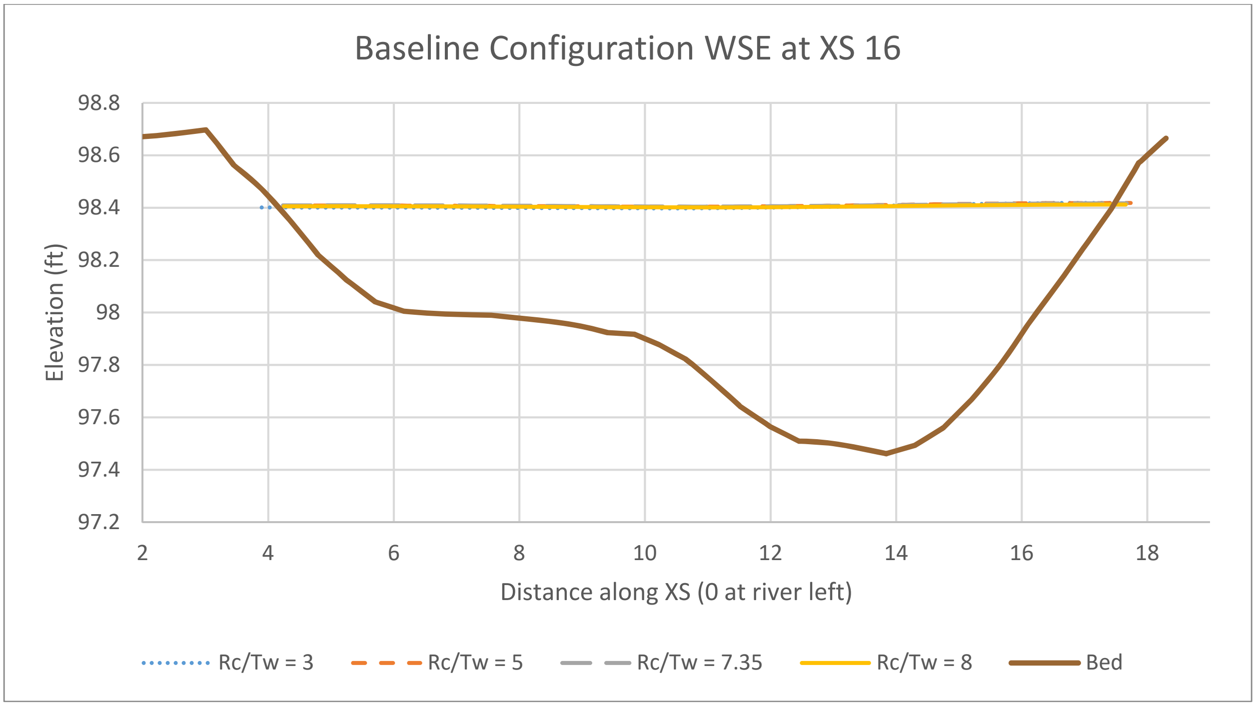

Figure 185: WSE across XS 16 in the baseline configuration

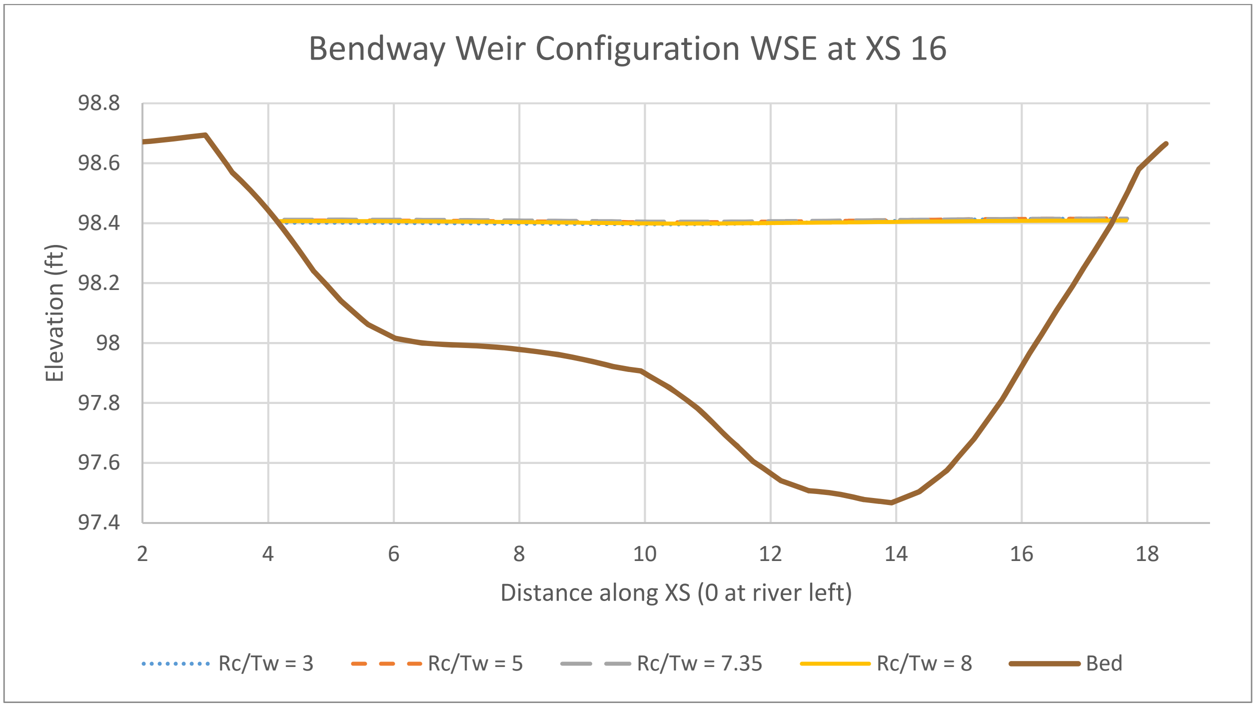

Figure 186: WSE across XS 16 in the bendway weir configuration

APPENDIX C. CROSS-SECTIONAL PLOTS OF WATER SURFACE ELEVATION AND VELOCITY – TRAPEZOIDAL CHANNEL

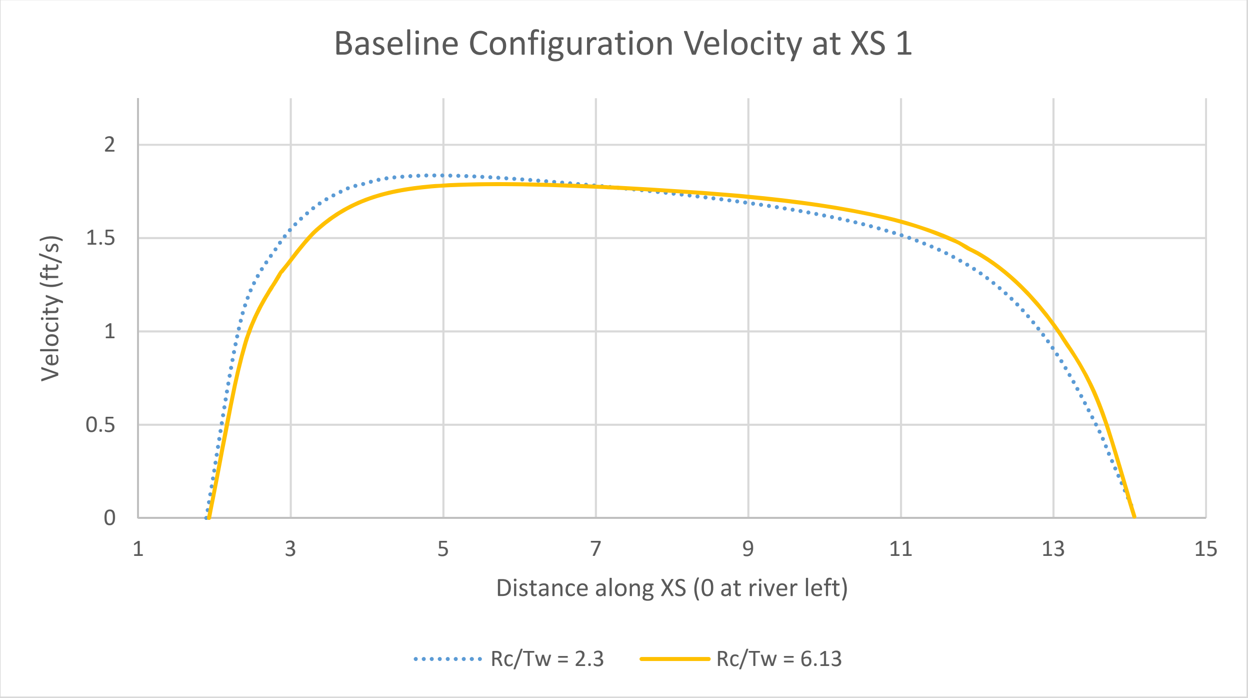

Figure 187: Velocity across XS 1 in the baseline configuration

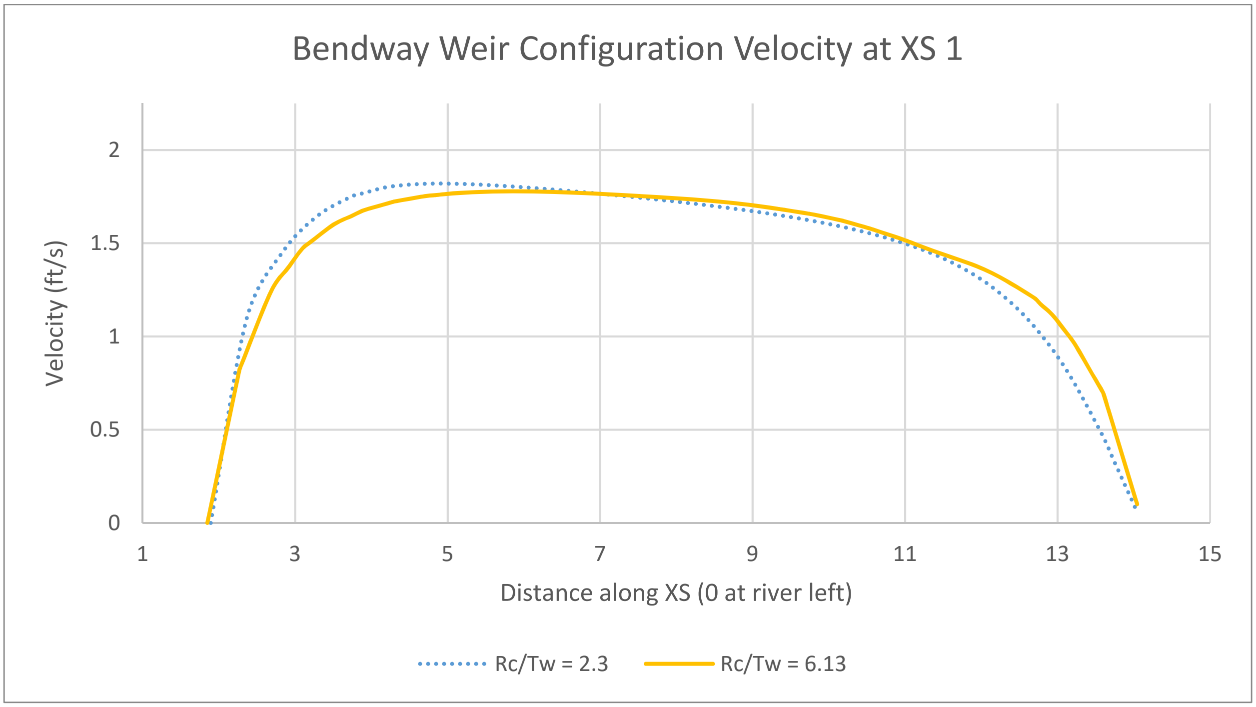

Figure 188: Velocity across XS 1 in the bendway weir configuration

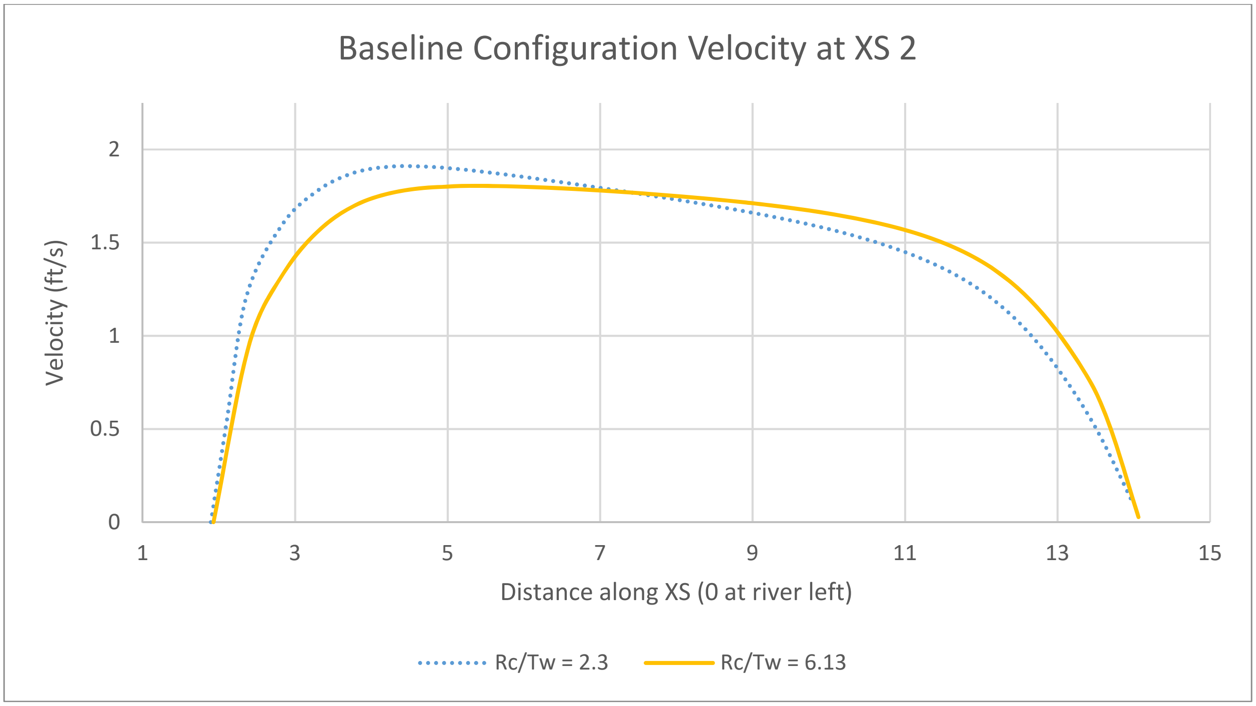

Figure 189: Velocity across XS 2 in the baseline configuration

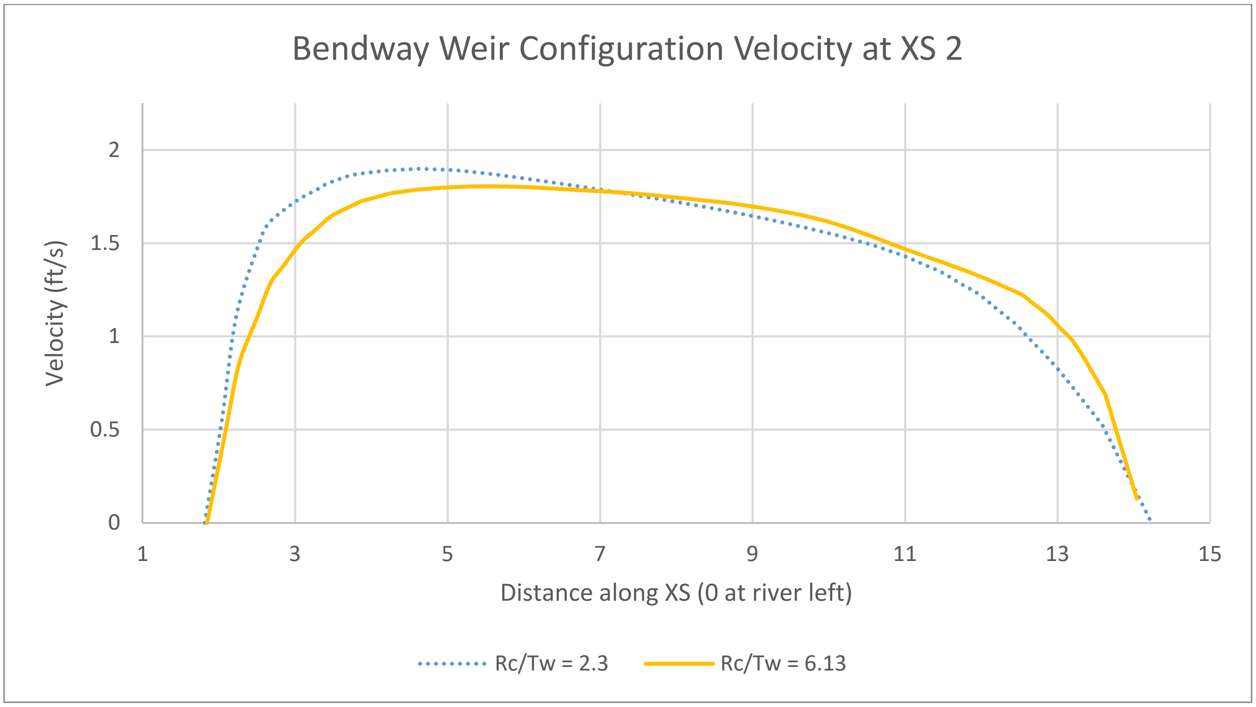

Figure 190: Velocity across XS 2 in the bendway weir configuration

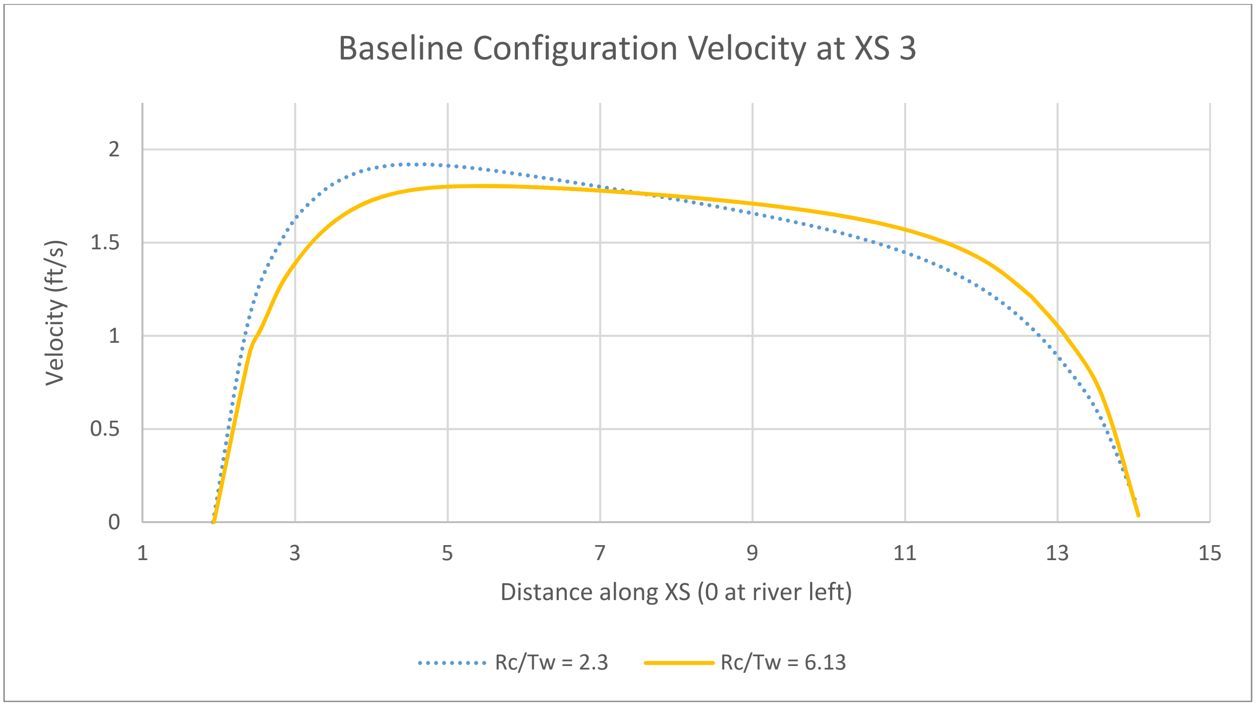

Figure 191: Velocity across XS 3 in the baseline configuration

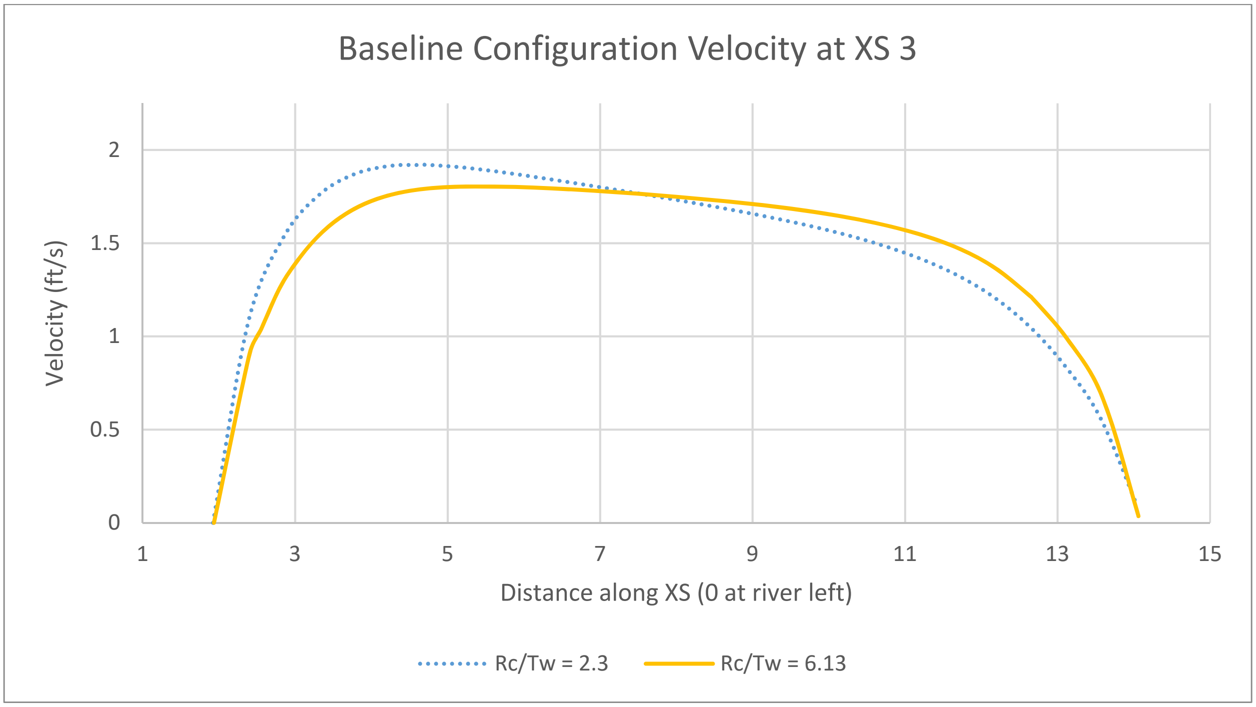

Figure 192: Velocity across XS 3 in the bendway weir configuration

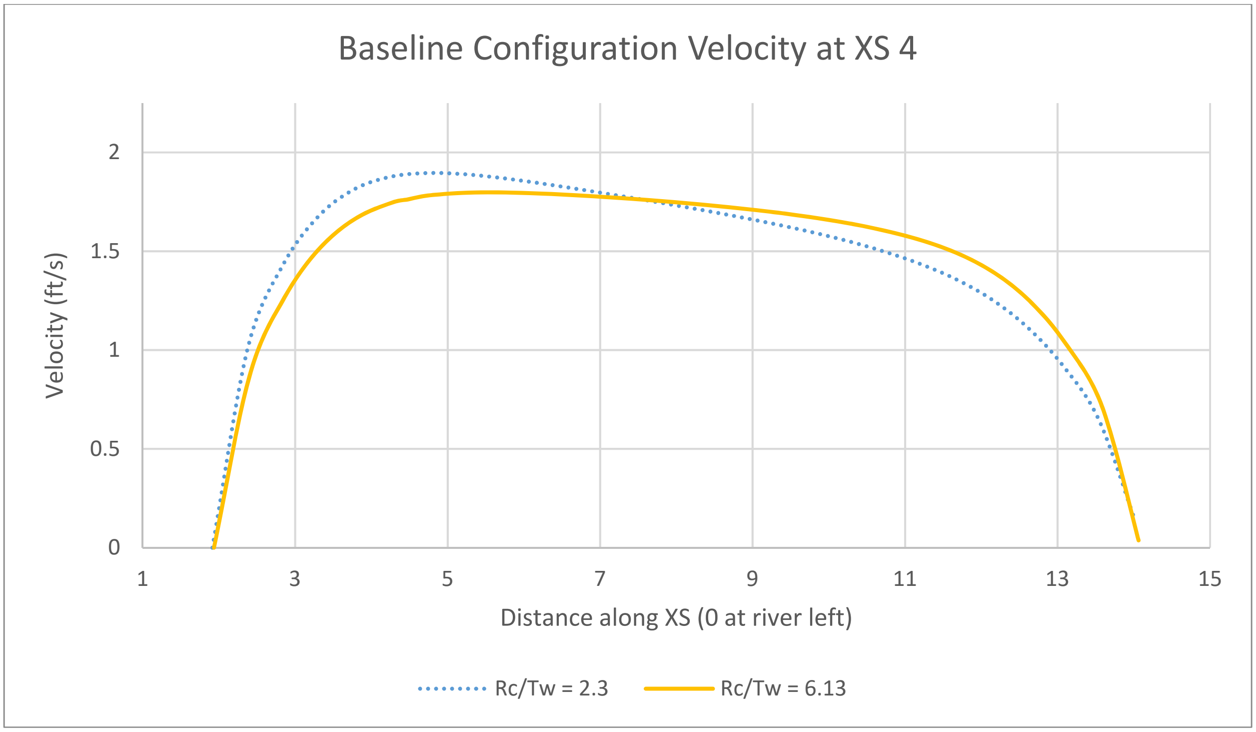

Figure 193: Velocity across XS 4 in the baseline configuration

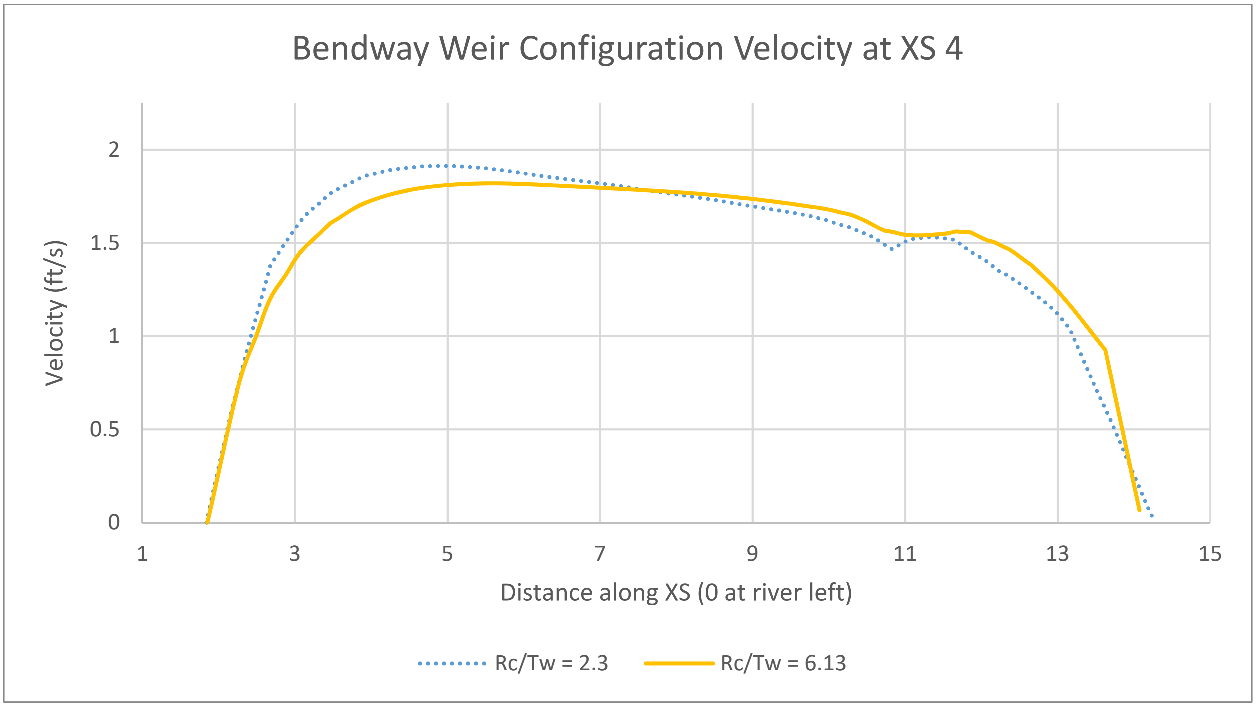

Figure 194: Velocity across XS 4 in the bendway weir configuration

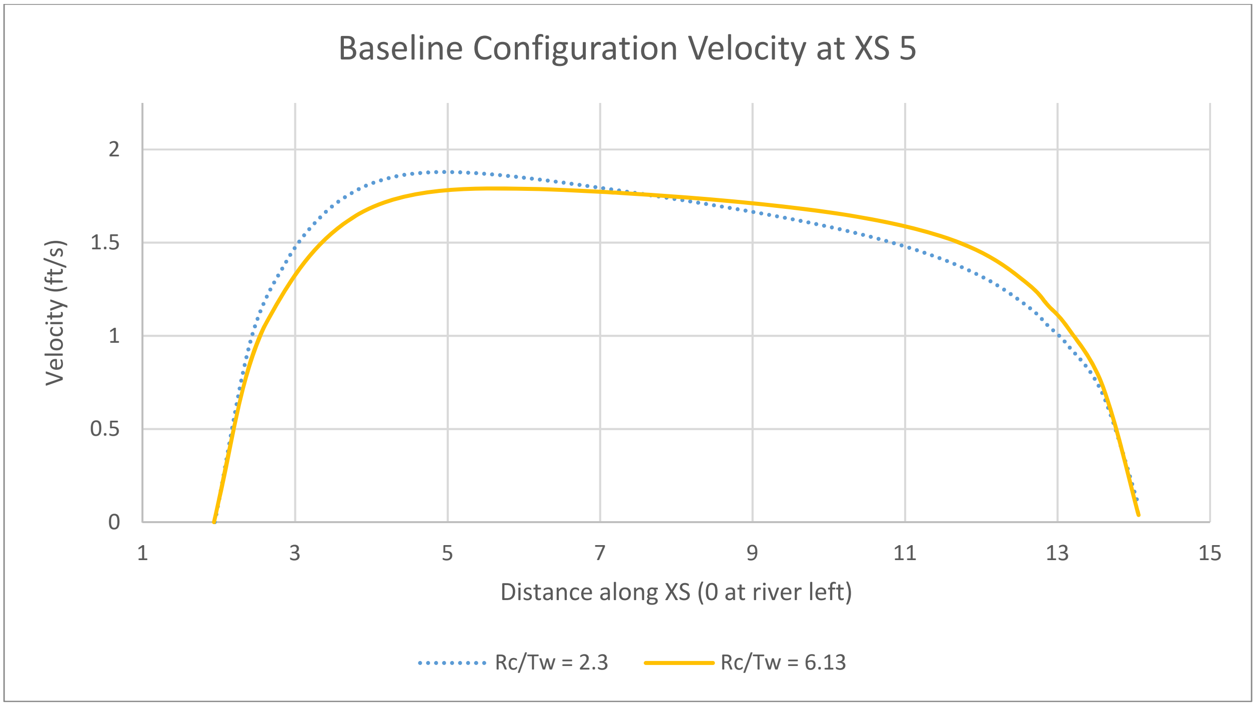

Figure 195: Velocity across XS 5 in the baseline configuration

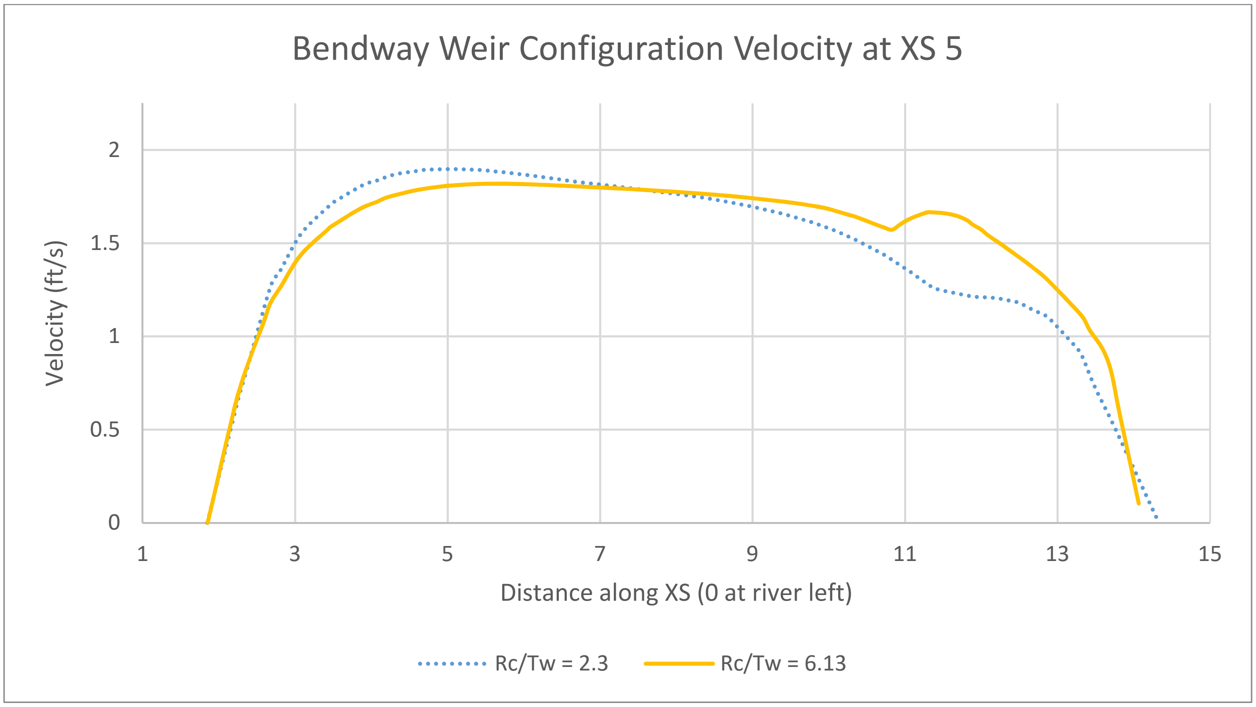

Figure 196: Velocity across XS 5 in the bendway weir configuration

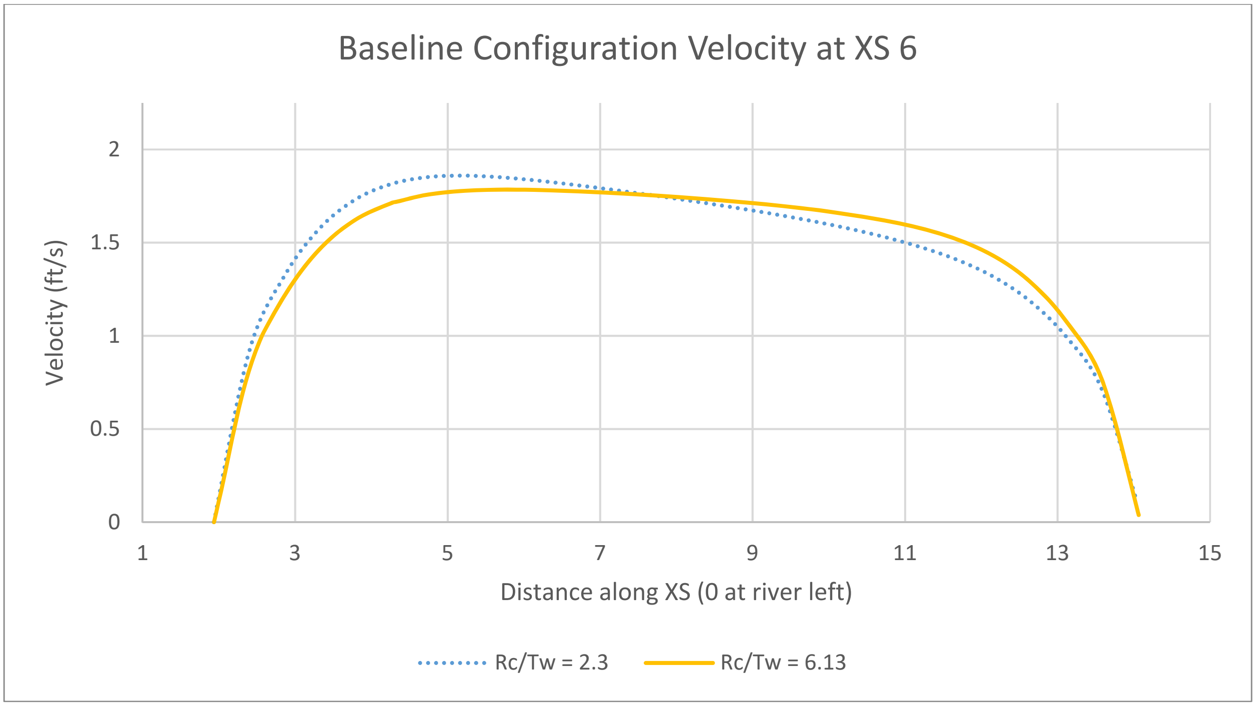

Figure 197: Velocity across XS 6 in the baseline configuration

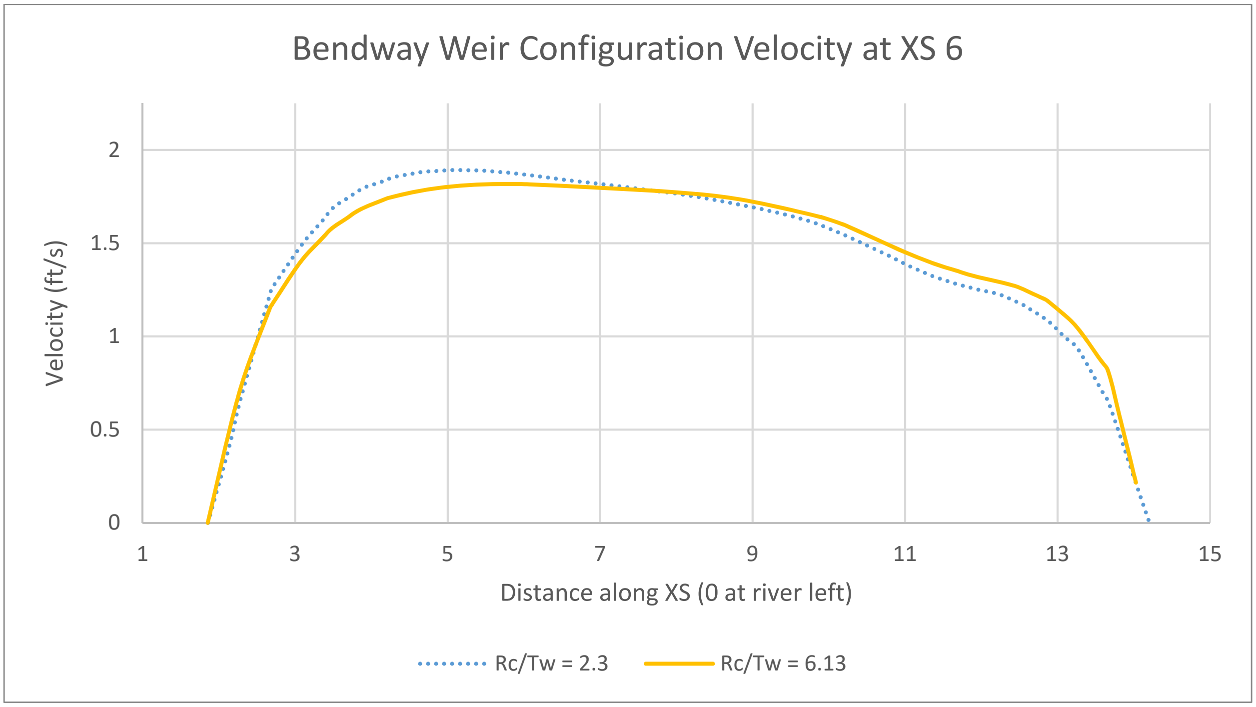

Figure 198: Velocity across XS 6 in the bendway weir configuration

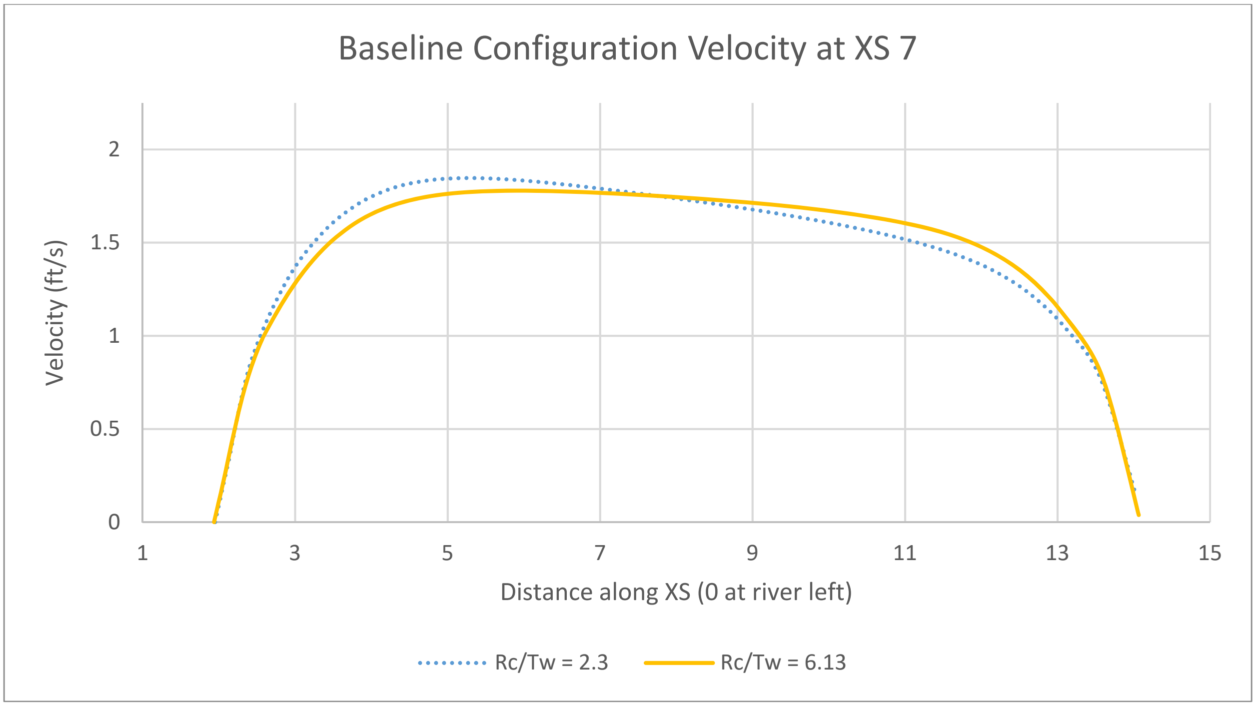

Figure 199: Velocity across XS 7 in the baseline configuration

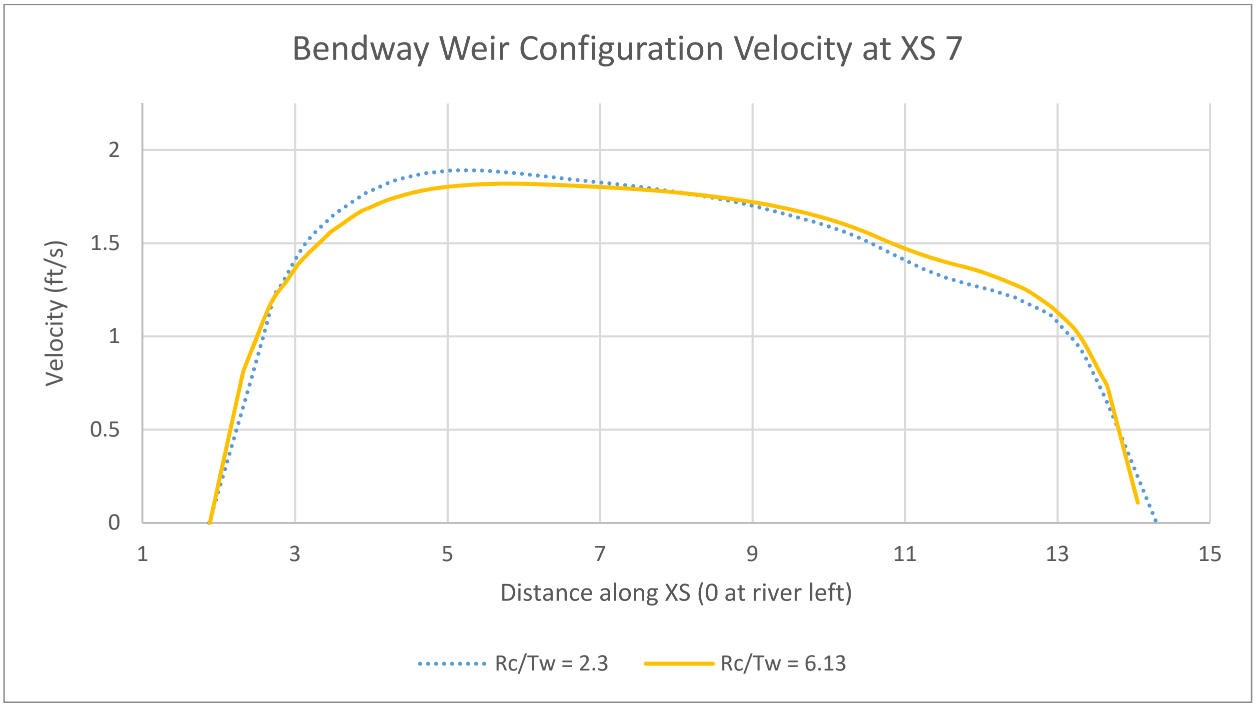

Figure 200: Velocity across XS 7 in the bendway weir configuration

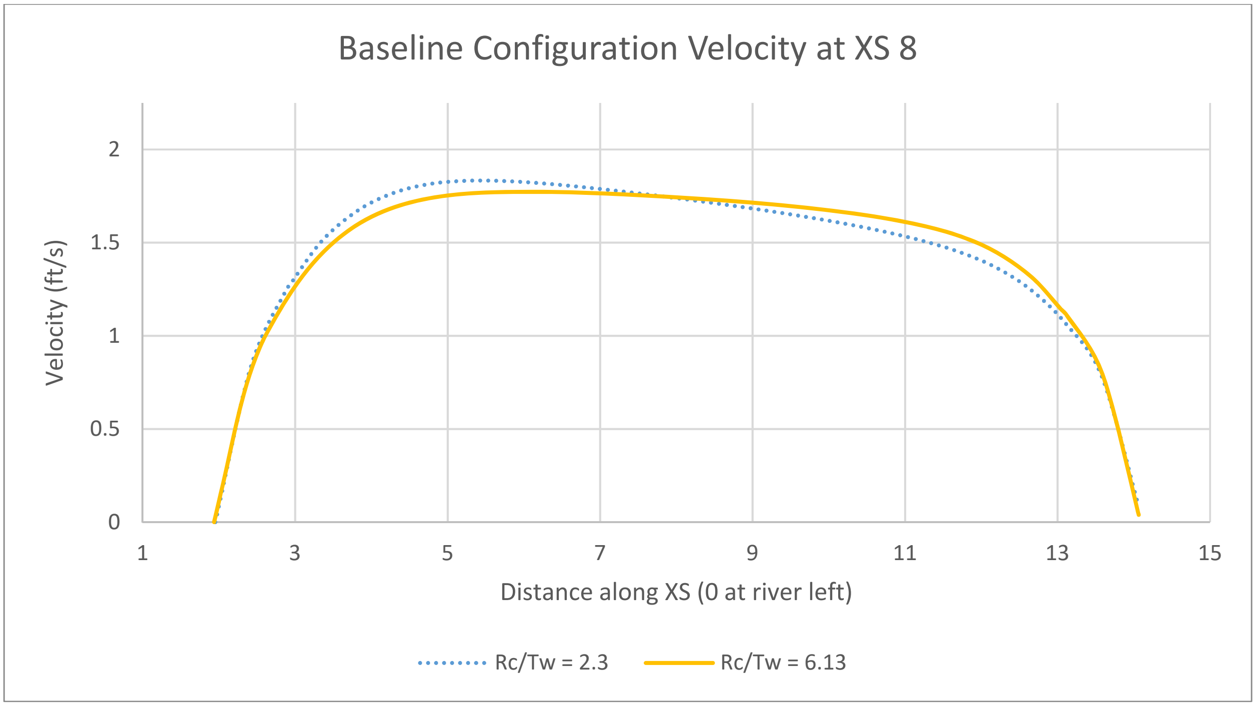

Figure 201: Velocity across XS 8 in the baseline configuration

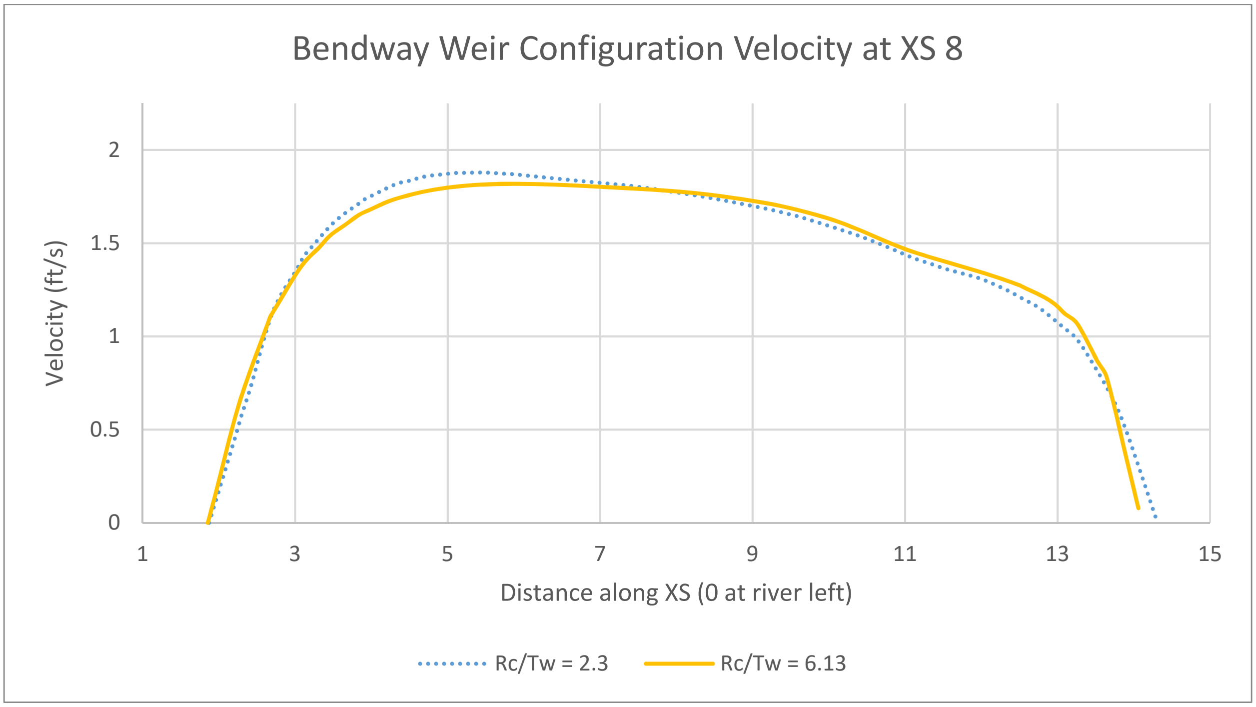

Figure 202: Velocity across XS 8 in the bendway weir configuration

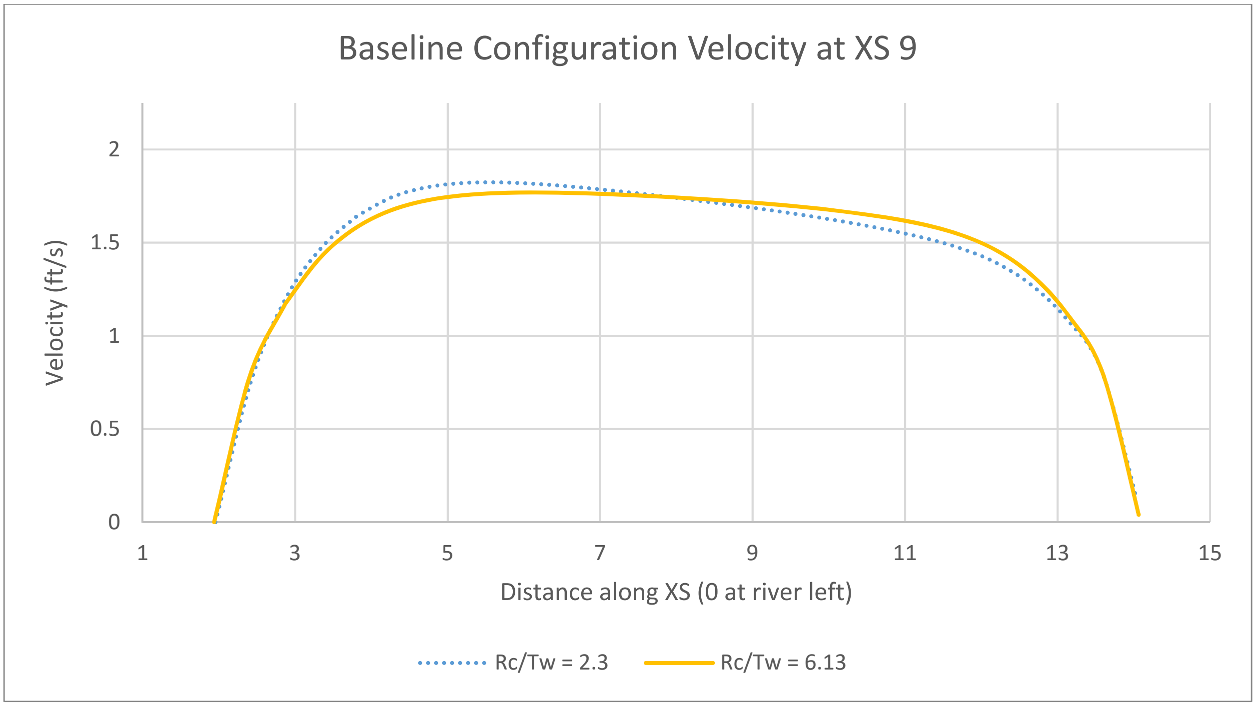

Figure 203: Velocity across XS 9 in the baseline configuration

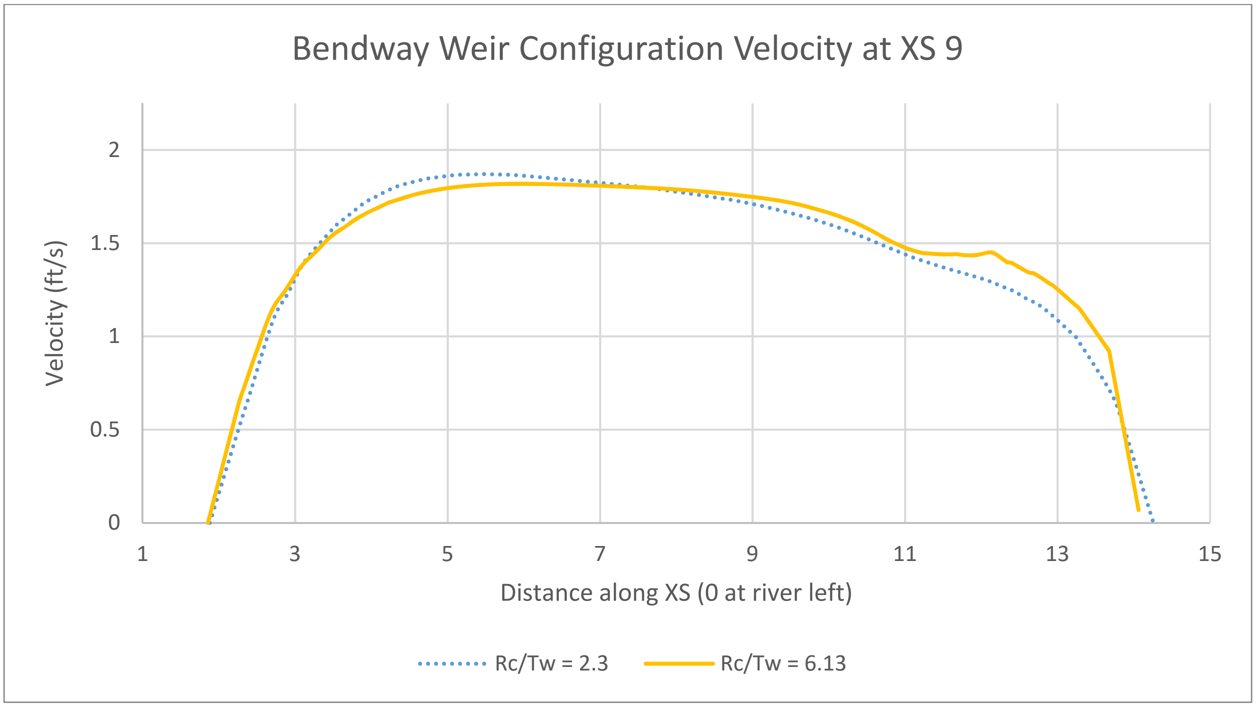

Figure 204: Velocity across XS 9 in the bendway weir configuration

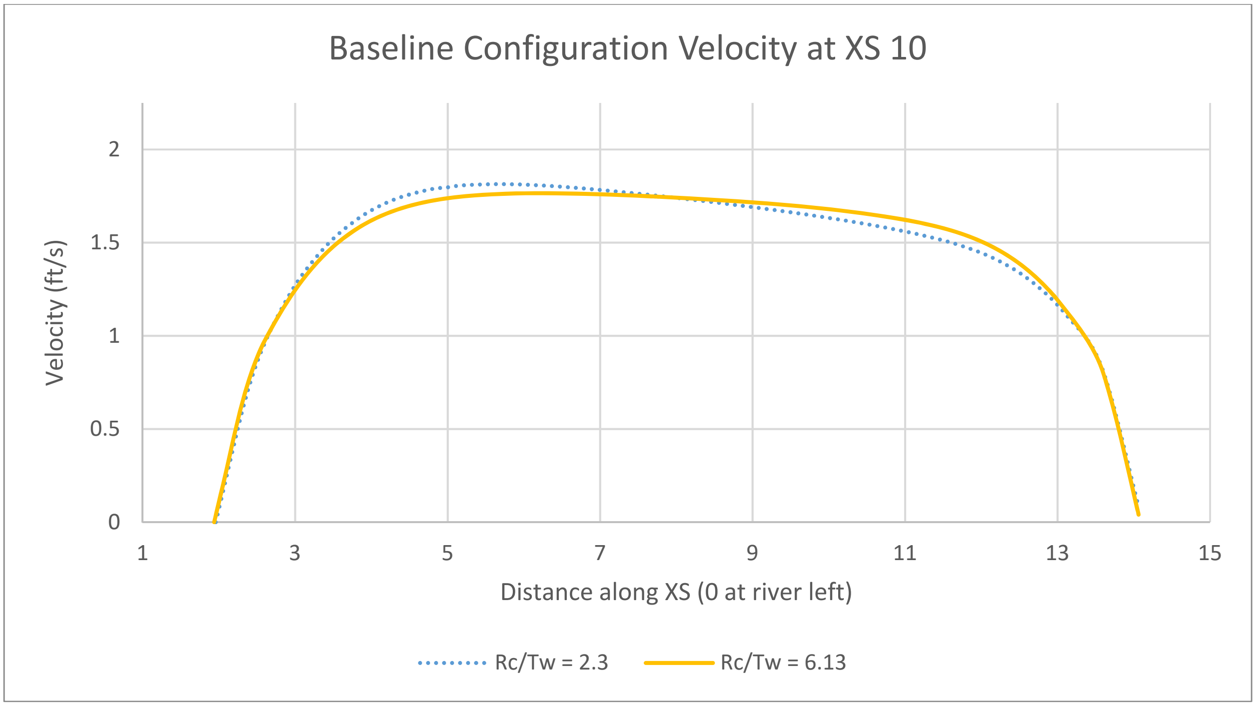

Figure 205: Velocity across XS 10 in the baseline configuration

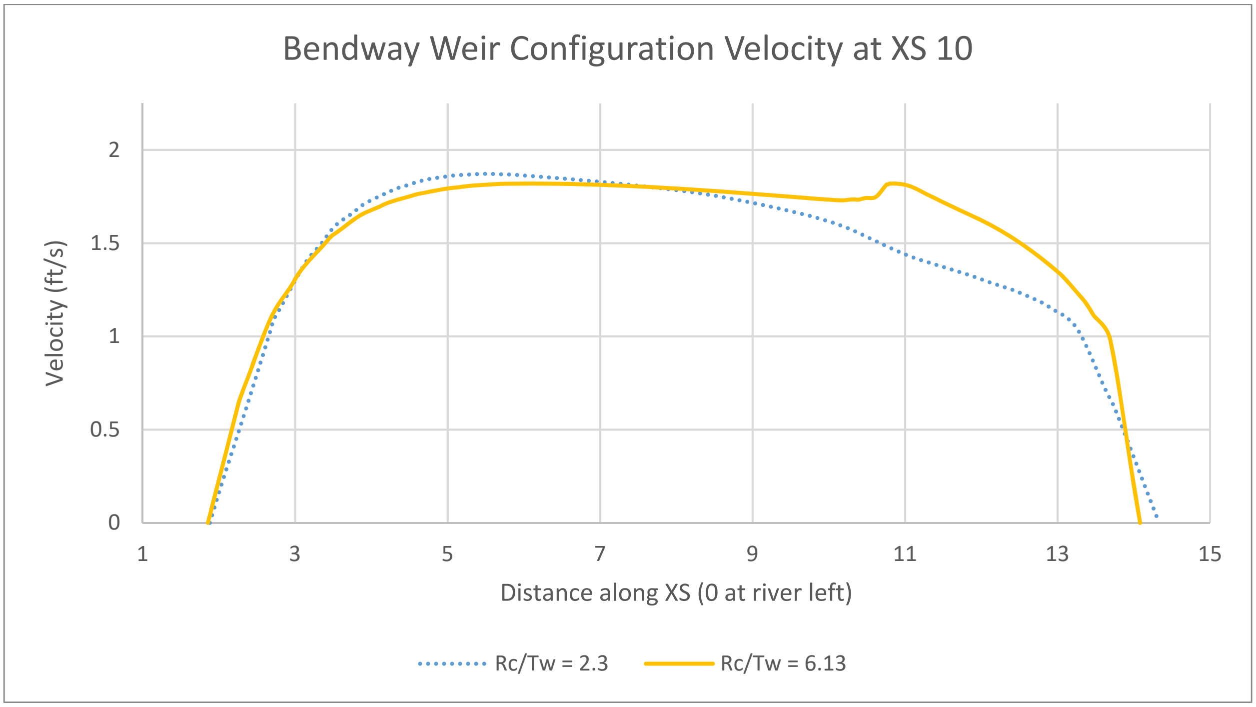

Figure 206: Velocity across XS 10 in the bendway weir configuration

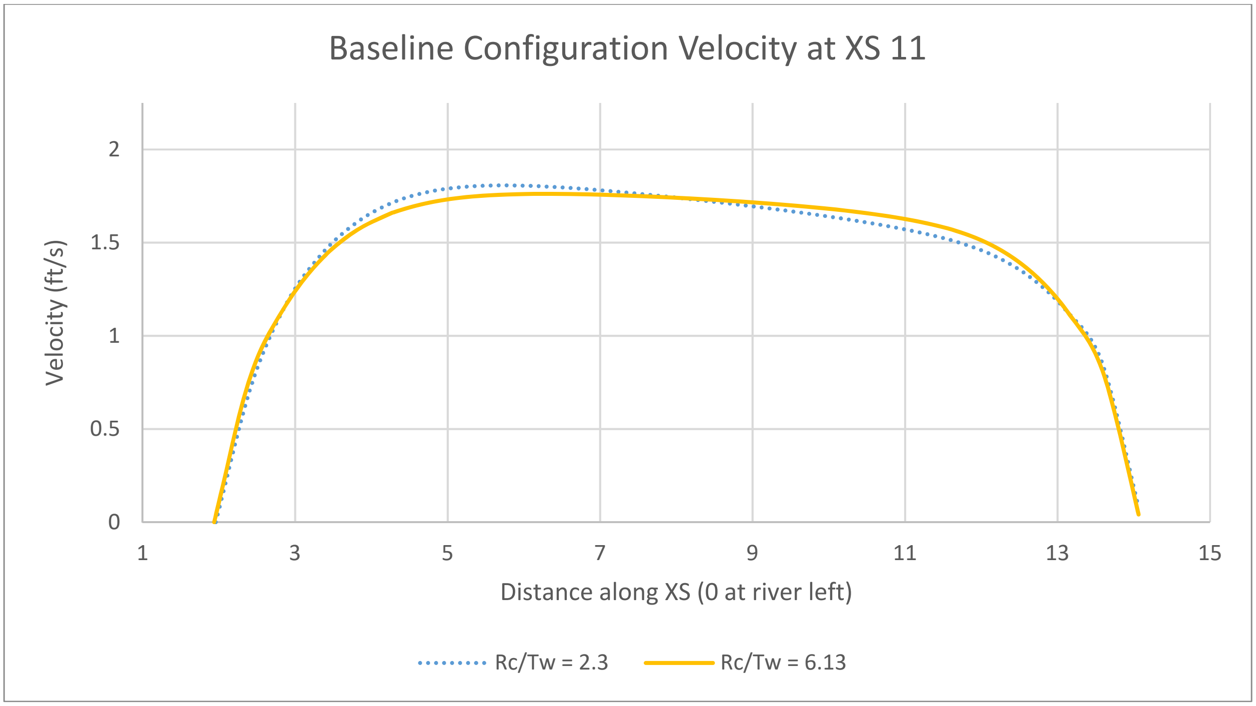

Figure 207: Velocity across XS 11 in the baseline configuration

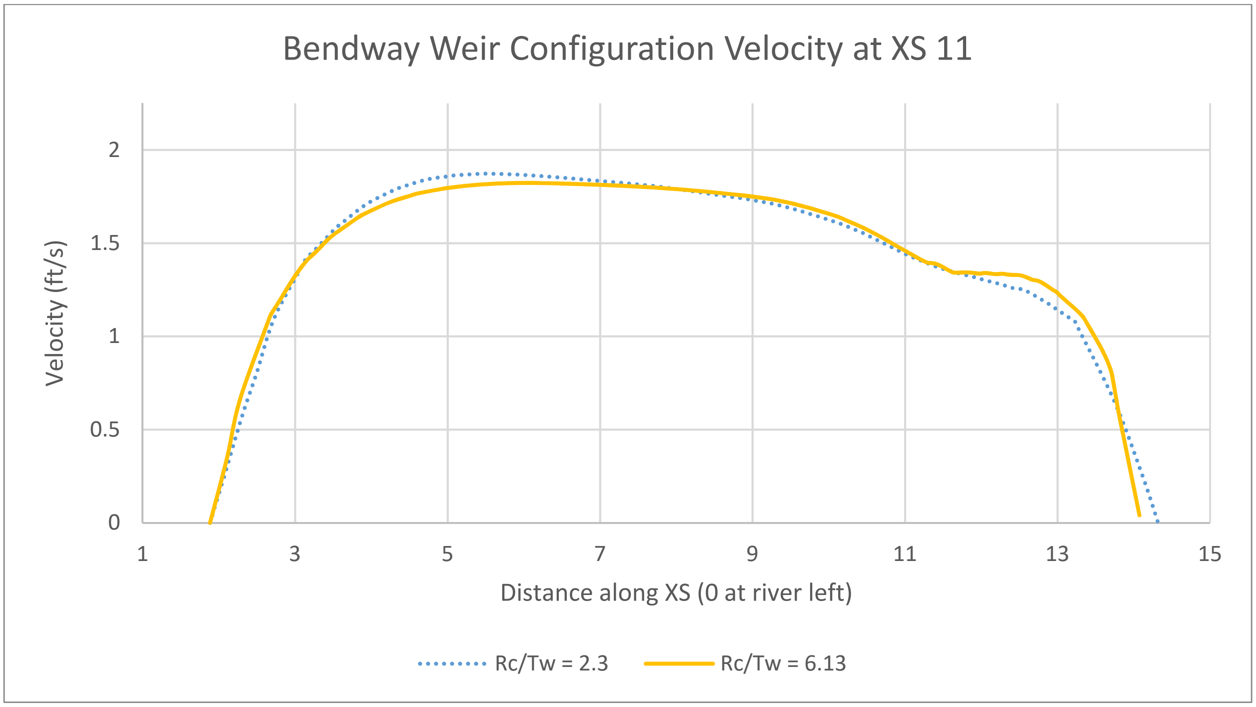

Figure 208: Velocity across XS 11 in the bendway weir configuration

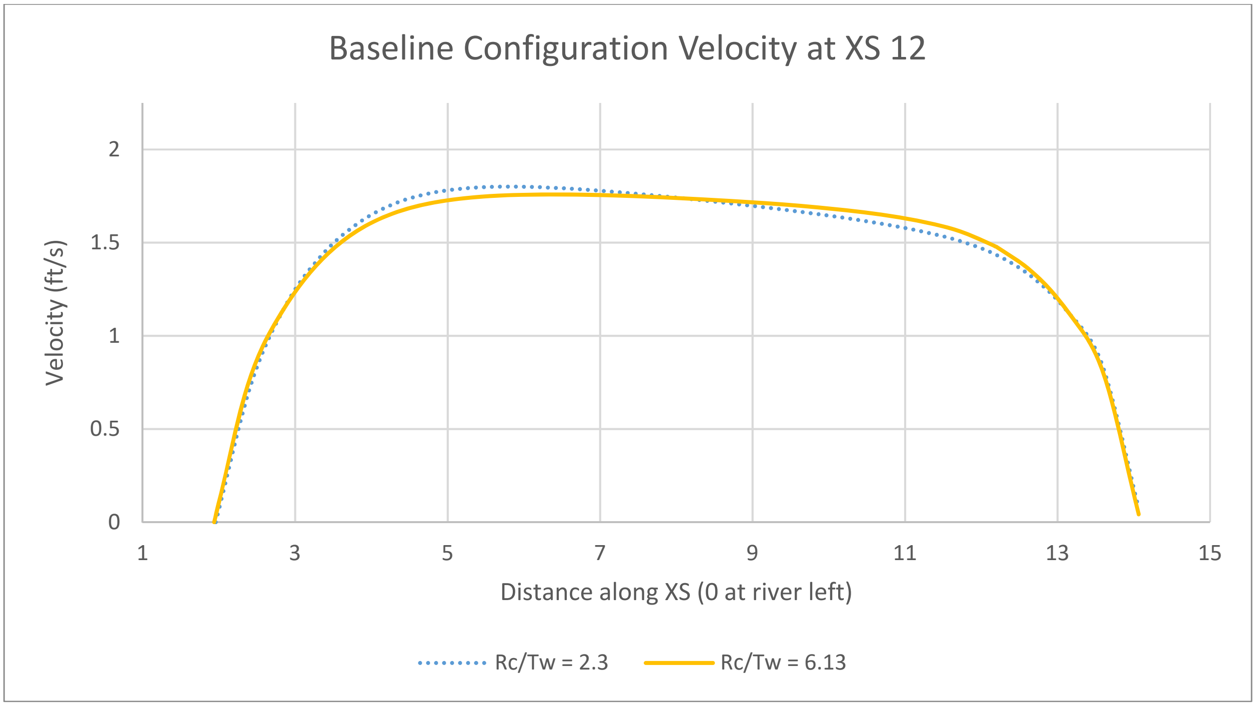

Figure 209: Velocity across XS 12 in the baseline configuration

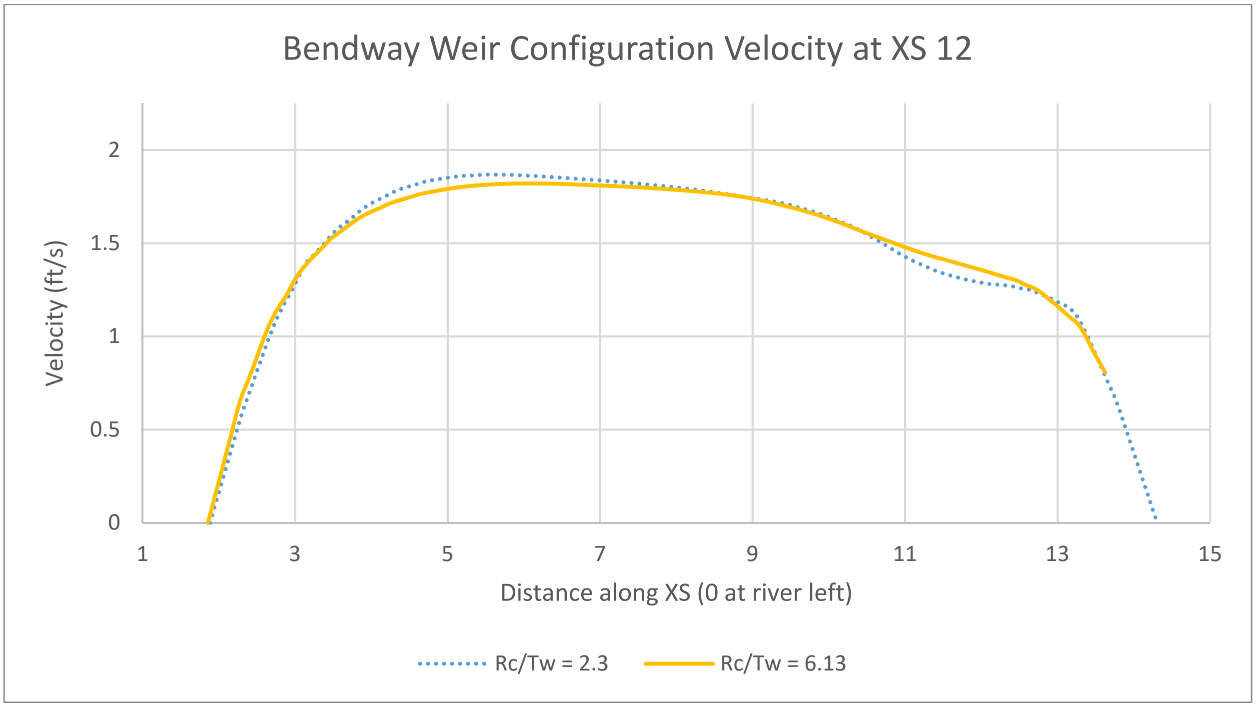

Figure 210: Velocity across XS 12 in the bendway weir configuration

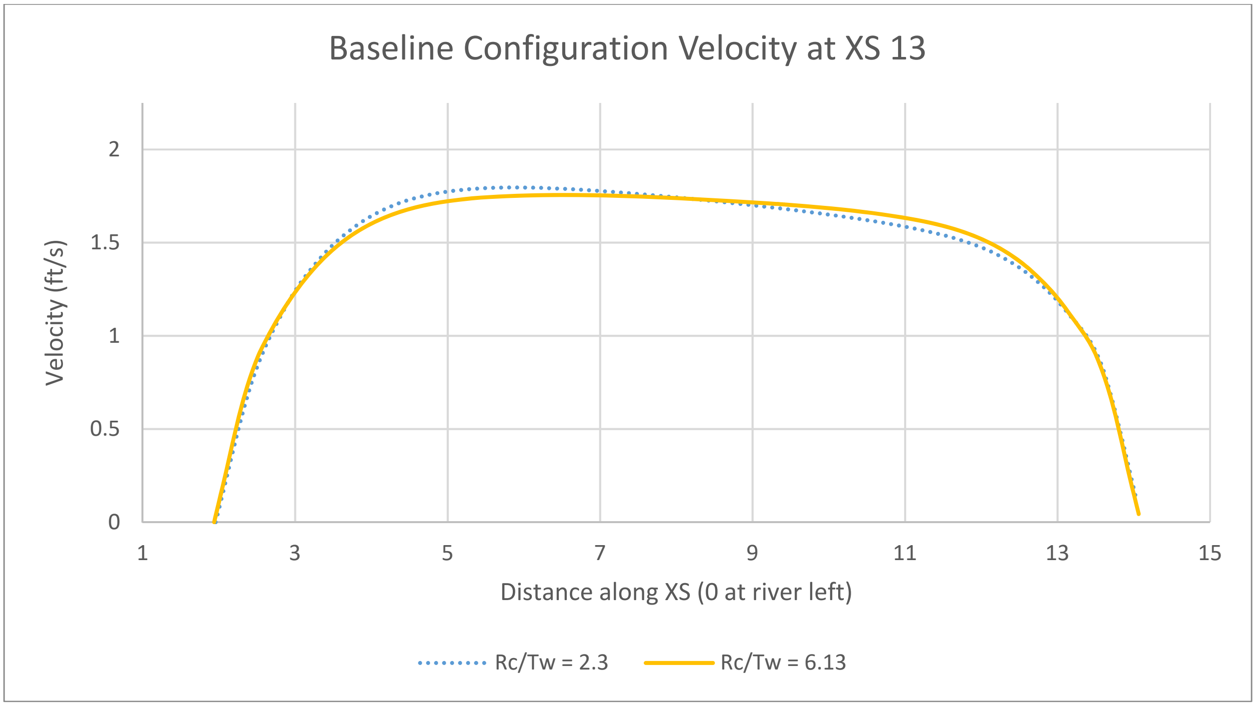

Figure 211: Velocity across XS 13 in the baseline configuration

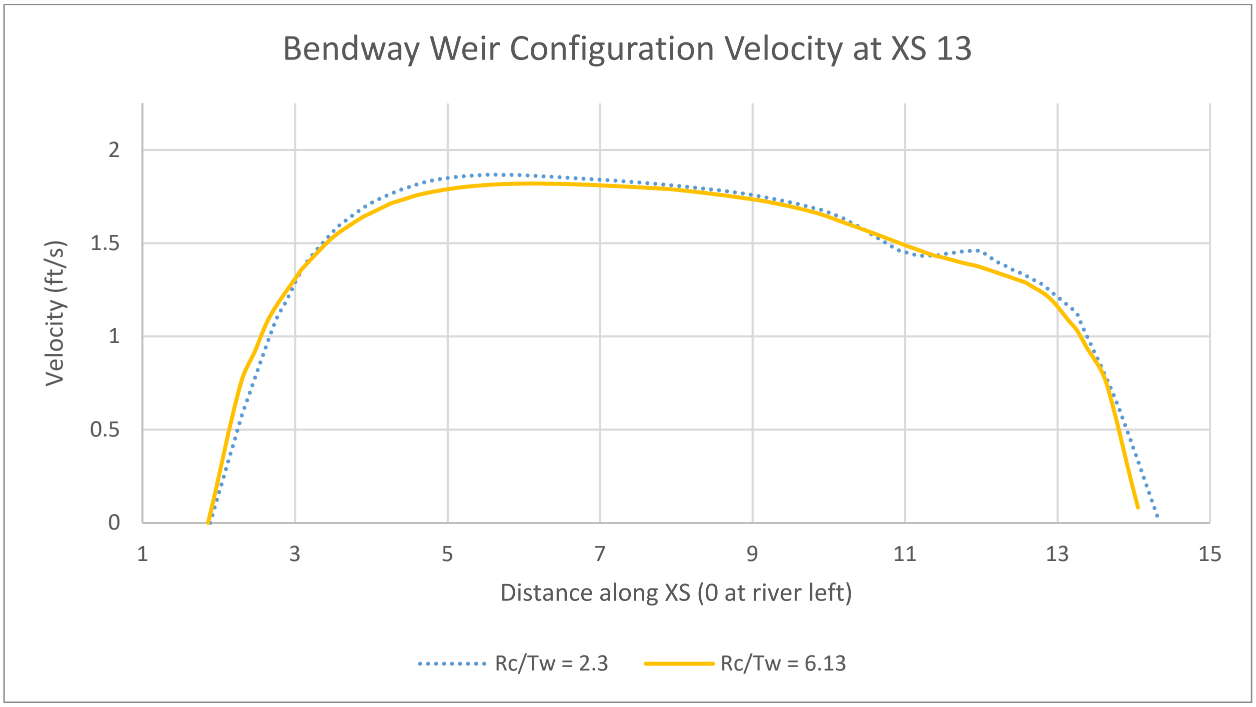

Figure 212: Velocity across XS 13 in the bendway weir configuration

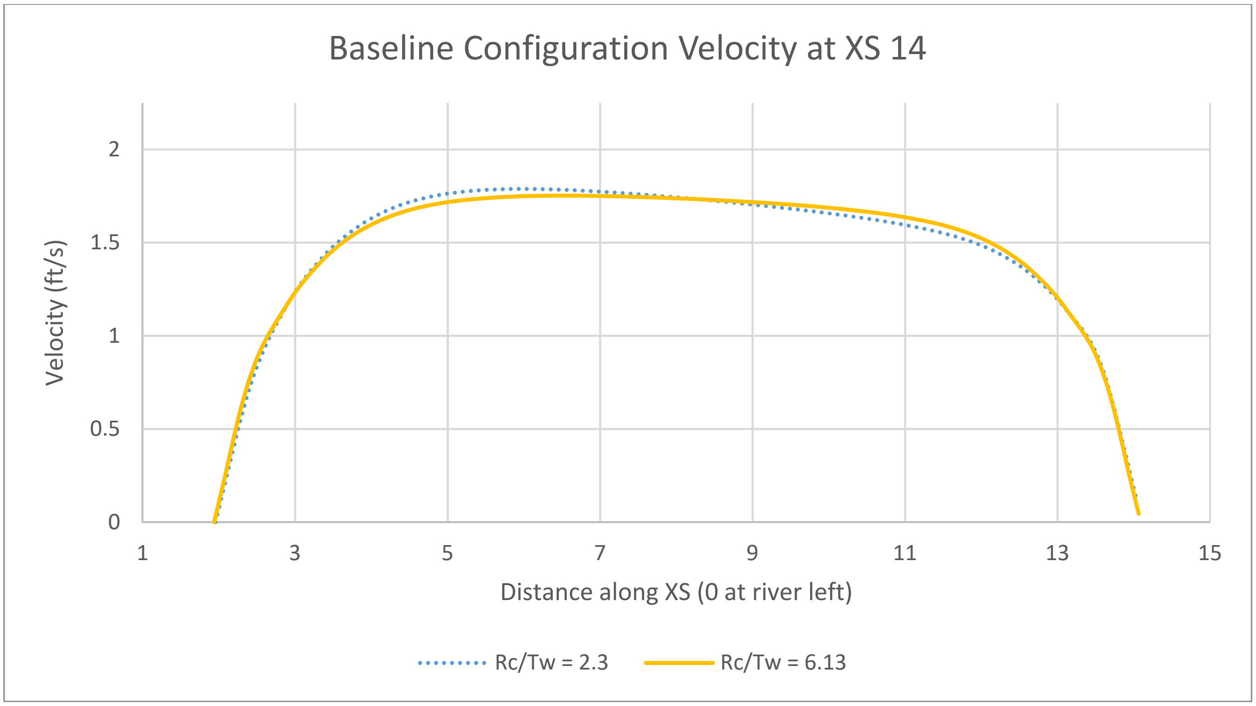

Figure 213: Velocity across XS 14 in the baseline configuration

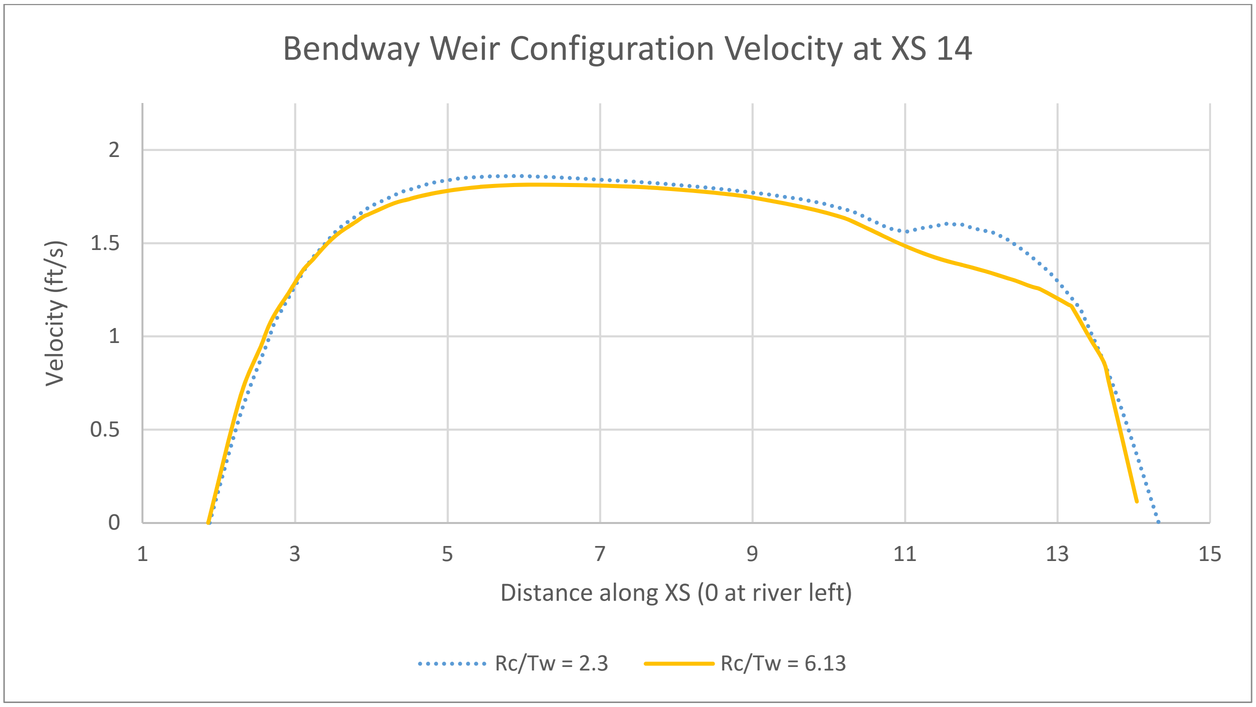

Figure 214: Velocity across XS 14 in the bendway weir configuration

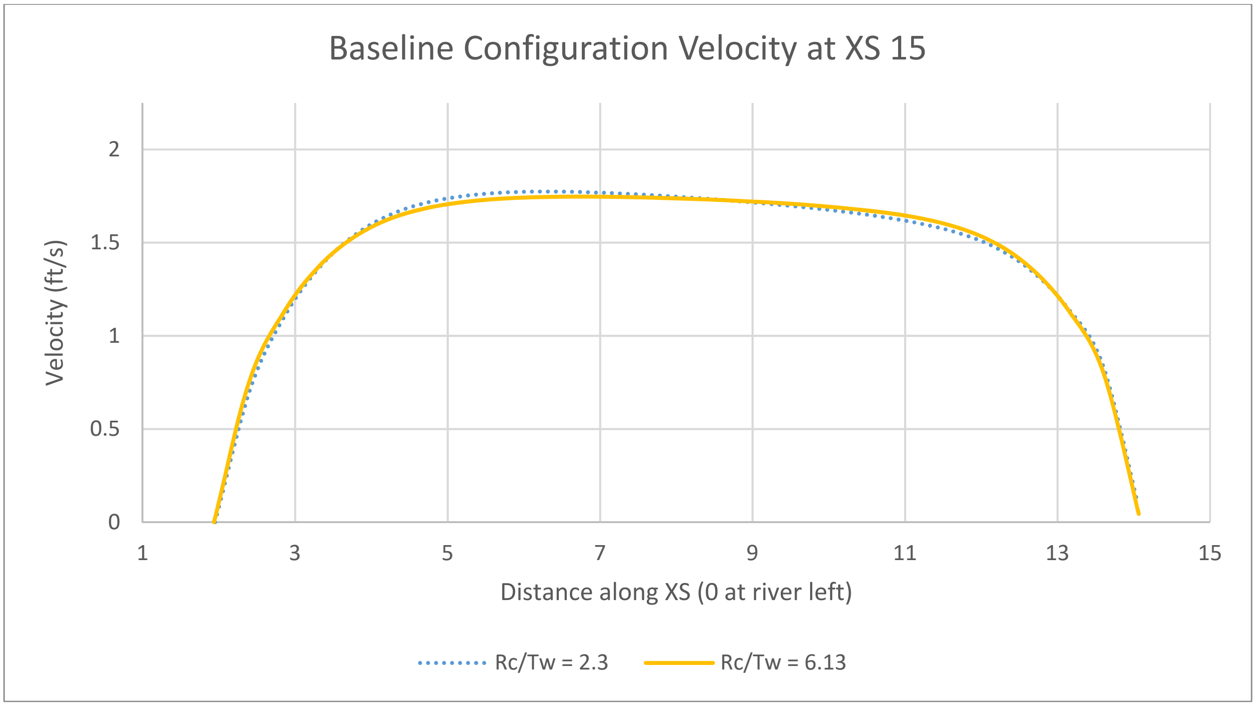

Figure 215: Velocity across XS 15 in the baseline configuration

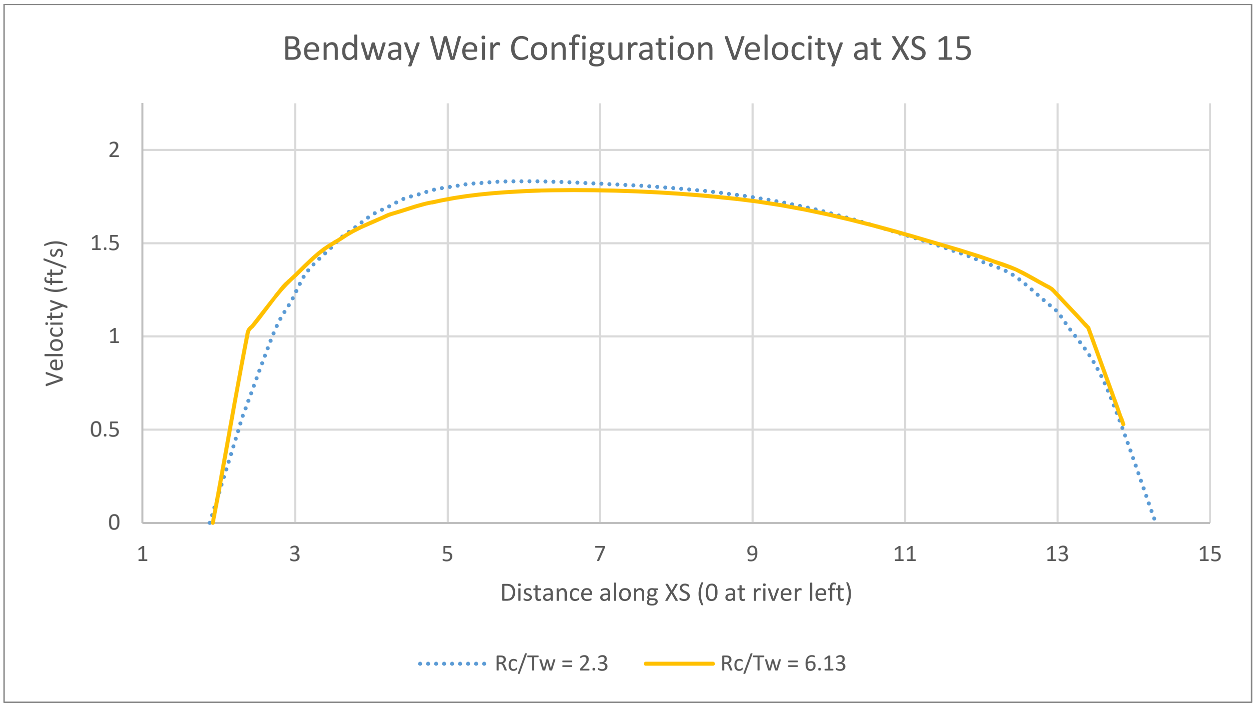

Figure 216: Velocity across XS 15 in the bendway weir configuration

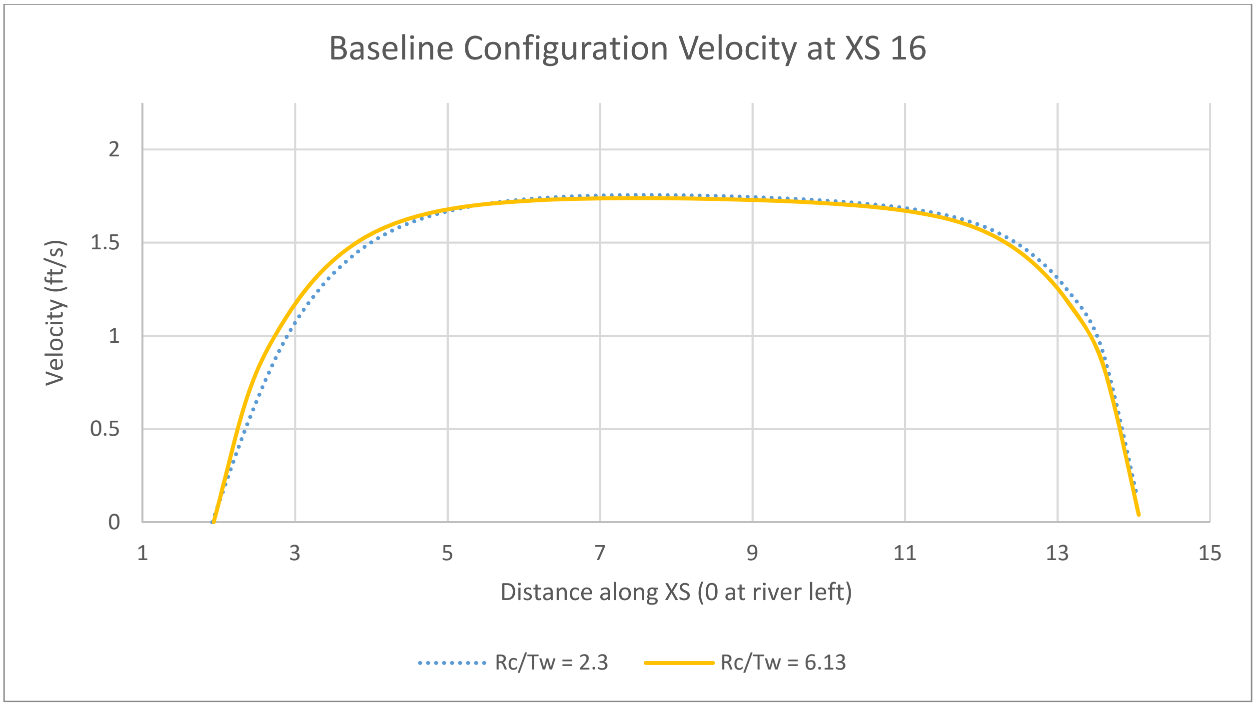

Figure 217: Velocity across XS 16 in the baseline configuration

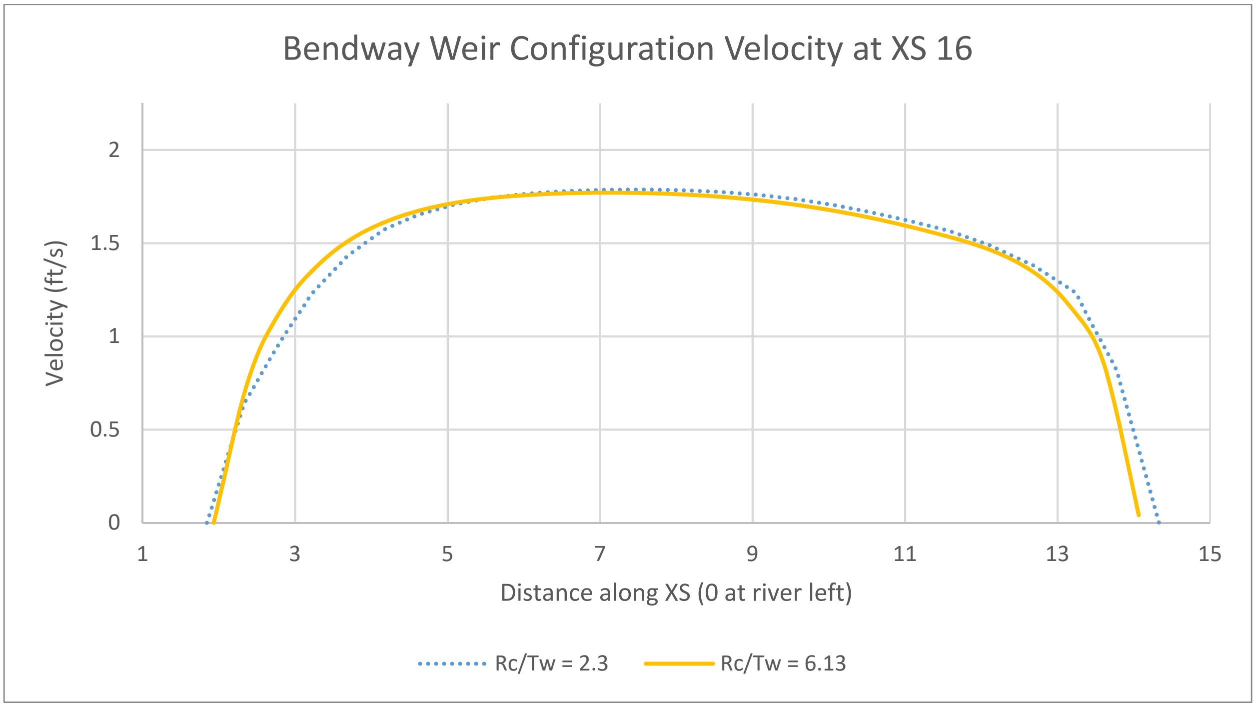

Figure 218: Velocity across XS 16 in the bendway weir configuration

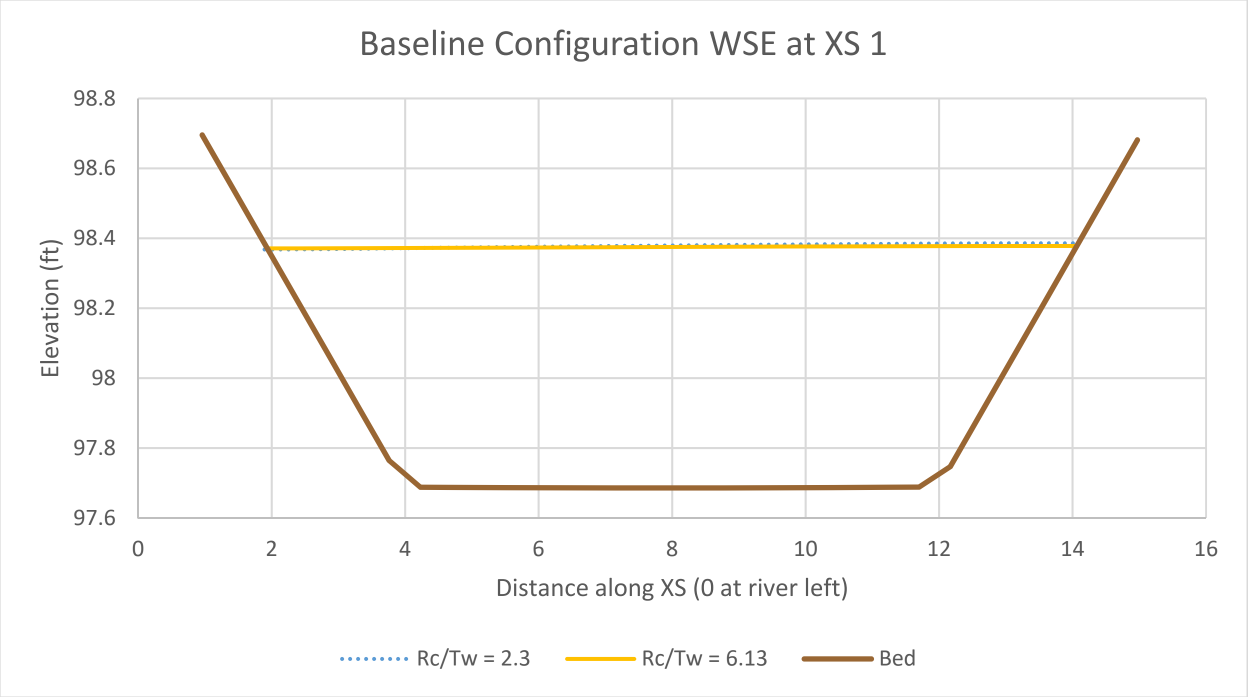

Figure 219: WSE across XS 1 in the baseline configuration

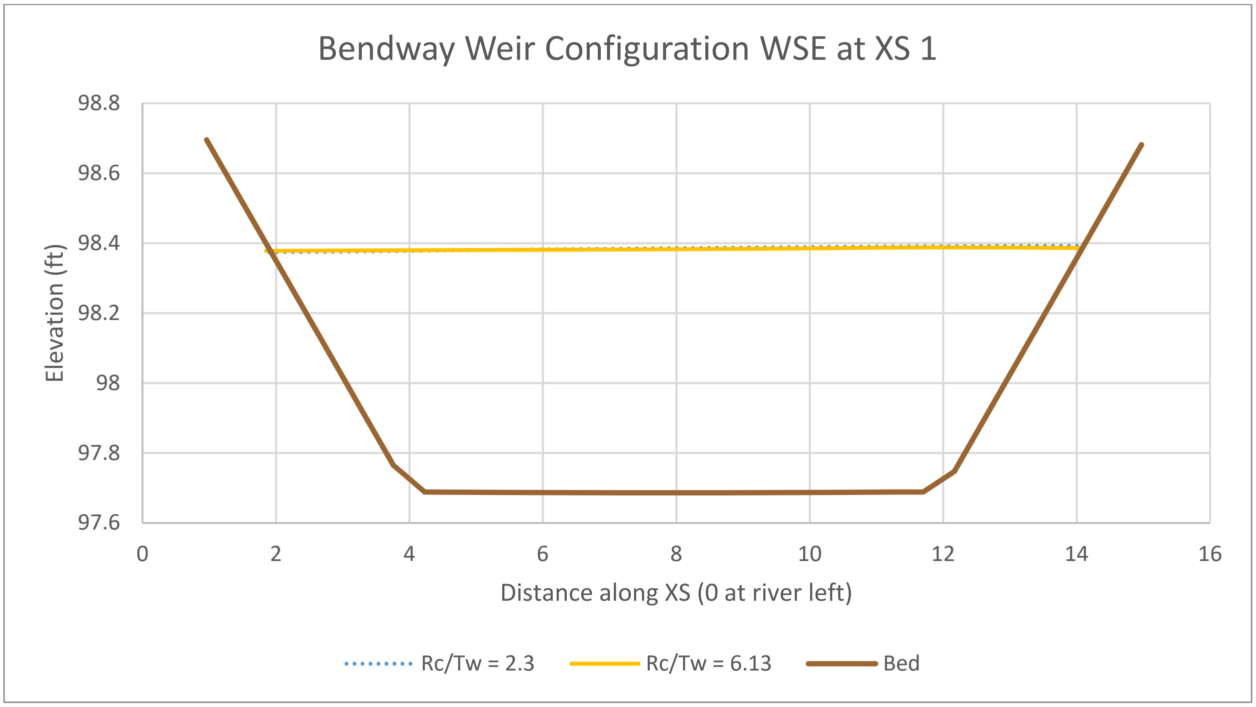

Figure 220: WSE across XS 1 in the bendway weir configuration

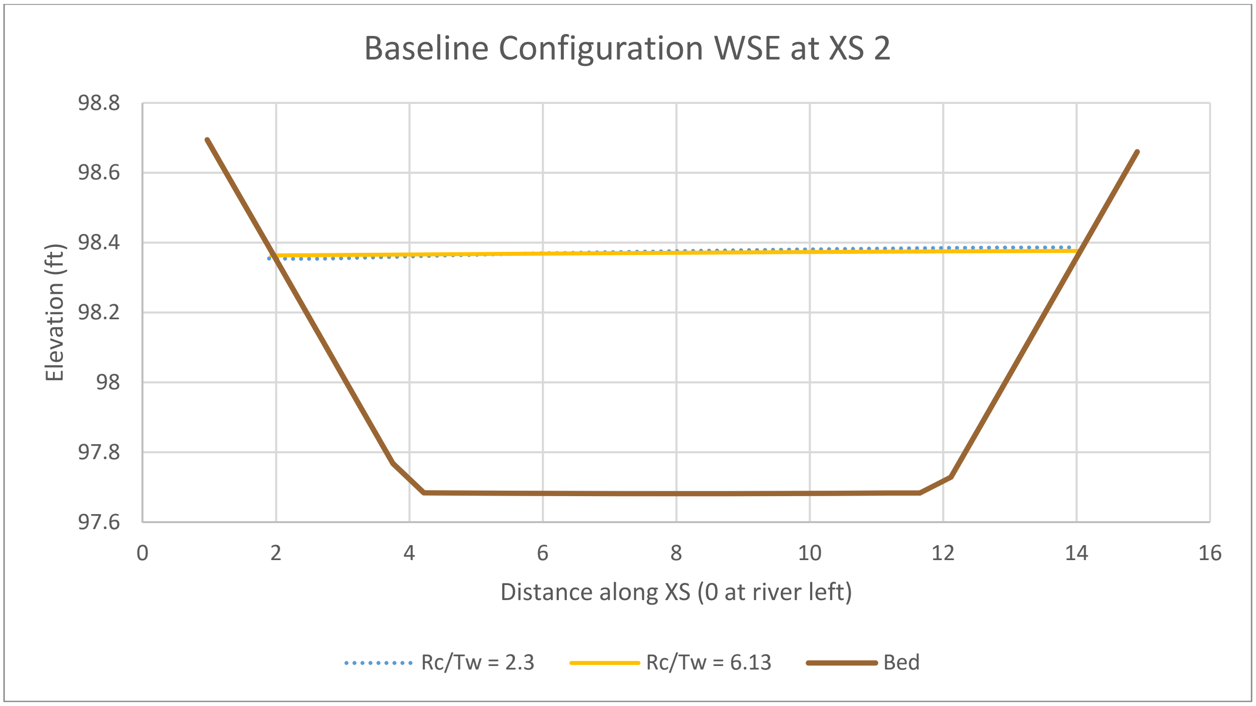

Figure 221: WSE across XS 2 in the baseline configuration

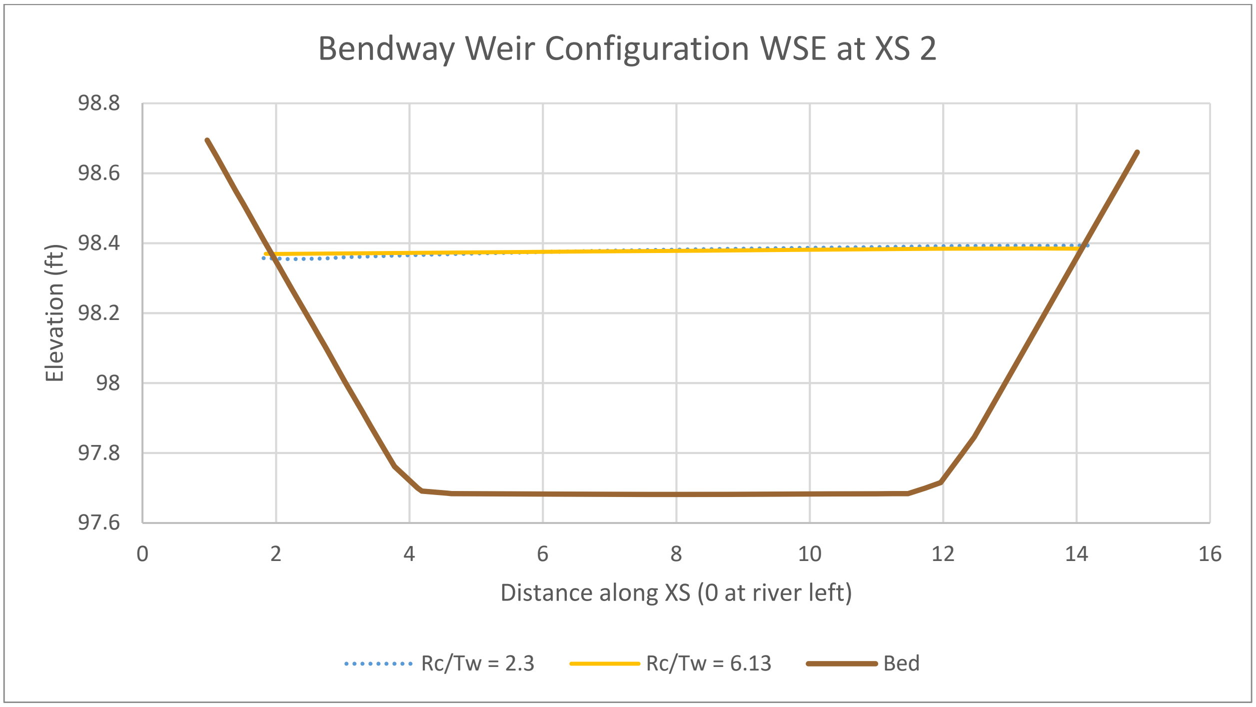

Figure 222: WSE across XS 2 in the bendway weir configuration

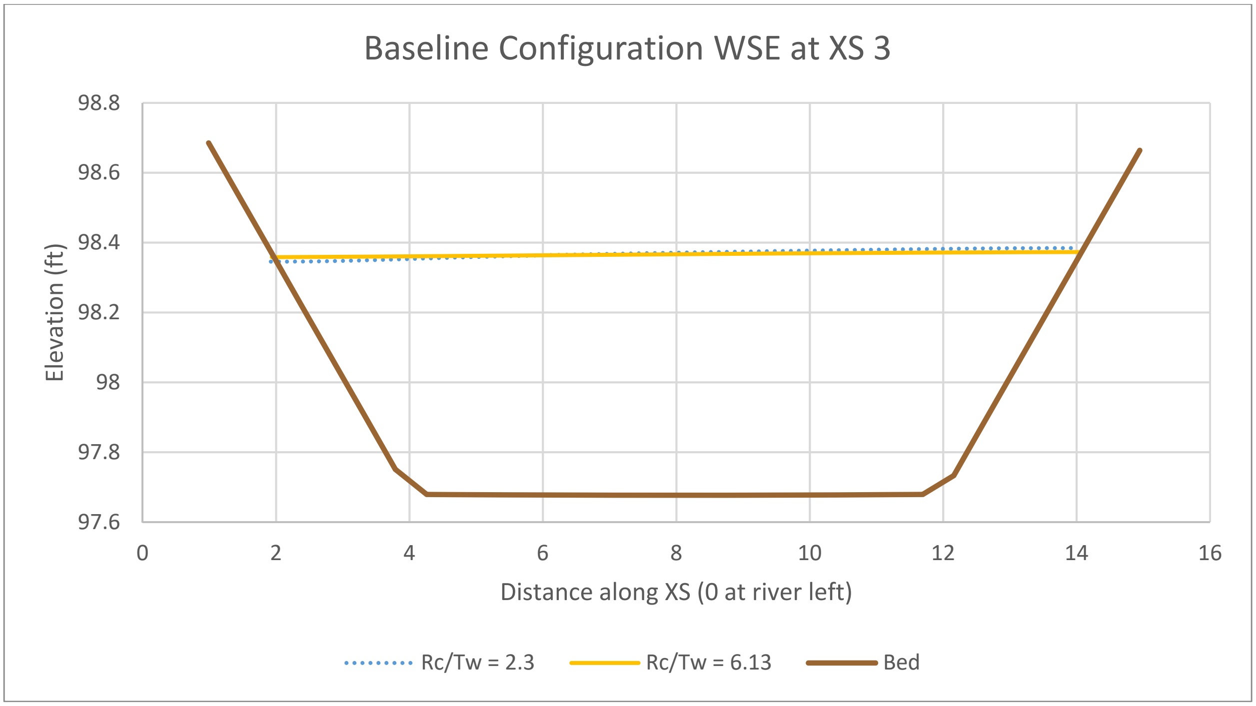

Figure 223: WSE across XS 3 in the baseline configuration

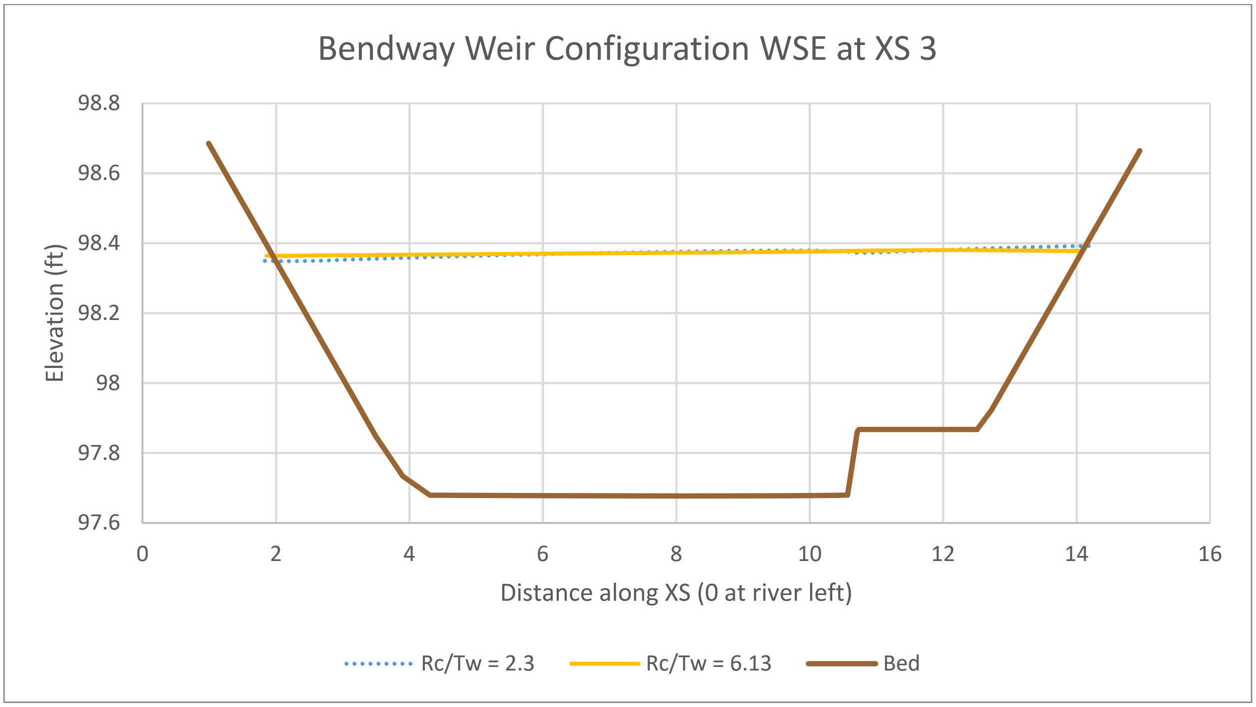

Figure 224: WSE across XS 3 in the bendway weir configuration

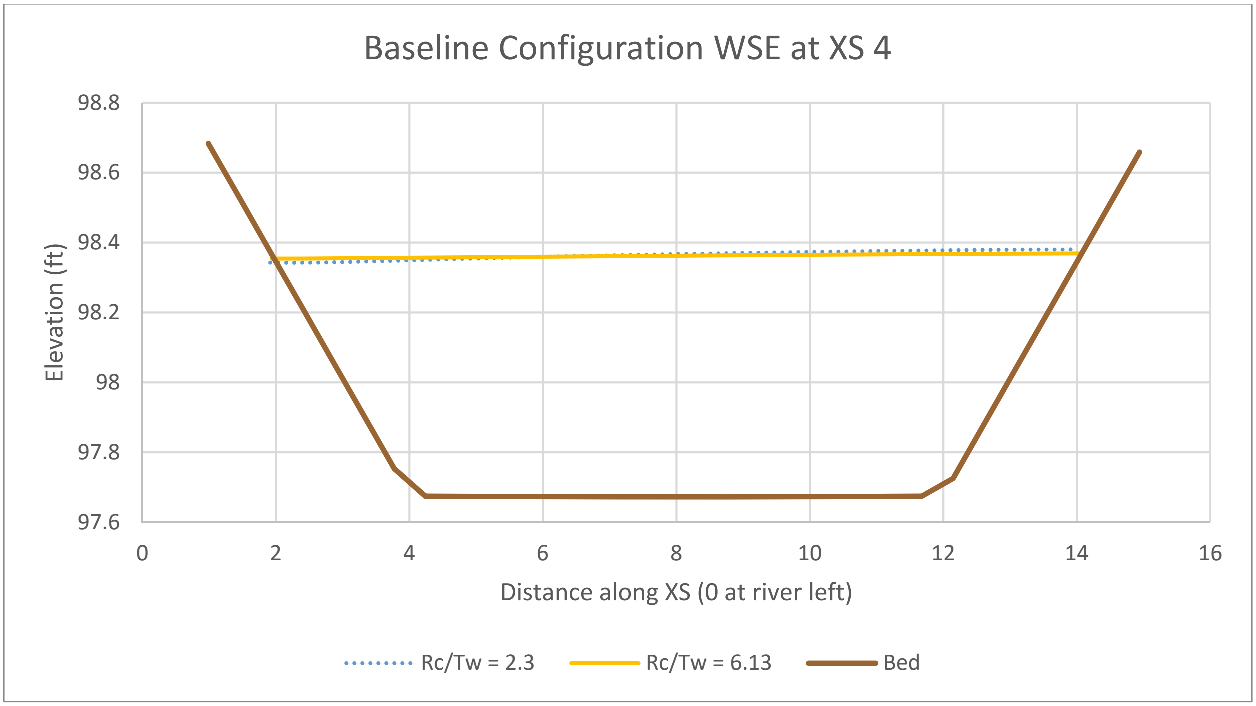

Figure 225: WSE across XS 4 in the baseline configuration

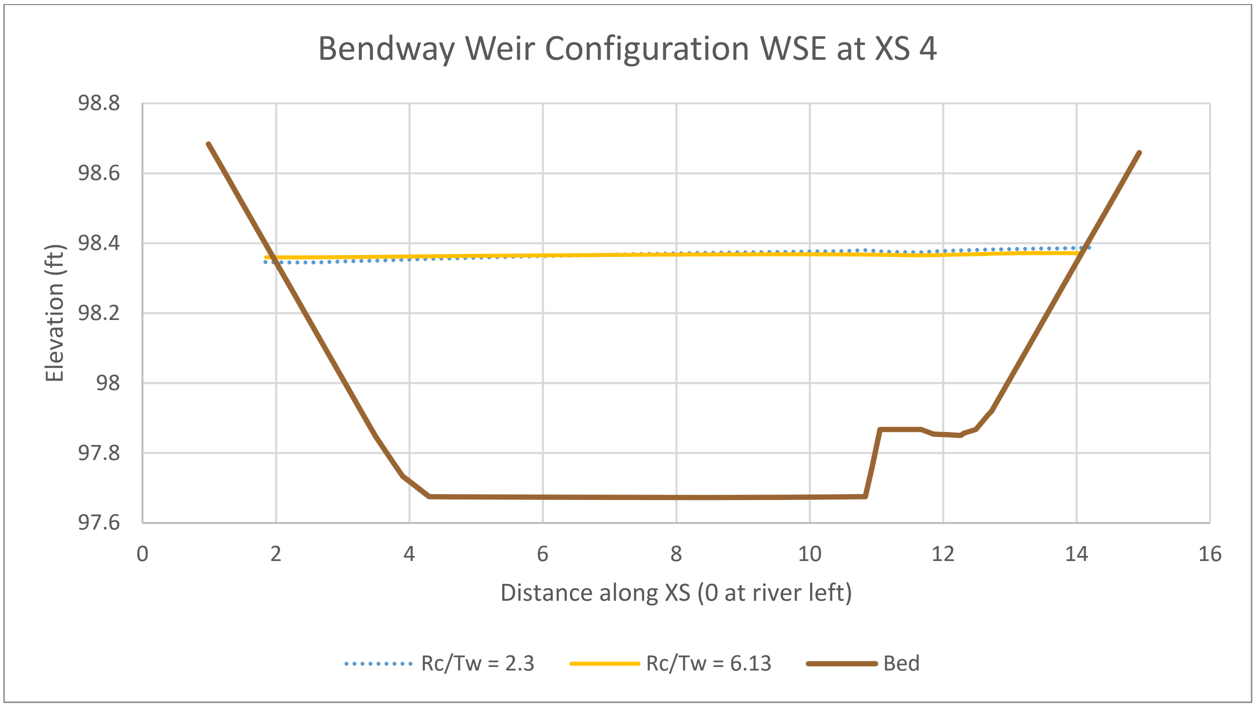

Figure 226: WSE across XS 4 in the bendway weir configuration

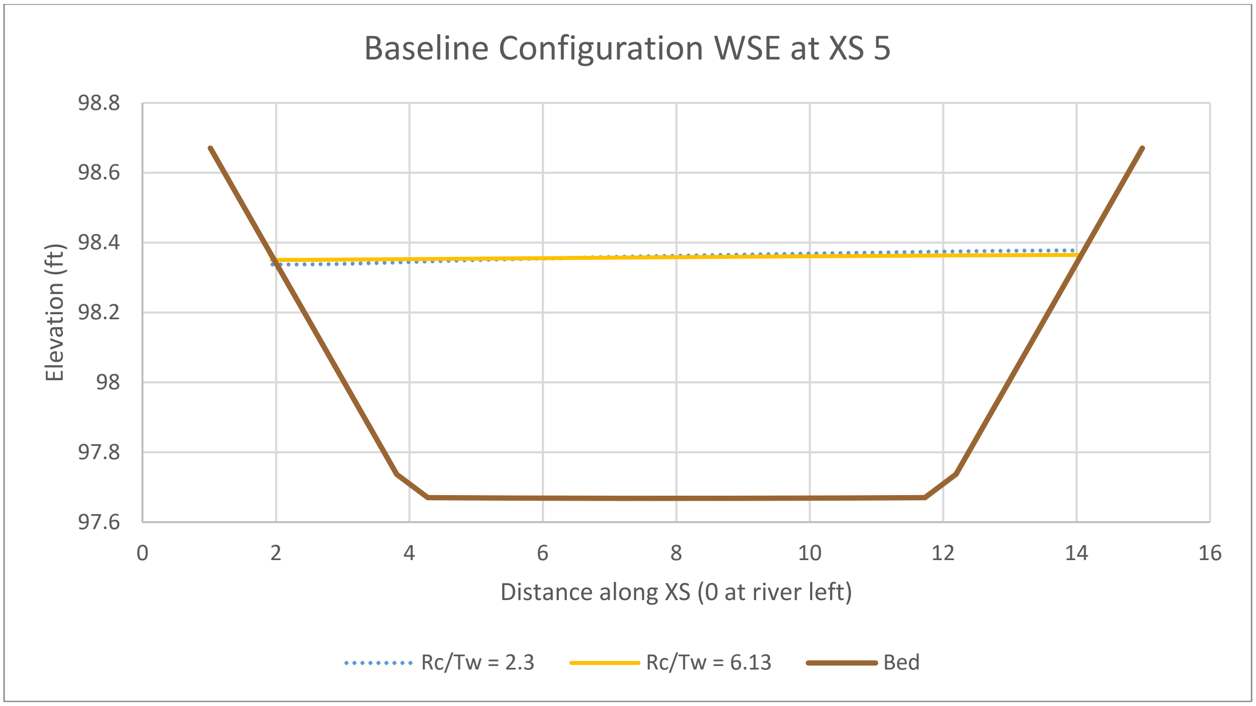

Figure 227: WSE across XS 5 in the baseline configuration

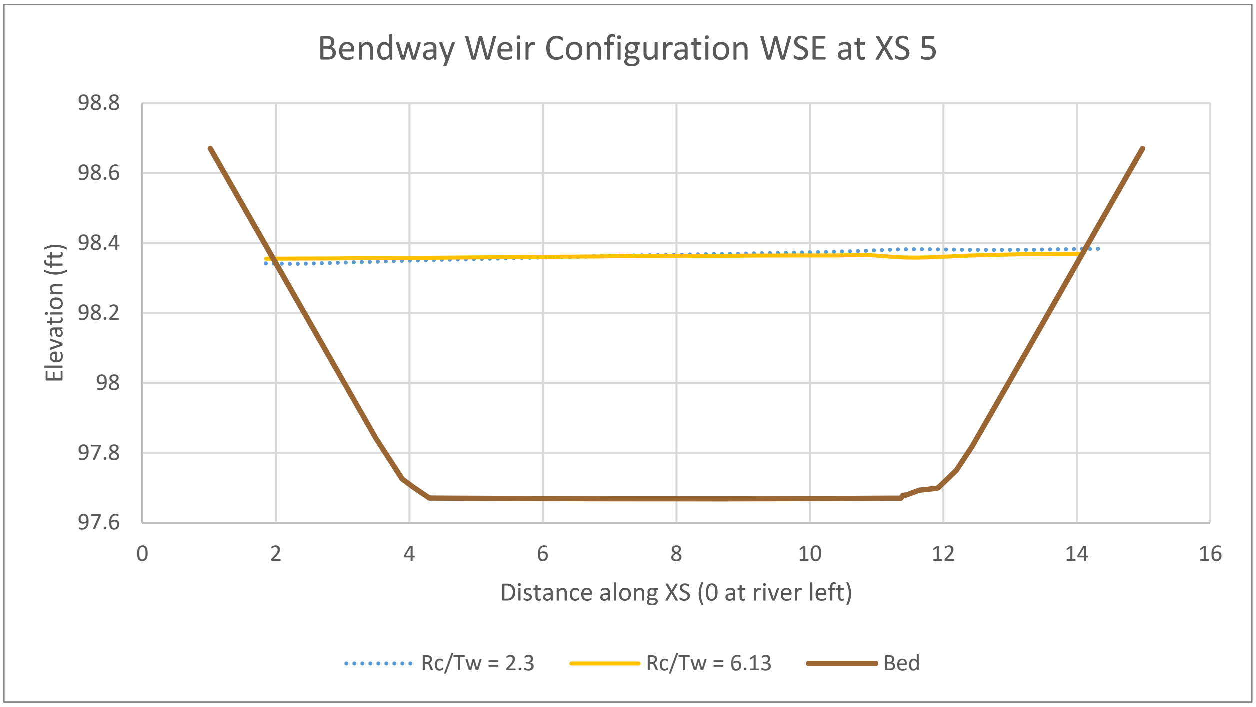

Figure 228: WSE across XS 5 in the bendway weir configuration

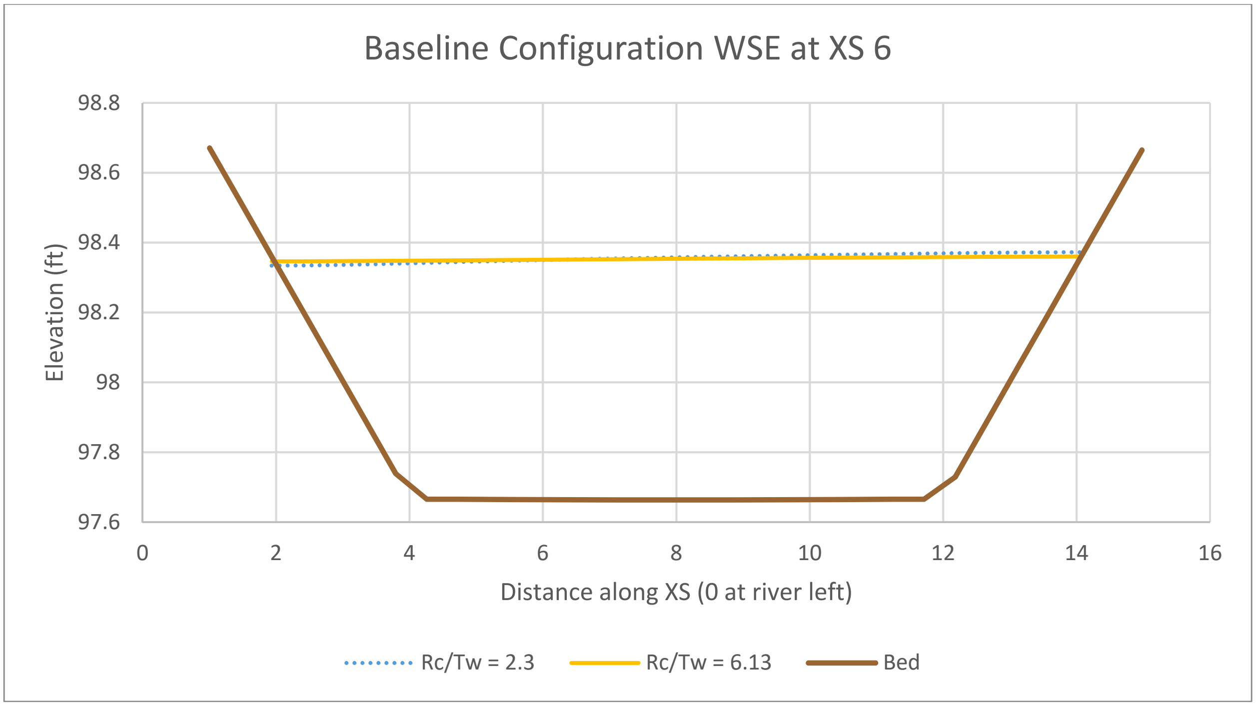

Figure 229: WSE across XS 6 in the baseline configuration

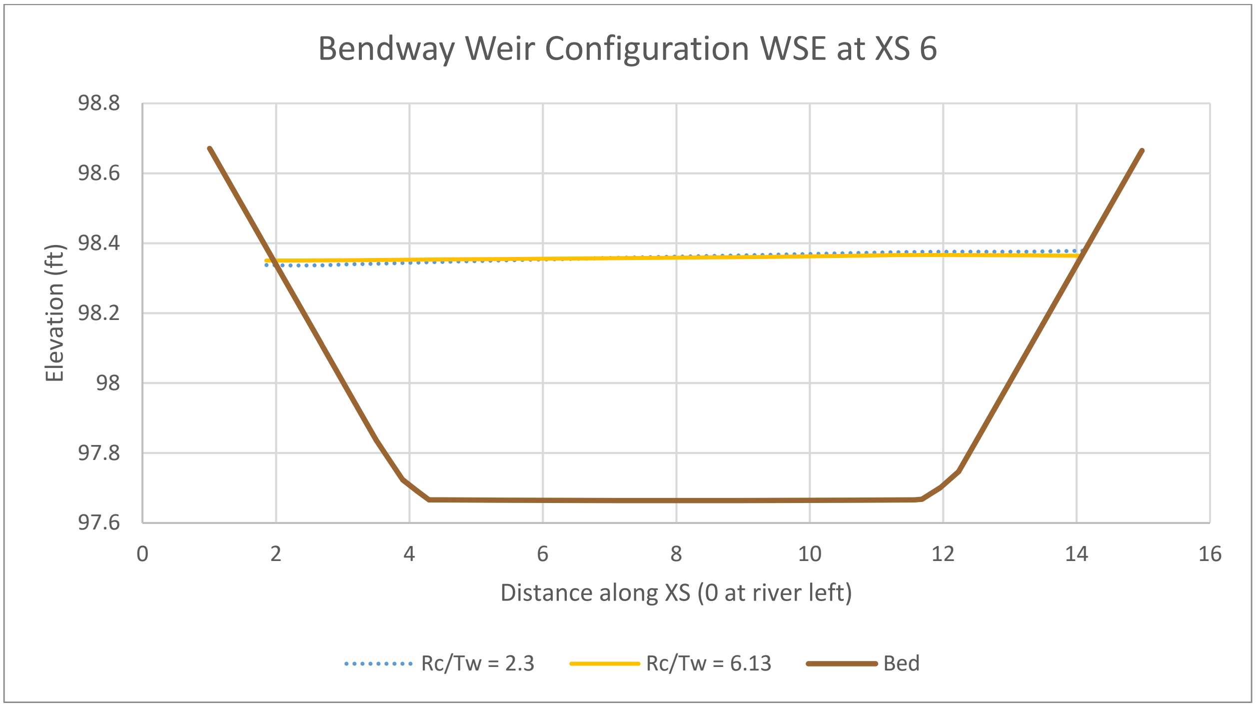

Figure 230: WSE across XS 6 in the bendway weir configuration

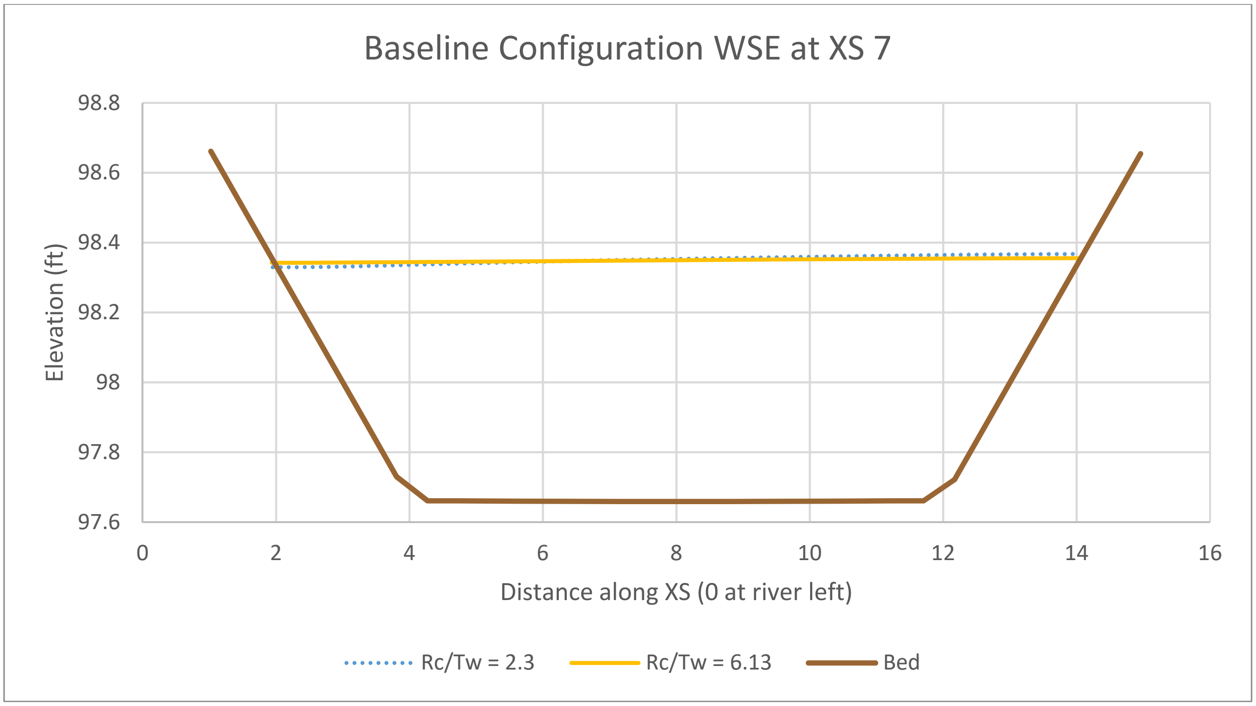

Figure 231: WSE across XS 7 in the baseline configuration

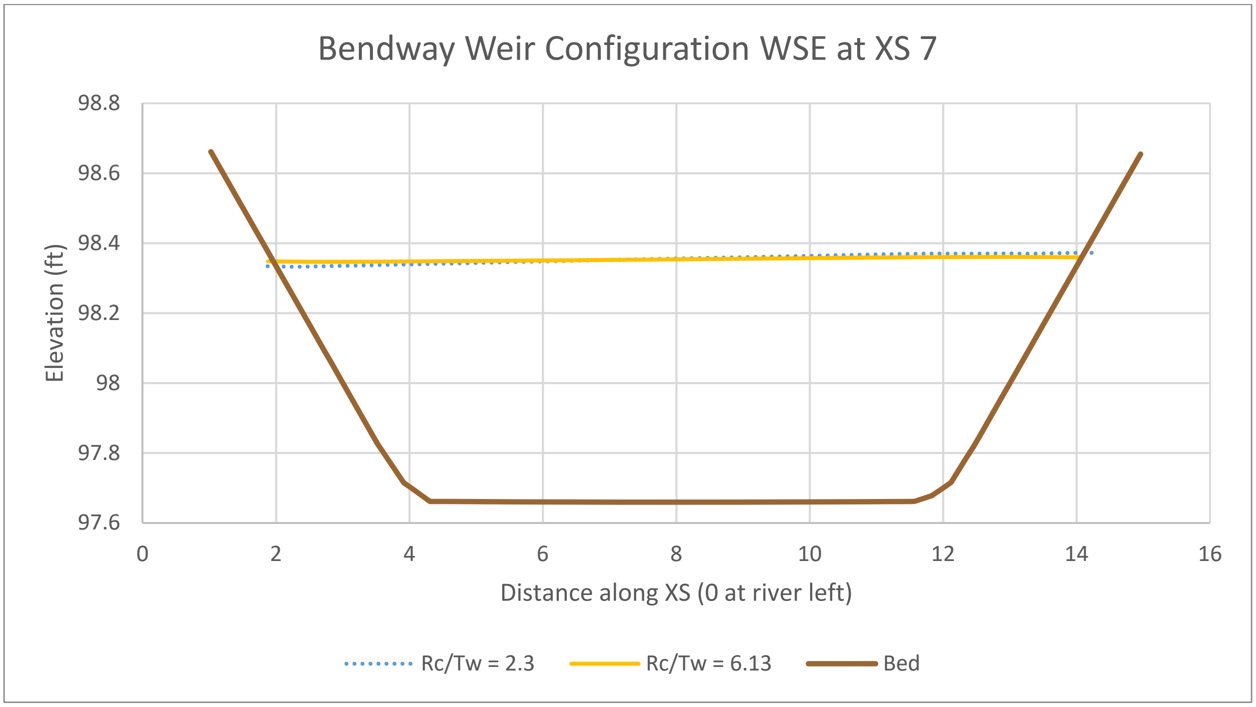

Figure 232: WSE across XS 7 in the bendway weir configuration

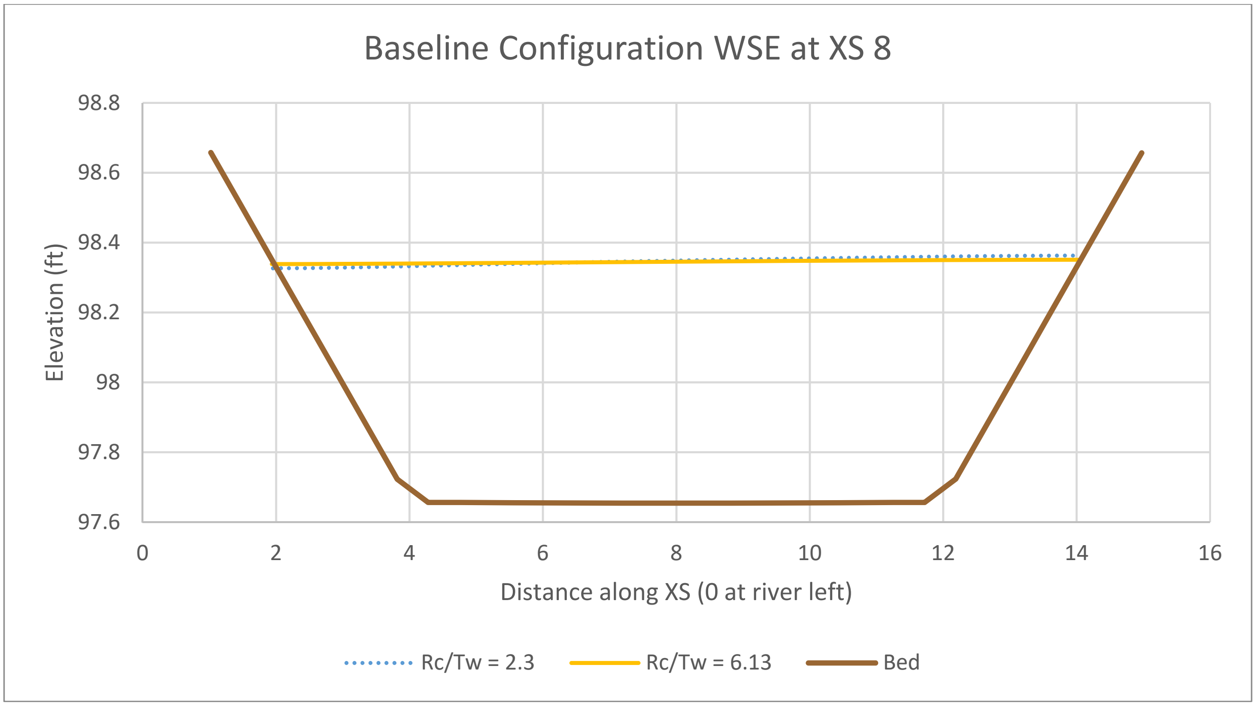

Figure 233: WSE across XS 8 in the baseline configuration

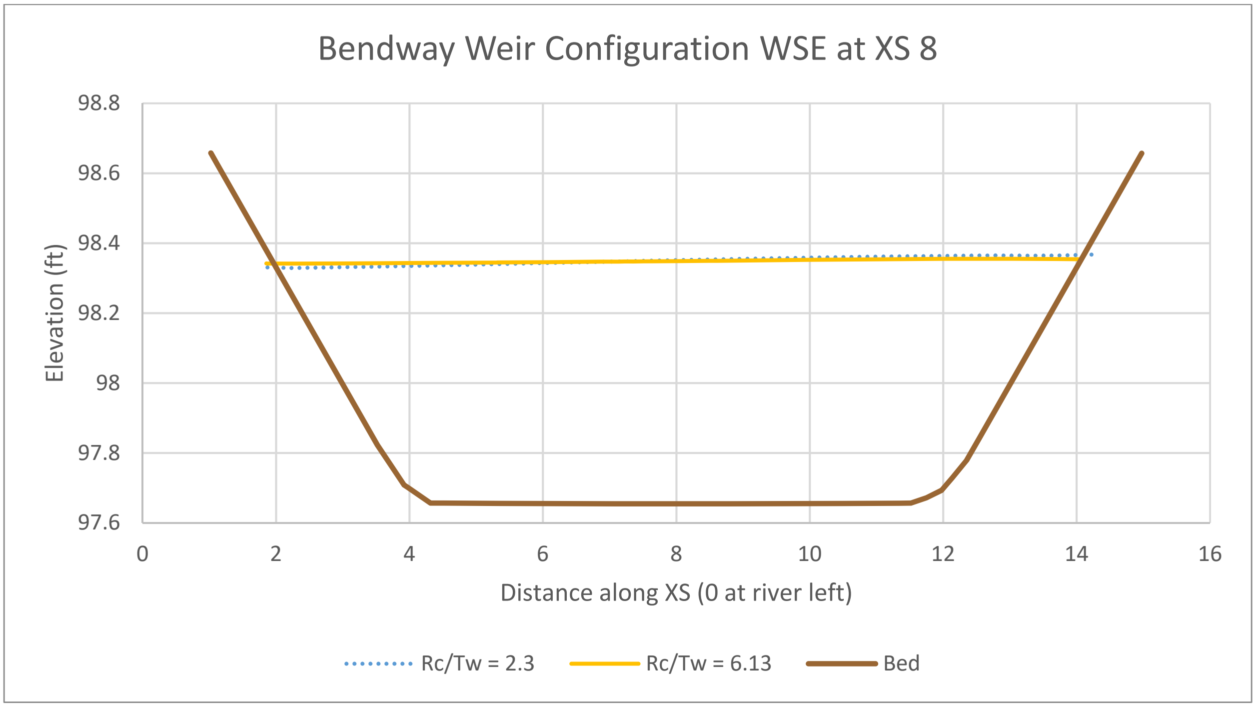

Figure 234: WSE across XS 8 in the bendway weir configuration

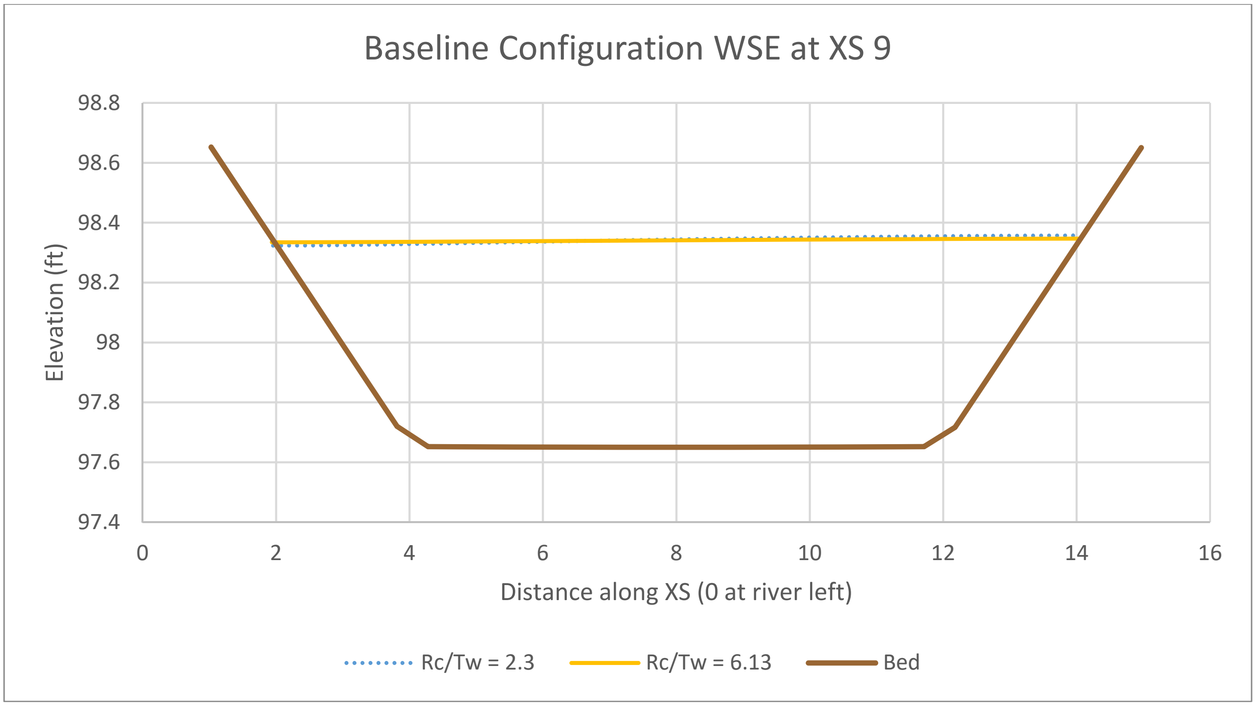

Figure 235: WSE across XS 9 in the baseline configuration

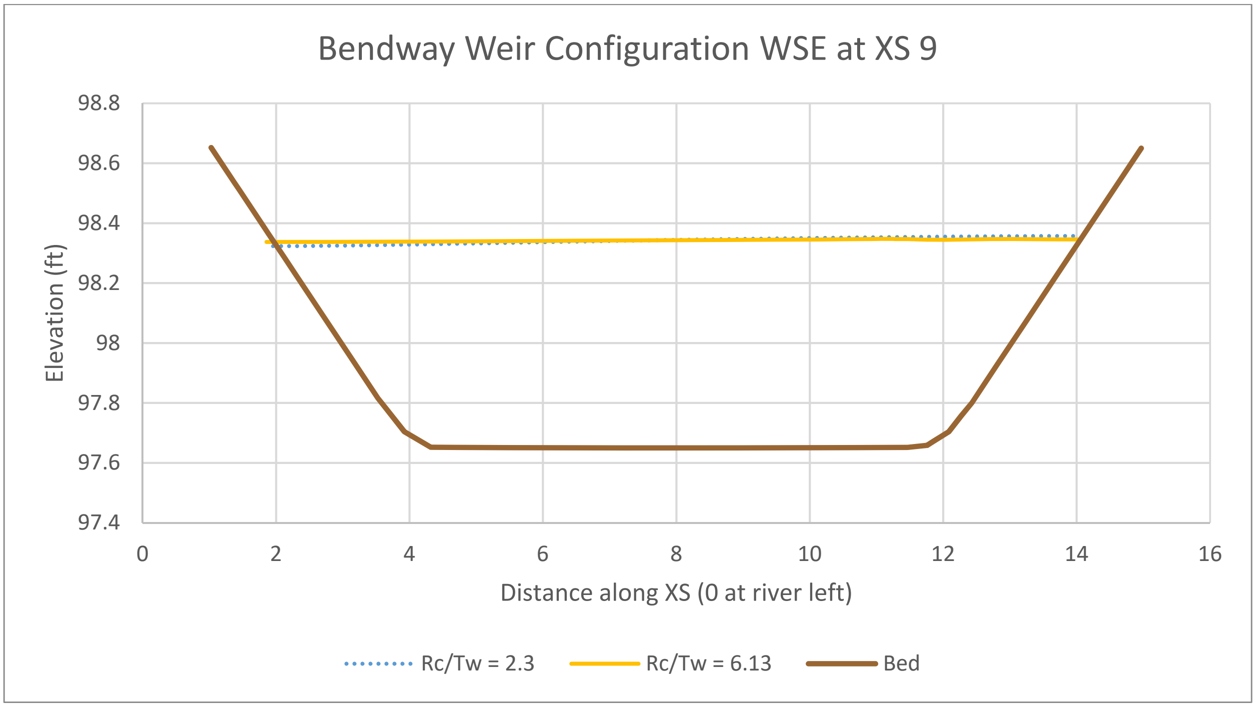

Figure 236: WSE across XS 9 in the bendway weir configuration

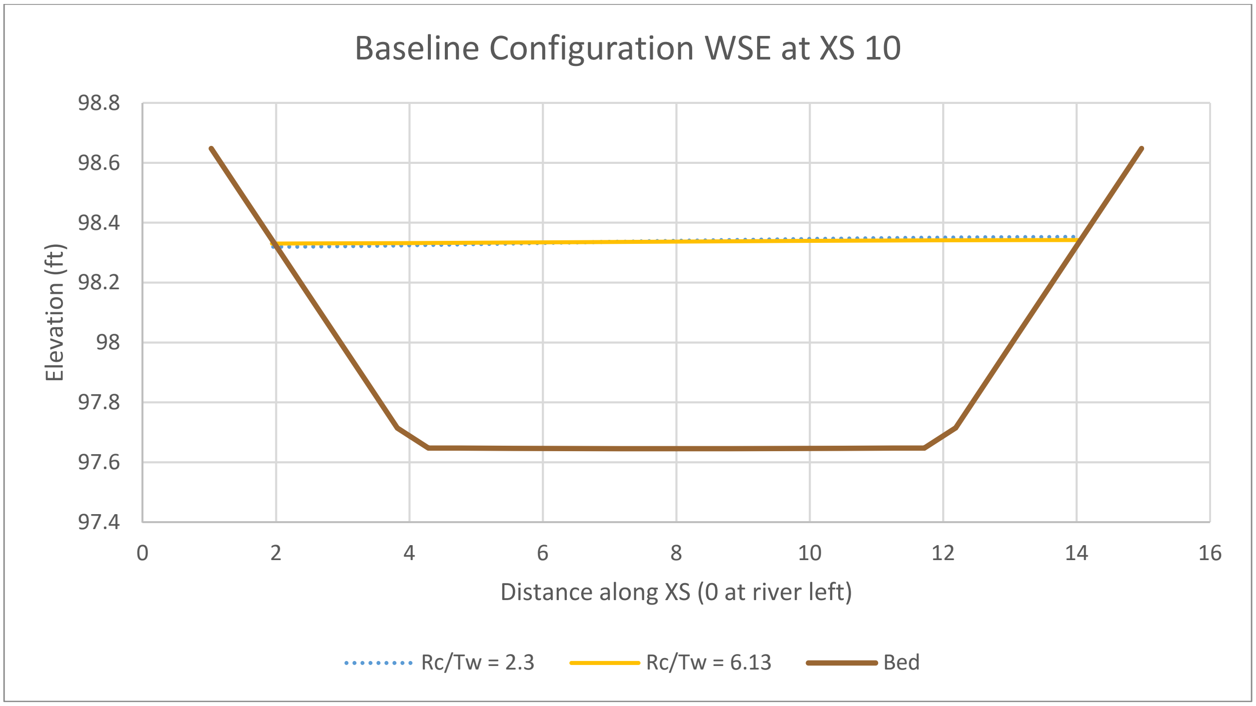

Figure 237: WSE across XS 10 in the baseline configuration

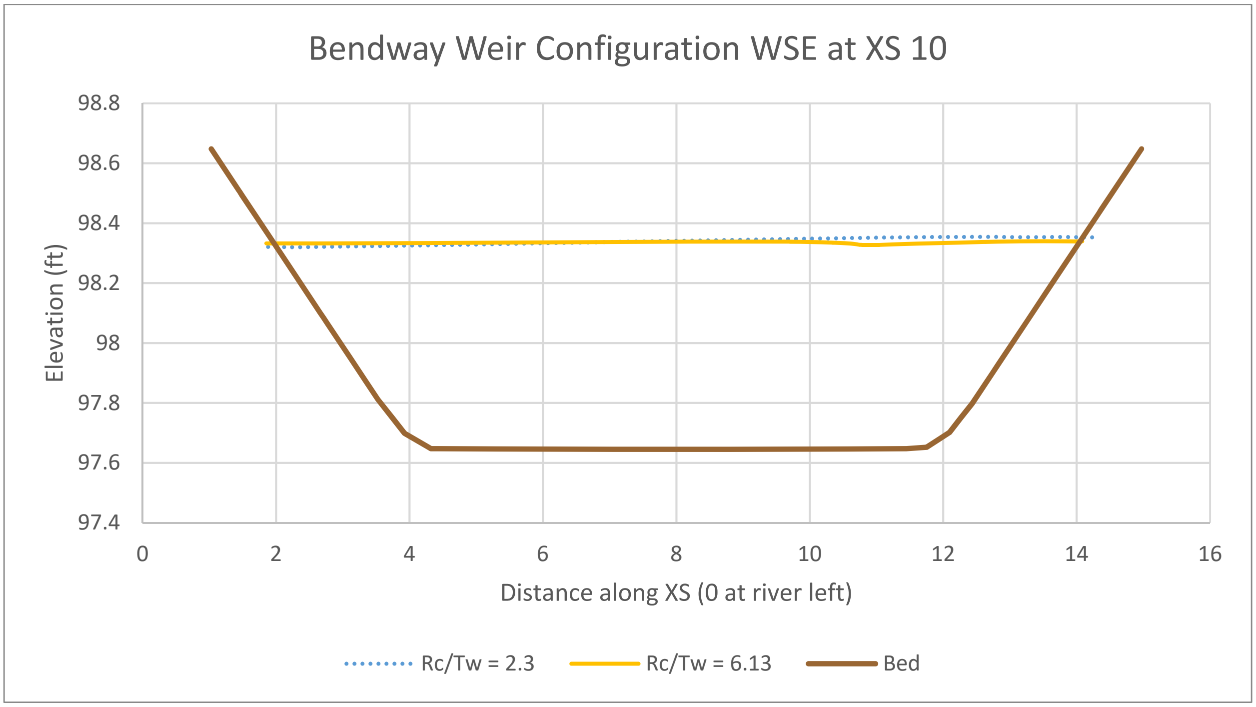

Figure 238: WSE across XS 10 in the bendway weir configuration

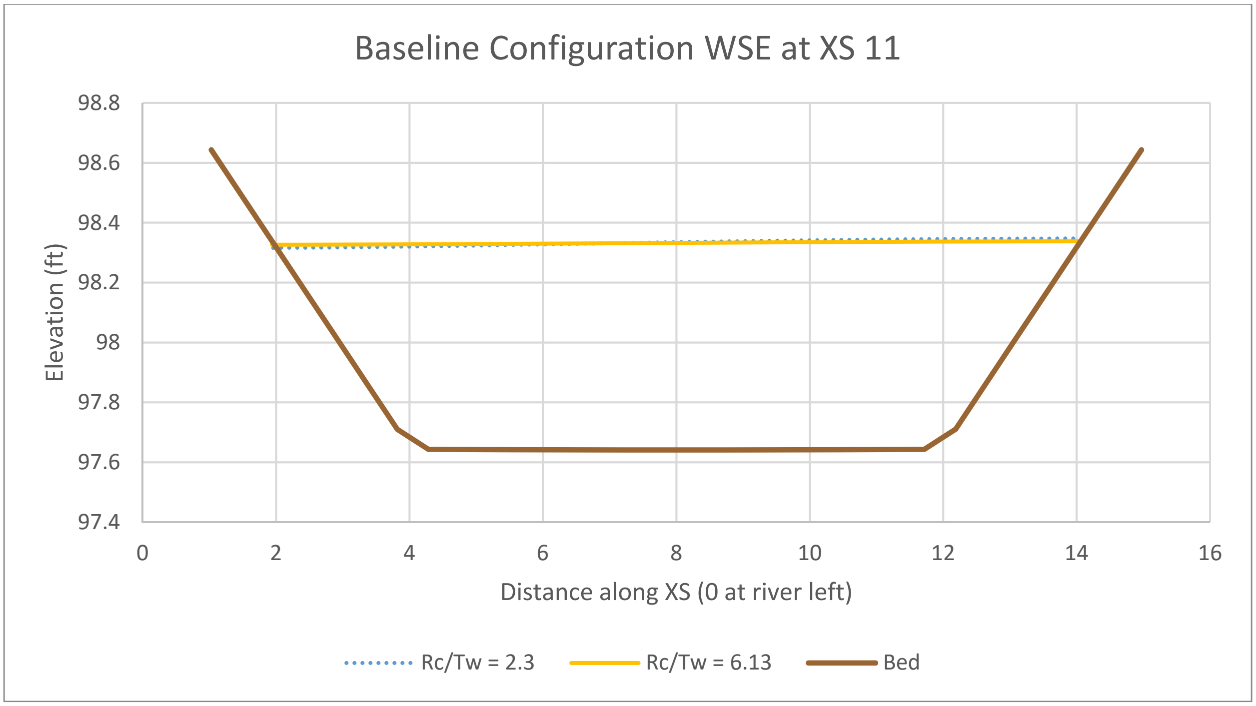

Figure 239: WSE across XS 11 in the baseline configuration

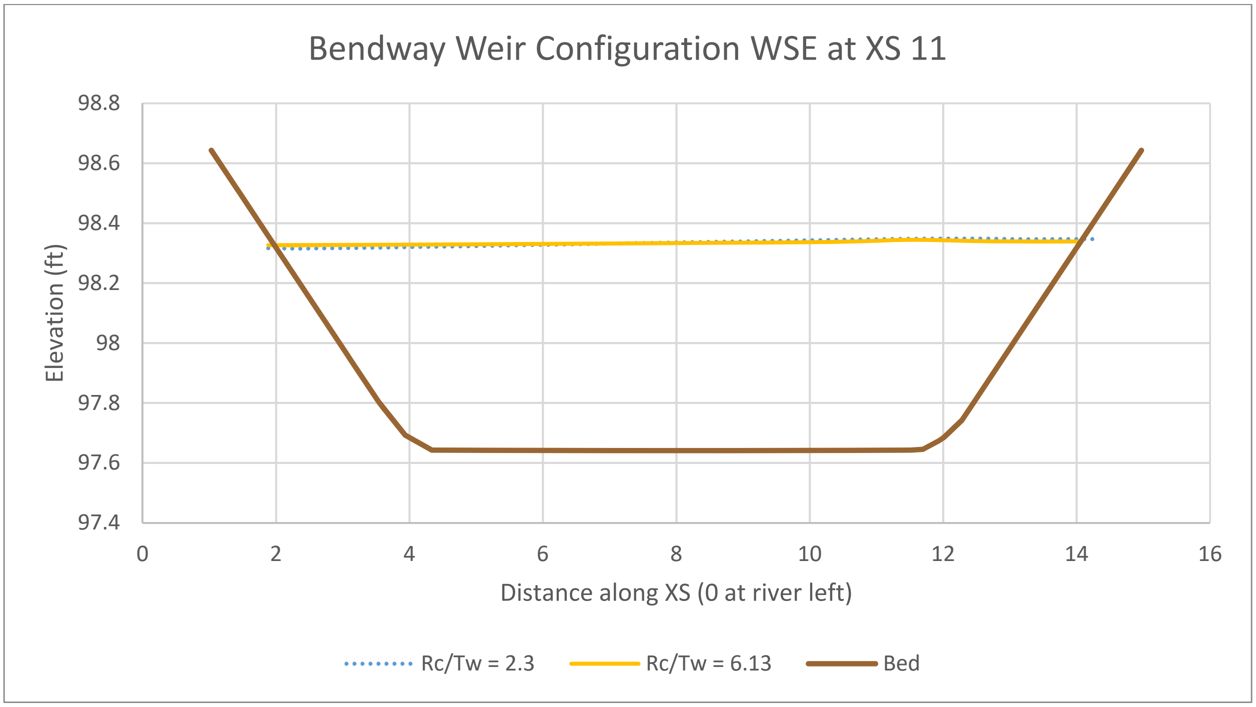

Figure 240: WSE across XS 11 in the bendway weir configuration

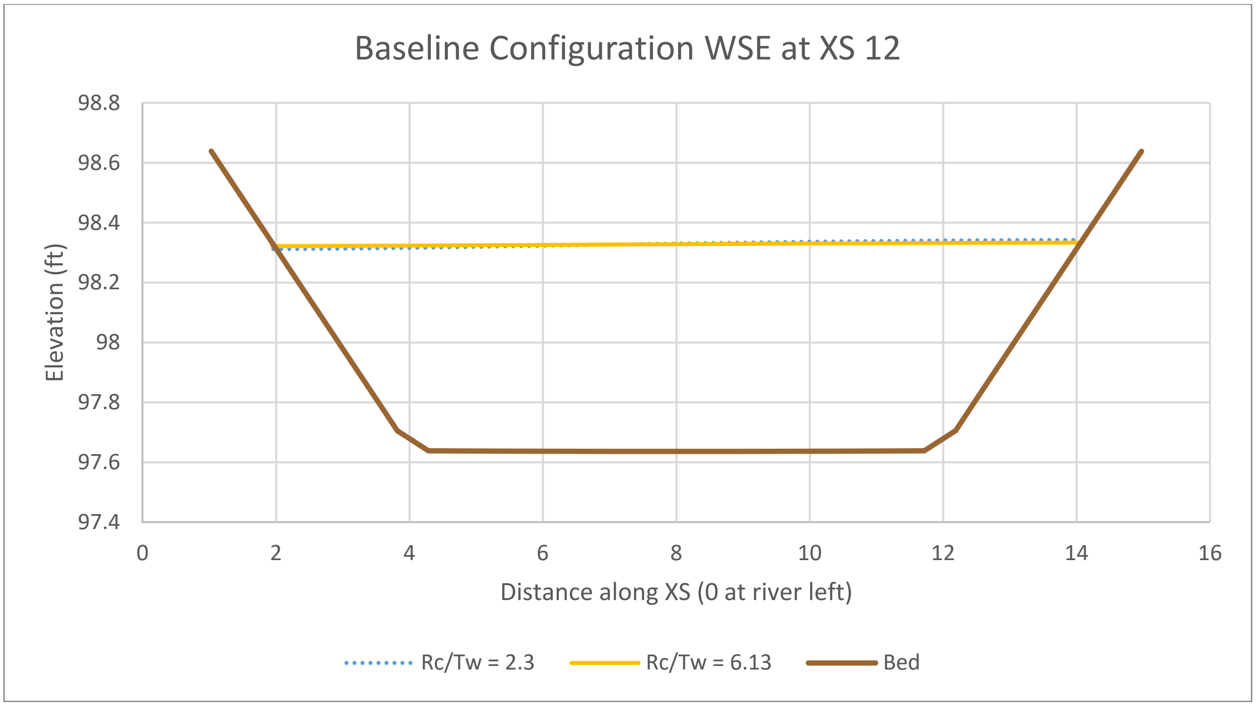

Figure 241: WSE across XS 12 in the baseline configuration

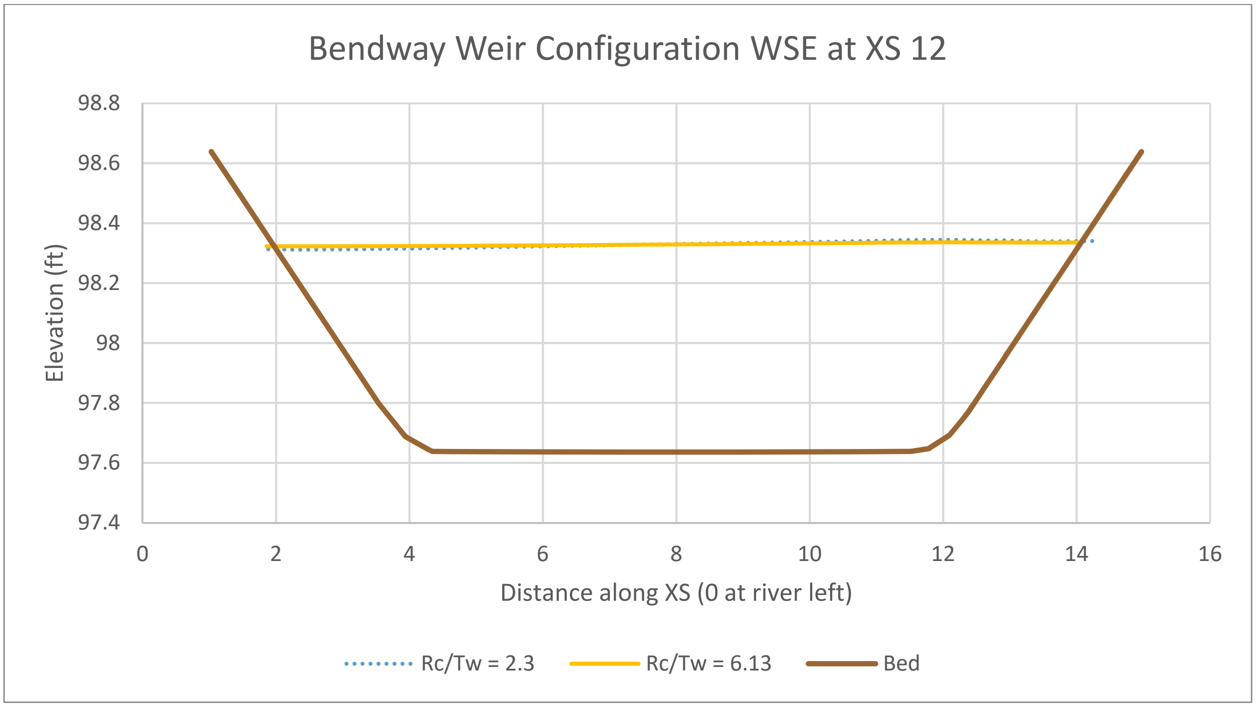

Figure 242: WSE across XS 12 in the bendway weir configuration

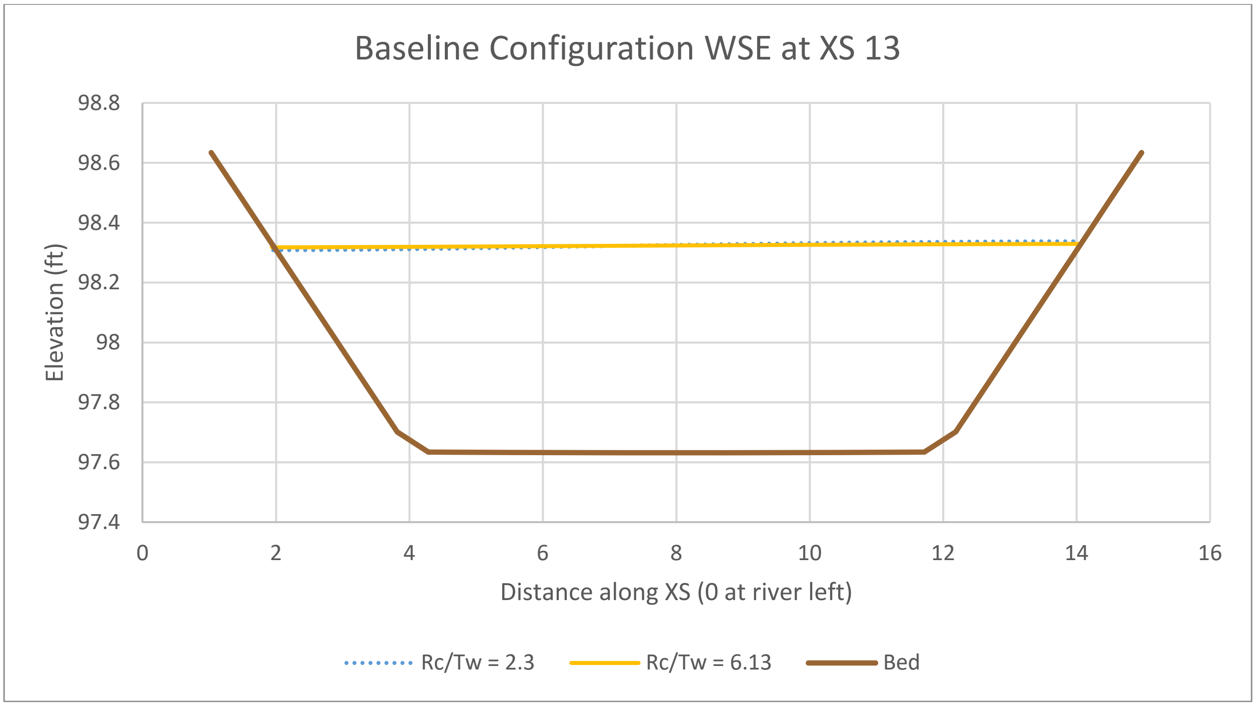

Figure 243: WSE across XS 13 in the baseline configuration

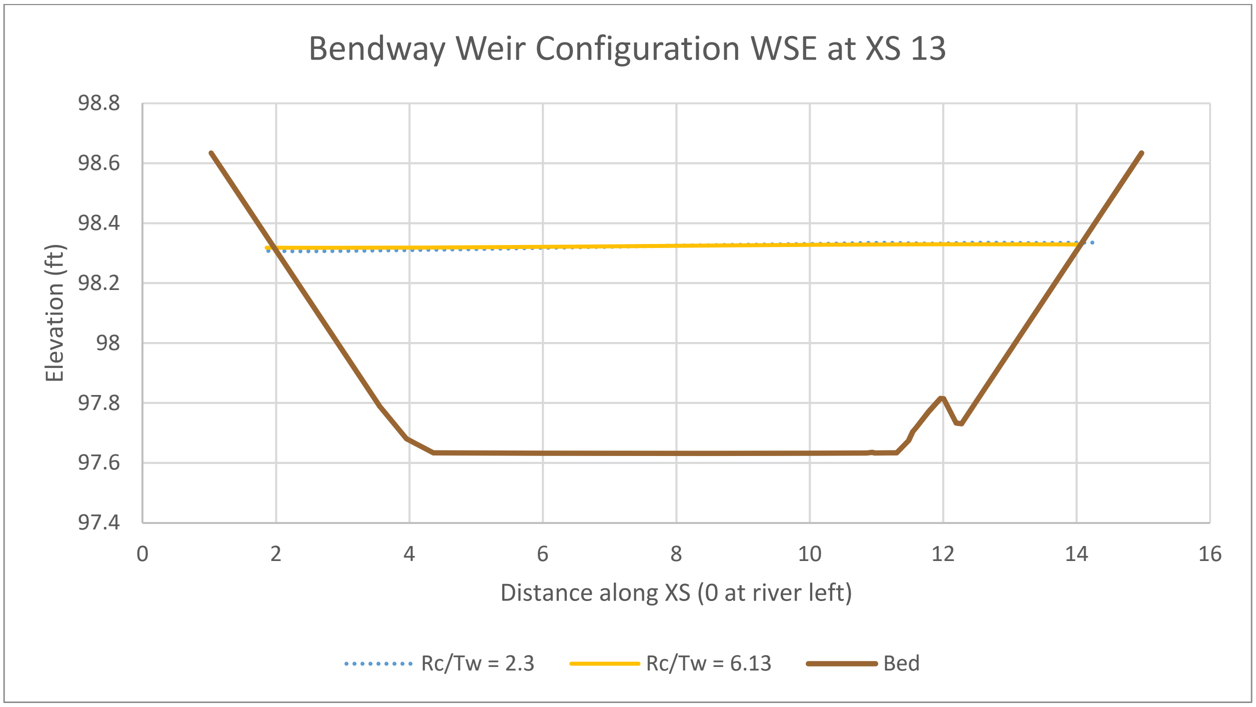

Figure 244: WSE across XS 13 in the bendway weir configuration

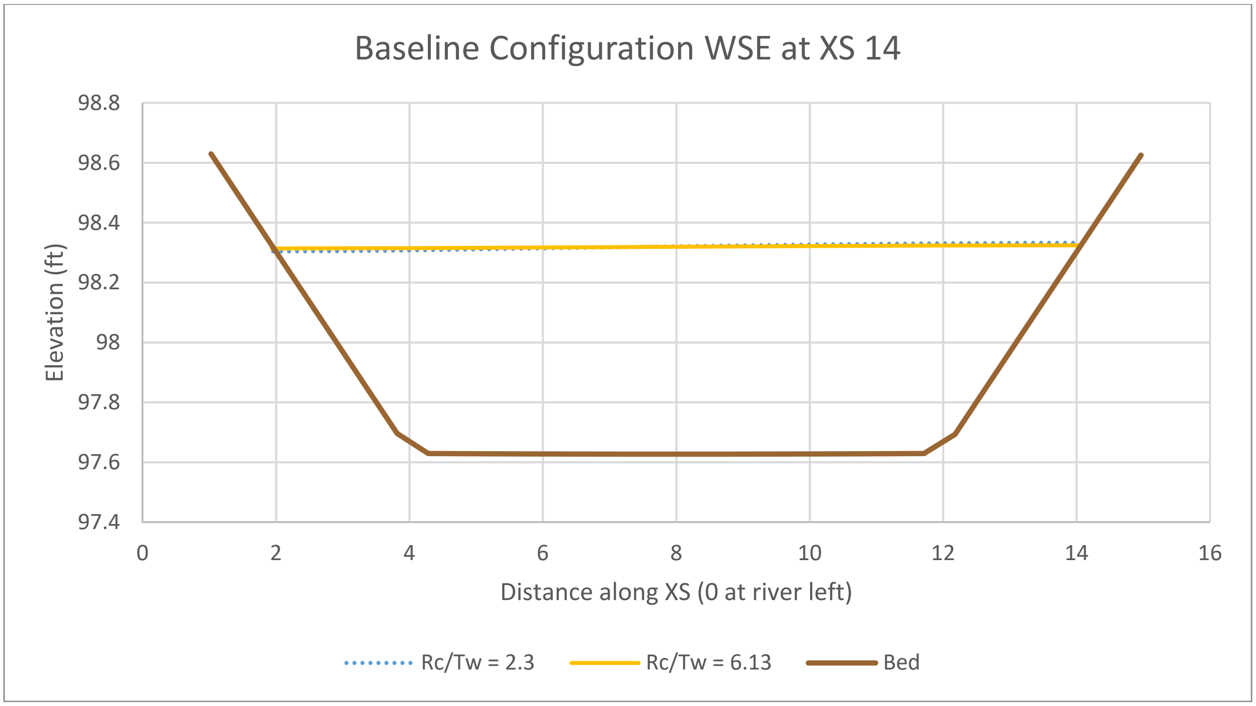

Figure 245: WSE across XS 14 in the baseline configuration

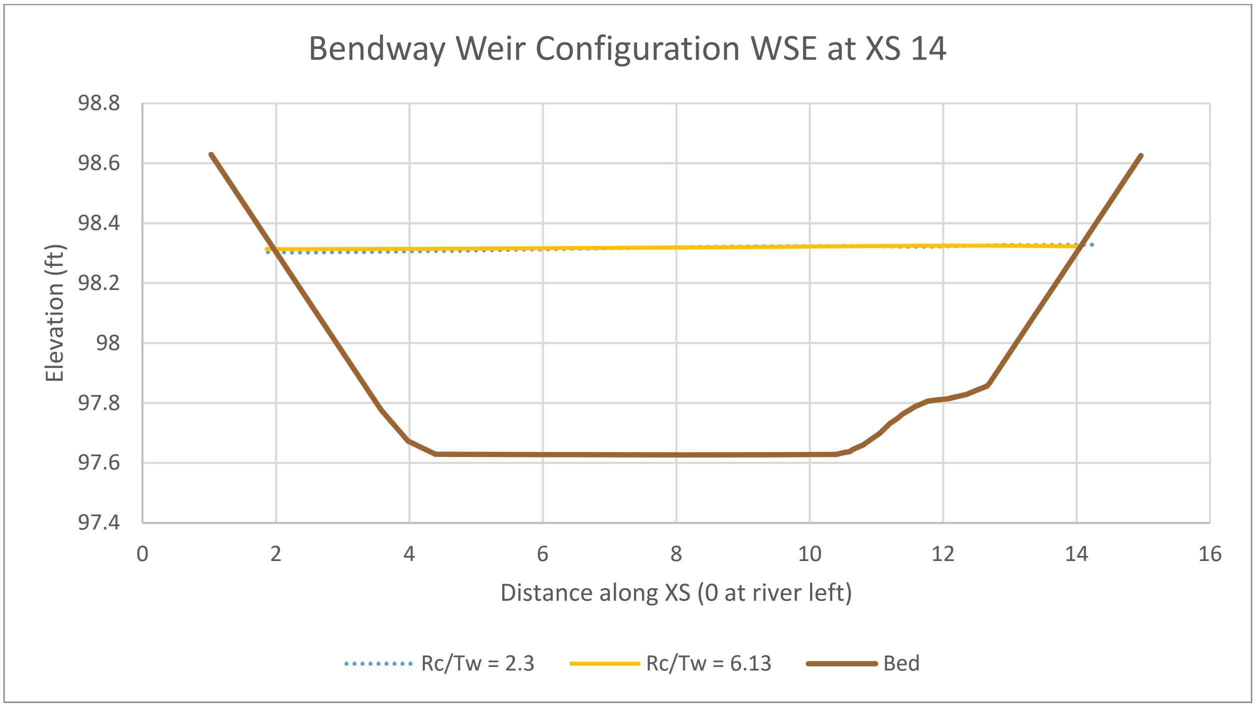

Figure 246: WSE across XS 14 in the bendway weir configuration

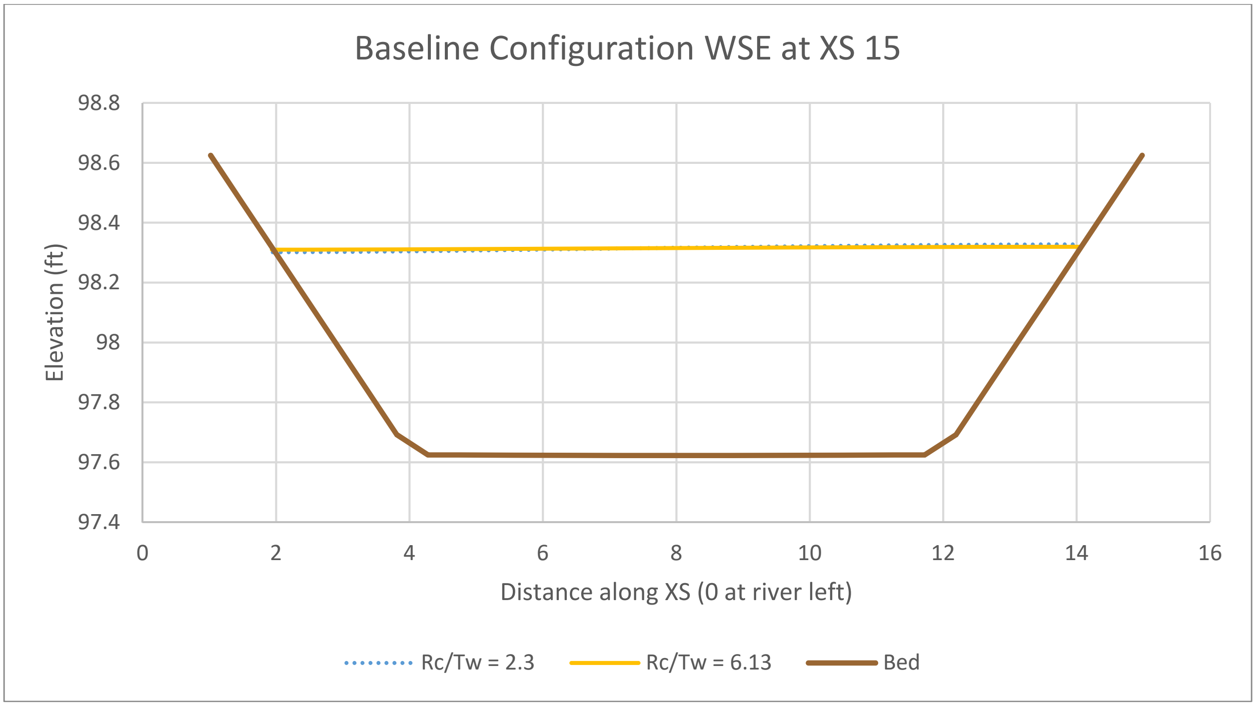

Figure 247: WSE across XS 15 in the baseline configuration

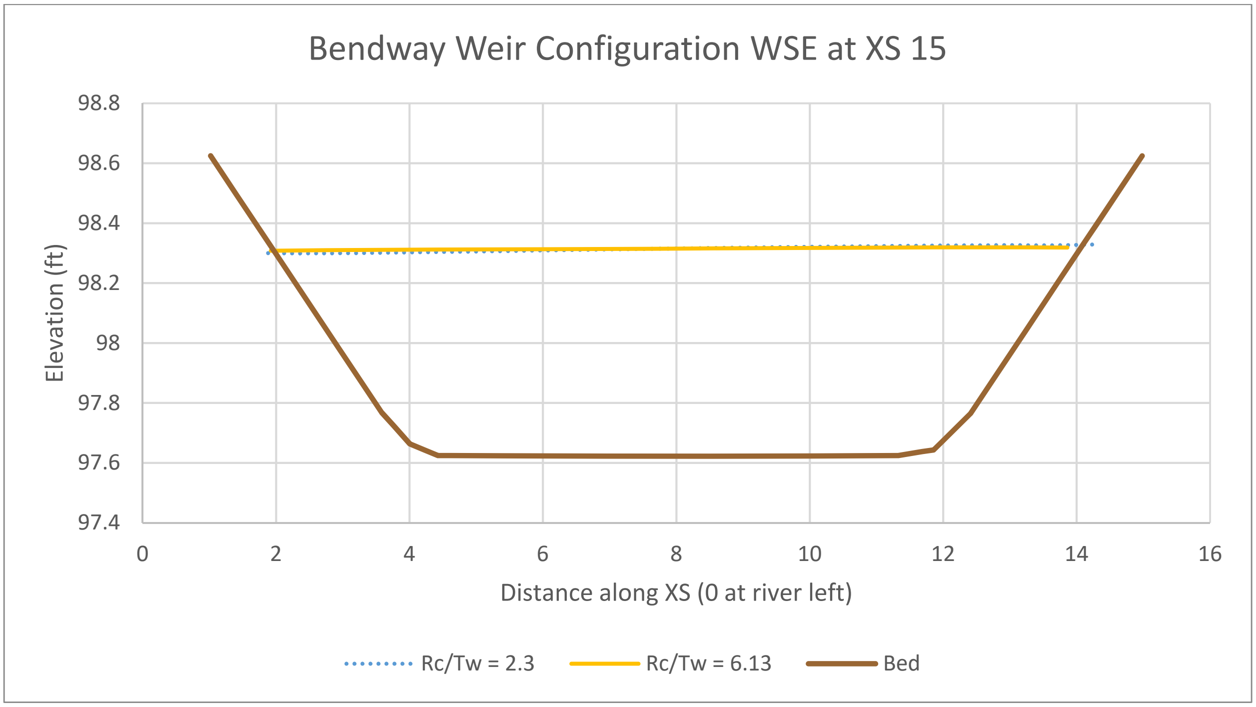

Figure 248: WSE across XS 15 in the bendway weir configuration

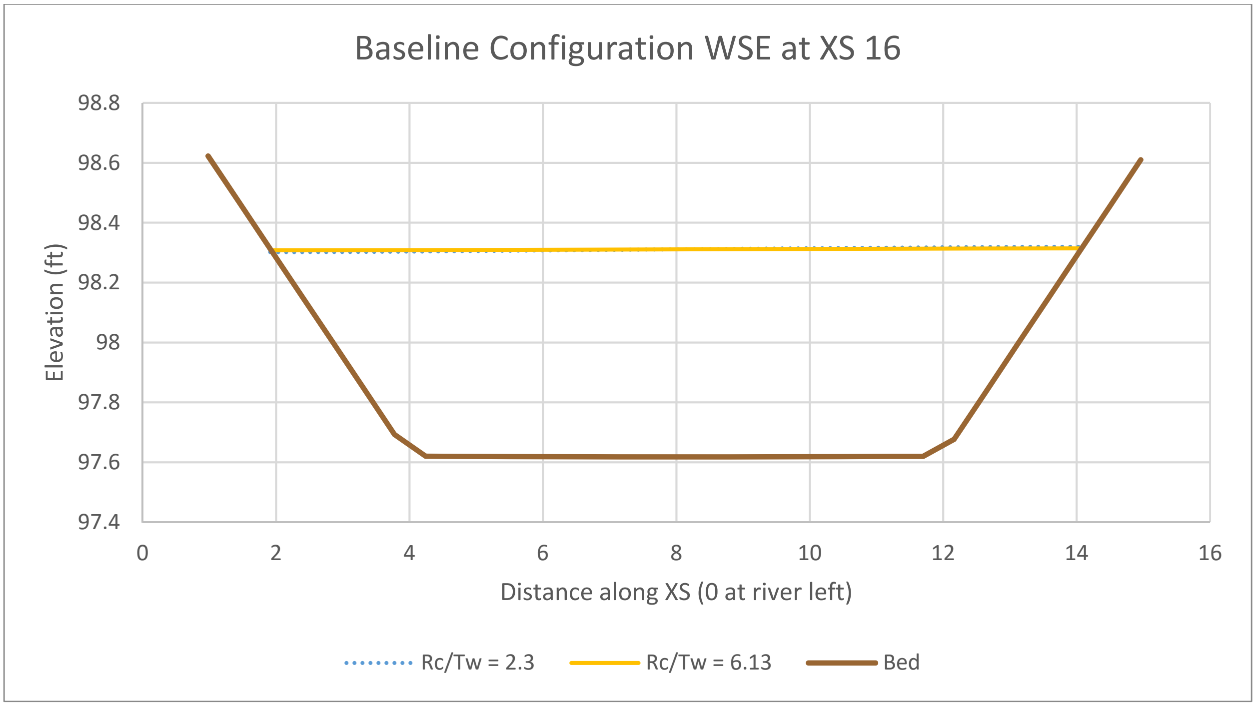

Figure 249: WSE across XS 16 in the baseline configuration

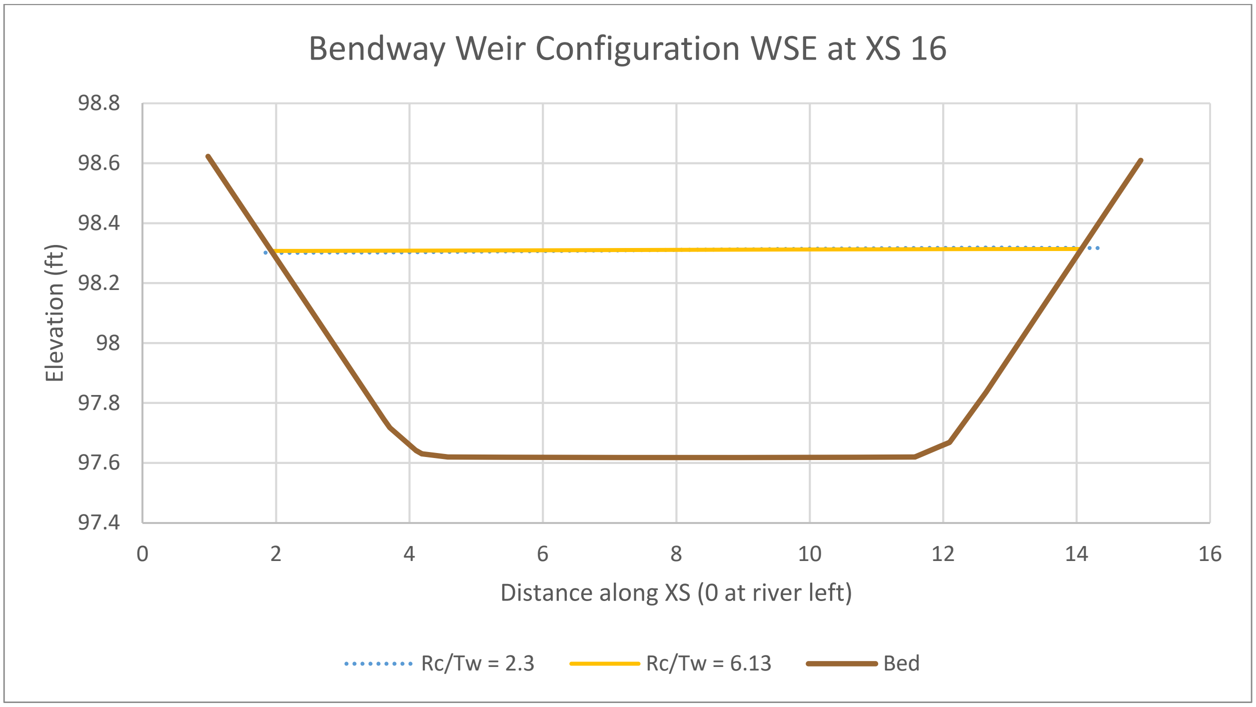

Figure 250: WSE across XS 16 in the bendway weir configuration

LIST OFABBREVIATIONS

BW	Bendway Weir
CFD	Computational Flow Dynamics
CFS	Cubic feet per second
CSU	Colorado State University
FHWA	Federal Highway Administration
FLOW-3D	3D CFD model by Flow Science, Inc.
GUI	Graphical User Interface
HEC-RAS	Hydrologic Engineering Centers – River Analysis System
LiDAR	Light detection and ranging survey system
MAPD	Mean Absolute Percent Difference
MAPE	Mean Absolute Percent Error
SMS	Surface-water Modeling System, a GUI developed by Aquaveo, LLC that runs the SRH-2D model
SRH-2D	Sedimentation and River Hydraulics – two dimensional
USBR	United States Bureau of Reclamation
WSE	Water Surface Elevation
XS	Cross-section